Synthesis, Characterization and Comparison of New Bulk Superconductors

Quentin Nouailhetas

To cite this version:

Quentin Nouailhetas. Synthesis, Characterization and Comparison of New Bulk Superconductors. Electric power. Université de Lorraine, 2022. English. NNT : 2022LORR0269 . tel-04213274

HAL Id: tel-04213274
https://theses.hal.science/tel-04213274v1
Submitted on 21 Sep 2023

Ecole Doctoral IAEM (Informatique, Automatique, Electronique-Electrotechnique, Mathématiques)

Laboratoire GREEN (Groupe de Recherche en Energie Electrique de Nancy)

Thèse

Présentée et soutenue publiquement pour l'obtention du titre de

DOCTEUR DE l'UNIVERSITE DE LORRAINE

Mention : Génie Electrique

par **Quentin NOUAILHETAS**

Sous la direction de Pr. Bruno Douine et Dr. Kévin Berger

Synthesis, Characterization and Comparison of New Bulk Superconductors

13/12/2022

Membres du jury :

Directeur(s) de thèse :	**M. Bruno Douine**	**Professeur des Universités, Université de Lorraine, Nancy**
	M. Kévin Berger	**Maître de Conférences, Université de Lorraine, Nancy**
Présidente de jury :	**M^{me} Anabela Gonçalves Pronto**	**Professeur, NOVA School Science & Technology, Caparica, Portugal**
Rapporteurs :	**M. Alvar Sanchez Moreno**	**Professeur, Universitat Autònoma de Barcelona, Barcelone, Espagne**
	M. Philippe Vanderbemden	**Professeur, Université de Liège, Liège, Belgique**
Membres invités :	**M. Michael Rudolf Koblischka**	**Privatdozent Docteur, Universität des Saarlandes, Saarbrücken, Allemagne**

Acknowledgement

First of all, I would like to thank the GREEN laboratory and the Université de Lorraine for giving me the opportunity of developing many of my skills with this PhD thesis.

I also would like to thank my colleagues and friends of the GREEN laboratory: Ghazi Hajiri, Remi Dorget, Dr. Walid Dirahoui, Boussad Moualek, Thomas Marcand, Rayan Hamidouche, Dr. Smail Mezani, Pr. Abderrezak Rezzoug, Pr. Jean Lévêque, Stéphanie Lamane, Dr. Thierry Lubin, Pr. Noureddine Takorabet, Dr. Hocine Menana, Sara Fawaz, Dr. Alexandre Colle, Dr. Bar-El-Boudour Bidouche, Dr. Jakub Kapek, Dr. Yazid Statra, Yanis Laib, Simon Chauvière and Francisco De Loredo for their warm support and welcome as well as for their help during my work.

My particular thank and gratitude go to my supervisors Dr. Kévin Berger and Pr. Bruno Douine for their in unwavering support, the time they spent for me, on my project and for their help over the redaction of this dissertation.

My gratitude also goes to Pd. Michael Koblischka from Universität des Saarlandes for giving me the opportunity to work on various subject and developing relation all over the word, as well as his colleagues Dr. Florian Schäfer and Dr. Andreas Tschöpe.

I wish to thanks Pr. Tetsuo Oka and Pr. Masato Murakami at Shibaura Institute of Technology at Tokyo, to Pr. Hiraku Ogino and Dr. Sugali Pavan Kumar Naik at AIST at Tsukuba for their warm welcome, their help and their patience.

I am indebted to Pr. Jacques Noudem and Dr. Yiteng Xing for their welcome, their help and for letting me use their facility at CRISMAT laboratory, Caen and to Dr. Thomas Hauet and Stéphanie Suire for the countless number of times I used their plateforme de magnétisme of the Institue Jean Lamour, Nancy.

I have a particular gratitude for Pr. Claire Marrache-Kikuchi and Dr. Claire Antoine for impulsing me the love of superconductivity and to Dr. Xavier Chaud for giving me the opportunity to discover more about the field of superconductivity and to confirm my will for working in it.

I address my gratitude to my father, my mother, my brothers and my close friends Lucas Gournay, Roland Cheung, Elie Servantie, Julie cailleret, Vincent Nezan and Thibault Astruc for their support along this journey and for always believing in me.

Finally, I would like to thank the French and German citizens for their financial support though their taxes without which this PhD would not have been possible.

Table of contents

Chapter I: Introduction on superconductivity and superconducting Bulks

I.1. Generality on superconductivity

In 1911, Heike Kamerlingh Onnes has observed a dramatic decreasing of the electrical resistivity inside a piece of mercury at a temperature of roughly 4.2 kelvin (K) as we can see in Figure I-1 while he was trying to liquify helium at this temperature. This phenomenon was called superconductivity.

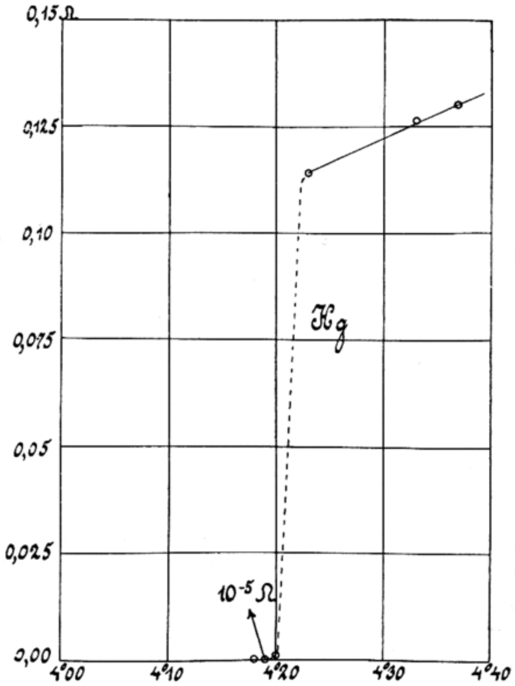

Figure I-1: Onnes discovered superconductivity by measuring the resistance of Mercury function of the temperature [1].

After this discovery, a tremendous interest on this new field of fundamental research leads to a large number of discoveries. In this way a lot of materials appears to be superconductors below a temperature called critical temperature (T_c) such as Aluminum, Lead or Niobium with respective T_c of 1.2, 7.2 and 9.3 K.

By reaching the critical temperature, when the electrical resistivity is vanished, the sample comes to a new state called the Meissner state, where the free electrons assembles in pairs called cooper pairs, which induce a perfect diamagnetism as well as a brutal evolution of the heat capacity as it is presented in Figure I-2. The direct consequence of this perfect diamagnetism is the generation of a supercurrent J_S called Meissner current on the surface of the superconductors which perfectly expels any external magnetic fields H_{ext} that can only penetrate over a thin layer called the London penetration depth λ_L (Eq. I.1) [2]:

$$\lambda_L = \sqrt{\frac{m_e}{\mu_0 n_s e^2}} \tag{I.1}$$

where m is the mass of an electron, e is its electric charge and n_s the number of carriers, i.e. the electrons.

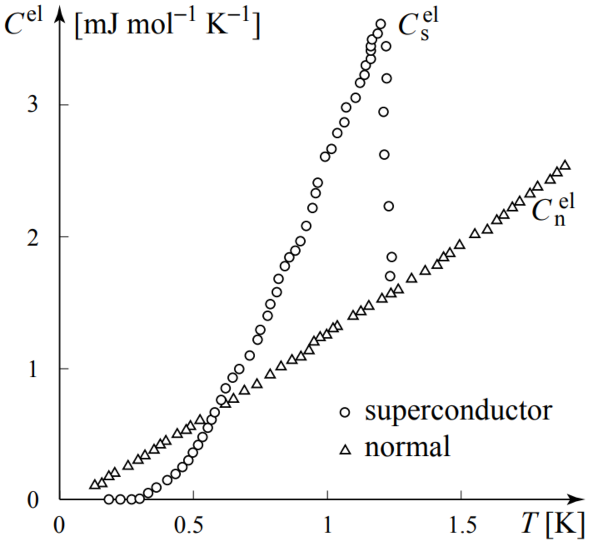

Figure I-2: Electrical heat capacity C^{el} of superconducting and normal Aluminum [3].

Indeed, this supercurrent exponentially increases from 0 at the surface of the superconductor to its maximal value at a distance $r = \lambda_L$ (Eq. I.2) meanwhile the magnetic field exponentially decreases from its maximal value, i.e. the external magnetic field B_0 to 0 over the same characteristic length (Eq. I.3).

$$J = \frac{B_0}{\mu_0 \lambda_L} e^{-\frac{r}{\lambda_L}} \tag{I.2}$$

$$B = B_0 e^{-\frac{r}{\lambda_L}} \tag{I.3}$$

Thus the magnetization $M_s(H_{ext})$ generated by the superconducting current has the exact value of $M_s(H_{ext}) = H_{ext}$ and follows any variation of H_{ext}.

However, this phenomenon quickly comes to a limit when H_{ext} reaches a characteristic value called critical magnetic field H_{c1}, then the material leaves the superconducting state, it is called a "transition". Depending on the material, this value is usually from a few milliteslas to a few hundred milliteslas. Above this value, two evolutions are possible depending on the value of the so-called Ginzburg-Landau parameter:

$$K = \frac{\lambda_L}{\xi} \tag{I.4}$$

where λ_L is the London penetration length and ξ is the coherent length responsible of the minimum length of variations of the superconducting carriers:

$$\xi = \sqrt{\frac{\hbar}{2m|\alpha|}} \text{ with } \hbar = \frac{h}{2\pi} \tag{I.5}$$

Where m is the weight of the charge carrier, the electrons, and α is a constant from the Ginzburg-Landau equations.
In a first case we have:

$$K < \frac{1}{\sqrt{2}} \tag{I.6}$$

The superconductor is of type I which means that above H_{c1}, the sample leaves the superconducting state and returns to the normal state.
In a second case we have:

$$K \geqslant \frac{1}{\sqrt{2}} \tag{I.7}$$

The superconductor is of type II which means that above H_{c1}, the sample moves into a new state called mixed state where the superconducting and the normal states are both existing in the material at the same time.
In consequence, a type I superconductor has a very narrow range of use as it leaves the superconducting state at a "low" magnetic field (below 1 T) where a type II superconductor still works in the so-called mixed state above H_{c1}.
The mixed state is characterized by the penetration of the external field into the superconductor through magnetic flux lines with a fixed value of flux called magnetic flux quantum, Φ_0 [4]. This value is a constant and is equal to:

$$\Phi_0 = 2.06783385 \times 10^{-15} \text{ Wb} \tag{I.8}$$

Those magnetic flux lines penetrate into the superconductor from the border to the center and/or though weak points where the superconductivity is weaker. In reaction to the flux lines, a Meissner current is generated around it in order to screen the magnetic field along the London penetration depth, this phenomenon is called Abrikosov vortex (see Figure I-3).

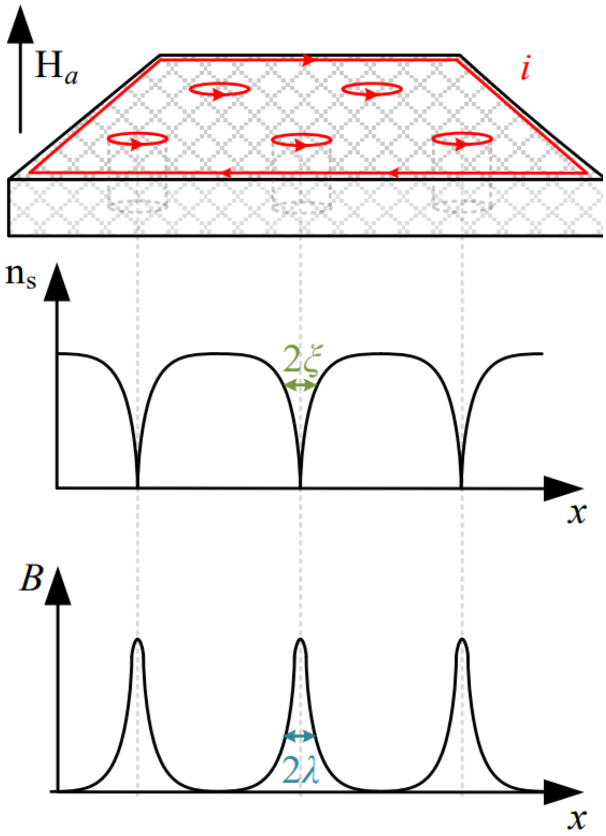

Figure I-3: Schematic drawing of an Abrikosov vortex with the repartition of the superconducting charge carrier n_s and the magnetic flux B in a superconductor where H_a is the external magnetic field and i the current.

The main consequence is that inside the vortices, the material is into the normal state and superconducting outside/between the vortices.

The number of vortices inside a superconductor increases with the value of the external magnetic field and, as vortices repel each other's, they form a regular matrix called Abrikosov matrix, Figure I-4 [4].

This mixed state is much more useful as it allows to work at a much greater magnetic field than the limited Meissner state and permits a current to flows though the superconducting area. This current can be either induced by an external magnetic field or transport current. However, as the number of vortices is increasing with the external magnetic field, the superconducting area is decreasing until a limit is reached. This limit is called second critical magnetic field H_{c2}.

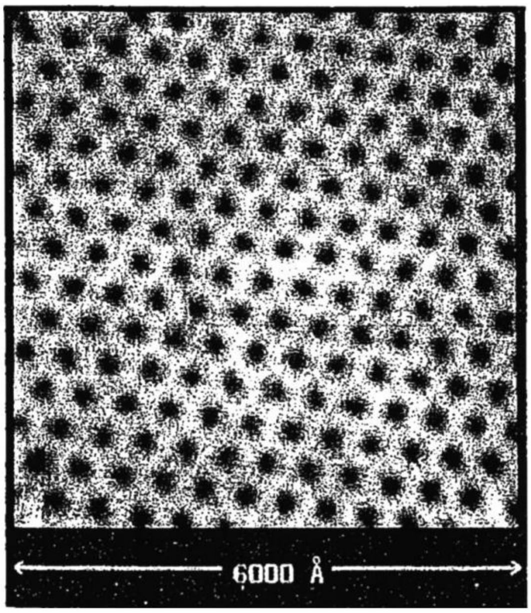

Figure I-4: Vortex lattice of a $NbSe_2$ superconductor measured by tunneling electron microscopy [4].

The apparition of those vortices arises another limit that comes with the Lorentz force induced on the vortices by the external magnetic field and the current flowing inside the superconducting part. Indeed, this force induces a motion of the vortices which causes an electrical field and so heats-up the sample. In consequence the temperature of the material increases by Joule effect until it reaches the critical temperature and then a transition occurs. Therefore, for a given magnetic field, it exists a current density where the vortices start to move, this current density will be called hereinafter the critical current density J_c.

In the literature, the superconductors are mainly compared with the following characteristic values: the critical Temperature T_c, the critical magnetic field H_{c2} and the critical current density J_c, a common way to represent those values and their close link is presented on Figure I-5.

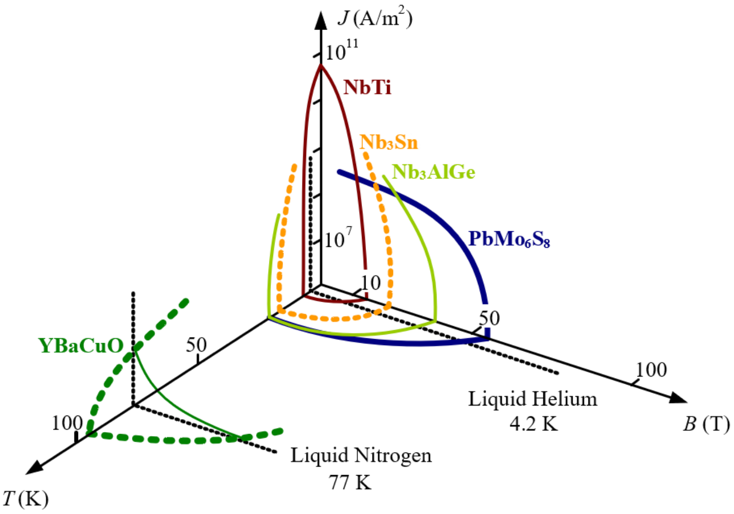

Figure I-5: Evolution of the superconducting properties J_c, B_c and T_c for various materials [5].

I.2. A large variety of superconductors

Following the formalization of the theory by John Bardeen, Leon Neil Cooper and John Robert Schrieffer in 1957, the so-called BCS Theory (which will lead to another Nobel prize in 1972), superconductivity received a wide focus along the past decades. This induces the discovery of a large number of superconducting materials as well as their tremendous development using various designs. Indeed, a lot of superconducting materials were already discovered but only a few are used in practice for various applications, a good overview comes with Figure I-6 where the successive discoveries over the past years of new superconducting materials increases the highest critical temperature.

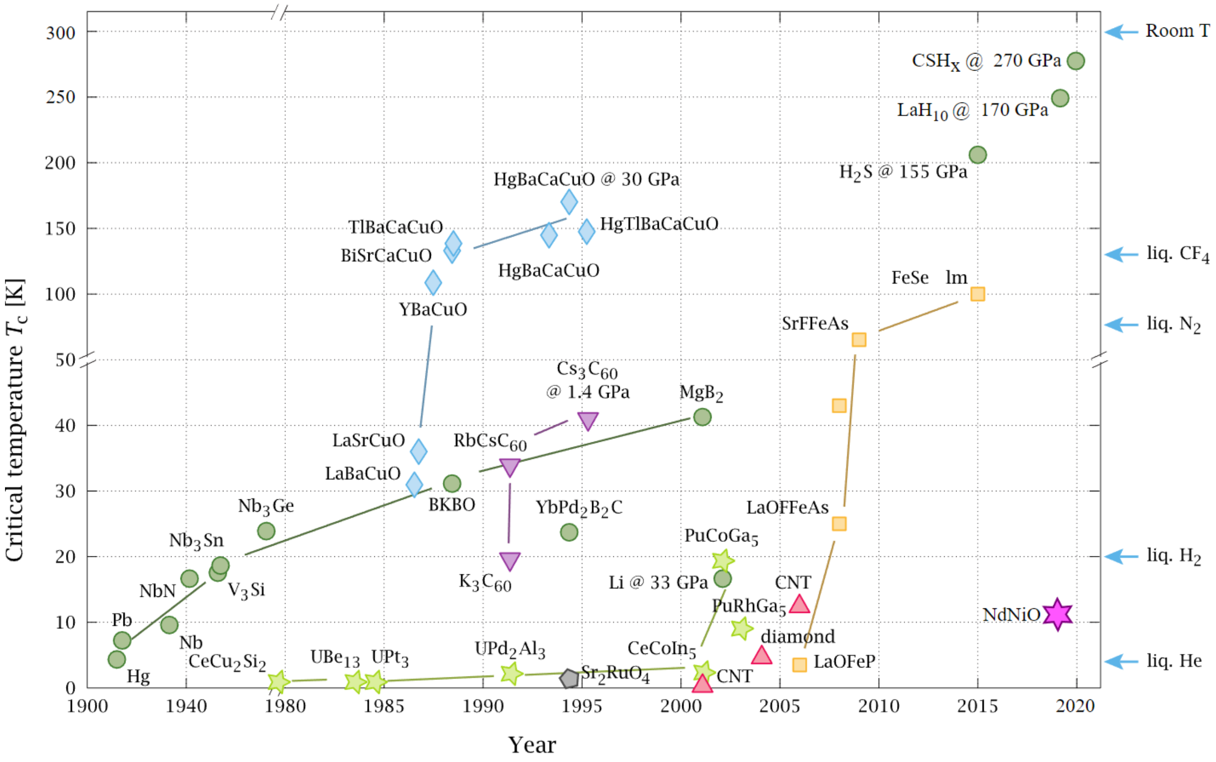

Figure I-6: Discovery one new superconductors over the time with their corresponding critical temperature [6].

An important parameter is the evolution of the critical current J_c with the surrounding magnetic field and the temperature or when using tapes, wire and cables the engineering current density J_e is also used. This current corresponds to the current density over all the cross section the wire/cable/tapes, such as the surrounding copper or the mechanical support, contrary to the critical current density J_c which is only over the superconducting cross section. The J_e of various materials and designs is roughly presented in Figure I-7. This information highlights the importance for choosing the appropriate material for an application and will be one of the guiding points of this manuscript.

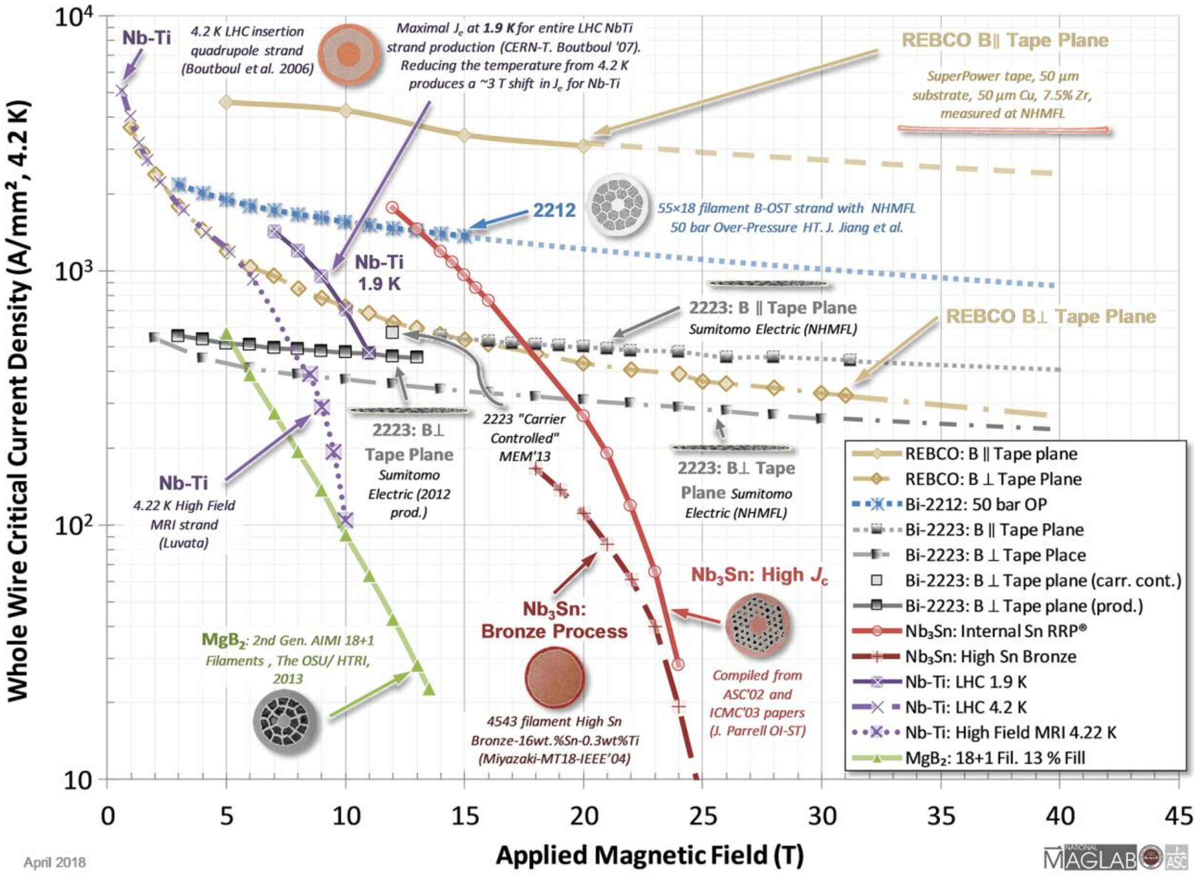

Figure I-7: Overview of the engineering critical current density J_e for various superconducting material and various designs, P. J. Lee.

I.3. Various design of superconductors

The most known design, used by low temperature superconductors, is wire made of superconducting filaments and a matrix mainly made of copper. Those wires are then assembled as a cable. To give an example, the so-called Cable-in-Conduit Conductor used for the ITER project is presented on Figure I-8.a-b with a picture of the wire. Superconducting cables also exist for many different materials, such as for the MgB_2 (Figure I-8.c) With the emergence of the HTS with the $Bi_2Sr_2Ca_2Cu_3O_x$ (Bi-2223) a new kind of design were developed: the so-called first generation of superconducting tapes (Figure I-8.d). Following this, a 2nd generation of HTS tapes arise with the development of REBaCuO (RE = Rare Earth) superconductors (Figure I-8.e). This particular design suits well with the presence of the anisotropy in Cuprates [7] and open the way of applications using HTS coils.

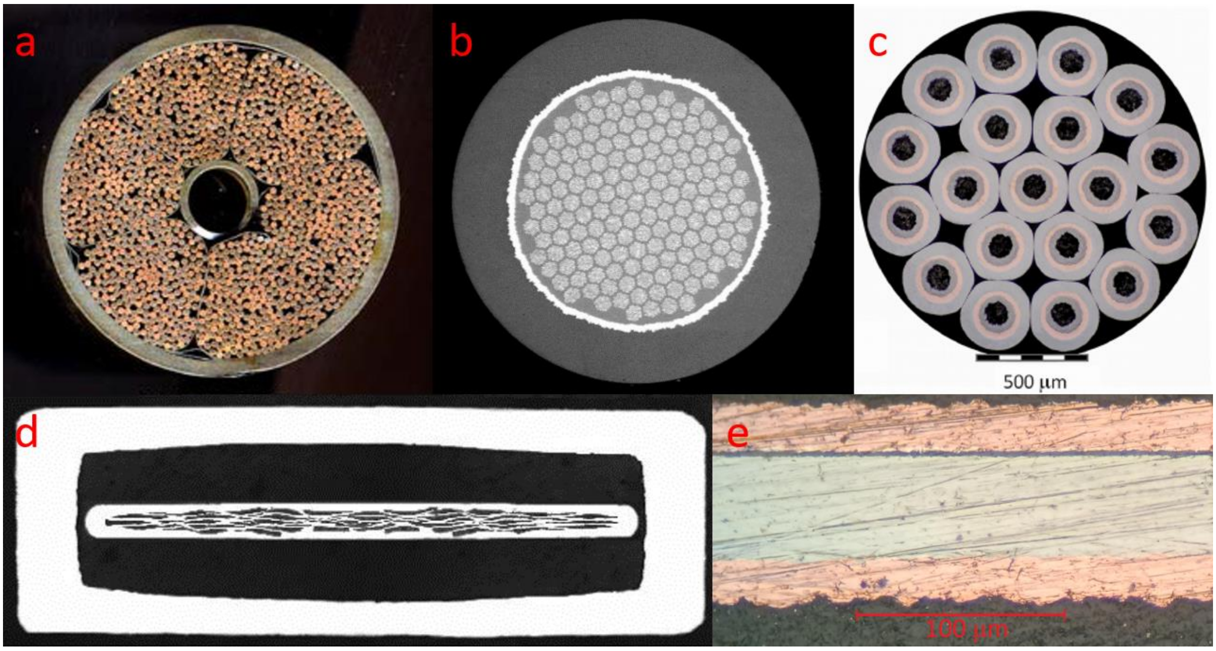

Figure I-8: Pictures of various superconducting design with the Cable used for ITER TF (a) and a zoom on a filament (b), a MgB_2 cable (c) [8], a REBaCuO tape (d) Superpower and a BiSrCaCuO tape (e) [9].

However, along this manuscript we will be focused on the bulk design. This kind of material will be defined, in this manuscript, as a macroscopic poly or mono-crystal bloc where dimensions are much bigger than the superconducting characteristic length λ_L and ξ and its fabrication does not require a particular support (contrary to a thin film or a tape based on deposition processes) or sheath (contrary to a cable). A bulk is also the easiest and cheapest way to prepares a superconductor as it does not require a lot of equipment or other complementary materials. This kind of material is used in electrical engineering, mainly as trapped field permanent magnets, magnetic shield or even current lead, so a good understanding of the superconductivity inside the bulk is necessary in order to maximize the performances.

As said, a superconducting bulk can be many different things such as a quasi-perfect single crystal, very hard to prepare and generally of a small size, perfectly adapted to measure specific properties to understand or evaluate physical phenomenon. It can also feature a high performance for a practical use as shown on Figure I-9.a with a commercial single-crystal YBCO, which could be machined in various shape as on Figure I-9.b with a hexagonal YBaCuO with holes filled with copper. They can also be polycrystal as shown by Figure I-9.c made of MgB_2 prepared by a fast sintering process called Spark Plasma Sintering (SPS). Finally, much more exotic bulks can be produced like a foam (Figure I-9.c), a very porous polycrystal made by Infiltration growth (a method detailed along Chapter IV.2) with a very complex inner structure but a promising design with many possible developments. In this way, it is necessary to use the crystallography to describe the crystal structure.

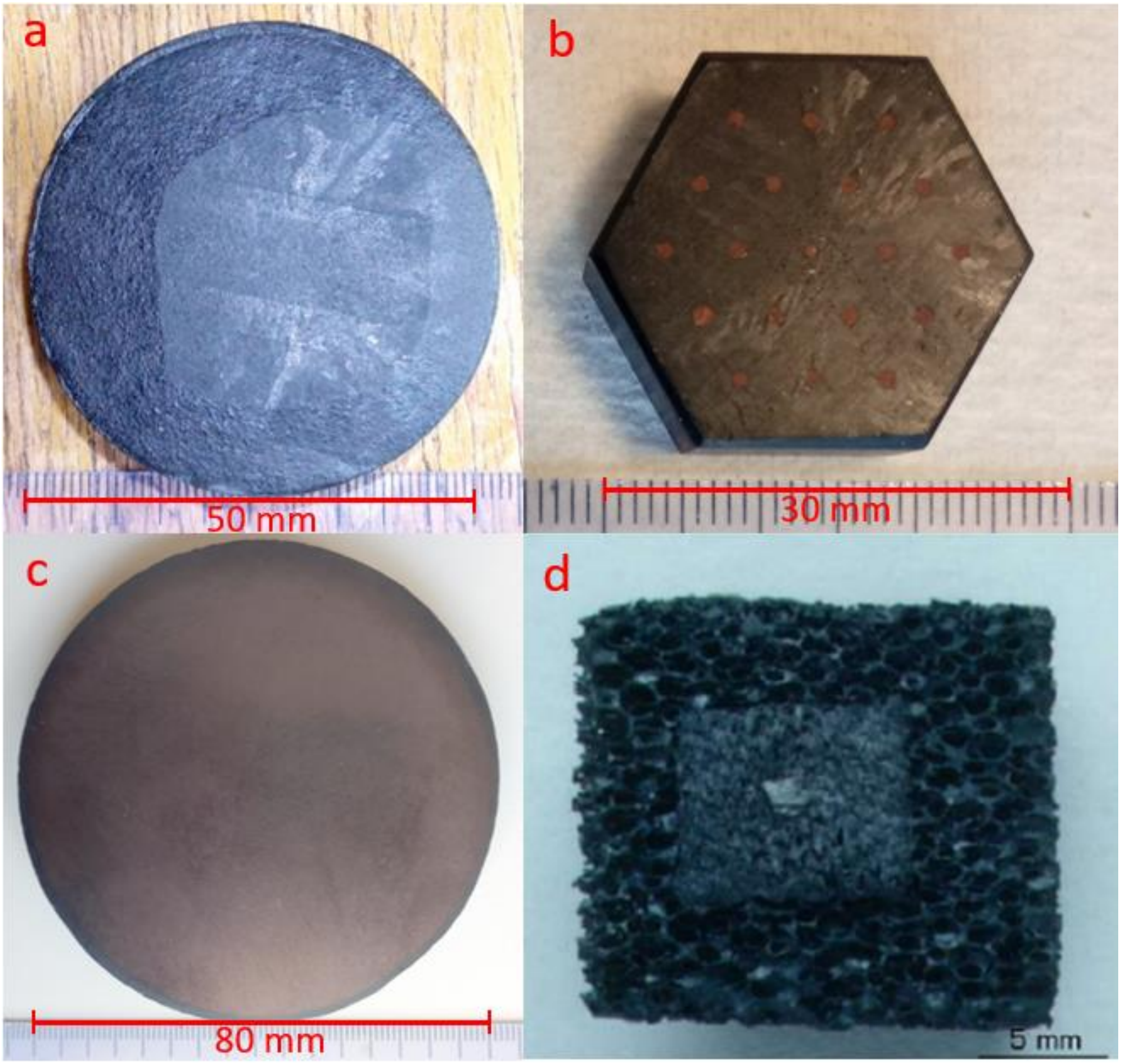

Figure I-9: Photo of superconducting bulks of various component and various design: (a) a 50 mm wide commercial bulks made of YBaCuO, (b) a commercial YBaCuO cut in hexagonal shape with holes field with copper, (c) a 80 mm MgB_2 bulk prepared by Spark Plasma Sintering by J. Noudem and (d) a 50 mm wide YBaCuO foam prepared by Infiltration Growth.

I.4. Superconducting bulk materials, basis on crystallography

I.4.a. Bonding of atoms

It is commonly known that below a certain temperature and above a particular pressure, the majority of element and alloy appears to be in the so-called solid state. This state is characterized by relatively strong links between molecules and atoms where for liquid and gaseous states the links are not strong enough to fix the structure.
To ensure the solid state, it exists different types of Bonding:

- Van Der Waals bonding: This force arises from the spontaneous disequilibrium of the charges of molecules or atoms caused by the movement of the electrons. This force is really weak compared to the others [10].
- Metallic bonding: The Valence electrons (electrons on the outer shell of an atom) of each atom are delocalized and then forms an “electron cloud” all over the group of atoms [10], [11]. This phenomenon is responsible for the properties of metallic elements.
- Valence or covalent bonding: Arises from the link made between 2 atoms that are sharing 2 or more electrons of their Valence shell [10], [12], it exists only for atoms with similar electronegativity.
- Ionic bonding: This last bond occurs when 2 atoms with a large difference of electronegativity shared electrons. Due to this difference, the electronegative atoms can attract electrons of the “electropositive” atom [10].

Valence and Ionic bonding are dominant in ceramics or non-organic structures like the superconductors discussed in the manuscript, i.e. REBaCuO and Iron Based Superconductors (IBS), this explains the relatively high hardness of those materials.
Also, when atoms form multiples links with one or several other atoms, they can form a periodic pattern called unit cell which is repeated in all dimension of the sample to forms a regular structure, a crystal.

I.4.b. Perfect ordering with single crystals

As presented above, crystal is defined as a solid three dimensional and regular framework of molecules or atoms linked together by an attractive interaction. This regular framework is called a lattice and the minimal distance made by translation between one point of the lattice to another is then called lattice parameter, as three dimensional, a crystal then possesses 3 lattice parameters:

$$|\vec{a}| = a_0, |\vec{b}| = b_0, |\vec{c}| = c_0 \qquad (I.9)$$

An elementary element of this lattice is called a unit cell and it is represented on Figure I-10:

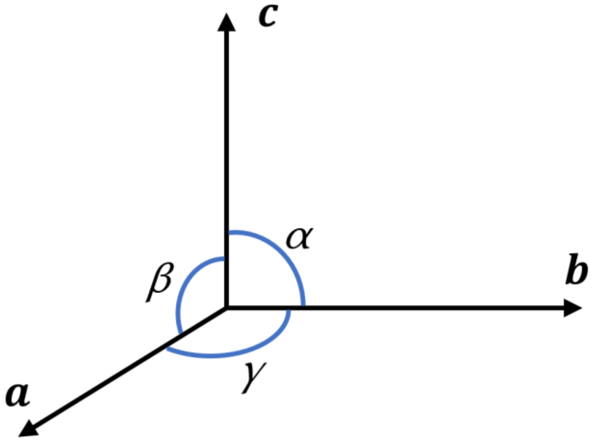

Figure I-10 : Representation of the lattice parameter of a unit cell, with the angles between each vector.

When the entire lattice can be reduced to the repetition of the unit cell by translation over the lattice parameters without irregularities, the structure is then called a perfect crystal.

It comes out that the length of each lattices parameters as well as the angles between each of them, i.e. a_0, b_0, c_0, α, β and γ, can be equals or different and each configuration is represented by a so-called Bravais lattice. There are 14 different Bravais lattices with a 3-dimensional structure and are well known and described in the literature [10], [13].

Furthermore, to study the possible symmetry of the crystal structure we will categorize then as point group. Each point group represents of particular symmetry in the crystal for a total of 32 groups for a 3-dimensional structure [10]. Associated with the 14 Bravais lattice, they formed the so-called 230 space groups. Those space groups are useful to define the crystallographic structures, properties and symmetries.

So, the space groups associated with the lattice parameters allows a discrimination of different single crystals associated with their various properties, a crucial basis of material science.

Finally, here is a simple example of a single crystal with the cubic structure lattice as it can be seen on Figure I-11:

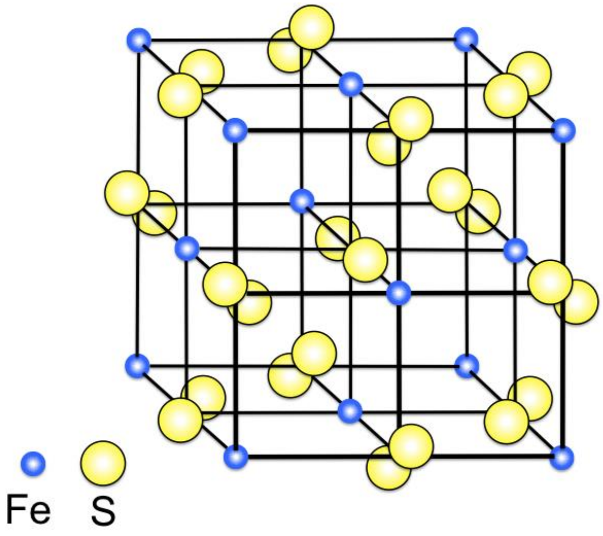

Figure I-11: Cristal lattice of a Cubic Pyrite.

I.4.c. Defects and impurities in crystals

The study of the crystal structure is manly done using the assumption of a perfect crystal, i.e. without any defect and impurities, however, the reality is highly different. Even in very high-quality crystal with a very high purity of 99.999%, where you have 10^{23} atoms in 1 cm^3, that mean you still have 10^{18} foreign atoms [10], let's say that there is more than 10^4 defect per milligrams of matter [14]. In our case it is much more as fabrication of large size superconducting crystal for practical applications makes even harder the guarantee of a good structure. To point out this problem, X-ray tomography has been realized on commercial YBaCuO bulks and the result is shown on Figure I-12. This kind of measurement highlights the high number of holes as well as their various sizes and positions. And it is only valid for "large" holes and does not measure the number of nanometric holes.

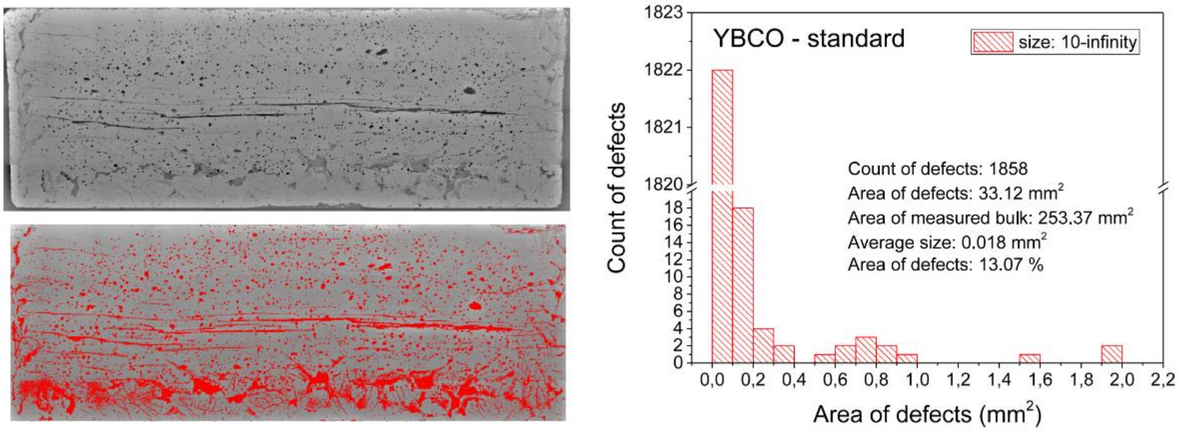

Figure I-12: Evaluation of the number of holes and cracks inside a commercial YBaCuO bulk using X-ray tomography, the red areas on the left-below pictures highlights the holes, P. Badica.

We will see that a "dirty" superconductor is even better for good superconducting properties.

Defects can be summarized in 4 different categories:

- Point like defects (0-D), it can be either a missing, a misplaced or an additional interstitial atom which creates a void or a local distortion in the crystal lattice. But it can also be due to a foreign atom, an impurity, in an interstitial space or even replacing one of the original atoms.
- Linear defects (1-D), it occurs when multiple atoms are linearly missing, misplaced or even when a complete grain or crystal is misaligned then a linear void is created.
- Surface defects (2-D), Similar to Linear defect but it's occurs on a 2-D plan, not a 1-D line.
- Bulk defects (3-D), Also similar with the 1 and 2-D defect but with a 3-D one when a foreign grain of impurity or a void is present.

Those various defects are generated by different processes which could be undergone:

- Precursors and elementary powders used in the process can't be perfectly pure as well as the surrounding atmosphere during the experiment, so foreign elements will pollute the sample during its fabrication.

- Creating a perfect crystal requires to cool down the bulks infinitely slowly which is, of course, impossible so the fabrication itself induces irregularities in the crystal structure and so a lot of structural defects of each dimension appeared.
- A bad protocol or synthesis process can lead to the generation of secondary phases [15]–[18] which can act as impurities when the ratio is low or can hold large areas and produce polluting properties or reduce/obliterate the desirable properties of the main phase.
- During the sample's life, all the interaction and stresses can induce new defects, such as the diffusion of impurities, chemical reactions but also mechanical stresses and chocs. Even more, high energy particles, i.e. irradiation, can induce point like defect by displacing atoms or performing nuclear reaction or even columnar/linear defect when the particle is energetic and big enough [19]–[25]. More generally, those processes are involved in the so-called aging phenomenon.

But the defects could also be induced intentionally:

- One can add one or several supplementary materials with the precursors which will act as doping element(s) present all over the sample or using a voluntary bad stoichiometry for using remaining secondary phases to enhance the superconducting properties [26].
- The doping element can also be joined after the synthesis via a diffusion process where the doping element will progress though the crystal from the border to the center (or top to bottom) using interstitial space or defect and accelerate using mechanical or thermal excitation [19], [20].
- Another technique will use some pillar of foreign materials of nanometric scale.
- Columnar or point like defects can also be created using heavy ion irradiation which can be done on several high energy particles accelerator [24].

The roles besides these induced defects is to upgrade or activate various properties. In this manuscript we will only briefly described the role of "artificial pinning or holes" or doping processes for their purposes on the superconducting properties.

A common way to improves superconducting properties of a superconductor is via doping processes where foreign materials change the lattice parameters [27], the number of superconducting electrons [28], [29], the electrical properties [30], [31] or even act as non-superconducting area and so as pinning sites as described in the first section of this chapter. Sometimes it appears that inducing defects, reaching a level of doping or distorting the crystal lattice is necessary to induce superconductivity or make it "useful". Such as the superconductivity in the PbO-type structure of the Iron-Selenide complex with a 1:1 stoichiometry which can reach a superconducting state below 9 K with a particular deficiency of Se or a doping of Selenium holes which distorts the FeSe crystal [32]. Another example comes with the $YBa_2Cu_3O_{7-x}$ or other cuprates complex where the superconducting properties is very dependent of the level of oxygen controlled during a diffusion process, the so-called oxygenation step [33]–[36].

As a vortex has a cylindrical shape, the best pinning site is of course also a cylinder of the same shape and size, it naturally comes out that a columnar defect of few nanometer could offer very interesting improvement of the pinning force and acts as pinning center for the Abrikosov vortices, even more if the defects are homogeneously distributed all over the sample. This could be performed using the so-called artificial pinning technique which consists of producing nanoscale pillars in thin films or superconducting tapes [37].

Finally, high energetic particles, though irradiation processes, can cause point like defects by displacing atoms or change them via nuclear reaction (electron, neutron, proton irradiation) or they can cause columnar defect when the particle is heavy (heavy ion) [21]-[23].

I.4.d. Single crystals versus polycrystals

Single crystals represent the majority of the superconducting bulks where, of course, a lot of defects are present. They have the advantage of being "simple" to study, close to the theoretical development of the materials properties and so the experimental development. However, they have an extensive preparation time or even very long for large sizes (several cm of diameter), an obstacle for an industrial production needed for electrical engineering applications.

In this way, a second type of bulk can bring some solution, the so-called polycrystal.

A polycrystal is basically made of several tiny microscopic crystals linked together in a macroscopic structure. Those microscopic crystals can have various sizes due to the starting material such as the size of the precursor powder but also the synthesis protocol like the synthesis time.

Another important point is that a macroscopic single crystal needs a slow cooling rate, needed for the formation of a coherent crystal [38] which is the exact opposite for a polycrystal where the cooling rate can even be instantaneous using the so-called "quench" cooling (very fast cooling rate with the help of cold water or air, metallic surface, …) [39].

Finally, the preparation of a polycrystal can be made using technics/machine unadopted for the preparation of single crystal but with a high industrial stability.

For those questions of time saving and industriability, polycrystals offer multiple solution compared to single crystals and their development should be considered important for applications in electrical engineering where large-scale low-cost productions are a need.

I.4.e. Analysis of a polycrystal

In a polycrystal, each grain could have a different size and/or shape but they are generally considered as small spheres and their sizes are averaged. This leads to the apparition of multiple voids and also interstitial areas called the grain boundaries. Those areas can be either the space between 2 grains and the border of the grain responsible for some skin-effect. A picture done with the help of a Scanning Electron Microscope (SEM) is given with Figure I-13 with the global structure (Figure I-13.a) of a polycrystal of Iron-Selenide (FeSe) with the presence of holes. A zoomed picture with visible grains and grains boundaries (Figure I-13.b). And an Inverted Pole Figure (IPF) showing the orientation of the crystal for each grain (Figure I-13.c), highlighting the random orientation.

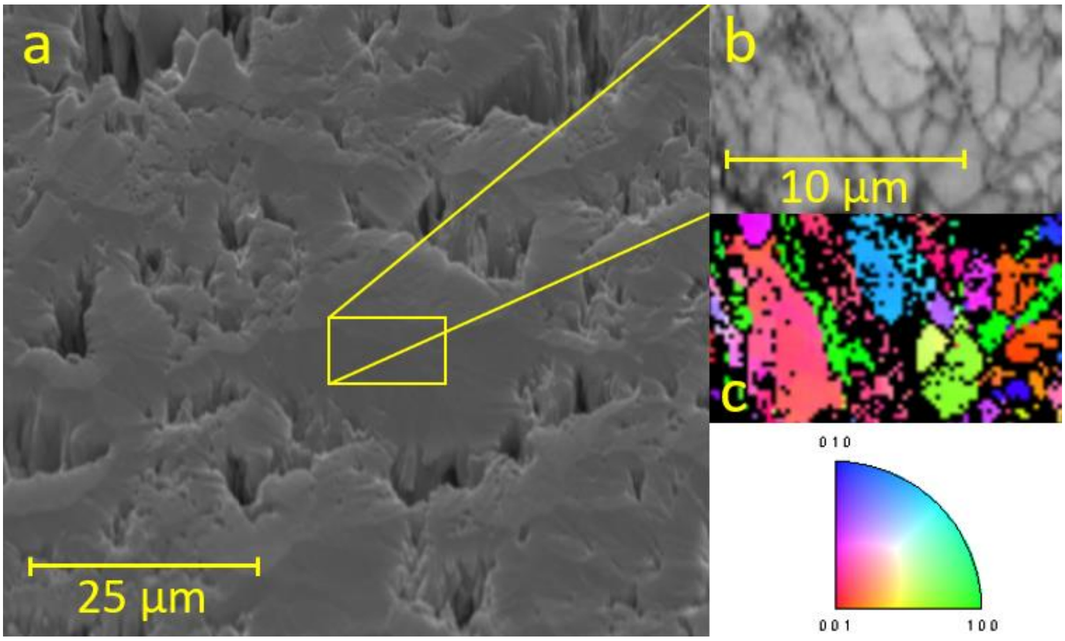

Figure I-13: Pictures taken with a scanning electron microscope of a FeSe polycrystal where we can see the holes (a), the grains (b) separated by the grain boundaries (black cracks) and an inverted pole figure showing the orientation of the crystal within each grain.

When the grains are mainly considered as “perfect” crystals, the grains boundary is considered as a very irregular, polluted and chaotic area. This inhomogeneity of structure induces a lot of defect and/or irregularities in the grain boundaries area.

Indeed, as its role is to fulfil the gap between 2 grains of different orientations, its crystal structure is necessarily made of misalignments and void [40]. Also, all the foreign elements from the crystal and/or doping will be more concentrated in this area [30].

This leads to potential tricky properties such as very different mechanical properties and electrical/thermal conductivity. Even more important, it has a huge effect on the superconducting performances of the bulk, its bad crystal quality makes this area less or not superconducting, this diminution of the J_c and critical/irreversible magnetic field limits its capacity of carrying high current density.

When a high superconducting current can be generated inside each grain, the grain boundary can hardly transmit it which greatly reduces the transport current as well as the magnetic moment after a magnetization process.

This is the occasion to introduce the concept of intragrain and intergrain currents, respectively present in each grain and all over the bulk. Some works in the literature were focused on the differentiation of each current using magnetization experiment [16], [39], [41]–[43] and some studies add a third kind of current, the surface current [41], [43].

This third current should be mainly present when the grain boundary is of bad quality and so this surface current act as a shell or barrier [44] which could be responsible of the asymmetry of the magnetic moment of many polycrystalline bulks [41], [45], [46].

Despite having serious drawbacks, polycrystalline superconductors have to be considered for applications and many of those drawbacks can be reduced/solved with a good synthesis protocol.

I.5. The presence of superconductivity in technologies and applications

Following the development of type II superconductors, superconducting materials reached a milestone in their readiness. Then, technologies using superconductivity arose over the past years using various designs such as wires, tapes, cables or bulks, so let's make a focus on those different type of designs.

One of the main uses of superconductor is for experimental research using large scale instruments. Among them we can find accelerator facilities that need superconductors as accelerating cavities or high field dipole magnets like for the LHC as it is presented on Figure I-14.a,b [47], [48] or fusion facilities, i.e. TOKAMAKs as shown by Figure I-14.c [49]–[53] and Stellarator, Figure I-14.d [54], [55], where high field magnets are needed.

Others widespread applications of superconductors are for MRI where large magnets with a very stable magnetic field are needed [56] or high field magnets for experiment in Laboratories, Figure I-14.e [57].

For those applications the currently used material is the Niobium-Titanium alloy (NbTi) because this material is really well known and can easily be prepared as cable using classic metallurgic processes. It also has really good hardiness and its superconducting properties are good enough for many of the precedent applications but always at the liquid helium temperature [48], [50].

However, new projects are aiming stronger magnetic field in order to reach new millstones, on this way, the new generation of fusion facilities need larger magnetic field to reach the so-called “breakeven” when the plasma is generating as much energy as it needs to heat itself or for bending more energetic particles in accelerators. For this purpose, Niobium-Tin (Nb_3Sn) was developed as a successor of the NbTi and gives access to a greater magnetic field (up to 30 T) but still at the liquid helium temperature of 4.2 K even if they are harder to produce and much more fragile [58].

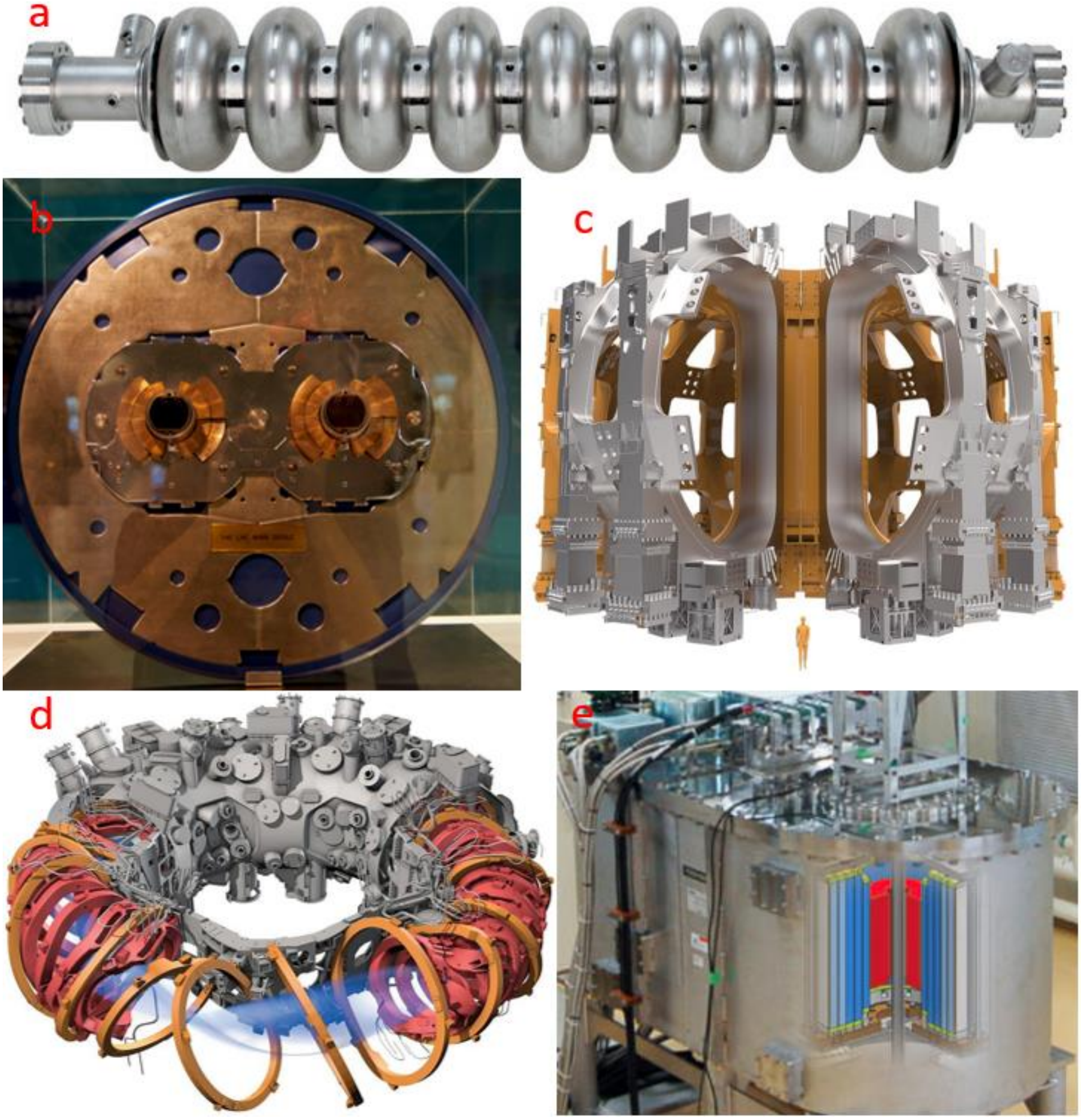

Figure I-14: Pictures or sketch of various superconducting materials for large scale experiments:

- *a) Pure superconducting Niobium cavities for accelerator [59].*
- *b) Cross section of the NbTi superconducting dipole magnets of the LHC, CERN.*
- *c) Representation of the Toroidal magnet of ITER made of superconducting* Nb_3Sn *and its mechanical support structure, ITER.*
- *d) Sketch of the Stellarator Wendelstein 7-x with a view on the superconducting NbTi magnet (orange rings), Max Plank Institute.*
- *e) The 25 T fully superconducting magnet of Tohoku University at Sendai, Japan. It is made of, from the outer extremity to the inner one: NbTi,* Nb_3Sn *and BiSrCaCuO/YBaCuO.*

Nevertheless, the relatively low critical temperatures, 9 K for the NbTi and 18 K for the Nb_3Sn and the price of liquid helium limit the use of superconductivity for electrical engineering, even if it has been tried [60], [61]. It is explained by the limitation of the designs because of the logistic capacity "on-board" as well as the production price as the objective are mainly industrial, not only for producing knowledges.

These limitations were overcome by the arrival of the High Temperature Superconductors (HTS) with the Cuprate family, mainly with the Rare Earth, Barium, Copper, Oxide (REBaCuO with RE = Y, Gd, Sm, …) [62] and the Bismuth, Strontium, Calcium, Copper, Oxide (BiSrCaCuO) [63] and their respective critical temperatures of 93 K ($YBa_2Cu_3O_{7+x}$ alloy) and 108 K ($Bi_2Sr_2Ca_2Cu_3O_{10+x}$ alloy). It is even more attracting as their critical temperatures are much higher than the one of liquid nitrogen (LN_2) which is 77 K, a very cheap and inexhaustible cooling liquid. More recently the development of cryocoolers also allows a use at temperature above 4.2 K with no need of external cooling liquid supply. Systems employing a cryocooler are called "cryogenic free" or "dry".

In this situation, a lot of tentative for using superconductors in electrical engineering applications arise for many purposes. We can point out a use as resistive type fault current limiter [64]–[66] to prevent faults where the superconductor is used for its capacity of having a wide increasing of resistance with a too high current, i.e. when the current is above the critical current I_c a quench occurs. They can also be used as a filter [67], an example is presented in Figure I-15 with a non-inductive superconducting coil.

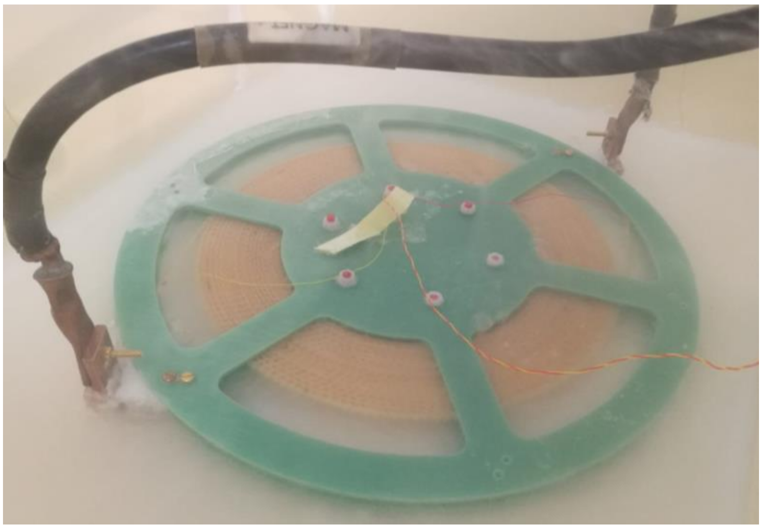

Figure I-15: Picture of a non-inductive superconducting coil made of HTS YBCO tapes for a power filter [67].

Another promising tentative is represented by AC/DC cables for current transport using LN_2 as coolant and some project are already existing [68]–[70] as well as others are under consideration or progress [71]–[73].

We can figure out a use in energy storage with the Superconducting Magnetic Energy Storage (SMES) [74], [75] for military, electrical engineering or space applications.

Superconducting electrical motors are, as well, at the center of many project for various purposes with different designs like for electrical aircraft [76]–[80] where project already achieved a high readiness for an in-situ test [81]. They are also studied for a use in ships

[82], wind generator [83] or even linear motors for levitation trains like the Maglev [84]–[86].

The development of bulk superconductors plays a crucial role into the performances of superconducting motors where they are used as magnetic screens [76]–[78], [87] (one exploded view is presented on Figure I-16) or as permanent magnet [79], [80].

But this design, simple and cheap, compared to wire or tape designs, is expected in more exotic applications such as in Docking system for satellite [88], portable MRI [89] and then plays a central role for the development of electrical engineering applications using superconductors. Also, as they are the simplest way to prepare a superconductor, they lead the discovery of new materials and it is then used prior to the development of other designs. This is why, through this PhD thesis, it has been decided to study the possibilities of preparation, synthesis, development and comparison of bulk's shape superconductors with a focus on electrical engineering applications.

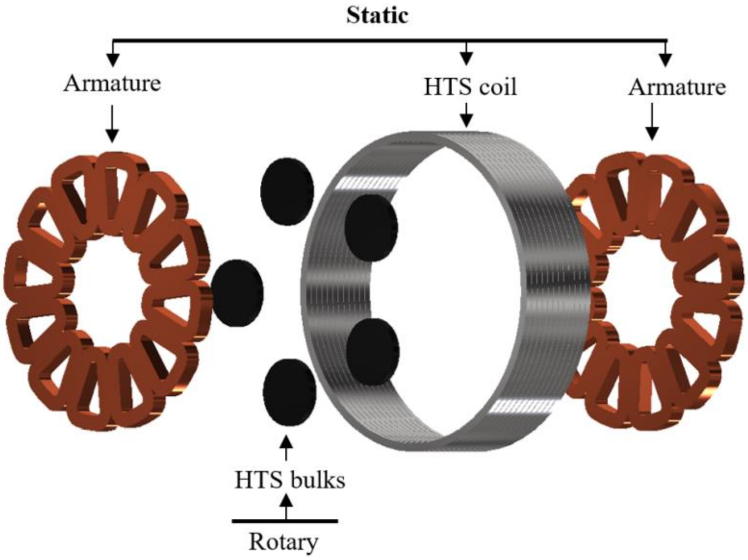

Figure I-16: Exploded view of the axial flux modulation machine prepared for aircraft applications design in GREEN [87].

I.6. The context, current research subject and the goals

Nowadays, the environmental consideration as well as the rarefaction of fossil fuel induce a wide focus on the development of alternatives to thermal motors as well as the optimization and modernization of the electrical grid of a country which make superconductors an important part of the near future.

Also, bulk superconductors are known enough to be seriously considered as a good alternative to ferromagnetic permanent magnets, such as the famous Neodymium-Iron-Bore. Several different materials are under consideration and their performances are constantly increasing so we need an extensive and continuous characterization of their superconducting but also material properties.

As example, the Magnesium-diboride alloy was discovered in 2001 and it is now disponible as a superconducting wire or bulk with great properties [15], [90]–[93] and those properties are constantly optimized. In consequence, this material is now considered to be used in many ongoing projects [87], [94]–[96].

The material is only a part of the problem, on the other hand the design, the synthesis process and/or the post-process have seriously to be considered. Surely, we spoke about the use of tapes, cables, wires, thin films or bulks for different type of application regarding the characteristic or the price or even the availability but even among bulk superconductors it exists many kinds of single and polycrystals and they need as well to be characterized and compared regarding the different applications.

In this way, an international collaboration between Université de Lorraine and Universität des Saarlandes was born with the help of the ANR/DFG grant SuperFoam (ANR-17-CE05-0030 and DFG-ANR Ko2323-10) on the exploration of new superconducting materials, focus on the characterization and comparison of superconducting bulks with exotic materials, fabrication processes or shapes such as a so-called superconducting foam [97], previously shown on Figure I-9.d.

I.7. Objectives of this PhD thesis

This PhD thesis, a part of the SuperFoam grant, takes place into that environment where many new superconductors are developed, optimized and prepared with a large number of various protocols. Each of them needs to be deeply characterized by different ways and a systematic rigor in order to be compared to each other and then brings out conclusions regarding potential applications.

Hence, along this manuscript an overview of the work done along the past four years will be detailed as follow:

- Along the first part, we have defined the general knowledge concerning the material science and properties of superconducting materials and how to characterize and compare them using materials analysis.
- With a second part, a focus on the characterization, the description and the formalism of superconducting and electromagnetic properties in bulk superconductors will be done.
- In a third part I will present my study of a relatively new superconducting material compared to cuprates : The Iron-Selenide (FeSe) alloy, with a focus on, its synthesis, its characterization and so its relevancy and competitivity toward electrical engineering application. Finally, a close look will be given on the future perspectives of development of this material and its potential uses on technological applications.
- The fourth part will highlight the advantage of a synthesis technique called Infiltration Growth technique (IG) used for the preparation of ReBaCuO single crystals. High field measurements have been applied on IG samples to study their properties. The particularity of this kind of measurement will also be the occasion to study the effect of the magnetic field sweep rate on the superconducting bulk properties. Further, an overview on the YBaCuO foam design will be done and of course an extensive part on the future improvements and the potential applications.

Chapter II: Characterization of superconducting bulk

II.1. Phase, crystal and bulk structure analysis

To ensure a good synthesis quality, determine the generated phases and analyze the crystal structure, the repartition of the secondary phases, the size of the grains, give an explanation the superconducting properties is essential. In this way, during this PhD I had the opportunity to use different instruments to understand the prepared samples or the sample I had to measure the superconducting properties.

A brief summary as well as a description of the processes I used are presented along this sub-section.

II.1.a. Optical microscopy

This well-known and easy to use method needs only a tiny preparation which make it really appreciated to gives a general idea of the sample's structure as well as its shape.

Indeed, when a sample is cut and prepared for further measurement such as magnetic properties measurement, it is necessary to have a look at it using an optic microscope as the sample is of mm-size. It is a fast way to check the presence of cracks, large doped areas and also the shape as well as the size. So, I used this method to measure the size of samples. As well as to verify the specification when the sample is of industrial production. A close look on the sample of Figure II-1 we can see very shiny among the YBaCuO crystal due to the presence of silver as precise by the fabricant.

Finally, by using a polarizer, an optical microscope can help to analyze the microstructure, the single phases with their sizes as well as the secondary phases, then gives an idea of the stoichiometry and the repartition of the as-prepared sample.

However, this method is rapidly limited by the wavelength of visible light (400-800 nm) which makes impossible a resolution below this length and also the depth of field, which depends of the resolution [98], needs a very flat sample for a high resolution which is difficult when analyzing the aspect of a polycrystal.

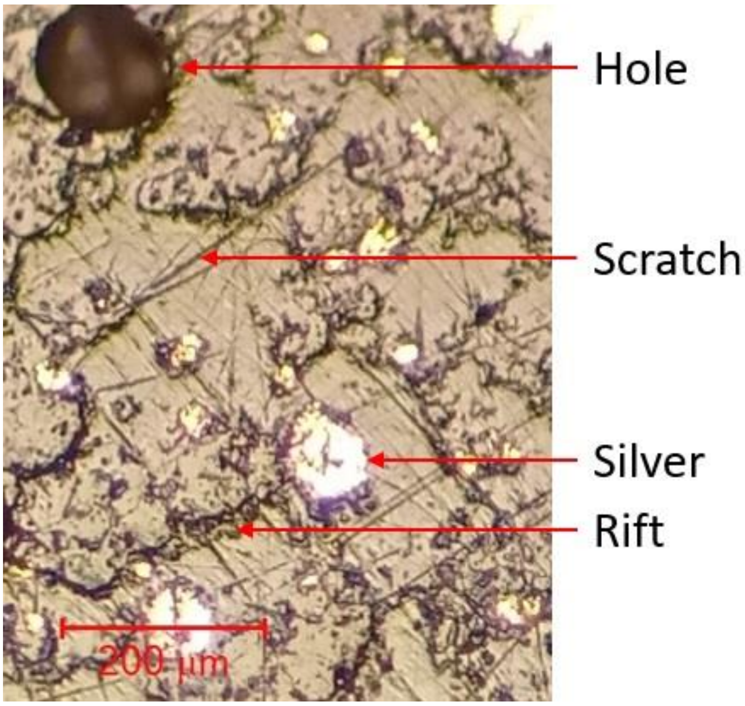

Figure II-1: Photo made with an optical microscope of the surface of a commercial YBCO. The shiny grains are made of pure silver which allows a better electrical and thermal conductivity but induces a paramagnetic signal (Figure II-14). We can also see holes and rifts due to the porosity of the sample as well as scratch linked with the grinding process.

II.1.b. Scanning electron microscopy

When visible light is limited by its wavelength, electrons can offer a much better resolution as their wavelength are directly linked with the energy that can be tuned. This is why Scanning Electron Microscope (SEM) was developed. Indeed, a SEM is a type of microscope which makes a picture of the sample's surface using an electron beam instead of light used with a classic optical microscope.

First of all, the sample needs a particular attention as it needs to be really flat, a long polishing processes using micrometric polishing powder, even plasma or ultrasonic polishing is necessary.

The prepared sample is placed inside the vacuum chamber of the SEM then a secondary vacuum (10^{-6} mbar) is realized, a necessity to prevent any beam losses.

A wire typically made of tungsten is used as electron source which are focused as an electron beam with an electrode called a Wehnelt cylinder [99], [100] with a potential of 0.1 to 30 kV (depending on the purpose).

When the electron beam hits the sample, different phenomena could append, here we will describe the two mains used during my PhD thesis:

- Electron Back Scatter Diffraction: the so-called EBSD measurement is a technique based on the detection of the Backscatter electrons after having hit the sample's surface. It is generally made using a 70° angle between the beam and the sample. This method allows to determine the topology of the sample and so, by reconstruction, gives a picture of the sample's surface (Figure II-2.a). Also, as the electrons hit the sample with a certain angle θ, in contact with the crystal, they will be scattered in all direction, but, according to the Bragg's law, there will be constructive diffraction depending on the crystal planes [98], [100]. This will then form the so-called Kikushi pattern which allows to know the crystal orientation as well as its structure. Generally, the crystal orientation is then represented by the so-called Inverted Pole Figure (IPF) and then allows to compare the evaluation of the orientation of the crystal all over the sample. As it can be seen on Figure II-2.c area of different orientations can be seen, this is a direct proof of different grain of a polycrystal and also highlight the presence of misalignment in the grain boundary.

- Energy Dispersive Spectrometry: the EDS technique consist of analyzing the X-ray beam generated by the interaction of the electrons with the sample. The emission spectrum or the wavelength of the detected X-ray is characteristic of the emitted atoms. So, while the electrons are perpendicular with the sample's surface, for EDS, there is an angle in order to emitted the x-ray beam in the direction of the detector, placed, for the SEM I used, on the side of the vacuum chamber. Finally, by using database of the x-ray emission spectrum for different atoms, we can determine the elements the sample is made of as well as their position and so their repartition all over the studied area.

The association of those 2 techniques will then give the composition of the crystals, the crystallographic phases and orientation of each grains, the presence of impurities as well as the quality of the grain connectivity in case of a polycrystal. Finally, this kind of microscope can offer a precision of the order of 10 nm which very good to look at grains of roughly 1 to 10 µm. But it only gives a local point of view of the sample and so a quantitative idea of the sample composition. For this, another method is needed.

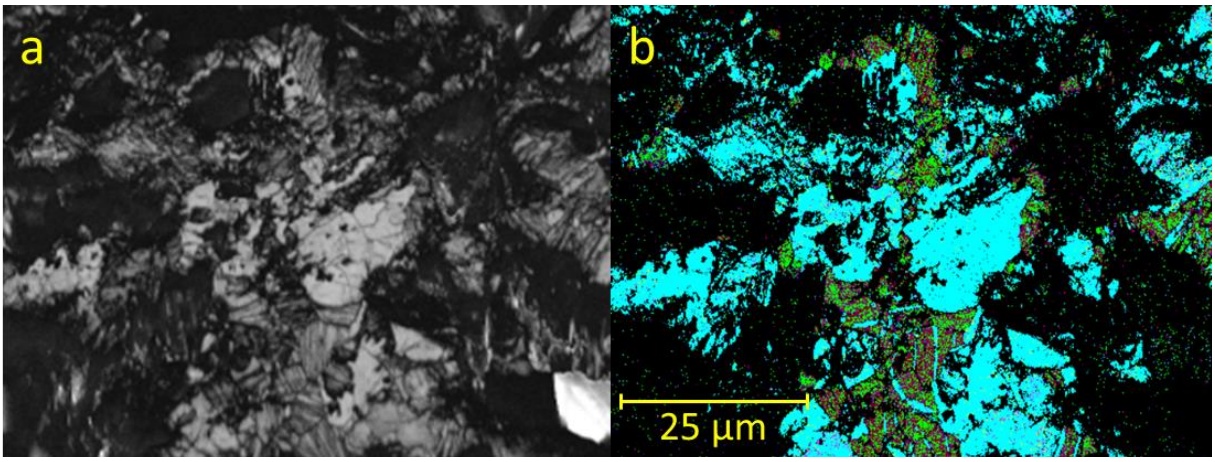

Figure II-2: Picture taken with a scanning electron microscope of a FeSe polycrystal (a). The EBSD picture allows to study the phase composition of the surface, the cyan (●), the violet (●) and the green (●) colors are respectively the β-FeSe, the Fe_7Se_8 and the α-Fe phases (b).

II.1.c. X-Ray diffraction

This is probably the most used way to determine the sample's composition and the proportion of each phases. Then in superconductivity this method is widely used to determine the presence of the superconducting phases and possible secondary phases.
This technique will, as its name is telling, give the diffraction coefficient of X-ray light to analyze the sample's nature and its associated crystal configuration.

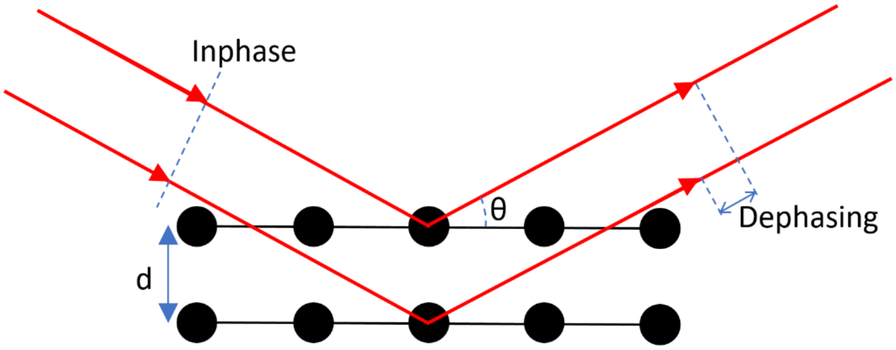

Figure II-3: Schematic drawing of the x-ray diffraction where two X-ray beams inphase come on the crystal to analyze, when diffraction occurs there is a dephasing. This is what we will detect.

The X-ray radiation is commonly generated by a Cu plate bombed by electron and with a selected wavelength of λ=0.1542 nm with an energy of 8.04 keV [98]. The emitted ray is then projected on the sample with an angle θ then when reaching the crystal planes, it is deflected with the same angle according to the optic geometry laws. What makes this technique interesting is that 2 spatially and temporally in phase incident beams (same wavelength and same phase) deflected by 2 different planes of the same crystal will have a phase difference after (illustrated by Figure II-3).
Depending on the phase difference, the beams can be constructive or destructive. When they are separated by an integer factor n they are in phase. This phase coherence depends on the angle θ and of the Miller indices of the crystal, i.e. the distance between the crystal planes (Eq. II.1) [98]. This dependence is expressed by the so-called Bragg's law:

$$n\lambda = 2dsin\theta \qquad (II.1)$$

where d is the distance between 2 crystal planes expressed with the Miller indices h, k, l and the lattice parameter a:

$$d = \frac{a}{\sqrt{h^2 + k^2 + l^2}} \qquad (II.2)$$

The Miller indices come with the reciprocal lattice [98]. As the diffraction measurement is widely used and known, it exists huge databases of the wide majority of the known crystallographic parameter for the majority of the element associated with their θ angle.
So, actual industrial machine will measure for angles from 0 to π all the value of θ when the phases are coherent. An example of such measurement is presented on Figure II-4 where the phases of a Fe_1Se_1 sample are identified though the presence of pikes of different amplitude. The angle 2θ is the angle between the transmitted beam and the reflected one.

Finally, using the databases, it will determine the associated Miller indices and then the crystal phases, the atoms they are made of, their occurrences and their orientation (higher the amplitude of a peak, higher the occurrence of the orientations of a phase).

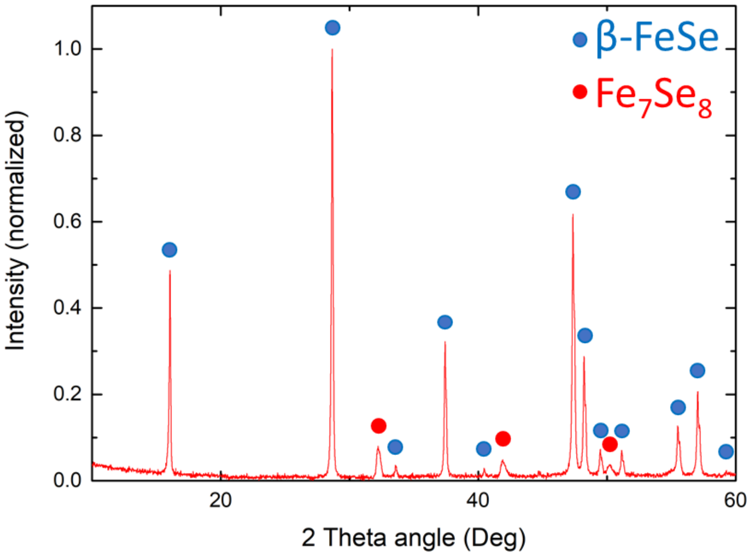

Figure II-4: X-ray pattern of a FeSe sample a 1:1 stoichiometry. The blue (●) and the red (●) dots indicate respectively the β-FeSe and the Fe_7Se_8 phases.

To works well, this method requires to use a very flat area to measure, so a prepared sample need to be polished. Also, analyzing only a face of the sample will give only information on the face composition and nothing about the overall bulk.

In this way, most of the time a part of the sample is reduced as powder flattened on a dish so all parts of the sample are statistically represented and randomly oriented but this is a destructive measurement.

This kind of measurements will only give information about the crystallographic phases but as we need a crystallographic arrangement, it does not work on amorphous materials. Also, it gives only a mean repartition of the phases over the studied area and nothing about potential region or information about the grain connectivity, sizes or the density.

II.1.d. Conclusion

We have seen that different methods are used to determine the material characteristic and composition but they all have drawbacks. Thus, to give a complete idea of the studied material and to be able to draw conclusions and to make links with the superconducting or electromagnetic properties, the presented methods have to be used together. Optic microscopy will give a fast and general idea of the bulk. Following this, X-ray diffraction will give statistical information of the crystal phases, their composition, occurrence and orientation. Finally, the Scanning Electron Microscopy will describe a local area of the sample with information of the grain size, the local crystal phases repartition, composition, occurrence and orientation.

II.2. Practical properties determination of superconducting materials

II.2.a. Critical and practical superconducting properties:

We have already presented the three mains critical properties of a type II superconductor: J_c, H_{c2} and T_c, however those properties are sometimes hard or currently impossible to measure, H_{c2} of YBaCuO is predicted to be above 100 T at low temperature [101], [102], and they are insufficient for comparing different materials regarding applications. The bulks are mainly used as permanent magnets or magnetic shields, so we need to define more "practical" properties such as the following ones:

- The magnetic moment m

Generally, the critical properties of a superconducting bulk can't be directly measured so it can be very difficult and magnetic measurements are preferred. In this way in most of the cases we measured the magnetic moment "m" in *emu* (a CGS unit which correspond to 10^{-3} A.m^2) of the sample. After, by applying the so-called Bean's model, described later in this section, the critical properties can be measured from the magnetic moment.

- The irreversible magnetic field H_{irr}

Due to the lowering of the critical current while the surrounding magnetic field is increasing, it comes a value where the critical current is too low to be considered: 100 A/cm². At this point, the magnetic field is called irreversible magnetic field H_{irr} and the superconducting current is considered null at higher magnetic field. It is illustrated in Figure II-5.

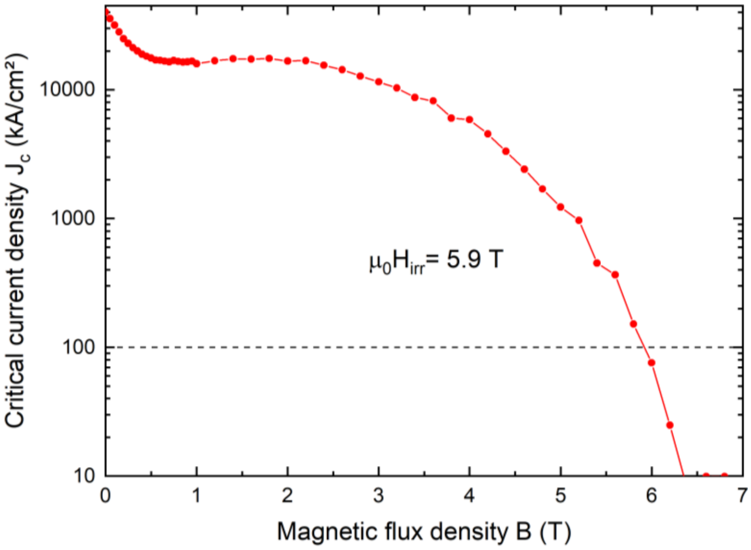

Figure II-5: Critical current density J_c in a log scale versus external magnetic field where the limit of 100 A.cm^{-2} is indicated and shows an irreversible magnetic field μ_0H_{irr} of 5.9 T.

- ### The pinning force F_p

Below the critical current and so a critical Lorentz force, the vortices are maintained fixe by the so-called the pinning force F_p. This force is linked to the crystallographic structure of the sample, the impurities or defects (defects of the material's structure on the superconducting properties were described in section I.2). This force can be easily determined as it is exactly equal to the Lorentz force when the critical current is reached:

$$||\boldsymbol{F_p}||[\boldsymbol{N.m^{-3}}] = ||-\boldsymbol{F_{Lorentz}}|| = ||\boldsymbol{J_c} \times \boldsymbol{B_{ext}}|| \qquad (II.3)$$

where $\boldsymbol{F_{Lorentz}}$ is the Lorentz force, $\boldsymbol{J_c}$ the critical current density and $\boldsymbol{B_{ext}}$ the background magnetic flux density.

The pinning force is a good way to compare different materials as it gives information on the trapping capacity at each magnetic field, which is a key point for optimizing the performances for applications as the working external magnetic field is generally given. The pinning force corresponding with the critical current of Figure II-5 is presented on Figure II-6.

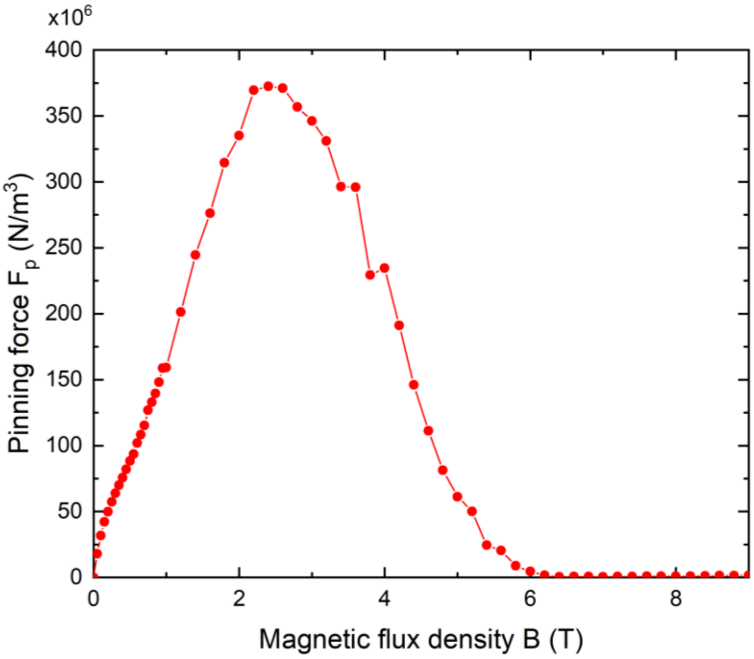

Figure II-6: Pinning force F_p function of the external magnetic field at 77 K.

- ### The trapped magnetic flux density B_T

One of the main uses of superconducting bulk is as a permanent magnet where a magnetic field is "trapped" inside the superconductors after a magnetization experiment (will be described later in this chapter). This trapped magnetic flux density, B_T, and its cartography give the same information as for a classic permanent magnet and let us know the distribution of the magnetic field on the surface of the sample (measured typically 1 mm above the sample's surface), a useful data for many applications. An example is presented on the Figure II-7 where the trapped magnetic flux density of a prepared commercial YBCO bulk was evaluated. With the repartition of the trapped field shown by this figure we can see where potential defects are present as a lower trapped field is measured. Also, we can determine the maximal trapped magnetic flux density at a given temperature and given applied field (here $\mu_0 H = 0.18$ T at 77 K with a 0.3 T permanent magnet) which greatly helps to size a future electrical machine and verify the quality of the measured bulk [76], [78], [87].

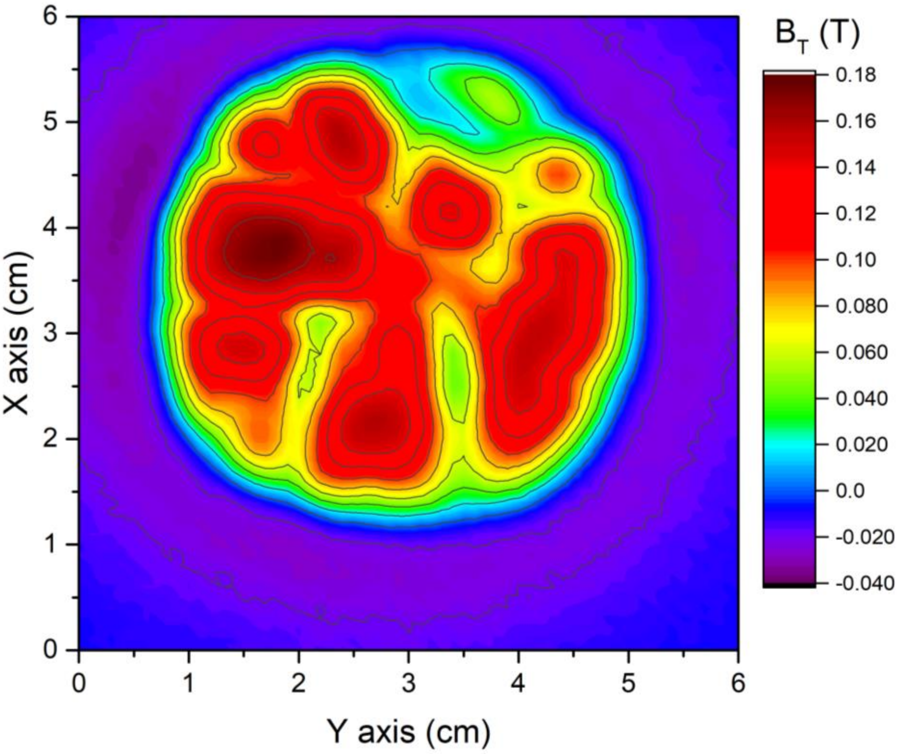

Figure II-7: Distribution of the trapped field B_T of a commercial YBaCuO superconductor at 77 K after a field cooling process using a 0.3 T permanent magnet.

II.2.b. Evaluation of the critical temperature and magnetic moment function of the temperature

Most of the time, the first property to measure is the critical temperature T_c as it is necessary to know below which temperature the other properties (J_c, H_c, $\mu_0 H_{irr}$) should be measured and gives a first idea of the potential applications. There are 2 commonly used protocols to determine the critical temperature: the resistivity analysis based on electrical measurement and the so-called Field Cooling (FC) and Zero Field Cooling (ZFC), FC-ZFC, technique based on magnetic measurement methods. This first technique consists of applying a very small current through the sample and measure the voltage. By varying the temperature, when superconductivity occurs, a drop of resistivity and so of voltage is measured. This method is relatively simple and it is not disturbed by the presence of other magnetic properties of the sample (such as a ferromagnetic hysteresis). We generally use a Physical Property Measurement System, PPMS (this machine will be described later in this section), an example of such measurement is given in Figure II-8.

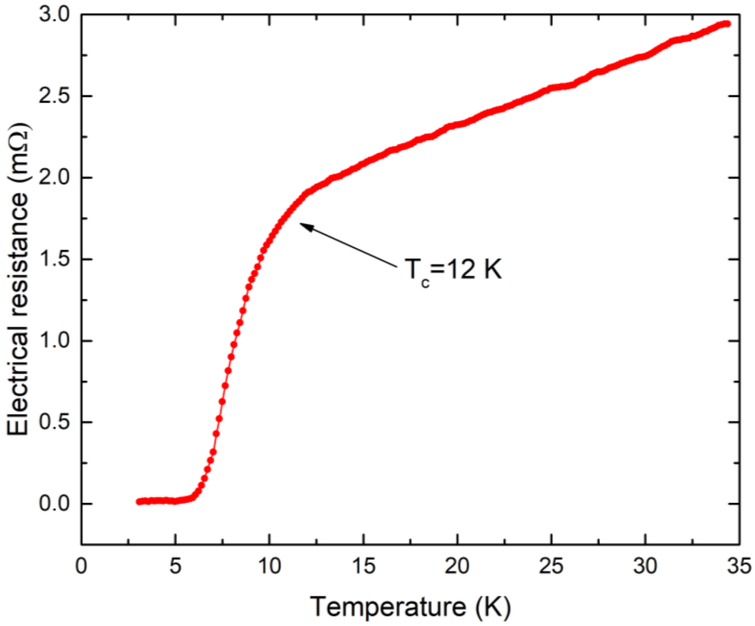

Figure II-8: Measure of the electrical resistance of a FeSe sample function of the temperature [103].

The second method uses a Magnetic Property Measurement System, MPMS (also described later in this section), for measuring the magnetic moment of the sample. The sample is cooled down at a low temperature (most of the time at 2 K) without external magnetic field then a relatively low magnetic field is applied (10-100 Oe) which induces a superconducting current, itself generating a magnetic moment. Following this, the temperature is sweeping up and the magnetic moment is measured, this is the so-called Zero Field Cooling (ZFC). On the other side, the Field Cooling (FC) process applied a magnetic field at high temperature, when the sample isn't superconducting, so no current is induced. The temperature is moving down with a constant external field (the same as for the ZFC) and then the magnetic moment is measured with the increasing of the temperature.

As a magnetic moment is generated when a field variation occurs at low temperature, i.e. below T_c, during the ZFC process, and stays present until the sample is no more superconducting, by measuring it we can determined its corresponding critical temperature T_c.

Furthermore, as the FC process induces no superconducting current in the material as the external magnetic field remains constant, any variation of the magnetic moment is necessarily due to other magnetic properties of the materials such as a paramagnetic or ferrimagnetic moment produced by a secondary phase.

So, by comparing the moment $M(T)$ function of the temperature of the FC and the ZFC like it is presented on Figure II-9, we could evaluate the critical temperature of our superconducting material. Hence, on this example we can see that the moment during the FC process almost does not change at any temperature. In addition, the ZFC curve clearly shows a strong negative moment which appears at a temperature of 90.5 K. It is a direct hint of a superconducting moment as it is acting as a strong diamagnet (by having a negative magnetic moment under a positive magnetic field), so 90.5 K corresponds to the critical temperature of the sample.

FC-ZFC process is a commonly used technique to evaluate the critical temperature of superconducting materials as it is fast and easy to do and gives information before proceeding to more complex measurements of the superconducting state which could be adjust according to the FC-ZFC measurement.

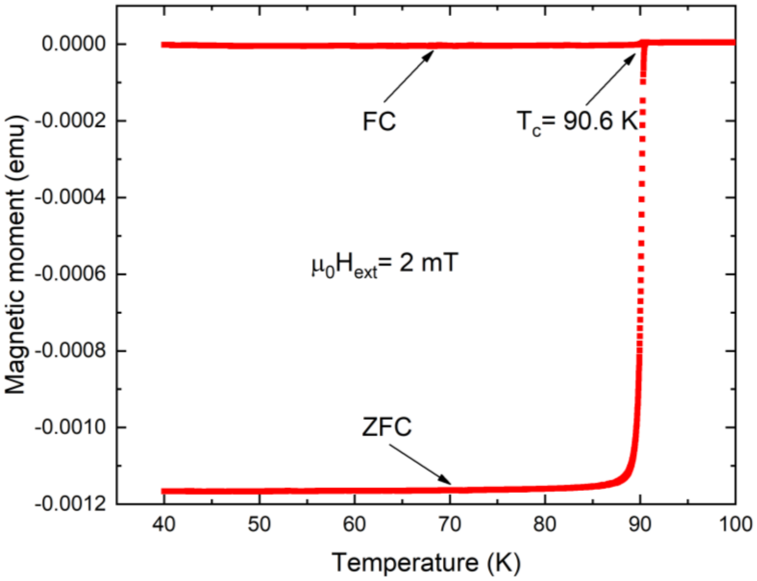

Figure II-9: Magnetization measured function of the temperature for the FC/ZFC process under a magnetic field of $\mu_0 H$ = 2 mT of an Infiltration Growth YBaCuO sample [104].

II.2.c. The Bean's model, magnetization for type II superconductors

Charles P. Bean described the first element of a modeling of the magnetization of type II superconductors in the mixed state in 1962 [105] but the formal description comes in 1964 with another paper of Charles P. Bean [106], this model is as follow:

First of all, we will assume that any electromotive force will induce the maximum current inside the superconductor as well as the current density is independent of the applied magnetic field. Finally, we are always considered into the mixed state ($H_{ext} > H_{c1}$).

If a magnetic field H_z is applied parallel to the surface of a slab of thickness D along x-axis, a current will be induced inside the superconductor. The consequence is a linear decreasing of the magnetic field according to the ampere's law (Eq. II.4) along a distance d depending of the applied field **H** and the current density **J** (Eq. II.5).

$$\nabla \times \mathbf{H} = \mathbf{J} \tag{II.4}$$

$$d = \frac{H_z}{J_y} \quad \text{in a 1D slab} \tag{II.5}$$

This current is corresponding to the critical current density $J_y = \pm J_c$. As we can see in Fig. 1.A from [106], represented on Figure II-10.a, depending of the value of H_z, the magnetic field is penetrating deeper in the superconductor until it's fully penetrated, at this point the magnetic field is called penetration field H_P. At the same time, the current density is also generated deeper inside the superconductor until all the conductor is full by current as it is illustrated on Figure 1.B from [106] and here on Figure II-10.b.

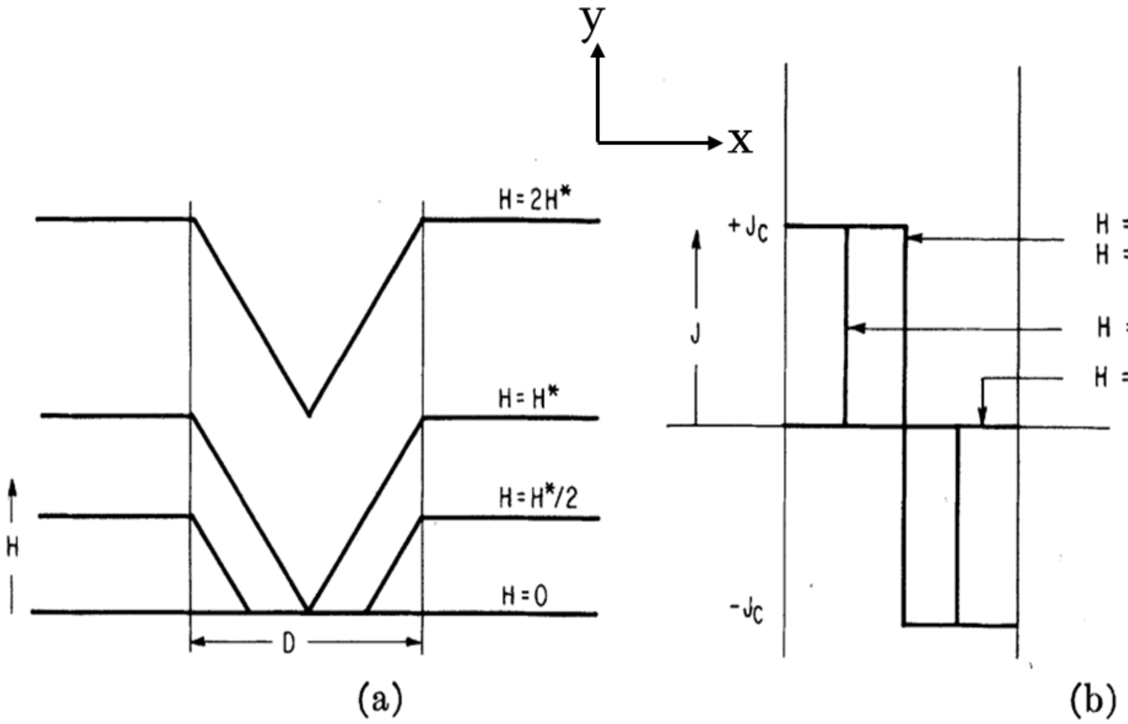

Figure II-10: Representation of the local magnetic field (a) and the critical current density (b) inside a slab superconductor of thickness D, for different value of the external field H. H corresponds to the penetration field. P. Bean et al. [106].*

At higher magnetic field, when $H_P \leq H_{max} \leq 2H_P$, the current remained equal to the critical current density, $J = \pm J_c$ and is present everywhere inside the superconductor.

In a second time, when the external magnetic field is reduced, a superconducting current is generated with an opposite sign of the obtained one when the magnetic field was increasing. Finally, when the external field is back to zero, two current densities with the same value but opposite directions are flowing in the superconductor and the maximal remnant magnetization in the superconductor is exactly half of the maximal external field H_{max}, as it is illustrated by Figure 2 from [106]. When H_{max} is exceeding $2H_P$, the maximal remnant magnetization is still equal to H_P at the center of the slab.

Despite of the huge assumptions, this model is still a reference to compute the critical currents and models the behavior of a superconductor inside a magnetic field. This model will be used all along this manuscript for the determination of the critical properties with the help of the following contribution and extension called the Kim's model.

II.2.d. Kim's model and Chen's formula

An extension of the Bean's model

As the Bean's model assumes that critical current density is independent of the magnetic field, it is clear that this model needs to be completed when this assumption is no more possible if we want to be able to fully determine the superconducting properties at magnetic field higher than the penetration field H_P.

Shortly after Bean's paper, Kim et al. presented an extended version of the Bean's model called critical state model (or in most of the time: Kim's Model) [107]. This model allows a better and easier comprehension of the magnetic properties of a superconductor in the mixed state as they are all associated with the critical current density which is determined using the following formula (Eq. II.6):

$$\frac{\alpha}{J_c} = B_0 + B \tag{II.6}$$

where α and B_0 are constants that can be determined experimentally [108].

Also, this model fits well with the superconducting hysteresis loop which is an important step for further development as many applications are using this phenomenon.

Other models were developed for fitting with different experimental measurement using various sample's shapes or magnetic fields [109]–[112].

However, the Kim's model only allows the computation of the critical current for tubular "clean" superconductors. On the other hand, when the magnetization curve is much more complex due to multiple properties intrinsic to the sample structure, the magnetization curve can be named as "dirty", corresponding to unconventional superconductors, as it can be seen on Figure II-14.

It comes that computing the critical current density function of different parameters such as the external magnetic field or the temperature on various sample looks absolutely essential. This is why Chen et al. [113] developed analytically an expression of the critical current density based on the Kim's model and the experimental value of the magnetization M, the so-called Chen's Formula:

$$J_c(H) = \frac{\Delta M(H)}{a\left(1 - \frac{a}{3b}\right)} \tag{II.7}$$

For a thin slab of dimension length: $2b$, width: $2a$, where $J_c(H)$ is the mean critical current density in the sample, $\Delta M(H)$ is the thickness of the superconducting hysteresis curve (explained later with Figure II-15) and H is the applied magnetic field considered homogeneous and in the direction of the sample's thickness c. It appears that the same equation can be used on a cylinder of infinite thickness than for a squared slab ($a = b$):

$$J_c(H) = \frac{3\Delta M(H)}{2a} \tag{II.8}$$

with this, it is also possible to work on samples with a finite size [114].

To illustrate the difference between the Bean and the Kim's model, the Figure II-11 is showing the magnetic polarization of a superconductors computed either with the help of an independent (Bean's model) and a dependent (Kim's model) critical current density regarding the applied magnetic field.

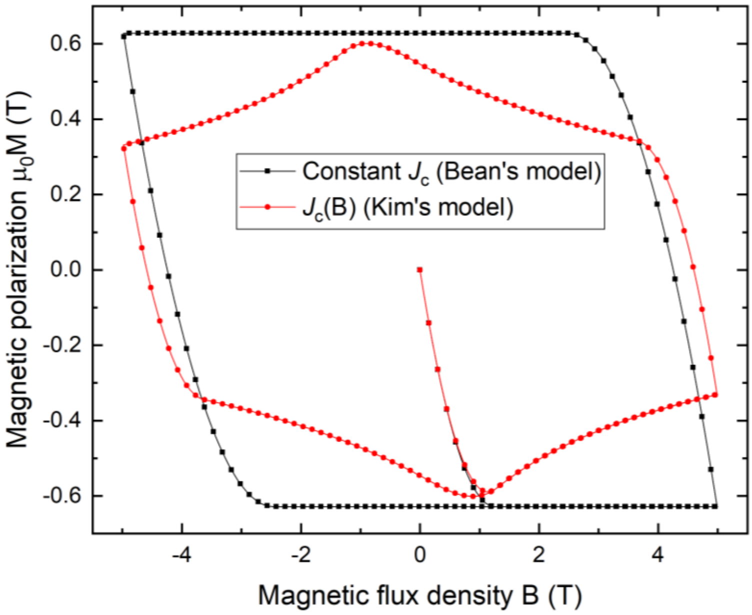

Figure II-11: Comparison of the computed magnetic polarization using the Bean's model where the critical current density is independent with the surrounding magnetic field and the Kim's model where the critical current density is varying with the surrounding magnetic field.

• Requirements and approximations for the Kim's model

With those equations, 5 very important requirements have to be considered:

1. Those equations are designed for a thin slab where the thickness $C = 0$ or for a cylinder of infinite length $C = \infty$. Of course, this requirement can't be respected in reality but at least an effort is needed on the dimension such as: $C < A \leq B$ for an orthorhombic sample and $A < C$ for a cylinder as shown by Figure II-12.
2. Following the precedent requirement, it is important to ensure, as much as possible with the given experimental conditions, the same dimensions for all samples of an experimental set. As example, for the majority of the samples I prepared, I tried to respect the following ratio of dimension: $C < A \leq B$ and the size of my sample will always be given.
3. It is really important to be always in the fully penetrated state, so with $H > H_p$. As explained right above, my samples were always quite small and so the penetration field rarely exceeds 0.3 T so a wide range of measurement is valid on a 7 T measurement machine. The same condition applied when the magnetic field is ramping down from the maximum field H_{max}. As a current in the opposite direction has to penetrate the sample during a magnetic field variation as high as $2H_p$, we are in penetrated state when $H_p < H < H_{max}\text{-}2H_p$.
4. An assumption is made on the local magnetic field H_i inside the sample as it is always considered constant and equal to the external magnetic field: $H_i = H$ and so the

variation of the critical current density along the sample has to be null. In other words, the screening effect due to the superconducting sample needs to be negligible which means $M \ll H$. This requirement is easily fulfilled above 1 T with small samples using the dimensions presented in the second requirement.

5. Like for other type of materials [115], the shape of the sample has an effect on the measured magnetic moment, either due to the demagnetization factor [116] and the approximation of the sample as a dimensionless dipole done by the MPMS machines [115]. This can be seen by measuring 2 similar samples but with a different shape as it is reported in [117] where a difference of magnetic moment for the same sample is as high as a factor 2-3. This difference can also be reported using samples of different shapes but with the same superconducting properties, more information is given later with a specific example using the critical current measured with the help of an MPMS-SQUID (Figure II-22).

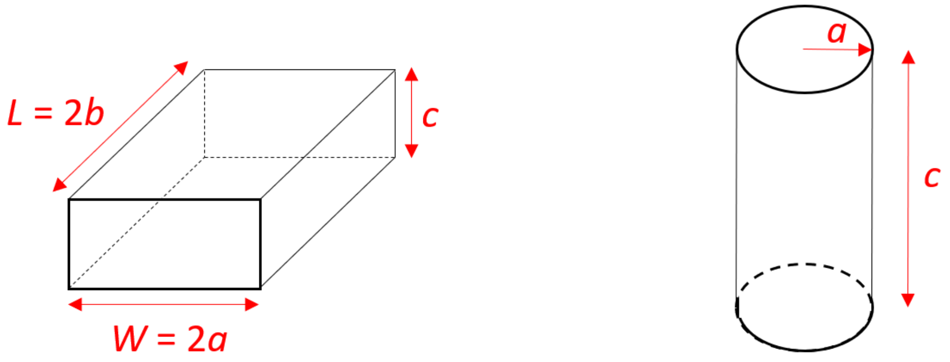

Orthorhombic sample: $3c < W \leq L$ Cylindrical sample: $a < c$

Figure II-12: Schematic drawing of the typical shapes of samples used with the Kim's model.

• Dimensional analysis of the Chen formula

In order to always fulfill those requirements, the shape of the samples will be kept similar in the limit of the materials and the experimental conditions. The comparison of the magnetic properties will always be made for applied magnetic field above 1 T (except in particular cases with the appropriate precisions and information).

In most of the cases for computing the critical current density from the hysteresis magnetization curve, a modified Chen's formula is used in order to fit with the experimental result and/or units to avoid unnecessary computation and then potential mistakes.

So, expressing the Chen's formula using the SI unit we have:

$$J_c[\mathrm{A.m^{-2}}] = \frac{\Delta M[\mathrm{A.m^{-1}}]}{a[\mathrm{m}]\left(1 - \frac{a[\mathrm{m}]}{3b[\mathrm{m}]}\right)} \qquad (II.9)$$

where ΔM is the thickness of the hysteresis curve (Figure II-15) and a, b are respectively half of the width and the length of the sample.

As the magnetic moment is generally measured in **emu**, a CGS unit of the magnetic moment, the so-called $M(H)$ curve (magnetization curve) will be presented function of the CGS unit with the sample's volume in **emu.cm^{-3}**, as it can be seen in Figure II-15. So, we will use the same units, i.e. **emu.cm^{-3}** and the sample dimension in **cm**. The corresponding change from CGS to SI is:

$$[\mathrm{emu.\,cm^{-3}}] \equiv 10^{3}[\mathrm{A.\,m^{-1}}] \qquad (II.10)$$

$$[\mathrm{cm}] \equiv 10^{-2}[\mathrm{m}]$$

$$\frac{\Delta M[\mathrm{A.\,m^{-1}}]}{0.5W[\mathrm{m}]\left(1-\frac{0.5W[\mathrm{m}]}{3\times 0.5L[\mathrm{m}]}\right)} = \frac{10^{3}\Delta M[\mathrm{emu.\,cm^{-3}}]}{\frac{10^{-2}W[\mathrm{cm}]}{2}\left(1-\frac{2\times 10^{-2}W[\mathrm{cm}]}{6\times 10^{-2}L[\mathrm{cm}]}\right)} \qquad (II.11)$$

where A and $B$are respectively the sample width and length (remember the Chen's formula is using half the sample's dimensions), so $a = 0.5W$ and $b = 0.5L$ which leads to:

$$J_{\mathrm{c}}[\mathrm{A.\,cm^{-2}}] = \frac{20\Delta M[\mathrm{emu.\,cm^{-3}}]}{W[\mathrm{cm}]\left(1-\frac{W[\mathrm{cm}]}{3L[\mathrm{cm}]}\right)} \qquad (II.12)$$

This will be the formula I will commonly use with the presented CGS unit as this is the most represented version of the Chen formula in the Literature [16], [18], [42], [118]–[120]. It is also important that, sometimes, the magnetic moment is presented function of the sample's weight [120], always using CGS units: **emu.g^{-1}**. In this case, the formula is:

$$J_{\mathrm{c}}[\mathrm{A.\,cm^{-2}}] = \frac{\Delta M[\mathrm{emu.\,g^{-1}}]}{\frac{W[\mathrm{cm}]}{2}\left(1-\frac{2W[\mathrm{cm}]}{6L[\mathrm{cm}]}\right)} \times D[\mathrm{g.\,cm^{-3}}] \qquad (II.13)$$

Switching to the SI units:

$$J_{\mathrm{c}}[\mathrm{A.\,cm^{-2}}] = \frac{\Delta M[\mathrm{A.\,m^{2}.\,kg}]}{\frac{10^{2}W[\mathrm{m}]}{2}\left(1-\frac{2\times 10^{2}W[\mathrm{m}]}{6\times 10^{2}L[\mathrm{m}]}\right)} \times 10^{-3}D[\mathrm{kg.\,m^{-3}}] \qquad (II.14)$$

A third formula can also be used, it will use directly the magnetic moment in **emu**, the volume of the sample is considered directly inside the formula:

$$J_{\mathrm{c}}[\mathrm{A.\,cm^{-2}}] = \frac{20\Delta M[\mathrm{emu}]}{W[\mathrm{cm}]\left(1-\frac{W[\mathrm{cm}]}{3L[\mathrm{cm}]}\right)} \times \frac{1}{V[\mathrm{cm^{3}}]} \qquad (II.15)$$

With $V$the volume as $V = A \times B \times C$ which leads to:

$$\frac{\Delta M[\mathrm{emu}]}{W^{2}Lc[\mathrm{cm^{4}}]\left(1-\frac{W[\mathrm{cm}]}{L[\mathrm{cm}]}\right)} = \frac{\Delta M[\mathrm{emu}]}{W^{2}c[\mathrm{cm^{3}}]\left(L[\mathrm{cm}]-\frac{W[\mathrm{cm}]}{3}\right)} = J_{c}[\mathrm{A.\,m^{-2}}] \qquad (II.16)$$

II.2.e. Computation of the critical current density using experimental magnetic moment

• Sample's size measurements

Let's make an example by studying the magnetization curve and evaluating the critical current of a commercial YBaCuO superconductor:

A small sample were cut from the big piece with respective dimension $W \times L \times c$ of $1.93 \times 1.58 \times 0.46$ mm^3 (Figure II-13). To measure those dimensions on a fairly irregular rectangular shape I firstly use a Vernier caliper to give an approximative size. Then I measured the width and the length on 2 or 3 different points and I average the dimensions, see Figure II-13. The thickness is measured using a Vernier caliper and I checked if the thickness is regular or not using an optic microscope.

So, this leads to an approximative size as this measurement is not precise. However, measure the ideal shape on an irregular shape is almost impossible and the lack of information concerning the current repartition (the current loop could be circular or following the edge of the sample) make a precise measurement questionable. This will, nevertheless, add an inaccuracy on the magnetic moment reported over the sample's dimension as well as the critical current density.

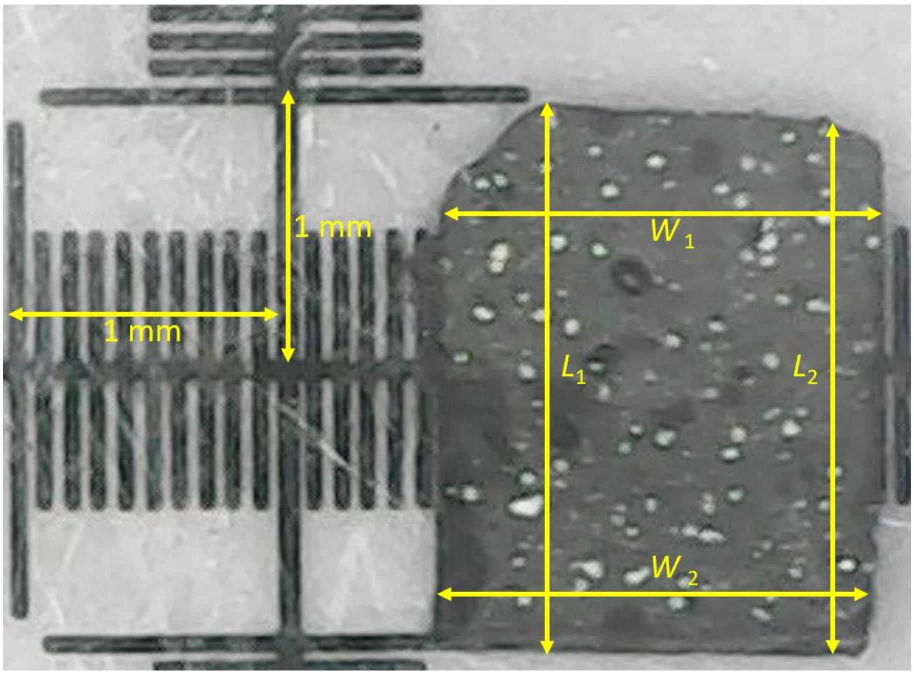

Figure II-13: Picture of a prepared piece of commercial YBaCuO bulk. The yellow lines show the technique used to measure the dimensions of the sample.

• The superconducting magnetic moment

The magnetic moment of the samples presented right above (Figure II-13), under a magnetic field parallel to the **c** axis of ±9 T, was measured at 77 K using a MPMS (details about such machine will be describe right below).

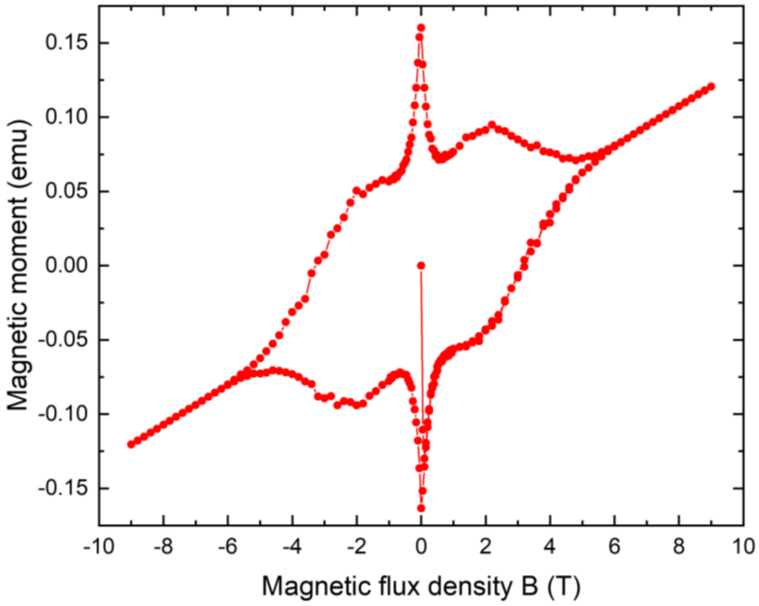

Figure II-14: Magnetic moment of a commercial YBCO sample doped with silver at 77 K.

The resulting signal is far from a theoretical $m(H)$ curve that can be seen in the literature [113] as it looks bent. It is due to the presence of a paramagnetic compound induced by the presence of silver [121] in this material [30], [31], this can be clearly seen as shining areas on the picture of the sample (Figure II-1 or Figure II-13). Thus, I simply removed this signal by interpolating a linear function between the points at -9, +9 and 0 T and subtract it to the signal. Following this the moment m(emu) is converted to the magnetization M(emu.cm^{-3}) using the sample's volume in cm.

The resulting superconducting signal is presented on Figure II-15. We can see the evolution of the magnetization for various magnetic fields. This graph is composed of 5 different quadrants:

- The first Quadrant is from 0 to +9 T (insert of Figure II-15) and represents the first magnetization as before applying a magnetic field the samples is free of any current. So, it begins by generating current from the outer to the center of the sample according to the Bean model until the penetration field is reached, below this value we have $M(H) = -H_{ext}$. After this point, the critical current density will always fill all the superconductor and will drop with the increasing magnetic field until the irreversible magnetic field is reached at roughly 6 T. Above this value the critical current density is considered as null.
- The second quadrant starts when the applied field is reducing from its maximum value to 0, so from +9 to 0 T. We can see that the moment is now positive and exhibit the same absolutes value as for the first quadrant between 6 and 0.25 T (respectively the irreversible and penetration fields). When the external field is reduced to zero, we can see an abrupt increasing of the magnetization until it reaches its maximum value.
- The third, from 0 to -9 T is exhibiting similar value as for the second quadrant at the same absolute field value.

- The forth quadrant, from -9 to 0 T shows the same magnetization but with the opposite sign for the same value of magnetic field than for the third or the second quadrant.
- The fifth quadrant, from 0 to +9 T will, as for the 3-precedent quadrant, show the same value of the magnetization at the same magnetic field. Also, above H_P (0.1 T on Figure II-15), it is superimposed with the first quadrant as expected.

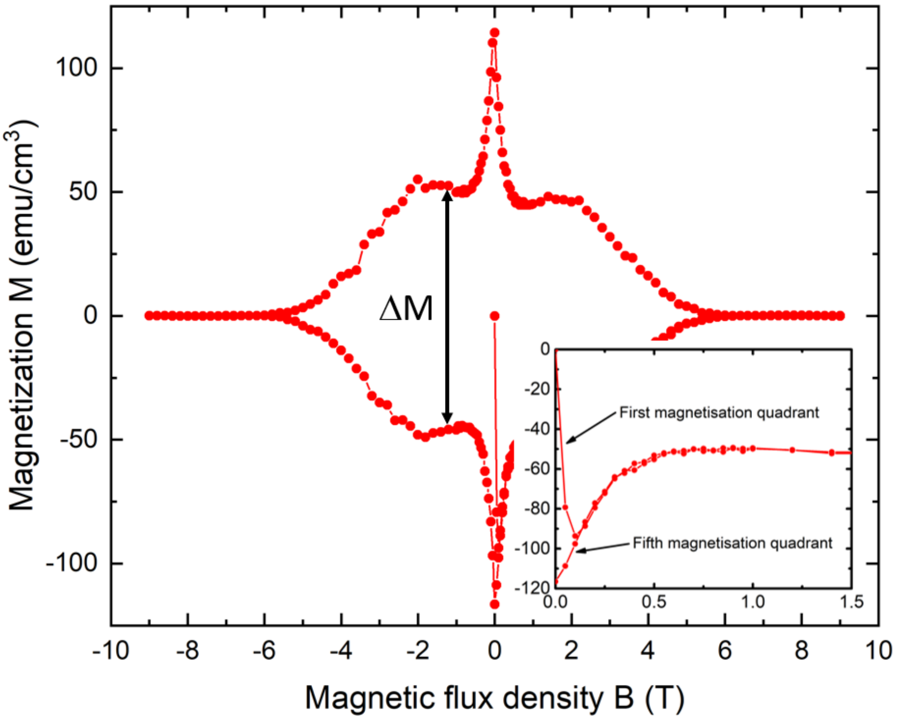

Figure II-15: Magnetization at 77 K of the Figure II-14 after removing the paramagnetic signal and divided by the sample's volume. The insert shows a zoom on the lower-right part containing the first and the fifth quadrant.

We can see that for all 5 quadrants, for magnetic field between 1 and 3 T, the magnetization has a local maximum, this phenomenon is called the "fishtail" effect, a phenomenon completely dependent of the sample's local aspect and its defect. As it was already pointed out in 1999, [122, p. 154], this phenomenon is not well understood. However, it is commonly seen in experimentation independently of the material as it appended using many materials with many designs:

- Single crystals Cuprates [123], [124] where it is hypothetically explained by the presence of wrongly oxygen doped areas with a lower H_{c2}. The consequence is the apparition of new pinning sites at high magnetic field which increase the pinning force and then the critical current density.
- Polycrystals [16], where, because of the presence of the grain's boundaries, there are intergrain and intragrain currents with different pinning mechanisms.
- It can also come from the presence of non-superconducting secondary phases that act as pinning center at high field [125], [126].

• The critical current density

Now let us compute the critical current using Eq. II.8, for that we will use the quadrants 2 and 5 or 3 and 4 for extracting the thickness of the $M(H)$ curve: $\Delta M(H)$.

The computed critical current from 77 to 30 K and from magnetic field from 0 to +9 T is presented on Figure II-16.

As expected the shape of the $J_c(H)$ curve is very similar to the $M(H)$ one of Figure II-15 as it is proportional, the “fishtail” effect is still visible (note that the pick value at 30 K is above 9 T) and the value of J_c dramatically increases below 1 T. As mentioned above, the critical current will be compared with other measurements at sufficiently high magnetic field like 1 or 2 T. At 77 K we have $J_c(1\ \mathrm{T}) = 16\ \mathrm{kA.cm^{-2}}$ and $J_c(2\ \mathrm{T}) = 16.7\ \mathrm{kA.cm^{-2}}$ which is comparable with the measured J_c of other commercial single-crystal YBCO bulk such as the ones presented in [127].

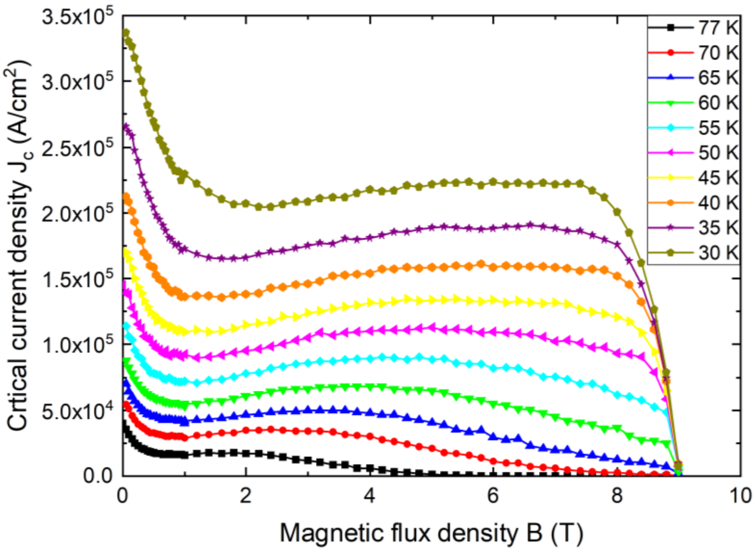

Figure II-16: Critical current density function of the magnetic field for various temperature extracted from the magnetization of Figure II-15.

Also, now we can measure the irreversible magnetic field which correspond to the value of the external magnetic field when the critical current density reaches $J_c(H_{irr}) = 100\ \mathrm{A.cm^{-2}}$ we can see an irreversible field at $\mu_0 H_{irr} = 5.9$ T, also comparable with a very similar material [127].

• Conclusion

To conclude about these paragraphs, this kind of procedure is typical and crucial for evaluating the critical properties of a superconducting material and of course for various temperatures, so the same computation will be done all along this manuscript. But we have seen, because of the various units and dimensions used by the community as well as the large number of needed approximations made by Bean, Kim and Chen in their respective models, basic mistakes can frequently happen, so it is important to strictly define all variables, dimensions and units of all experimental results. This led to the need of standards in experimental protocols and procedures presented above.

II.3. Measurements methods and characterization of bulk superconductors

In this section we will describe multiple methods of characterization of the superconducting properties I used along this PhD thesis such as the critical temperature, current density, field or the trapped or irreversible magnetic field. Only a general and/or theoretical description will be given, more details on specific techniques used are presented in a dedicated section for each material in the Chapters II, III and IV.

II.3.a. Magnetic Property Measurement System

A Magnetic Property Measurement System (MPMS) is based on the measurement of the magnetization M of a typical mm^3 size sample or below, either solid, liquid or reduced as powder. This setup has the advantage of being disponible as a ready-to-use commercial machine. This system gives a very precise measurement (precision $\approx 10^{-5}$ emu) of the moment or even the most precise measurement at the moment when a Superconducting Quantum Interference Device is used as the detector (precision $\approx 10^{-8}$ emu).

During my PhD I used three different MPMS, all from the Quantum Design company, one was using a susceptometer with a Vibrating Sample Magnetometer and a ±9 T superconducting magnet (a picture of a 14 T PPMS, very similar to the 9 T one, is showed on Figure II-17.a). The second one was using a first-generation SQUID susceptometer with a magnetic field of up to ±5 T (MPMS-1 SQUID, Figure II-17.b).

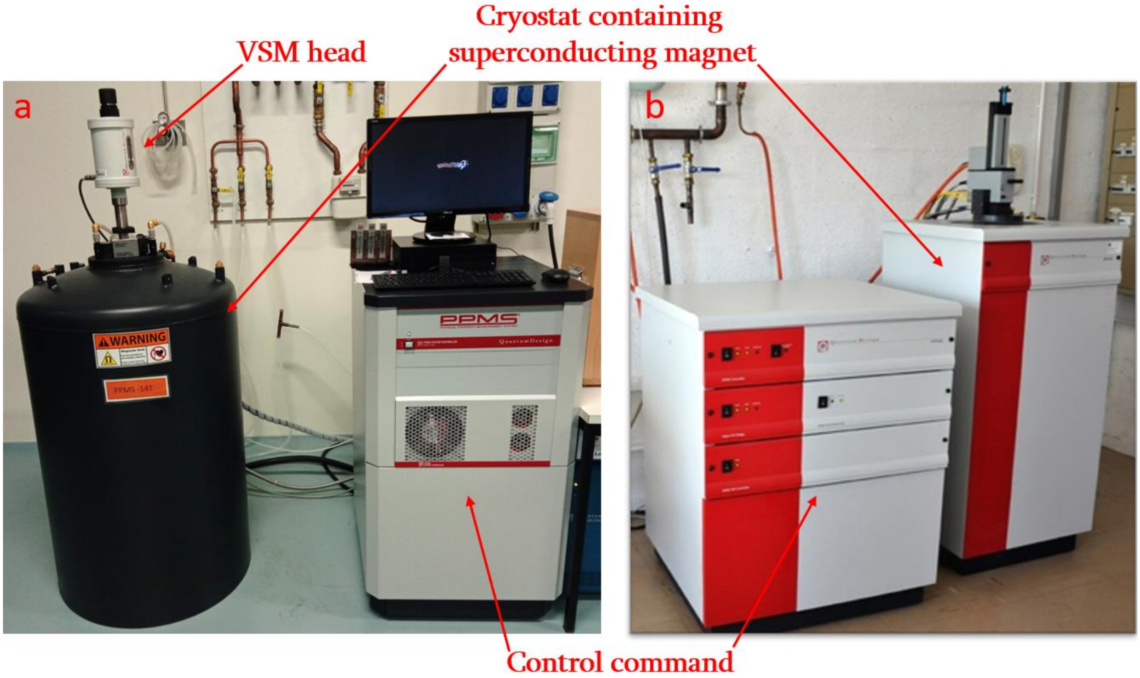

Figure II-17: (a) Picture of a 14 T PPMS magnet with its control command and a VSM head for magnetic measurement from Quantum design. The 9 T PPMS I used to be exactly the same. (b) A first-generation MPMS-SQUID from Quantum Design with a 5 T magnet with its control command. Those materials allow to work down to 2 K with a very stable magnetic field and a high precision of 10^{-5} emu.

The last one was using a second-generation SQUID susceptometer with a VSM head and a magnetic field of ±7 T (MPMS-3 SQUID, Figure II-18)

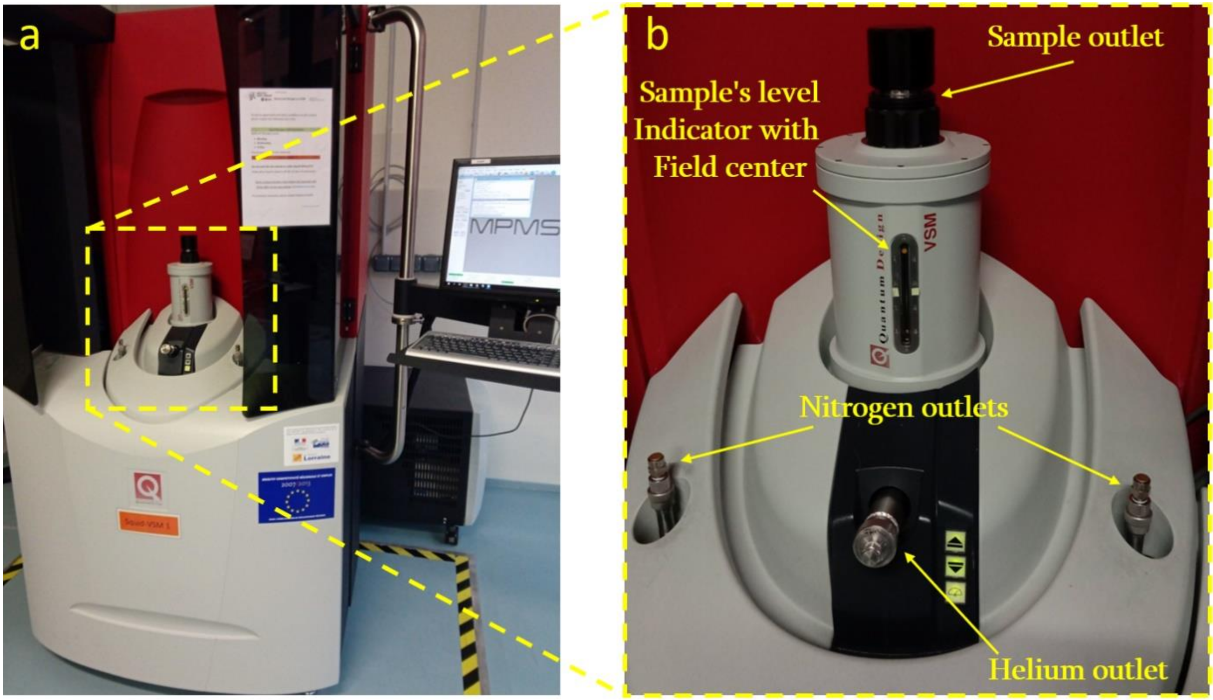

Figure II-18: (a) The 7 T MPMS-SQUID of third generation from Quantum design. This machine offers a better, easier and faster control of the magnet and temperature (higher sweep rate). (b) Magnification of the upper part of the machine where we could see the different outlets as well as the VSM head.

Despite being disponible as a commercial and simple to use machine, the measurement of the moment is very complex and a bad approximation or understanding of the measurement process can lead to big mistakes during the interpretation of the results and the computation of the critical properties.

So, it comes out that a description of the operation of a MPMS is necessary. Only a MPMS-SQUID will be described as it is used in most of the cases, however a classic MPMS is very closed to a SQUID despite having a lower precision as the susceptometer does not use superconducting technologies.

First of all, the sample is fixed inside a plastic straw, itself fixed on a rod as we can see on Figure II-19, a schematic drawing of the cross section of a PPMS. Then the cane is placed inside the chamber tube of the MPMS (see Figure II-18.b), which will thermally isolate the samples. The outer blanket of the MPMS is fulfilled with liquid Nitrogen while the superconducting magnet is filled with liquid and/or gaseous Helium. The temperature inside the sample's tube is control via a bellows dived into liquid helium and rounded by impedance tube, itself connected to a heater. The bellows itself is connected to the wall of the sample's tube which will thermalize the sample by radiation. Also, most of the time MPMS machines can go below 4.2 K the temperature of liquefaction of Helium, for that they will use a so-called "pre-cooling" chamber which enables to go down to 2 K. The temperature inside the chamber is measured by 2 different temperature sensors placed at the bottom of the sample's tube and at the top of the temperature on the sample is then interpolated.

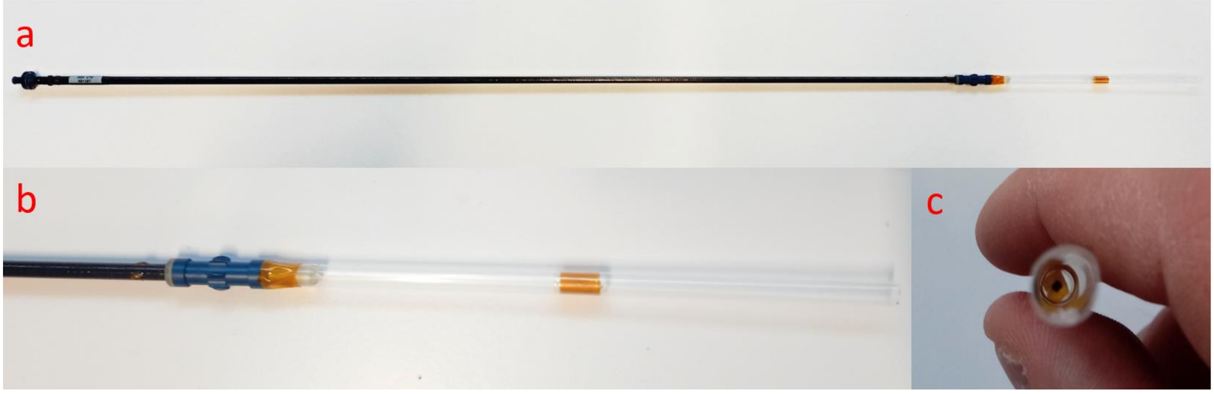

Figure II-19: (a) Sample holder of the SQUID where a straw, containing the sample, is fixed. (b) A zoom on the straw with the sample inside a cap rounded with Kapton. the straw is perforated to evacuate the air during the purge of the vent. (c) A view on the top of the straw where we can see the sample (A piece of commercial YBaCuO). The sample is laying on a Teflon leaf and trap inside a cap rounded by Kapton.

It is really difficult to obtain information on this kind of machine (which mainly act as a black box) so it is necessary verify the calibration of the MPMS. I made a simple experiment using a superconducting sample made of iron-selenide (FeSe). By measuring the variation of the magnetic moment function of the time *M*(*t*) while changing the temperature continuously *T*(*t*) from 2 to 20 K, so we can see if the temperature computed by the MPMS considers the thermal inertia of the samples and its holder. Figure II-20 shows the curves of the temperature and the magnetic moment function of the time, we can see that the variation of the moment stops exactly when the temperature is fixed (measurement step of 2 s), which means that the temperature of the sample itself is also fixed. In other word, the temperature given by the MPMS is the calculated temperature of the samples based on the calibration made by the manufacturer Quantum Design [128].

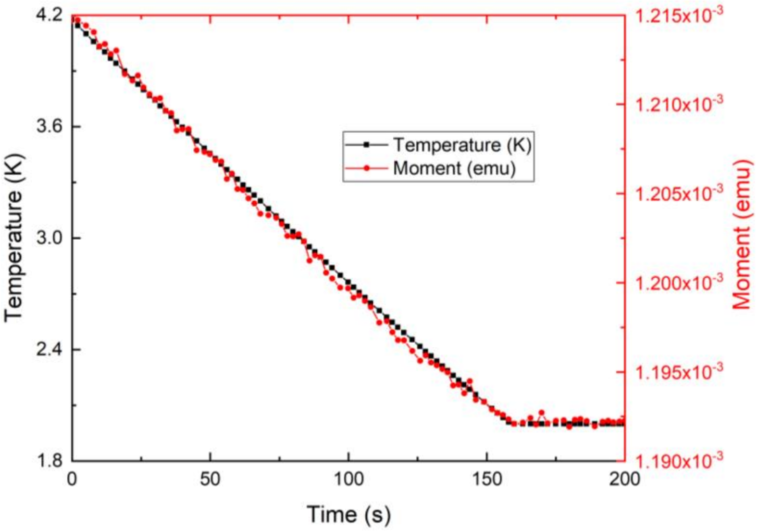

Figure II-20: Measurement of the magnetic moment during a temperature decreasing function of the time. We can see that the variation of the moment is very synchro with the temperature variation which highlights a good control and calibration of the temperature controller.

The magnetic field is generated by a superconducting solenoid magnet that can applied in both *z* and -*z* axis (in other words it can be "positive" or "negative") and it works with two modes: ramping and persistent.

- The ramping mode is used to change the magnetic field, so the solenoid is connected to the DC power supply. Depending on the model of the machine, the sweep rate of the magnetic field can be chosen.
- The persistent mode is used when the magnetic field is fixed, the magnet is then separated from the power supply and so the current will loop in the closed circuit without losses as there is no electrical resistance. This allows a very accurate and stable magnetic field during the measurement.

Depending on the machine, the maximal magnetic field could be 7 T for the MPMS-SQUID, 9 T on the PPMS or even higher (14 T on a PPMS).

The use of superconducting magnet is really important for the persistent mode and also to avoid a huge electrical consumption. However, as the magnet is never quenched, a remnant current is generated by the trapped flux inside the magnet. This remaining current can generate a non-negligible persistent magnetic field (above 30 Oe) so it needs to be removed between measurements or when low field experiments are needed. The solution is to apply a decreasing field (typically from 1 to 0 T) using an oscillating function. So, the magnetic field will oscillate between 1 and -1 T with a decreasing amplitude until it is stabilized at 0 T, it will generate successive hysteresis loops with a decreasing width to a value as close as possible to 0 T.

The measurement of the magnetic moment is done by vibrating the sample though a second derivative gradiometer which uses a superconducting wire wounded as 4 pick-up coils, the 2 central ones are wounded in one direction when the external ones are wounded in the opposite direction. This avoid the perturbation of external fields and reduce the harmonic of the flux of the sample (which is then considered as a simple magnetic dipole). This wire is used in a superconducting flux transformer which will induce perturbation in a DC SQUID made of two Josephson's junctions [129] in parallel, flow by a DC current, isolated from any field variations and kept at low temperature. Finally, the voltage of the SQUID is measured as function of the sample flux and position with an extreme precision, i.e. 10^{-11} T [115], [128], [130].

In order to measure a good and clean signal, the translation movement of the sample through the pick-up coils need to be at least longer than the height of the pick-up coils.

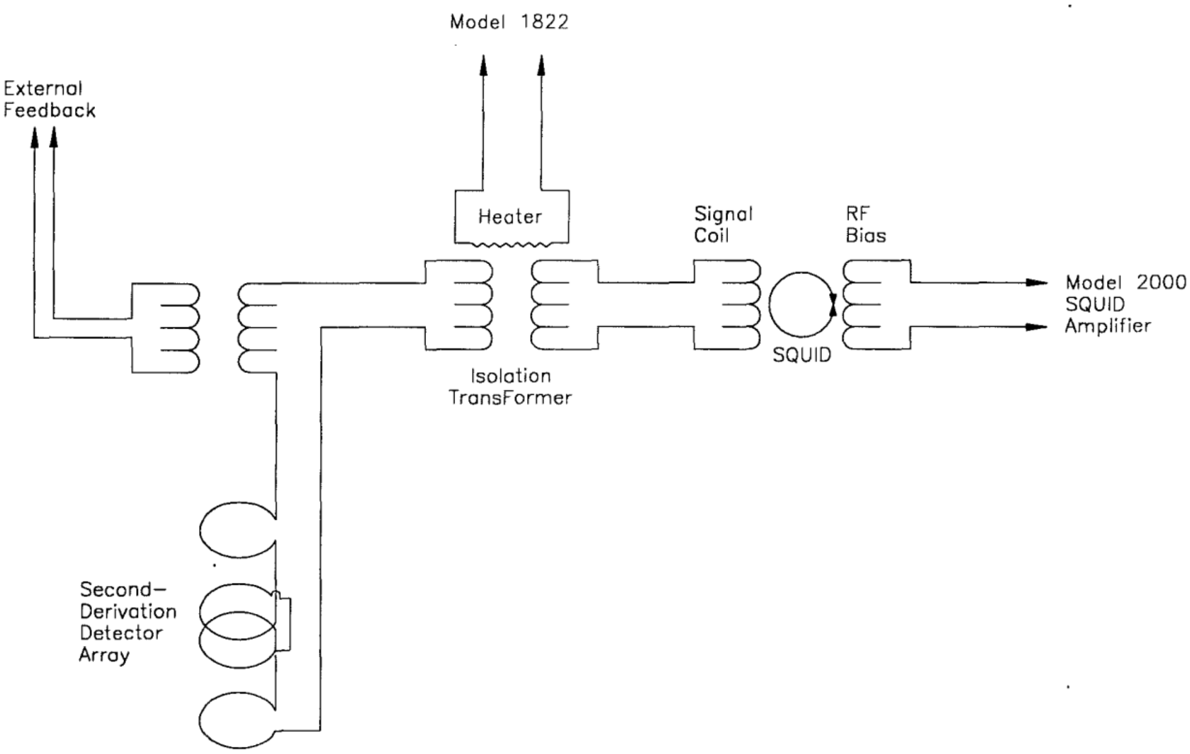

Figure II-21: Schematic drawing of the SQUID system presented by Quantum Design, [131].

Some limitations exist using a SQUID device for measuring the magnetic moment of superconducting bulks. A long straw (>10 cm) is used to avoid parasite signal as the amplitude is smaller than the straw so the pick-up coils never see any variation of the magnetic behavior of the straw. The capsule as well as the Kapton that surround the sample are emitting a signal but small enough to be neglected compared to the superconducting signal tested during this thesis.

An optional device is widely used for a more accurate measurement, it is called the Vibrating Sample Magnetometer (VSM). By making the sample vibrate over an amplitude of 1-5 mm (5 mm most of the time), the variation of moment will be easier to detect and so more data are collected by the SQUID which processed on a mean value of the magnetic moment at each measurement iterations (between 1 and 2 seconds).

To study with more detail the reliability of the measurement as well as the impact of the ratio of the sample size, i.e. the length *B*, the width *A* and the thickness *C*, a sample taken from a commercial YBaCuO bulk (similar to the one of Figure II-13) was cut as a $2.45 \times 2.12 \times 0.89$ mm^3 rectangular piece. Then using the MPMS-SQUID, the magnetic moment and so the critical current density were extracted at 85 K. Following this, the sample was cut again: $2.45 \times 2.06 \times 0.46$ mm^3 with a new SQUID measurement, and again for a $1.95 \times 1.59 \times 0.46$ mm^3 sample but 2 months later.

All those measurements were compared on the following Figure II-22 on which we can clearly see that the critical current for all size are really similar, at 1 T, the largest difference is of 11.8% between the $2.45 \times 2.12 \times 0.89$ mm^3 which is the largest sample and the $1.95 \times 1.59 \times 0.46$ mm^3 sample which is the smaller one (3.2 times smaller than the biggest one). Also, the $2.45 \times 2.06 \times 0.46$ mm^3 sample (2 times smaller than the biggest one) has a critical current density between the 2 others. It seems than the size of the sample impacts the computed critical current density and so samples of very different sizes will show different critical current densities. However, this difference is only of 11.8% for a volume factor of 3.2 times and 7.7% for a volume factor of 2. Finally, a much larger difference can be seen at lower magnetic field and we can clearly identify a tendency: smaller the sample higher the critical current density.

Although, as shown previously with Figure II-13, the shape of the samples isn't perfect and the associated dimensions are roughly measured. Also, we could argue that the superconducting performances are not perfectly homogeneous over the sample and so it can explain a part of, if not all, the differences in the critical current densities.

A last point comes with the reliability of the measurement for exactly the same sample. This was done using the 2.45 × 2.06 × 0.46 mm^3. Two months separate the first and the second measurement and we can see on Figure II-22 that the largest difference between the 2 critical current densities is of 30% at 1 T with 1 307 and 1 006 A.cm^{-2} respectively for the measurement done in November 2021 and in January 2022 or even 50% at 1.2 T, so a diminution of the J_c when it is almost 0% at 0.3 T (roughly 10 690 A.cm^{-2} both). As the effect of aging on Ag-doped YBaCuO has been studied [132] with a conclusion of an increasing J_c with time, of about 25% over 4 years, this difference can't be explained because of a possible degradation on a 2 months period. But by many parameters or events: a slightly different position during the measurement, some damage during the installation and removal or a shift of the measurement tools (temperature, magnetic moment…). This measurement is basically highlighting the lack of precision and will be use as the limit of significance.

It shows that, for a similar rectangular shape, the critical current density of a commercial YBaCuO sample is, considering the incertitude as well as the measurement precision, the same if the volume ratio is similar.

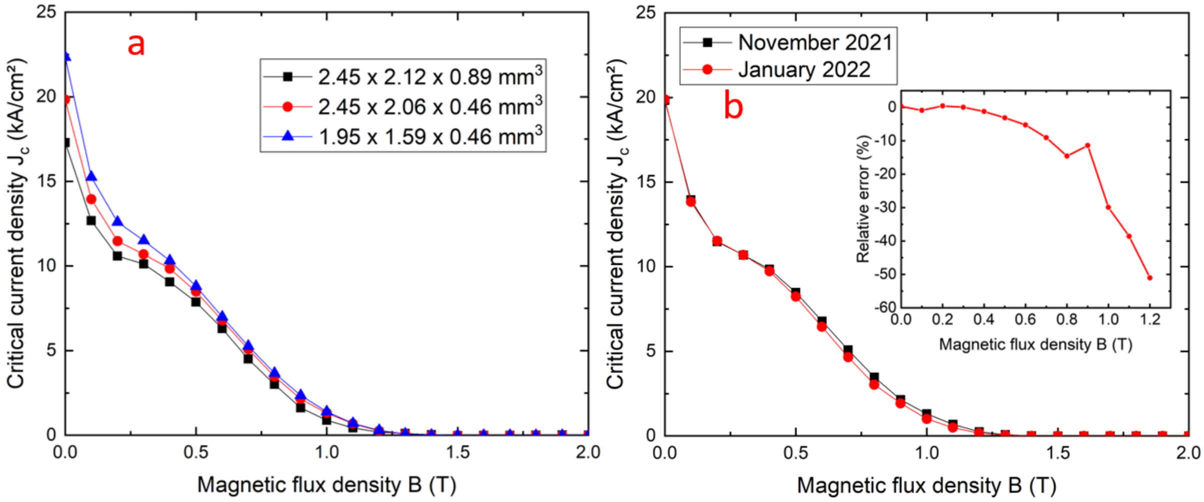

Figure II-22: (a) Comparison of the critical current density J_c for the same sample, successively cut in different sizes. We can see that smaller is the sample, higher is the computed J_c, (b) Comparison of the critical current density J_c for the same sample measured on the same machine, with the same protocol but separated by 2 months. The insert displays the relative error between the measurements of November 2021 and January 2022.

In conclusion, the dimensions of the sample play a crucial role for the determination of the superconducting properties, a too big sample can lead to the saturation of the detector which makes the measurement useless. On the other hand, as explained in the Kim's model section, the dimensions of the sample have a wide impact on the measurement as it will change the demagnetization factor. This is why maintaining the size of the samples such as $3C < A \leq B \leq 2$ mm is necessary. Finally, comparing a difference of critical current density should be done with samples of similar size and an acceptable error could be computed from insert of Figure II-22 using the arithmetic average of the relative error from 0 to 1.2 T when the $\mu_0 H_{irr}$ is reached. This error is of 12% and so for the rest of this PhD thesis, a difference of critical current density lower than 12% will not be considered significative.

Finally, the measurement of the sample's flux can also be adapted on large sample using adapted or homemade pick-up coils and magnets [133].

II.3.b. Flux magnetometry

One of the main problems when measuring the magnetic flux of a sample with a standard pick-up coil is of course the demagnetization factor which depends of the size and shape of both the sample and the pick-up coils. This problem could be solved by directly wind the coil all around the sample as we can see on Figure II-23, extracted from [134].

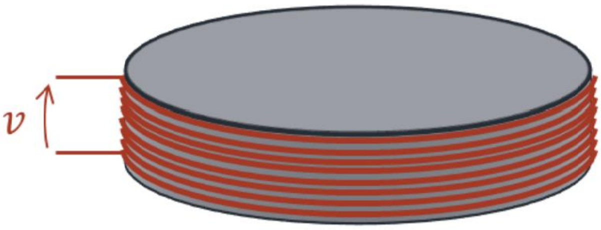

Figure II-23: An example of a coil wound directly on the sample in order to have no demagnetization factor. This picture was taken from [134].

Then with the help of a constant sweep rate on the surrounding magnetic field, the magnetic flux variates which induces a voltage in the pick-up coil via the Lenz-Faraday equation:

$$V = -\frac{d\Phi}{dt} = -\frac{1}{dt}\iint \boldsymbol{B}\cdot\boldsymbol{dS} \text{ where } \boldsymbol{B} = \mu_0\boldsymbol{H} + \boldsymbol{M} \qquad (II.17)$$

with V the induced voltage in the pick-up coil, Φ the time-varying magnetic flux, B the flux density in the coil (so in the sample) of section S, M the magnetization of the sample and H the local magnetic field.

This measurement method also possesses the advantage of working in limited space as the coil is roughly the size of the measured sample. But we can also add more equipment on the sample at different locations, such as hall probes, to get more information about the sample properties [135].

However, it is necessary to prepare a new coil for each sample which is time consuming and can be a bit tricky for sample with a complex shape even by placing the coil at different position over the sample as it looks to have a limited effect [134]. Also, it could be hard to obtain a really good relevancy of comparing 2 samples measured with 2 different pick-up coils. Finally, to get an induced voltage, the external magnetic field has to be varying all the time which changes the resulting value of the magnetic moment produced by the sample and thus the determined value of J_c. The effect of the sweep rate on the critical current density and the absence of relaxation effect lead to slightly overestimate the J_c. More explanation about this effect are given along Chapter IV.

II.3.c. Torque and force magnetometry

Another common way to measure the magnetic properties of a small magnetic sample is by measuring the displacement of the sample due to the magnetic force generated by the interaction of the sample's moment and the external magnetic field.

The measurement of such displacement can be realized through a capacitive measurement done between two plates. One is placed on a so-called cantilever, a small plate made of a soft material (generally copper) on what the sample is fixed. The other plate is placed on a fixed position facing the first one at a distance *d* as we can see on Figure II-24. Under the effect of a magnetic force perpendicular to the sample's surface, the sample will start to move vertically with the cantilever and so induces a variation of the distance *d* and so of the measured capacitance between the two plates.

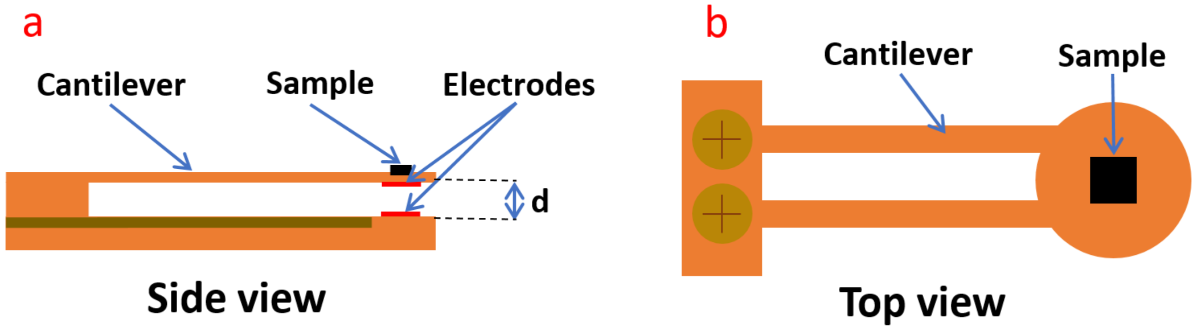

Figure II-24: Drawing of a cantilever with capacitive measurement. (a) is a side view of the cantilever where we can see the sample placed at the end of the cantilever, above the electrodes spaced at a distance "d". (b) top view of the cantilever I used for force magnetometry (described in Chapter IV).

This method has many advantages such as a very high precision (aF range). It can easily be homemade, operated in various conditions and in a limited space, and be adapted to any sample's shapes or sizes.

In such experiment, the magnetic force can be extracted from the measured capacitance as follows.

The capacitance for parallel plates can be defined as:

$$C = \frac{\varepsilon S}{d} \qquad (II.17)$$

where C is the capacitance, ε the dielectric permittivity of the medium between the electrodes, S is the surface of each electrode (supposed equals) and d is the distance between the two electrodes.

In this experiment, we will then measure the variation of the capacitance as follow:

$$\Delta C = C_2 - C_1 = \frac{\epsilon S}{d_2} - \frac{\epsilon S}{d_1} \qquad (II.18)$$

where C_1, d_1 and C_2, d_2 are respectively the capacitance measured when the external magnetic field is null (capacitance at the origin), with its associated distance and the value of the capacitance with a magnetic field applied, and the distance between the electrodes at that magnetic field.

$$\Delta C = \frac{\varepsilon S(d_1 - d_2)}{d_1 d_2} \qquad (\mathrm{II}.19)$$

with $d_2 = d_1 + \Delta d$, we have:

$$\Delta C = \frac{-\epsilon S \Delta d}{d_1^2 + d_1 \Delta d} \qquad (\mathrm{II}.20)$$

By isolating the variation of the distance Δd, we obtain:

$$\Delta d = \frac{-d_1^2 \Delta C}{\varepsilon S + \Delta C d_1} \qquad (II.21)$$

$$\Delta d = \frac{-d_1^2 \Delta C}{(C_1 + \Delta C) d_1} \qquad (II.22)$$

Finally, the variation of the distance can be expresses as:

$$\Delta d = \frac{-d_1 \Delta C}{C_2} \qquad (II.23)$$

We also know, according to the Hooke's law, that the magnetic force **F** depends on the variation of the distance such as:

$$F = ||\mathbf{F}|| = k|\Delta d| \qquad (II.24)$$

with F the norm of the force and k the elastic coefficient of the cantilever, so it can be expresses as:

$$F = k\frac{d_1|\Delta C|}{C_2} \qquad (II.25)$$

Finally, the force can be either a linear force or a torque within small variations which leads to two almost similar configurations: the torque and the force magnetometry.

Torque magnetometry

This method consists of applying an angle, θ_{orque}, between the external field and the sample’s superconducting moment normal to the sample’s surface as presented on Figure II-25. This generates a torque τ, proportional to the magnetization M, the external field H_{ext} and the angle θ_{orque}:

$$\tau = M\,H_{\text{ext}}\,sin\left(\theta_{\text{torque}}\right) \tag{II.26}$$

So, the angle θ_{orque} has to be as small as possible to measure a magnetization as close as possible to the maximum one under H_{ext}.

This method is mainly used to study anisotropic samples, either due to their intrinsic properties [136] or due to their shape [137]. It has already been used to determine the magnetization and so the critical current density of superconducting samples with the help of the Bean model [137], [138] and it can be used for large size sample [139].

A schematic drawing of a torque magnetometry is presented with Figure II-25, when the external field is null (Figure II-25.a) there is no induce current in the sample and so no torque despite the angle θ between the magnet and the sample axis. When a magnetic field is present (Figure II-25.b) a current is induced and so a torque due to the angle θ_{orque}. This torque will bend the cantilever then change the distance d.

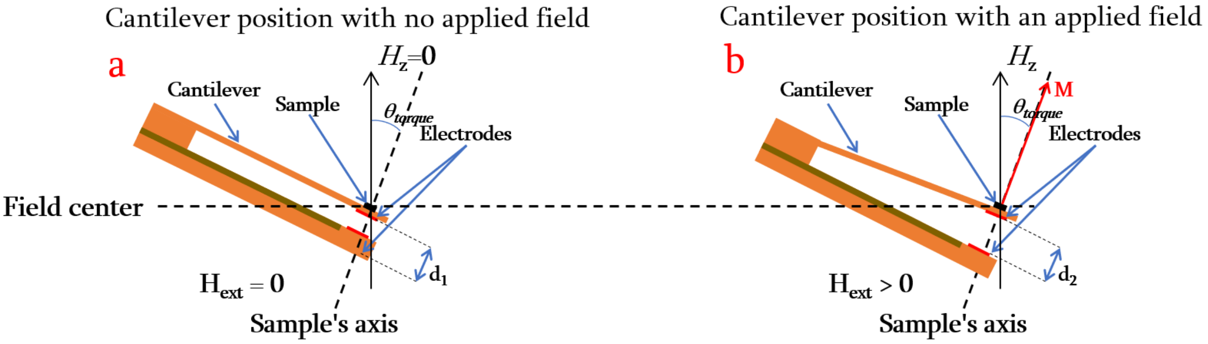

Figure II-25: Drawing of a cantilever used for a torque magnetometry experiment. (a) is the case without magnetic field and/or without angle between the sample’s moment and the external magnetic field. (b) an angle is applied between the sample’s moment and the external field with lead to the generation of a torque which bents the cantilever.

Force magnetometry

Contrary to torque magnetometry where an angle is applied between the sample’s magnetization and the external magnetic field, with force magnetometry the sample’s moment is aligned with the external field but above or below the field center where the magnetic gradient is not null. If the sample is already superconducting at zero magnetic field and then a magnetic field is applied (zero field cooling), the sample will try to move away from the field center due to the presence of the magnetic gradient, Figure II-26. The Laplace force generated is then proportional to the external magnetic field and the currents generated by the superconductor, i.e. its critical current.

Compared to the torque magnetometry, no particular attention is necessary regarding the sample’s anisotropy or shape which release from one approximation.

On the other hand, the sample isn't placed in the field center so the applied magnetic field is slightly lower than the one generated by the magnet at its center as it can be for the torque magnetometry.

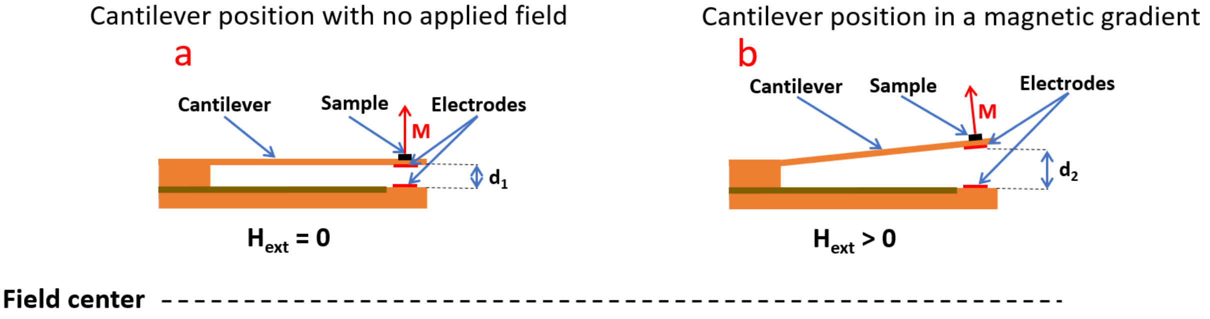

Figure II-26: Drawing of a cantilever used for a force magnetometry experiment. (a) is the case without external magnetic field. (b) is the case with a magnetic field applied. The sample is placed above or below the field center of the magnet, so the sample tries to move away from this center due to the presence of the magnetic field gradient.

Finally, as for the torque magnetometry, this method allows a determination of the critical current density but though a slightly different process so a details explanation of the critical current computation is necessary.

• Computation of the critical current density from the capacitive measurements

Let's consider our sample as a perfect single crystal with an orthorhombic shape and placed above the field center of a solenoid producing an increasing magnetic field B_z along the z-axis. W, L and c are respectively the width, the length and the thickness of the sample. The current induced in this superconducting sample is supposed to be equal to the critical current density J_c and following the sample's shape along the **ab** plane, with the **c** axis parallel to B_z, leading to the current distribution as follows:

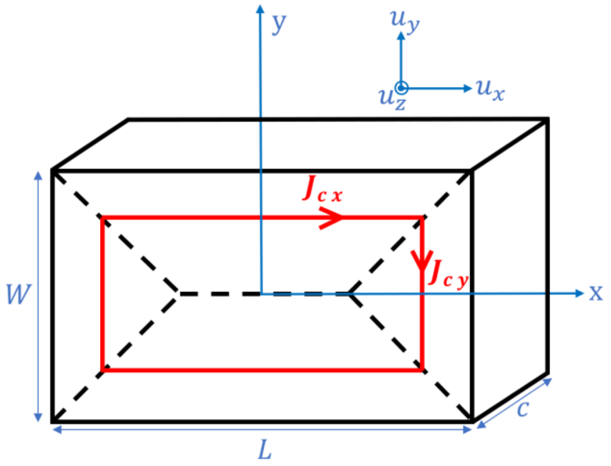

where J_{cx} is the current density along $\boldsymbol{u_x}$ and J_{cy} the one along $\mathbf{u_y}$ with $J_{cx} = J_{cy} = J_c$.
Due to the symmetries of the problem, only one fourth of the sample must be studied in the interval $0 \le x \le \frac{L}{2}$, $0 \le y \le \frac{W}{2}$:

Let us consider $B_x = \alpha B_z$ constant all along the area of the sample as it is considered very small compared to the magnet emitting the background magnetic field, the same approximation is applied on B_y.
To compute the Laplace force due to the interaction of the induced current and the B_x and B_y component, the area presented right above can be dived in 3 different parts (in green).

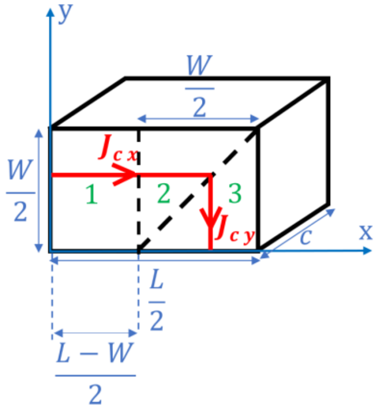

In part 1, we have a current J_c crossing a section $\frac{W}{2}.c$ along a distance $\frac{L-W}{2}$, then we have

$$F_{z,1} = J_c\alpha B_z.\frac{L-W}{2}.\frac{W}{2}.c \qquad (II.27)$$

For the second area we can start considering the following section:

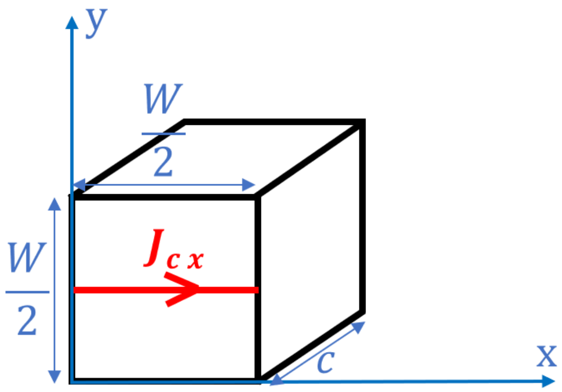

Where the Laplace force can be expressed as:

$$F_{z,2} = J_c\alpha B_z.\frac{W}{2}.\frac{W}{2}.c \qquad (II.28)$$

As the section 2 is exactly half of it we have:

$$F_{z,2} = J_c\alpha B_z.\frac{W}{2}.\frac{W}{2}.c.\frac{1}{2} \qquad (II.30)$$

The same condition can be applied for the third section which lead to the Laplace force:

$$F_{z,3} = J_c\alpha B_z.\frac{W}{2}.\frac{W}{2}.c.\frac{1}{2} \qquad (II.31)$$

So, the force applied over the 3 sections is:

$$F_{z(1+2+3)} = J_c \alpha B_z . \frac{L-W}{2} . \frac{W}{2} . c + J_c \alpha B_z . \frac{W}{2} . \frac{W}{2} . c . \frac{1}{2} + J_c \alpha B_z . \frac{W}{2} . \frac{W}{2} . c . \frac{1}{2} \qquad (\mathrm{II}.32)$$

$$F_{z(1+2+3)} = J_c \alpha B_z W L c . \frac{1}{4} \qquad (II.33)$$

Finally, as the section studied here is a quarter of the total sample, the Laplace force over all the sample is:

$$F_z = J_c \alpha B_z W L c \qquad (II.34)$$

By injecting Eq. II.25 into Eq. II.34 we have the critical current density function of the measured capacitance:

$$J_c = K \frac{d_1 |\Delta C|}{C_2 \alpha B_z W L c} \qquad (\mathrm{II}.35)$$

II.3.d. Trapped field measurements

A more relevant measurement for evaluating the performance of a superconductor as a permanent magnet or a magnetic shield is by making a trapped field measurement and then measure the so-called trapped magnetic flux density B_T. Using a classic permanent magnet or an electromagnet like a coil or a solenoid, a magnetic field is applied on the superconducting bulk which will, according to the Bean's model, induces a magnetic moment proportional to the critical current. As presented above, two different techniques can be used to magnetize a superconductor: The Field Cooling (FC) and the Zero Field Cooling (ZFC).

FC consists of cooling the sample within a magnetic field and then to remove it. The main advantage of this process is the capacity to trap the same magnetic field than applied when it is lower that the penetration field H_P, according to the Bean's model [105], [106], [113]. Generally, this method is used with permanent magnet, placed close to the sample before the cooling process and then removed at the desired temperature. It is a very simple and rustic method but it is limited by the strength of the permanent magnet, most of the time 0.3 T at its surface. Nevertheless, 0.3 T is usually sufficient at high temperature for giving an outline of the magnetic topology at the surface of the superconductor as it is shown on Figure II-27 [87]. Additionally, this method is used for trapping high field (>10 T) using large scale magnets [140], [141].

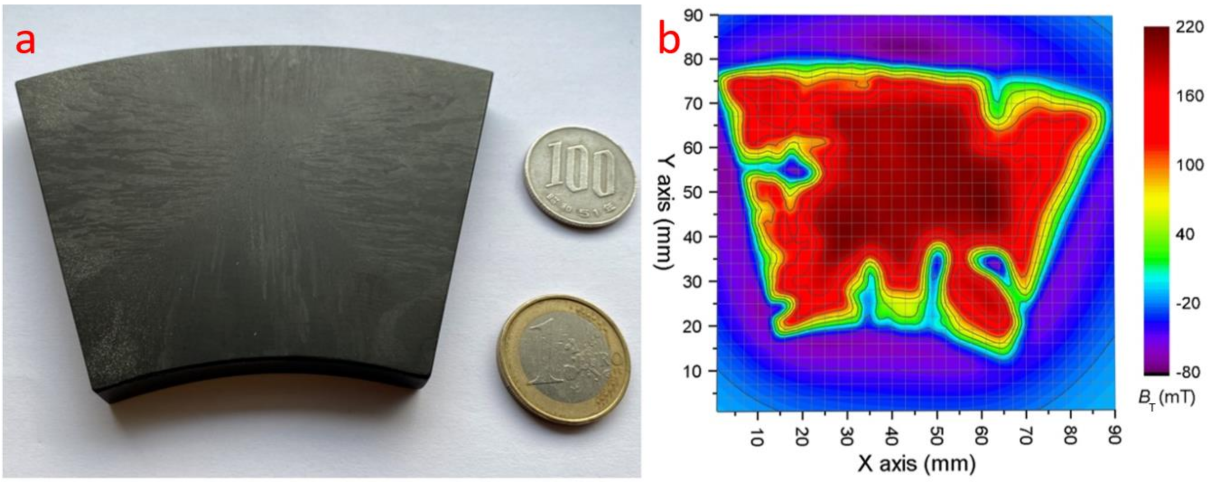

Figure II-27: (a) Picture of a prepared GdBaCuO commercial bulk for motors applications, [78] and (b) its associated trapped magnetic flux density distribution, after a FC process at 77 K using a 0.3 T permanent magnet placed on the top.

The ZFC method as for MPMS measurements in section II.2.e, consists of applying a magnetic field on the sample after the cooling down process. This method can also be used in a pulsed way known as Pulsed Field Magnetization (PFM), as a simple coil fed with a high current can produce several Tesla in a short period of time (<1 sec). However, the quick variation of magnetic field induces a lot of heat [142], [143]. These thermal issues greatly limit the trapped field, as the critical current density decreases with increasing temperature. So, PFM can hardly be used on materials with a low heat capacity such as MgB_2 [144]. Finally, using the ZFC, the same maximum trapped magnetic field as the FC can be achieve if twice the external magnetic field is applied.

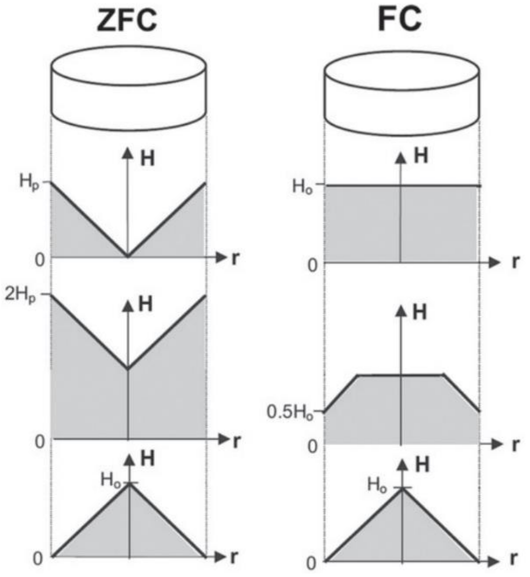

Figure II-28: Comparison of the Zero Field Cooling process (ZFC) and the Field Cooling process (FC). To trap a magnetic field equals to H_P at the end of the process, twice H_P must be applied with ZFC (left) compared to only one H_P with FC (right) [145].

II.3.e. Simulation assisted characterization

The penetration field of a stack of two superconducting bulks can be determined when a magnetic field is detected at the center of the stack, e.g. with a Hall probe, as shown in Figure 9 from [146]. According to the size of the stack and following the Bean's model, this penetration field can be defined as:

$$B_{\mathrm{PB}} = \frac{\mu_0 J_c . L}{4} . \ln\left(\frac{\sqrt{R^2+(L/2)^2}+R}{\sqrt{R^2+(L/2)^2}-R}\right) \qquad (II.36)$$

with R the radius of the sample and L its total height.

In reality, this penetration field varies with the magnetic field sweep rate V_b and the exponent n related to the flux creep in the material. To compensate this variation, an analytical formula has been derived in [147] from numerical simulations so that the measured penetration field B_{PM} should be equal to:

$$B_{\mathrm{PM}} = B_{\mathrm{PB}}\left(1 + \frac{\alpha \ln(V_b) + \beta}{n}\right) \qquad (II.37)$$

α and β are constants equal to 1.2 and 3.4 respectively.

An improved method has been defined in [147] with the main advantage of being easy to use as the measurement of the magnetic field can be done at the top of one sample and not between a stack of two. However, as large bulks can easily have a very high trapped field at low temperature (several Tesla or more), this method is more convenient to use at liquid nitrogen temperature (77 K).

II.3.f. Four points measurement

Another way to measure critical properties of a superconducting material is using the so-called four points measurement. It is based on the direct measure of the sample voltage while a transport current is applied. When the applied current is very small, by varying the temperature we can determine the critical temperature with the fall of the electrical resistance when the superconducting transition occurs as presented on Figure II-8. The critical magnetic field H_{c2} can be measured by the same way for a fixed temperature. Indeed, comparing to MPMS measurement where computation is needed, this technique gives a direct measurement of the T_c and/or H_{c2}. Those measurements on bulks are mainly done using a so-called PPMS and generally on mm-size sample such as for magnetic measurement.

Furthermore, one of the main uses of the four-point measurement is of course for measuring the critical current for different temperatures or magnetic fields but with different objectives as for magnetic measurement. Truly, this critical current measured by magnetic procedures gives a good idea of the "magnetic performances" like for a use as permanent magnet where the superconducting current find its own way to loop back in the bulk (like forming one loop inside each grains). Contrary to the uses of transport current which have to cross the sample from a point “A” to a point “B” and gives an idea of a potential use as current lead.

So the four point measurement is mainly used in tapes, wires or cables for measuring the transport current [7], [148], but it is also considered to use bulks and so some measurements have already been made [149], [150].

To realize such measurement on a YBaCuO bulk we were limited by a 300 A power supply, the critical current density was evaluated at 70 A/mm² from magnetic measurement assumed to be closed to the transport current. This gives a cross section of roughly 3 mm² in order to have margin or in case of a large difference between the transport current and the induce current. A 1mm thick plate could be cut from a bulk which means a 3 mm large bridge.

Following this, another problem arises with the contact resistance with the currents leads. A precedent work done by J. Kapek, has evaluated a maximum current density of 0.57 A/mm² before the apparition of perturbation in the applied current due to a possible melting on the interface of the current leads and the sample. So, to support 300 A, a surface of at least 530 mm² is necessary.

This leads to the design presented with Figure II-29 on a 30 mm wide sample which presents a cross section of 3 mm² at the center and a contact surface of 275 mm² per side with can be doubled if current leads are installed above and below the sample, so a total of 550 mm².

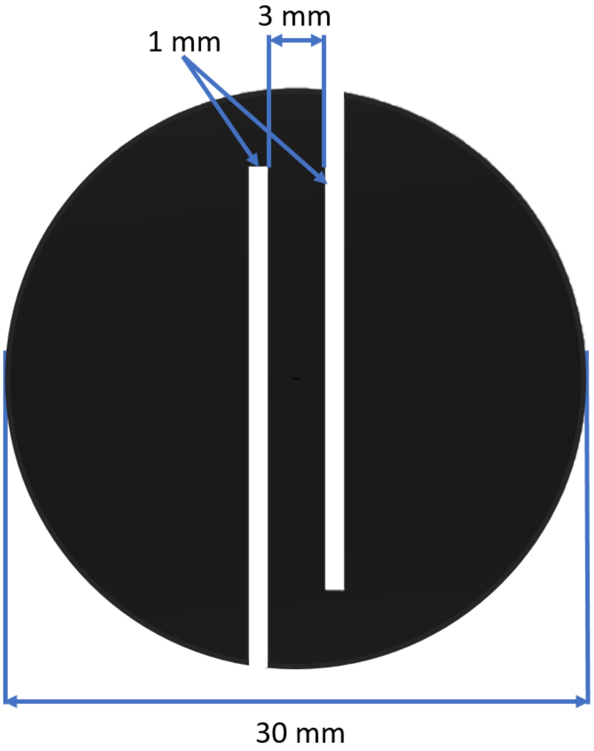

Figure II-29: Drawing of the design of a 30 mm REBaCuO bulk (1 mm thick). Both sides in a half-moon shape are used as contact surfaces with the current leads and the center area of 3 mm² of section is used for measuring the critical current.

With this, a sample holder was design to fix the sample between two copper plates and fix it to avoid any mechanical stress on the very fragile central bridge, see Figure II-30.a,b. This sample holder used screws with 3D printed ball joints to smoothly move the 2 upper currents leads and avoid any angles between the current leads and the sample and so avoid any possible mechanical stress or bad contact surface.

A commercial YBaCuO single crystal of 47 mm was used as a prototype, its larger size will allow a larger contact surface and so less heat, the sample is presented with Figure II-30.c. However, during the preparation of the sample with the help of the wire diamond saw of the lithopreparation platform of the GeoRessources laboratory, the very fragile sample has broken in few parts as we can see on Figure II-30.d. This highlights the necessity to work on a thicker central bridge and so a larger sample as well as a stronger power supply is needed. In this way, new prototypes could be prepared with a thicker cross section with a use of a 900 A power supply in a near future and four points characterization on a thin bulk will be done.

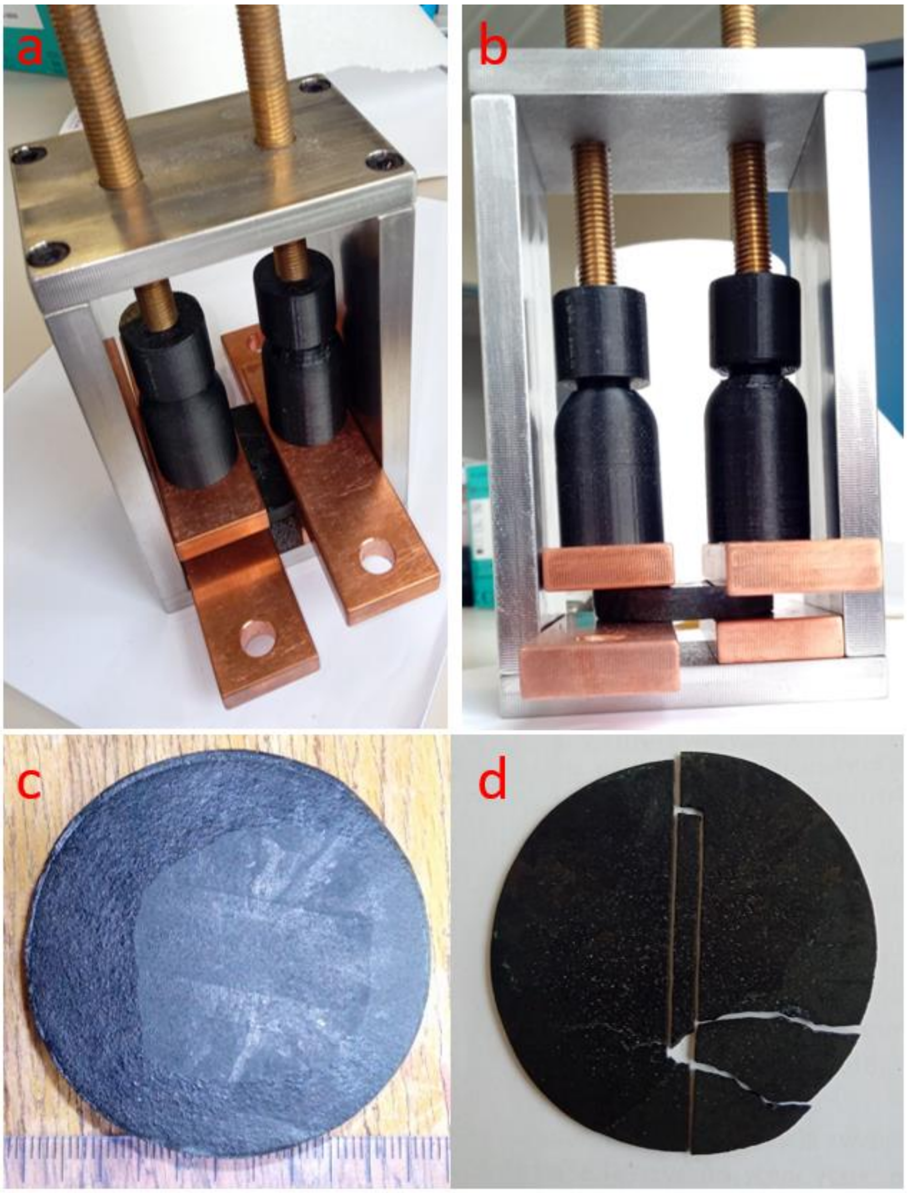

Figure II-30: The a-b pictures show the sample's holder with the four copper current leads to ensure a large contact surface with the sample. The top current leads can be moved with the screws and the ball joints to install and fix the sample (a thick sample is installed as example). The pictures c-d respectively show the samples used before and after the machining. The sample has broken in few parts during the cutting.

II.4. Conclusion

Through this second chapter we have seen how a superconducting bulk can be characterized and so how its materials and superconducting properties can be measured. This kind of measurements is essential to compare the different materials and then determine the best material/design for a potential use in applications.

Also, by studying the different characterization methods and in particular the so-called Bean's model, associated with the widely used MPMS-SQUID, we have seen that many assumption/approximations are needed which makes difficult to efficiently compare two very different materials. This, however, gives us a good view of the characterization of superconducting materials and a solid establishment before going deeper in the synthesis, characterization and comparison protocols of specific materials such as the Iron-Selenide complex, the subject of the next chapter.

Chapter III: Polycrystalline Iron-selenide superconductors

III.1. Introduction

A point that hasn't been discussed before is the occurrence of elements and their actual production over the world. It is now known that the industry is based on the extraction of minerals and their preparations. Some of them are considered as "critical elements" because of their necessity on our current and future technologies and their production limitations. Among them we can find numbers of the rare-earth elements, including Neodymium, Gadolinium, Yttrium, Europium, Lanthanum or Samarium which are all at the center of development of high temperature superconductors or permanent magnets. Even more problematic is the fact that 80% or more of the rare earth are produced by only one single country, China, which leads to political pressures.

One solution is the use of superconductors free of any rare earth elements and other critical elements. In this way, the newly discovered Iron-Based (IB) superconductors family can give multiple solutions: It was discovered in 2006 that LaOFeP become superconductor at 4 K [151], soon after, superconductivity was discovered in Iron-Pnictide with the LaOFFeAs complex at 26 K [152] and Iron-Chalcogenides in FeSe at 9 K [153]. Now, a lot of Iron-Based superconductors were discovered, mainly in the family of Iron-Pnictide [29], [154], [155] and show promising properties, such as a critical temperature of up to 56 K in SrFeAsF [156]. However, a big part of them are using rare-earth element and, perhaps even more problematic, use Arsenide, a hazardous material which need to be handle in special condition and could be hardly adopted in many countries so a use in a large number of electrical machines may cause serious problems.

In this way, a focus on the second main family, i.e. Iron-Chalcogenides, seems to be a better idea as Selenium is not as toxic as Arsenide is and both Iron and Selenium are not critical elements. Another argument comes from the fact that their properties are not well understood, as example the critical temperature of FeSe reaches 37 K under a pressure of 7.6 GPa [157] or even 109 K while using a single layer films [158].

Finally, it appears that this material has a lot of doping possibilities, such as silver [42], [159] or Tellurium [160] and what makes this material really interesting is the effect of the alkali and alkaline earth metals (Li, Na, K, Cs, Ca, Sr and Ba) on the superconducting properties of FeSe [27], [28], [161]–[167], the critical temperature can go as high as 46 K with Sodium doping [27], [28] or can also show interesting critical current or irreversible magnetic field by adding potassium [166], [167]. As Iron-selenide is a new material, we can believe that a lot of doping possibilities will be discovered, follow by a wide increasing of its superconducting properties. So, it could represent a serious competitor of MgB_2 or Iron-Pnictides for a use at liquid hydrogen temperature (20 K).

So, along this chapter, we will start by presenting the Iron-Selenide material, then we will see how I prepared and synthesized this material using either a classic furnace sintering or a Spark Plasma Sintering (SPS) process. Then the following part will display the result of the synthesis with the help of a systematic characterization protocol. After, we will focus on the extraction of the critical current density of a FeSe sample I prepared using a new technique. Finally, we will make a focus on the effect of doping on the FeSe synthesis as well as the effect of aging on the properties. Then we will conclude about the superconductivity of a FeSe polycrystal according to my results.

III.2. Physical and magnetic properties of FeSe

III.2.a. Physical properties of Iron-Selenide

Iron-Selenide is a very simple compound as it is only made of two components, however, its phase diagram is very complex and many kinds of properties can be reached by playing on the stoichiometry or the annealing temperature.

Phase diagram of FeSe is presented in Figure III-1, [168], [169], it shows how complex is this alloy and demonstrates the complexity for preparing large size single domain crystals. The superconductivity only appears into the tetragonal β-FeSe phase [153] that can only be reached between 350 and 450 °C with a stoichiometry near 1:1 (so 1 atom of Iron for 1 atom of Selenium), this phase is easier to see with the zoom on the interesting part of Figure III-1. The superconducting β-FeSe has many neighbors and some of them could be really problematic due to their magnetic properties:

- A α-Fe phase present with an excess of Iron (Fe + FeSe), it displays a soft ferromagnetism (so a totally reversible magnetic moment with no remnant field) as it is made of iron [170].
- A Fe_7Se_8 phase appears with an excess of Selenium (above 52 atomic percent of Selenium) and below 600 °C. It exhibits hard ferrimagnetic properties [171]–[173].
- At higher temperature the γ-FeSe and the δ-FeSe can be reached for 1:1 stoichiometry or with an excess of Selenium. Those phases can be antiferromagnetic, paramagnetic or ferrimagnetic depending of the stoichiometry [174], [175].

Those phases play a tricky role due to their magnetic properties when they act as secondary phases. So, reducing their impact and ensure the purity of the prepared sample is the key for the best magnetic and so superconducting properties.

The superconducting β-FeSe phase has a relatively low critical temperature of 8-10 K but it has been reported that a superconducting transition appears at 14-15 K [39], [176], [177].

The works done on single crystal of FeSe shows the presence of a very large critical magnetic field H_{c2} [39], [178], [179], which is really necessary for potential high field applications. However, FeSe shows a quite low critical current such as roughly 10^4 A.cm^{-2} at 4.2 K [178], [180]. comparing to the one of MgB_2 at the same temperature, 10^5 A.cm^{-2} [181], [182]. But doping this material has said above with alkaline materials, leads to a wide increasing of the critical properties as reported in the literature.

Finally, as for many superconductors, the FeSe possesses anisotropic superconducting properties [167], [180], [183] due to its matrix structure but it is sufficiently low to not be problematic as it is for a YBCO bulk, so it can be both used as single or polycrystal.

As discussed above, this PhD thesis is focused on the development of polycrystals with a focus on the optimization of its magnetic and superconducting properties with the objective of study a potential application as superconducting bulk for electrical engineering. In this way, the samples I was working on were all prepared by furnace sintering and/or Spark Plasma Sintering as a polycrystalline pellet or bulk.

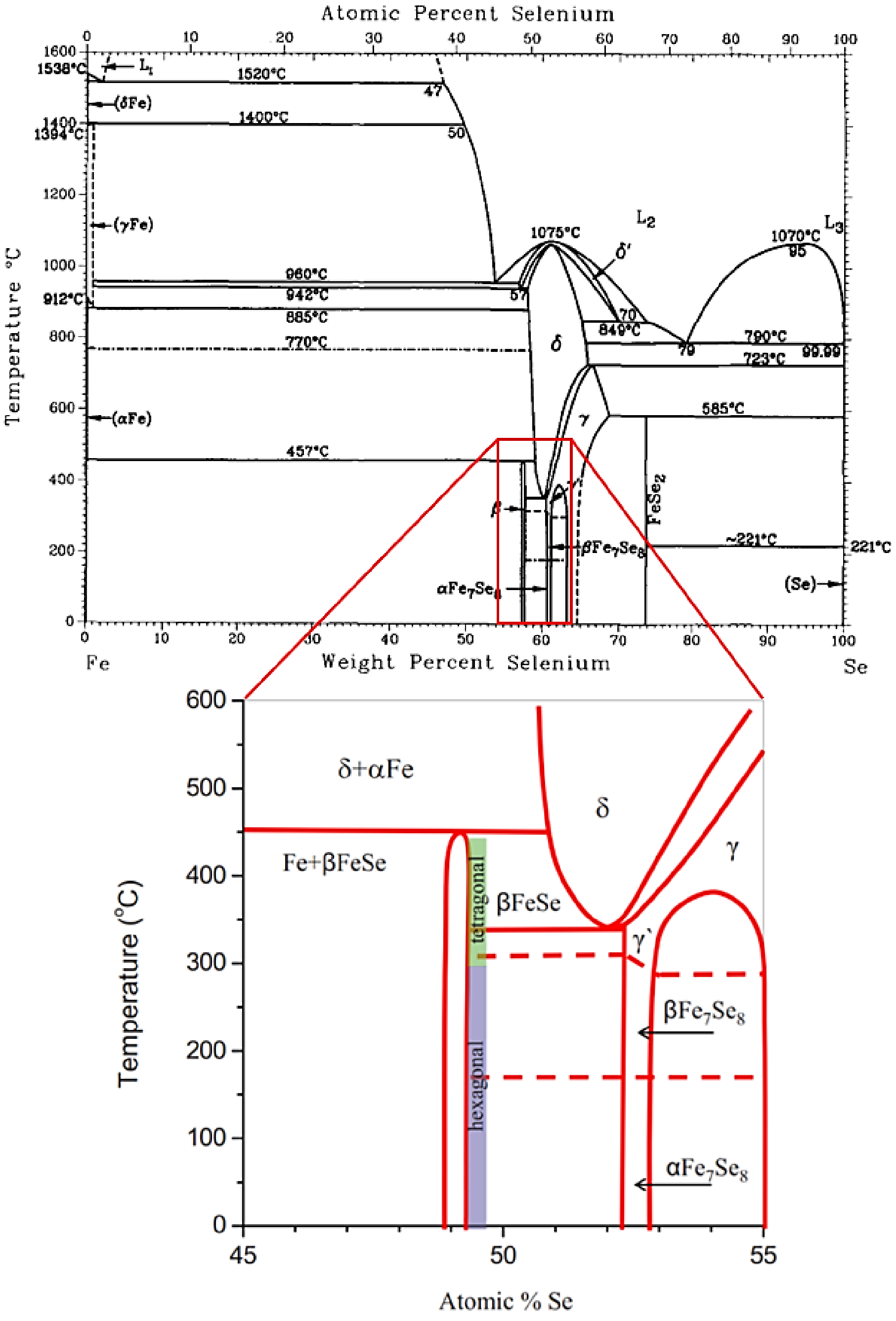

*Figure III-1: Phase diagram of the Iron-Selenide [168] complex with a zoom on the working part [169]: The tetragonal β-FeSe phase is supposed to be the superconducting one, the α-*Fe *one shows a soft ferromagnetic moment and the Fe_7Se_8 phase is a hard ferrimagnet.*

III.2.b. Magnetic properties of electron irradiated Iron-Selenide polycrystals

The first way to study a superconducting material and understand all its properties is to start with an already prepared sample. In this way I was able to characterize the properties of polycrystalline Iron-Selenide samples prepared by Muralidhar et al. [18] with a "classic" sintering protocol.

Several samples, extracted from the bulk, were then irradiated using 2.5 MeV electrons with the help of the Sirius facility of the French Polytechnic school.

Two different fluences were used: 2×10^{19} e-.cm^{-2} and 4×10^{19} e-.cm^{-2}. Then the magnetic properties of a sample from each group as well as an unirradiated one (hereinafter Ref for reference sample) were determined using the already presented SQUID-MPMS of the Jean Lamour Institute.

The samples are presented on Figure III-2, they possess irregular and different shapes and, more important, far from thin plates or long cylinders so it makes hard to use the Bean model and the Chen's formula on those samples to compute the critical current density or even to clearly compute the average length, wide and height. However, it is still worth to compare the magnetic moments expressed in emu.g^{-1}.

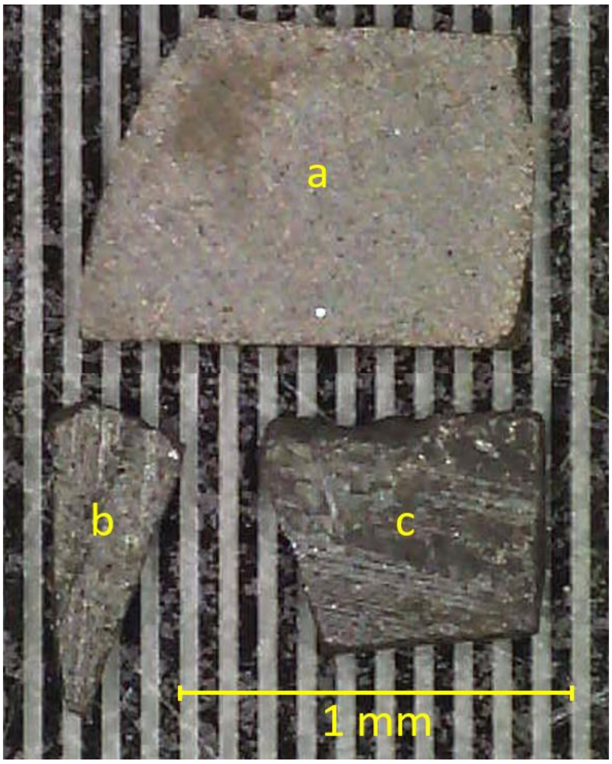

Figure III-2: Picture of the samples from the bulk of Pr. Muralidhar [18] with the unirradiated sample (a), the sample irradiated with 2×10^{19} e-.cm^{-2} (b) and 2×10^{19} e-.cm^{-2} (c).

The magnetic moment of the sample was then evaluated and the normalized between 0 and 1 magnetic moment function of the temperature ($m(T)$) is presented on Figure III-3 from 2 to 20 K.

We normalized the magnetic moment because the samples have a really different magnetic moment at 20 K, supposed above the critical temperature which is at 8-10 K for a “standard” FeSe superconductor [153].

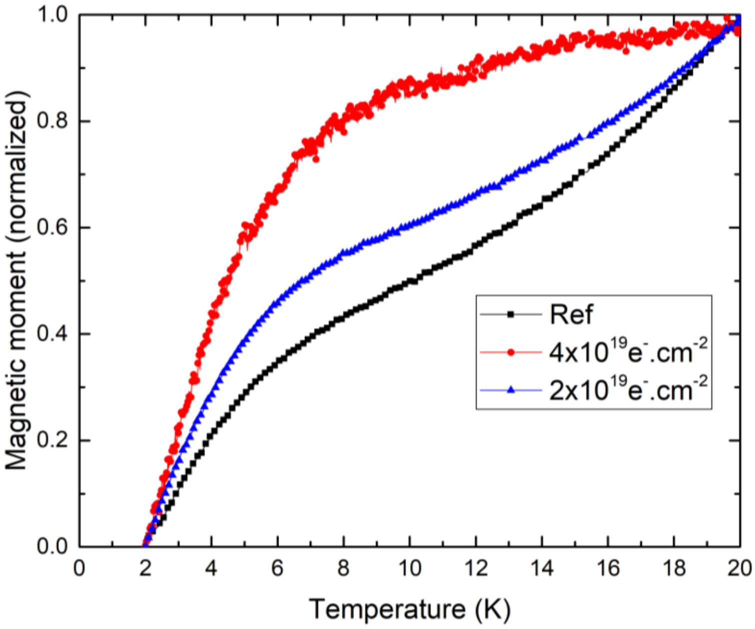

Figure III-3: Magnetic moment versus temperature for the 3 samples presented with Figure III-2 with a background field of 10 Oe. We can see a potential superconducting transition between 2-10 K for the 3 curves.

On the superconductor presented over the second Chapter, i.e. the YBaCuO complex, the transition temperature can be easily identified from the $m(T)$ curve as seen in the previous chapter (Figure II-9) with a brutal variation of the magnetic moment. However, here it is really hard to identify a superconducting transition, at least we could hag a smooth transition of the $m(T)$ shape between 6 to 8 K for the Ref one but it is clearly far from being an obvious superconducting transition. Also, it is clear that a non-superconducting magnetic moment is present over each sample.

With this, the magnetic moment function of the applied magnetic field $m(H)$ of the Ref sample at 20 K and 2 K is presented on Figure III-4.a, as the samples were prepared with the same protocol as presented in Muralidhar et al. [18], the presence of a very strong ferromagnetic signal is not surprising. More interesting is the almost absence of difference between the $m(H)$ at 20 K and 2 K which suggests a very weak, if not null, superconducting moment. Comparing the different magnetic moment at 2 K of the samples with each other also shows practically no difference on Figure III-4.b.

The presence of a very strong ferrimagnetic signal, probably expressed by a Fe_7Se_8 secondary phase, completely overcomes the superconducting one (if there is one) so with this current samples it seems impossible to study the superconducting properties with the presence of this secondary phase. Also, the $m(T)$ curves from Figure III-3 suggest that the ferrimagnetic signal change with the temperature between 10 to 20 K where no superconductivity is expected, so subtracting the $m(H)$ curve at 20 K on the one at 2 K can’t remove the ferrimagnetic signal without leaving a remaining parasitic signal but this will be discussed at the end of this chapter.

In conclusion, the lack of information about the superconducting properties does not allows to evaluate the effect of the electron irradiation on the superconducting properties of FeSe materials. But it points out the necessity to produce an Iron-selenide complex free of secondary phases, a requirement for the development of such material in more practical applications such as large size bulks for electrical engineering technologies.

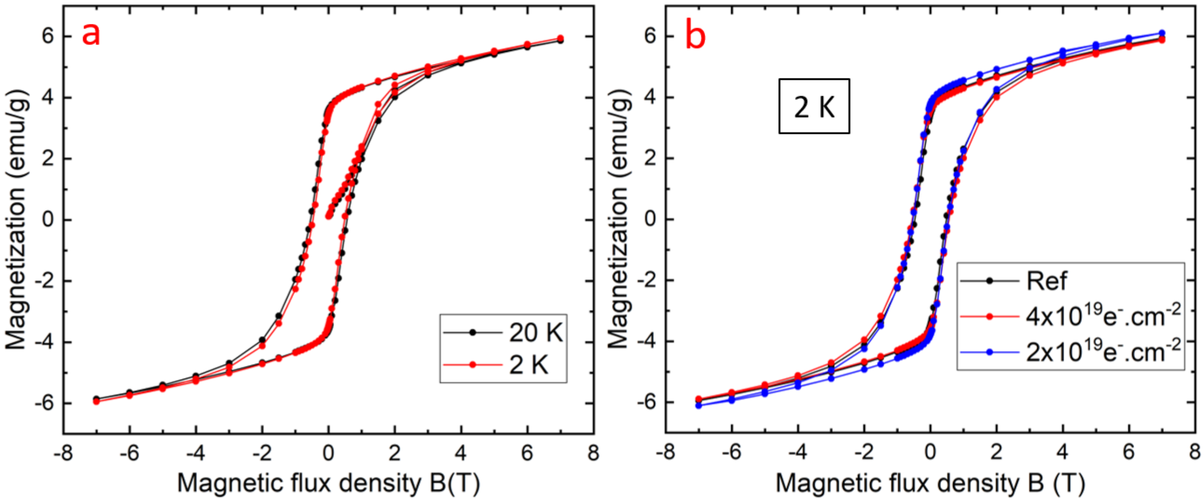

Figure III-4: Magnetic moment per grams function of the magnetic field for the Reference sample (without irradiation) at 20 and 2 K (a) and at 2 K for the Reference sample as well as the irradiated ones with $2{\times}10^{19}$ and $4{\times}10^{19}$ e-.cm^{-2} (b).

III.3. Problematic, objectives and global protocol

III.3.a. Problematic and objectives

By looking to the literature [16], [42], [169], [182], [184], [185], we can see that a large number of papers highlight the problematic presence of ferrimagnetic (Fe_7Se_8) or ferromagnetic (remaining Fe metal) secondary phases.
Also, William et al. [185], Mcqueen et al. [184] and Pomjakushina et al. [169] highlight the sensitivity of the magnetic properties of the sample with the stoichiometry. But information is still missing, such as:

- Is it possible to greatly reduce the secondary ferro/ferrimagnetic phases in a polycrystal?
- Is it possible to keep good superconducting properties and reduce the secondary phases at the same time?
- And is it possible to rapidly prepare FeSe polycrystals such as using the Spark Plasma Sintering (SPS) process (more than 7 days in Mcqueen et al. [184])?

So, to study the superconductivity of the β-FeSe superconductor and gives a conclusion on its potential for a use in electrical engineering applications, it seems important to see if a good single phase FeSe polycrystal can be prepared via a “rapid” classic sintering protocol or via SPS.

This is why I decided to go to Japan, Tsukuba in the National Institute of Advanced Industrial Science and Technologies (AIST), Research Institute for Advanced Electronics and Photonics, in the Team of Ogino-sensei during 4 months to prepare Iron-selenide polycrystalline superconductors.
After it, I made 2 other trips, 3 weeks each, to Caen in the CRISMAT Laboratory in the team of Prof. Noudem for further synthesis and analysis.

The goals of those trips were to:

- Find a way to reduce as much as possible the secondary ferro/ferrimagnetic phases.
- Reduce or limit the synthesis time.
- Extract and study the superconducting properties.
- Deliver a conclusion on its potential use in applications or the necessity of further improvement, particularly in comparison with the promising MgB_2 complex.

III.3.b. Global protocol and systematic approach

During all the synthesis campaign of FeSe bulks, I follow the same global protocol for the realization and the characterization:
First of all, the needed tools such as spoon or mortar and pillar… are loaded into a Glove Box with pure Argon atmosphere. Then, the powders are weight and mixed together in the needed stochiometric proportions. They are, most of the time, pressed as a pellet and placed inside an evacuated quartz tube (furnace sintering) or loaded into a carbon mold (Spark Plasma sintering). The quartz tube or the carbon mold are loaded into the furnace or the SPS chamber then the powder is sintered and/or annealed following the desired protocol.
The resulting pellet is released in the glove box if more synthesis processes are required or in air if not.
A part of the pellet is used as a sample used for a magnetic characterization using a MPMS-SQUID. I was measuring the magnetic moment function of the field and/or the temperature with the objective of studying the impact of the ferro/ferrimagnetic content and the superconducting one.
The final results are compared with the precedent ones and give a direction for the next preparation.
This basic protocol was used either during my stay at AIST or at CRISMAT with some specific variations depending of the goals of the synthesis, this will be described later along this chapter. But first, let's make a focus on the equipment used for the sample preparation.
I usually do a first qualitative test with a permanent magnet to give an idea of the amount of the secondary ferro/ferrimagnetic phases.

III.4. Sample preparation and synthesis equipment, materials and protocols

III.4.a. Powder preparation and mixing

The starting point to synthetize a polycrystal is by preparing the equipment and the precursor powder, so let's describe point by point how to prepare the starting powder:

- An example of the tools I typically used and load into the GB is presented on Figure III-5 where we can see a spoon (a) used to collect and manipulate the powders, the dish and the paper (b,c) to contain and weight the powders, the mortar and pillar made of agate (d,e) for mixing and grinding the powders. Tweezers of different sizes (f) are used to help manipulating the materials when the large gloves are very bulky and the aluminum foil to prepare the work space. Finally, a scalpel (g) and/or scissors could be useful. Also, the needed materials for the sample condition, specific to each synthesis technique, have to be loaded at that time in the GB (they will be described later in the next section).
- To load that equipment in the GB, it is placed into the vacuum airlock visible on the Figure III-6.(a). A vacuum is done over 15 min in order to evacuate the air then it is fulfilled of pure argon, the same atmosphere than into the GB, using the pipe/pump system Figure III-6.(b). It is also possible to do a vacuum/refill 3 times a row in less time (time saving but Argon consuming). When the fulfilling is finished, it is now possible to open the inner gate of the vacuum airlock watching at the oxygen/water detector Figure III-6.(c) to check on any pollution event.
- To manipulate the materials inside the GB, I use the holes with gloves Figure III-6.(d) which are protected both from my hand with clean latex gloves and from the material I manipulate using over gloves. it is highly important to keep the GB gloves clean and safe as they can't be easily change and ensure the confinement.
- Now it is time to prepare a working space (Figure III-6.(e)) using the aluminum which protects my work from potential resulting powders or dust but also prevents my materials to pollute the GB.
- The starting powders are placed in the materials rack Figure III-6.(f), here I always used pure powders of Iron and Selenium. It is essential to use very pure powders and know the average size of the grains as they can both play a huge role on the synthesis quality. The Table III-1 is presenting the characteristics of the powders I used either in Japan and at Caen.

	AIST		CRISMAT	
Chemical element	Purity	Grain size	Purity	Grain size
Iron	99.9 %	150 µm	99.5 %	10 µm
Selenium	99.9 %	75 µm	99.8 %	75 µm

Table III-1: Sizes and purities of the Fe and Se powders used either at AIST and CRISMAT.

- The powders are collected with the spoon and placed on the dish/paper and weight (Figure III-6.(g)) in the chosen stochiometric proportions. I typically worked with a total weight of 0.3-0.6 g at AIST but sometimes more (up to 3 g) at CRISMAT.
- The powders are successively placed in the mortar and with the help of the pillar a manual grinding and mixing is done on the powders with the objectives of getting a homogeneous mix which greatly optimizes the synthesis quality and efficiency.
- Now the resulting mixture has to be conditioned for the desired synthesis process. I will describe the specificities of each methods in the next section.
- The as-prepared setup is now taken out from the GB, so all the tools, as well as the working place and the over gloves are placed inside the aluminum foil. For that, if the atmosphere inside the vacuum airlock is still pure Argon, I can directly open the inner gate and place all my equipment, if not, a new vacuum/refill have to be operated with the same protocol as for entering the tools. then everything is outing.

Now a last but not least part comes with the cleaning or throwing of every used equipment or produced wastes. We use ethanol and scouring powder to clean the tools, when metals are stuck in the mortar, a solution of nitric acid is used to dissolve it, then it is clean with ethanol.

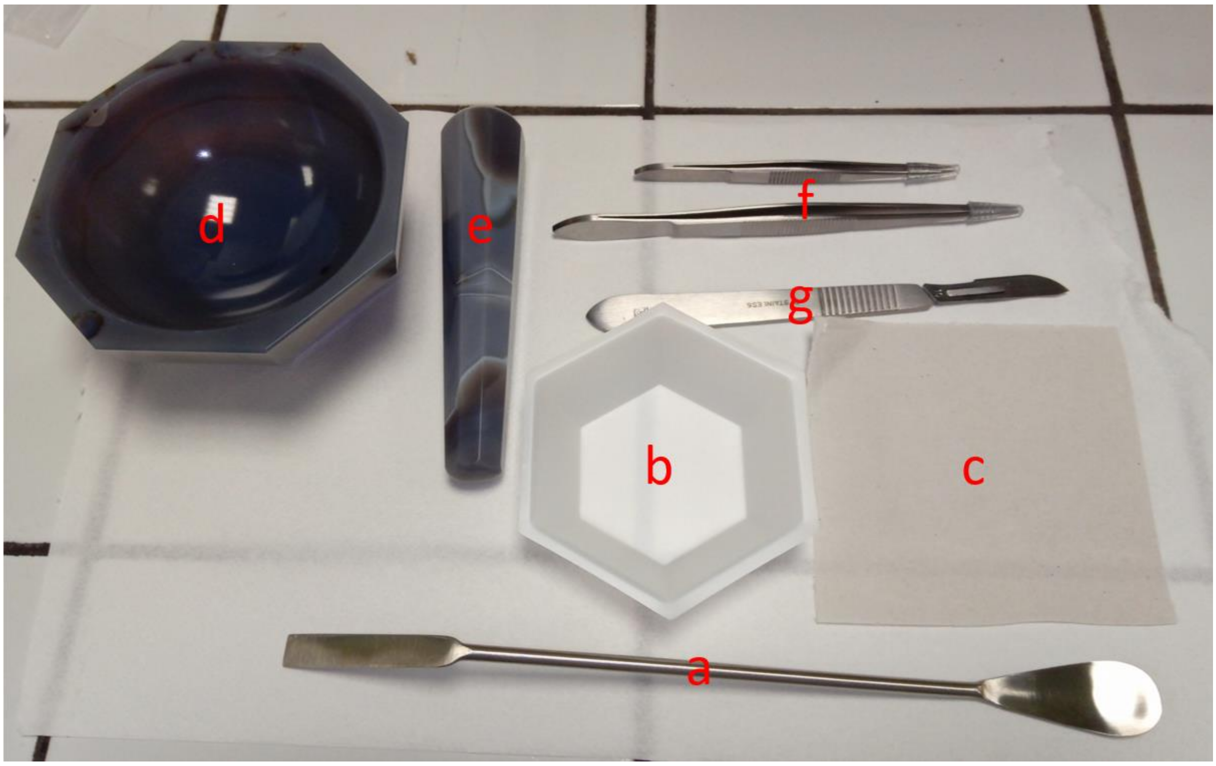

Figure III-5: Picture of an example of tools I used to prepare the samples both at AIST and at CRISMAT. We can see a spoon (a), a dish (b), a Joseph paper (c), a mortal with its pillar (d,e), tweezers (f) and a scalpel (g).

Figure III-6: A picture of the tool box I used at AIST (left) and at CRISMAT (right). We can see the different important materials used for the preparation of samples: the vacuum airlock to enter the materials (a), the pipe/pump system to control the GB's atmosphere (b), the oxygen level controller (c), the access holes with gloves (d), the working space with the tools (e), the powders racks (f), the weight machine (g) and the hydraulic press (h).

III.4.b. Classic furnace sintering: conditioning and general synthesis protocol

- #### Starting powder conditioning

After mixing the powders in stochiometric proportions, we need to condition and prepare the mixture for the synthesis process:

- To add a supplementary protection and guaranty a good synthesis, the prepared pellet or powders are rounded by a tantalum foil which acts as an oxygen getter [186] but also keeps the Selenium and the iron together during all the process and far from the Silicon of the quart tube. An example of a sample rounded by a Tantalum foil is given on Figure III-7 as well as a quartz tube with a rounded sample. Before that we sometimes place the powder into a mold with the desirable size (typically 3 mm width) and press it as a pellet, sometimes we directly use the powder.
- The rounded powder/pellet is placed into a quartz tube with one close side, it has a higher fusion temperature than the materials we use (1670 °C) and a low reactivity with either the Iron and the Selenium.
- A vacuum tube with a valve is installed on the open side of the tube and the valve is closed for maintaining the pure argon atmosphere inside the tube when extracting out of the GB.
- Closely after outing the tube of the GB, it is plugged on a pump then a primary vacuum of 10^{-2} to 10^{-3} mBar is done and using a flame made of methane mixed with pure oxygen we are able to fuse the quartz tube and so seal the rounded sample into the newly evacuated quartz tube. A picture of the torches is shown on Figure III-8

and a picture of an as-prepared sealed tube is presented with Figure III-7.b. and can be seen inside the GB of Figure III-6.(e).

The samples are now protected from any pollution and are ready to be loaded in the furnace for the sintering reaction.

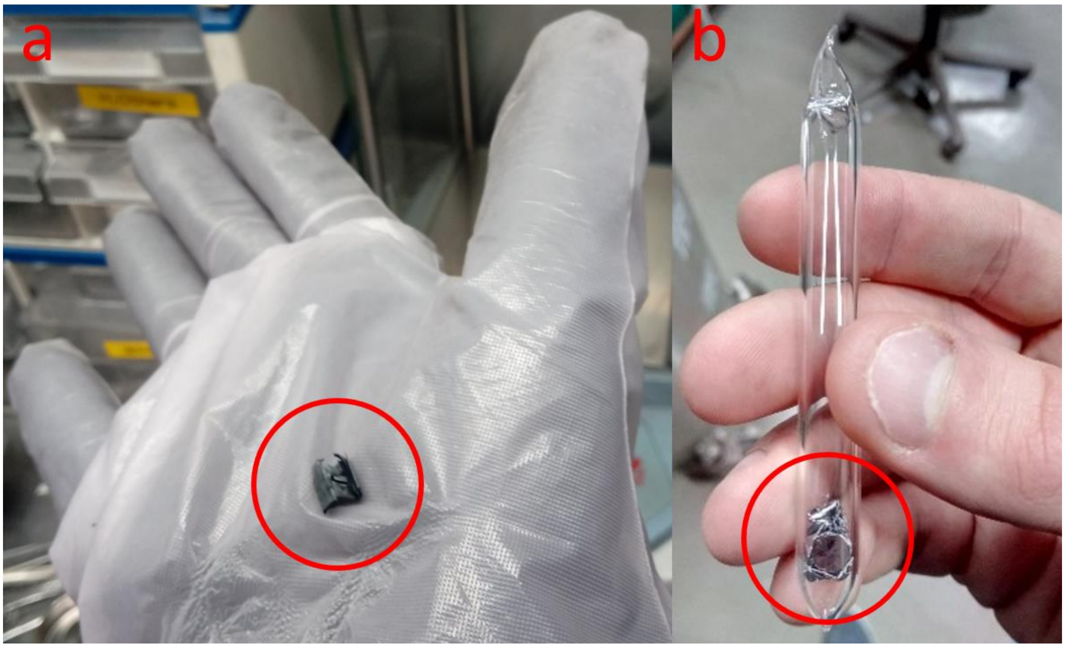

Figure III-7: Picture of a FeSe pellet rounded by a Tantalum foil inside the GB (a) and after the sealing in an evacuated quartz tube (b).

Figure III-8: Pictures of the torch and the pipe/pump system to melt and seal the quartz tube used at AIST (left) and at Caen (right). We can see the flames at roughly 1300 °C (a), the pipe bringing the gas and the oxygen for the combustion (b), a quartz tube with the sample plug on the pump before the sealing (c), the pump (d) and the remaining quartz tube after the sealing (e).

- Furnace

For all the furnace synthesis I did, I always used a muffle furnace as the one presented on the Figure III-9. Let's describe the general protocol I used for the furnace sintering:

Figure III-9: Muffle furnace I used at CRISMAT with 3 samples loaded inside with alumina crucibles.

- The furnaces have to be calibrated by measuring the temperature at the place where the samples will be (typically at the center of the chamber).
- The quartz tube(s) is/are placed inside an Alumina crucible which helps to homogenize the temperature around the sample, fixes it and protects the furnace in case of explosion or leaking.
- Then everything is placed in the furnace, at the center at it can be seen on Figure III-9.
- Now the furnace can be closed and the heating protocol can be entered by using the controller panel right below the door. Basically, two things can be programmed: the temperature and the time to reach or stay at it. An example of a heating protocol is presented on Figure III-10.
- Finally, when the protocol is ending I proceed with a so-called air-quench which consists of removing the sample from the furnace and let it cooldown in air or, as in my case, in contact with a cold metal plate. This is a fast way to cooldown the sample and stop any reaction, this is commonly done for polycrystal synthesis and I did it every time during my work.

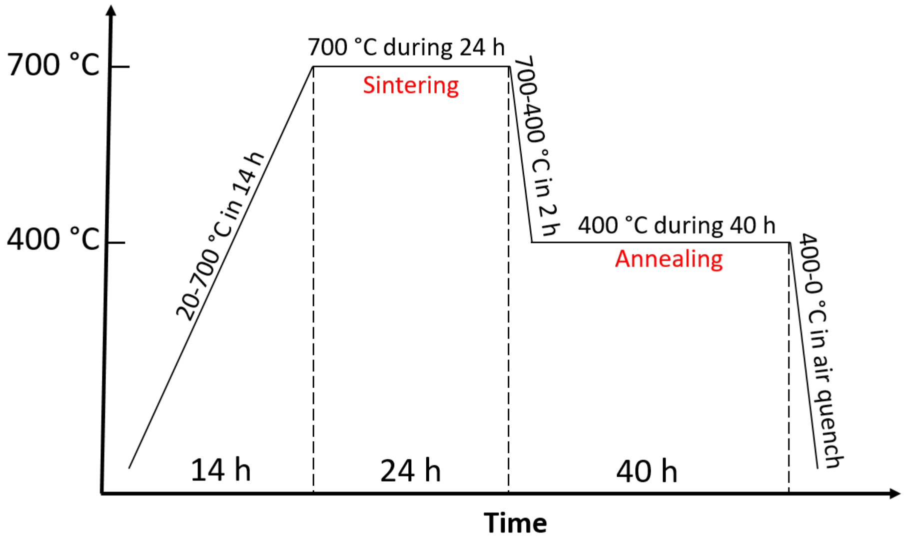

Figure III-10: Layout of a typical sintering profile with the temperature and the duration of each step. In this example, we do the annealing right after the synthesis which is call a 1-step synthesis in this manuscript.

- Some of the quartz tube after the synthesis are shown with Figure III-11 where we can see that the tube is clean when the sample is rounded by a Ta foil, Figure III-11.a, and with white deposition (some Se) when the sample is not loaded (Figure III-11.b,c) which indicates no pollution of Se or Fe as well as no leaks.

Figure III-11: Picture of quartz tubes with reacted sample after a furnace sintering. On the top the sample was rounded in a Ta foil while the 2 others were not. The consequence is the loss of Selenium deposited on the quartz tube (white smoke)

Now, depending on the next part of the protocol, the quartz tube can be open in air and the sample prepared for the characterization, or open in the GB for a new grinding and conditioning for a second furnace heating, or for an SPS protocol.

III.4.c. Spark Plasma Sintering: conditioning and general synthesis protocol

- Preparation of the mold

When the furnace synthesis requires a quartz tube with a one closed side, the SPS process needs a more complex sample older.

The carbon mold is made of 3 different parts: a carbon pipe and two carbon cylinders which fit with the hole of the pipe. The powders will be placed in the middle of the pipe between the two cylinders. The powders can easily damage the mold during the process so we cover the inner bore of the pipe as well as the sides of the cylinder in contact with the samples with a carbon sheet, this also helps a better confinement. Figure III-12 is showing the mold used in Caen when it is ready to use with loaded powder (Figure III-12.a) and after the experiment where we can see the different parts of the mold and the pellet between the carbon cylinders rounded by the carbon sheet (Figure III-12.b).

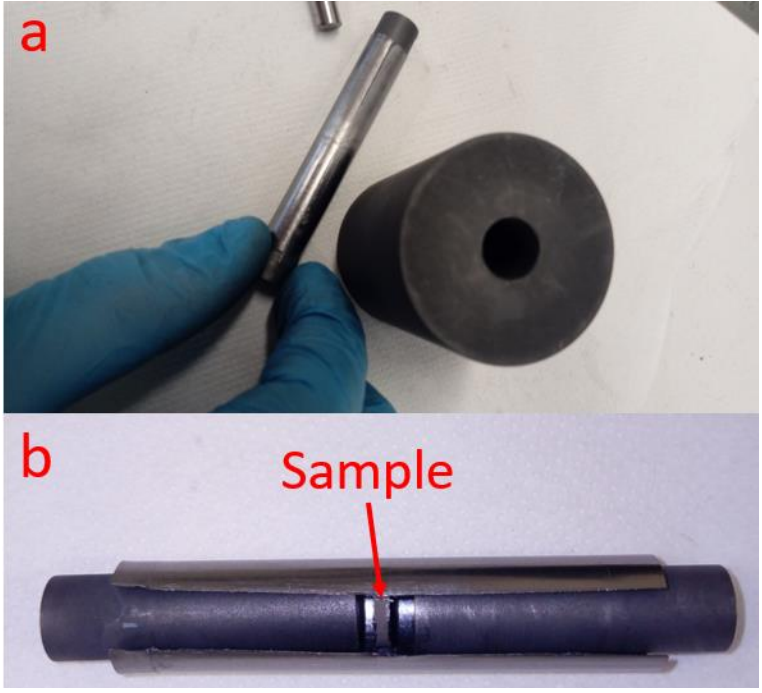

Figure III-12: Pictures of the carbon mold with a sample loaded between the pipe and rounded by a carbon foil (on those pictures, the sample is already reacted).

- Starting powder conditioning

As for the furnace sintering, the prepared powders in stochiometric proportion have to be conditioned for the upcoming SPS process:

- The mold has to be prepared outside of the GB (easier), which means that the carbon sheet is loaded inside the mold and on one of the cylinders which obstructs one side.
- The prepaid mold and the remaining part (one cylinder with the two pieces of carbon sheet to protect the sides of the cylinder in contact with the powder) are loaded into the GB.

- The powder is then charged in the mold with the open side only in contact with the carbon sheet. The remaining cylinder close the mold and pressed with the hydraulic press to remove the remaining argon, flatten the powder and ensure an airlock.
- The mold can now be removed from the GB and installed into the SPS machine. The powder is kept protected from the air because of the airlock.

Doing the synthesis using SPS machine, so reacting the Fe and Se powders mixed together, is called an in-situ process as the synthesis is done with the SPS machine. When the powders are firstly synthetized using classic furnace technique then the result is handled and reconditioned in the SPS mold under Argon atmosphere only for an annealing process, it is called an ex-situ process. During my PhD both methods have been experimented, the preparation and synthesis protocols are very similar, only the working temperature and durations are different.

• SPS machine

The Spark Plasma Sintering or "Frittage Flash" in French can be summarized as a synthesis technic which heat-up the sample via an electric current using the so-called Joule effect while the sample is pressed.

The two machines I used either in Japan and at Caen are presented in the Figure III-13 and were used as follow:

- The prepare mold is installed inside the vacuum chamber Figure III-13.(a) and placed between the carbon holders. On the Japanese SPS we can see hot walls Figure III-13.(b) they are used to synthetize by the hot-pressing protocol as it heats the sample like a furnace, an intermediate technique between classic furnace and SPS processes tried on FeSeTe materials [187].
- The current leads Figure III-13.(c) are pressed on the mold to maintain it in order to place the thermocouple inside a small hole on the mold Figure III-13.(d). This allows to measure a temperature very closed to the sample's one and will be used by the machine to regulate the current.
- Now the chamber can be closed, the air is evacuated and we fulfill the chamber with a low-pressure Argon gas or work with pressured Argon (1 bar or above) using the pipe and pump system Figure III-13.(e).
- Now the synthesis program can be prepared using a computer and upload on the machine. This program will control the desired temperature, atmosphere, pressure on the mold, the number of steps and their durations. the SPS protocol, called SPS profile will be shown with the results for each sample.
- The control panel Figure III-13.(f), is used to regulate the current control which can be adapted depending on the sample's resistance or the heat capacity change, here we use a standard function for metals. And then it is used to launch the program.
- After the ending of the program, the vacuum inside the chamber is leaked and the sample is then air quenched.
- Finally, the chamber is opened, the mold is removed from it and extracted. It results a cylindrical and dense pellet as shown in Figure III-13.(g).

Figure III-13: Pictures of the vacuum chamber (a) of the SPS machines used at AIST (top left) and CRISMAT (top right). The AIST machine possesses a Hot-Wall (b) which allows a Hot-pressing process. We can see the current leads (c) and the thermocouple used to measure the temperature (d). The 2 others pictures are the face and the back of the SPS machine used at CRISMAT with the pump/pipe system (e) and the control panel (f). A 10 mm size sample after the SPS synthesis is presented at the bottom (g).

III.5. Synthesis and characterization of FeSe polycrystal

This section will present the results of the synthesis of FeSe superconductors I prepared either using furnace or Spark Plasma Synthesis. I will start by presenting the characterization methods I choose to compare the different samples and why some other methods have been put aside. Then a section will be dedicated to the furnace sintering with an exploration of the synthesis parameters based on the selected method and a second part will add some supplementary analysis using the best synthesis parameters. A last section will do the same work on the Spark Plasma Sintering process either with an in-situ and an ex-situ approach.

III.5.a. Starting point and characterization method

Some works on synthesis have been tried with the routine presented in Grivel et al. [186] which consist of a two steps process: a first sintering at 700 °C then the prepared sample is removed from the quartz tube in the GB then re-grind and re-sealed in a new quartz tube for a second sintering at 700 °C follows by an annealing at 400 °C.

As it is mainly done in the literature, we were focused on characterization by the X-ray pattern and the measurement of the $m(T)$ curve to identify the transition's temperature. Some $m(H)$ curves where done but as a time-consuming experiment, they haven't been done on all samples.

Several different synthesis parameters have been tried by me. However, I quickly conclude that X-ray pattern isn't the best way to optimize the superconducting properties of a material. Indeed, in the literature, we can find very different interpretation of the pikes of an X-ray pattern [18], [182], [186], [188], [189]. This could come by the presence of multiple and very closed to each other spikes from various phases which can be a tricky interpretation for the auto-analysis of the various different software used. Thus, I wasn't able to clearly identify which samples were "good" or "bad", in other words, which one have a good superconducting phase and properties and which have bad ones.

Finally, the $m(T)$ curves can't give a very accurate value of the ferrimagnetic moment as the moment is typical of a hard ferrimagnet and so any magnetic field applied to the sample prior to the measurement will change it. In fact, this occurred all the time since I was testing the presence of ferrimagnetism in my samples using a permanent magnet. As a magnetic field in the range of 10-100 Oe is applied to the sample at room temperature for centering toward the detection coils, it also magnetizes the sample and leads to uncertainty when measuring the $m(T)$ curves.

With those observations I concluded that working mainly with the X-ray pattern cannot lead to the best FeSe superconductor and the $m(T)$ curve isn't enough to determine accurately the magnetic properties and with this the superconducting properties.

So, to evaluate the "quality" of the prepared sample we will focus on the $m(H)$ curves which gives a much more accurate way to evaluate the important parameter: the ratio superconductivity/ferri-ferromagnetism (hereinafter SC/Ferr). As said above, time limitation only allows a quick measurement of a 5 quadrants $m(H)$ curve at 1 T sometimes associated with a $m(T)$ curve, still interesting to evaluate the critical temperature.

The method I propose to study the ratio SC/Ferr is based on the comparison of the magnetic moment under self-field ($\mu_0 H_{ext}$ = 0 T), where the superconducting part is maximal and the ferri/ferromagnetic one is low and at max field ($\mu_0 H_{ext}$ = 1 T) when the ferri/ferromagnetic signal is maximal and when the superconducting one is minimal. Also, always for time saving reason, the samples weren't properly cut and/or polished so for a more suitable reading the curve have been normalized with $m(H_{max})=1$ with $\mu_0 H_{max}=1$ T. So, we can easily extract a ratio between the magnetic moment at $m(H=0)$ and at $m(H_{max})$ which is always equal to 1 here. An example is given on Figure III-14, where we have for one of the curves: $m(\mu_0 H=0) = 0.8$; $m(H_{max}) = 1$; which gives a ratio of 0.8.

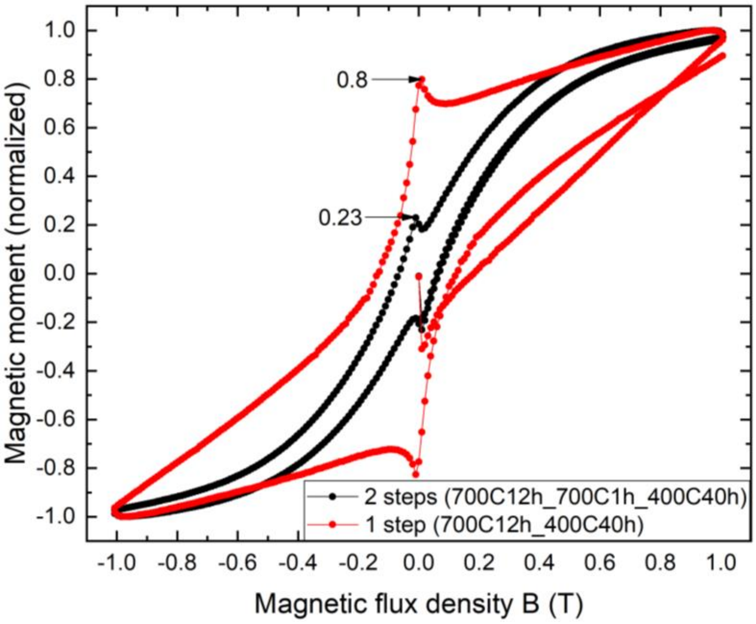

Figure III-14: Normalized magnetic moment of 2 FeSe samples at 2 K with a 2-steps and a 1 step synthesis process with a respective ratio of 0.23 and 0.8.

III.5.b. Furnace Sintering

In this section, we will present the optimization of the synthesis parameter using a classic furnace sintering. For this, we will name the produced samples with the synthesis parameters as follow:

For a sample with a 1:1.1 stoichiometry, sintered during 12 h at 700 °C then re-sintered at 700 °C for 1 h follow by an annealing during 40 h at 400 °C we will say: FeSe$_{1.1}$_700C12h_700C1h_400C40h. If necessary, other information are given right after this denomination.

- Exploration of the synthesis parameters

The first work was to verify if a 2-steps synthesis is needed or if a simple one is good enough. For this a sample following the routine presented right below but with a 1:1 stoichiometry (FeSe$_{1.1}$_700C12h_700C1h_400C40h) and a sample with a one-step routine of FeSe_700C12h_400C40h were prepared and measured. Their respective $m(H)$ curves are presented with Figure III-14. The ratio of the 2-steps synthesis is 0.23 where the one of the 1-step is 0.8 which clearly highlight the unnecessity of the 2-steps process which is coherent with the general results seen on the literature, particularly in the Grivel et al. [186].

Another important parameter to study is the stoichiometry. Some attempts have been done with different synthesis times but a comparison using a 700C12h_400C40h synthesis protocol with a 1:0.965, 1:1 and 1:1.05 stoichiometry. The result of this second comparison is presented in Figure III-15. Some papers underline the sensitivity of the magnetic properties with the stoichiometry [184], [185], [190] and here, the 1:1 stoichiometry looks to be the best and as it is hard to be more precise (some powder is always lost during the preparation and the conditioning) we will continue with this stoichiometry. A supplementary work, including X-ray, will be presented later with the results of the CRISMAT campaign but from now we will focus on the 1:1 stoichiometry.

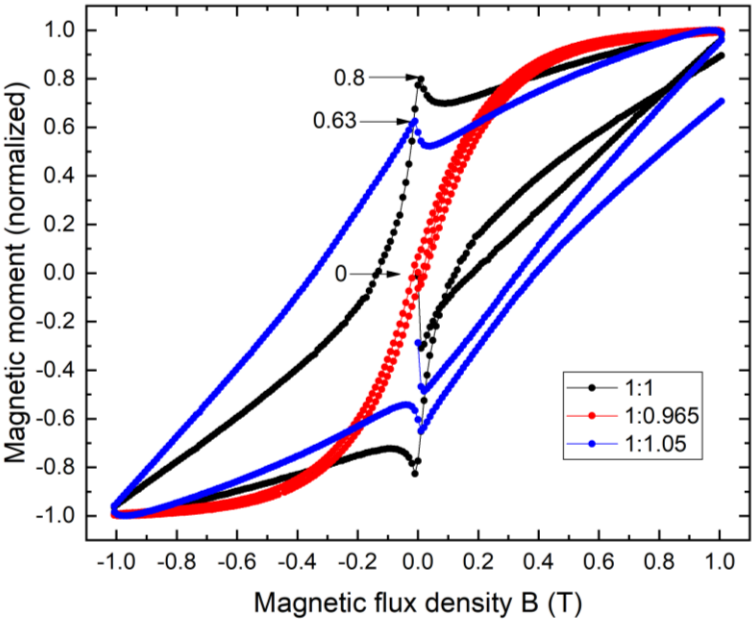

Figure III-15: Normalized magnetic moment of 3 FeSe samples at 2 K with different stoichiometry: $Fe_1Se_{0.965}$, Fe_1Se_1 and $Fe_1Se_{1.0.5}$ with a respective ratio of 0 (invisible superconducting magnetic field at H=0), 0.8 and 0.63.

Another important parameter with the stoichiometry is of course the temperature for the sintering process which is essential to nicely make a homogeneous and complete reaction over all the sample. And the annealing temperature which forms the desirable phase, here the β-FeSe phase.

According to the phase diagram (Figure III-1, [168]), the β-FeSe phase is formed between 350 and 450 °C, so 375, 400 and 425 °C have been tried and compared as we can see on Figure III-16.a and the 400 °C temperature seems the best one.

The sintered temperature was chosen to be 700 °C for the samples already presented for being above the boiling temperature of the Selenium, 685 °C. In this way we verified the difference between a sample sintered at 650 °C, i.e. below the boiling point of Se, and above (700 °C) with the Figure III-16.b. This figure shows that working above the boiling point of

Se gives a better result, which should be explained by a better homogeneity of the selenium during the process as the gaseous Se could spread all over the Fe powder.

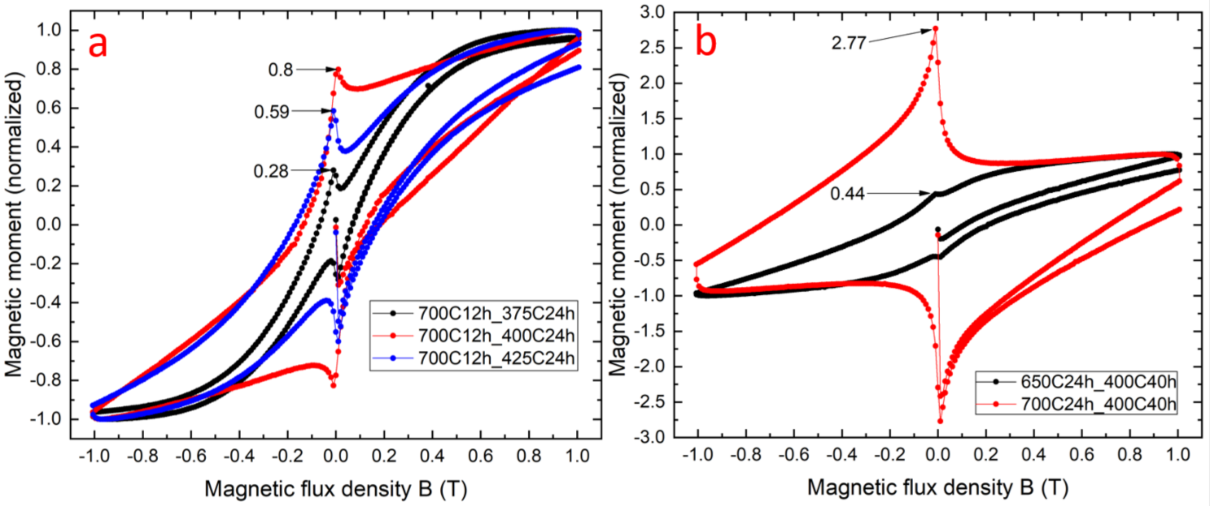

Figure III-16: Normalized magnetic moment of FeSe samples at 2 K. (a) shows the effect of the annealing temperature at 375 °C, 400 °C and 425 °C, their respective ratios are 0.28, 0.8 and 0.59. (b) presents the effect of the synthesis temperature at 650 °C (below the boiling point of Selenium) and at 700 °C (above the boiling point of Selenium). Their respective ratios are 0.44 and 2.77.

I have worked on other parameters such as the duration of the synthesis and annealing and the best one finds so far comes with the sample FeSe_700C24h_400C40h with a $m(H)$ at μ_0H=1 T presented with Figure III-17 with a ratio of 2.77.

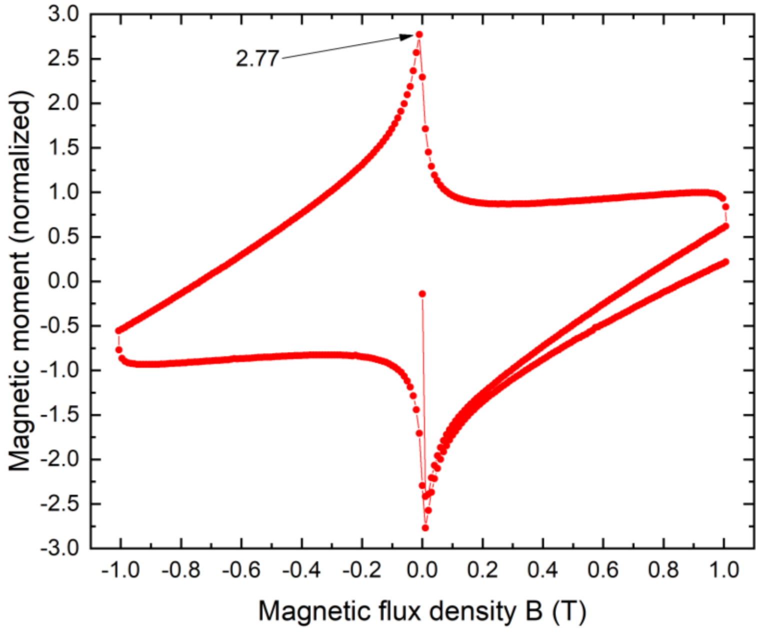

Figure III-17: Normalized magnetic moment of a the FeSe_700C24h_400C40h sample at 2 K. The ratio is as high as 2.77 which means that the magnetic moment at H=0 is 2.77 times higher than at 1 T.

So, to conclude with this part the FeSe_700C24h_400C40h is the best sample I prepared according to its ratio of 2.77. The reproducibility has been tested and the results are shown on Figure III-18 the results are both “good” as their ratio are both above 1 but still with an important difference of 69 % which denotes a lack of reproducibility.

However, 0.3 g gives very small samples for the following SPS process or even for being considered convenient for applications (YBCO bulks can now be above 200 g). So, we tried to work on 2 times heavier sample: 0.6 g. The produced samples are shown on Figure III-18.b where we see ratios of 1 and 0.3, much lower than for the 0.3 g samples (2.77 and 1.64). As the synthesis process were exactly the same as well as the shape of the samples (cylindrical pellets of the same diameter but 2 times longer height), this huge difference is surprising, maybe a lack of thermal homogeneity for larger samples could be responsible of this difference. Anyway, a deeper study should be done on this particular observation.

This justify a new work with this time more consideration on the X-ray pattern of each samples beside $m(H)$ curves to have complementary information.

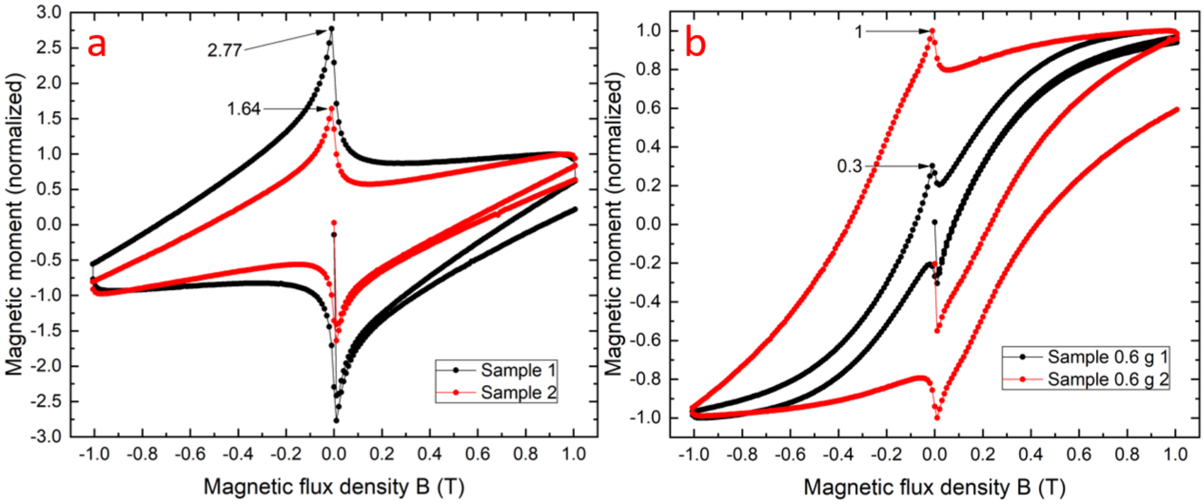

Figure III-18: Normalized magnetic moment of FeSe samples at 2 K. (a) displays the reproducibility of the FeSe_700C24h_400C40h samples of 0.3 g, we can see that the ratio is varying a lot but both ratios are better than the other ones presented before. (b) presents the reproducibility of the FeSe_700C24h_400C40h samples of 0.6 g. The ratios are really different (by a factor around 3) and worse compared to the ratios of the 0.3 g.

• Additional studies with X-ray analysis

We have determined a protocol for preparing superconducting FeSe with a relatively high proportion of superconducting moment compared to the starting one but the remaining ferri/ferromagnetic signal is still problematic.

As said above, the stoichiometry looks primordial and so, as reported in the literature [184]-[186], a stoichiometry around 1:0.975 would give a good result.

So, this has been realized along another try with the 1:1 stoichiometry. The resulting $m(H)$ loops at 1 T and 2 K are displayed with Figure III-19, and we can see that the $Fe_1Se_{0.975}$ is nearly not superconducting (someone can see a small bump around H_{ext}=0) and the magnetic moment looks like a soft ferromagnetic hysteresis. On the other hand, the Fe_1Se_1 displays a ratio of 0.9, higher than for the $Fe_1Se_{0.975}$ sample but lower than for the best sample prepared in Japan with Figure III-17, even while measured at 2 K. But the ratio is in the range of the one of Figure III-18.b equals to 1. Maybe this comes from the much larger size of this sample: 3 g (10 times larger than the one of Figure III-18.a).

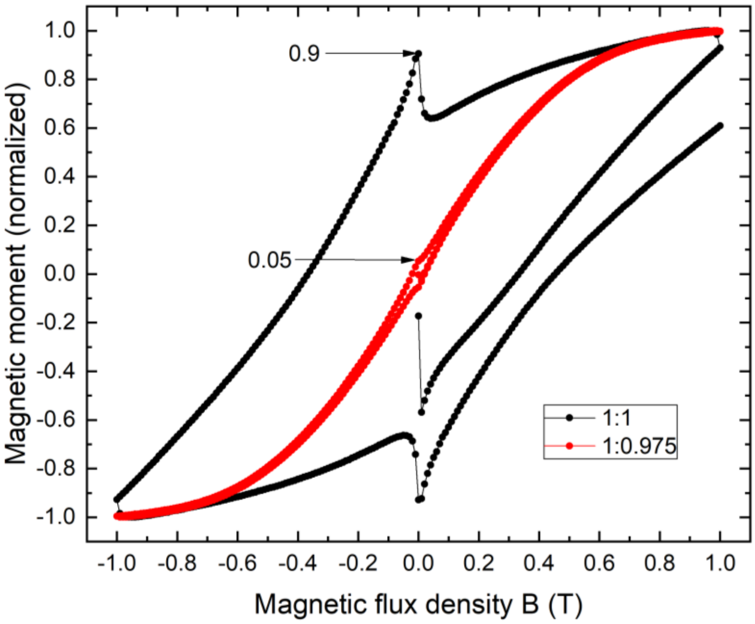

Figure III-19: Normalized magnetic moment of FeSe samples at 2 K of 2 samples prepared with the "best" routine found at AIST, i.e. 700C24h and 400C40h with a 1:1 stoichiometry and 1:0.975. Their ratios indicate a much better results with the 1:1 stoichiometry. The 1:1 sample was of 3 g and unpressed when the 1:0.975 is a 0.3 G pressed sample.

However, those really different curves allow a much better understanding of the X-ray pattern of a FeSe polycrystal. Indeed, such patterns are shown with the Figure III-20, by having a close look at the corresponding ray for each phase and by comparing with the *m*(*H*) we can give the following interpretation:

- The spikes with the blue dot (●) are present in both curves and are dominant, so this should be the so-called β-FeSe phase.
- The spikes with the red dot (●) are present in all the FeSe samples, except when the *m*(*H*) curve looks like a soft ferromagnetic hysteresis curve. As a hard ferrimagnetic is expected from the Fe_7Se_8 [171]–[173], those spikes should correspond to this phase.
- Finally, the spike with the gray dot (●) corresponds to a remaining Fe phase which is a soft ferromagnet with a dominant magnetic moment on Figure III-19.

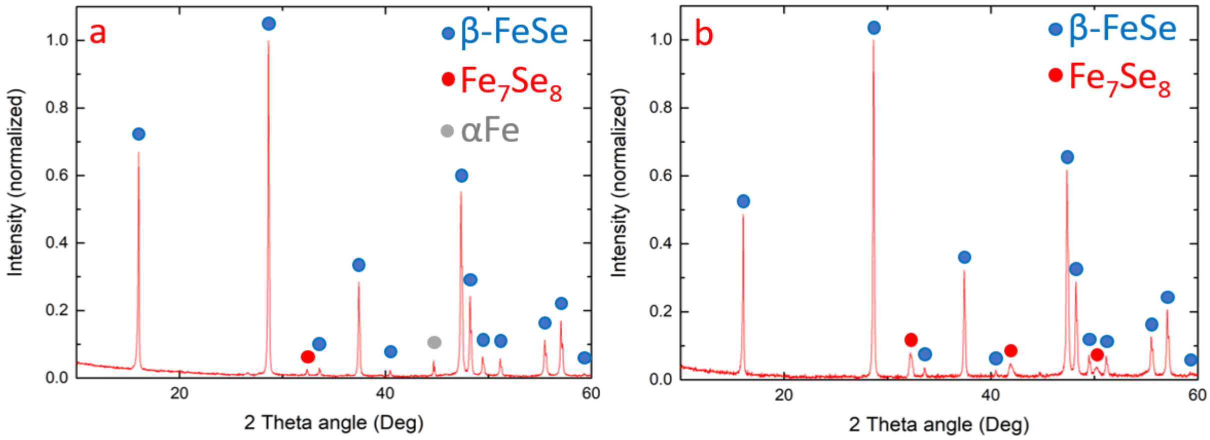

Figure III-20: X-ray patterns of the FeSe samples prepared by furnace at CRISMAT with a 1:0.975 (a) and a 1:1 stoichiometry (b) with the 700 °C 24 h 400 °C 40 h routine. The blue (●), the red (●) and the grey (●) dots indicate respectively the β-FeSe, the Fe_7Se_8 and the α-Fe phases.

This interpretation is shared with the one given by some papers in the literature [169], [184], [185], and we will see right after that this was also confirmed by the samples prepared by SPS.

So, following this interpretation, we can see that, we have an almost pure β-FeSe phase both with the $Fe_1Se_{0.975}$ and the Fe_1Se_1 stoichiometries but with the presence of remaining soft ferromagnetic Iron ($Fe_1Se_{0.975}$) or the secondary Fe_7Se_8 phase (Fe_1Se_1), a hard ferrimagnetic one. But the superconducting phase of both samples are really different which can hardly be explained only by their different X-ray pattern, both majorly presenting a dominant β-FeSe.

The lack of reproducibility shows that a key and unknown parameter should play a role during the preparation, synthesis or annealing. We may cite the precision on the stoichiometry and of the weight, some lost powder during the conditioning and transfer between the different tools (from the spoon to the mortar or to the mold or the tantalum foil…). Maybe an inhomogeneous size of grain of both powders (Table III-1) can explain such variations. A much deeper study is needed to solve the lack of reproducibility.

III.5.c. Spark Plasma Sintering

As for the furnace sintering, we will use a very similar denomination to gives the synthesis parameters of all samples and to indicate any pre-sintering using a furnace I used the term pre-sin in the name such as FeSe_700C24h_pre-sin_400C30min_SPS, where the "pre-sin" is placed right after the furnace step and right before the SPS one. I add the term "SPS" right after to avoid confusion with conventional sintered samples.

- #### In-situ SPS

As explained during the first section of the chapter, the Spark Plasma Sintering process offers a simple way to prepare very dense and efficient superconducting bulks with large size in a very short time (<1 h). For this, the in-situ routine is the best as it allows to synthetize, densify and anneal at the same time which make a ready-to-use sample in one step. This is why we naturally choose this routine as a first step.

So, a mix of Selenium and Iron in 1:1 stoichiometry were placed in the mold and a first try with a 1 step synthesis at 650 °C was applied under an evacuated argon atmosphere. This temperature comes from the fact that under SPS condition, the phases transitions occurs at lower temperature.

One of the key tools to study the SPS process comes from the data record by the SPS itself. Here we will focus on the 2 most important ones, called hereinafter the SPS profiles: the temperature measured by the thermocouple which is assimilated as the temperature of the sample, and the variation of the thickness of the sample measured though the variation of the piston during the process.

So, the resulting SPS profiles for the FeSe_650C15min_SPS is presented on Figure III-21.

Let's describe the process into different steps:

- (a) The temperature is increasing at 50 °C.min^{-1}, at around 150 °C a huge diminution of the sample's thickness is recorded which could mean a very fast chemical reaction with the consequence of reducing the volume of the sample by organizing the atoms though a crystal or because of a loss of matter. Then the volume increases again while the temperature is still increasing. This can be due to the thermal dilatation of the sample or a slow chemical reaction.

- (b) Now the temperature is slightly increasing until it reaches 650 °C (to avoid overheating) and maintained during 15 min. When the maximum temperature is reaching the sample stops to grow-up which highlight its connection with the thermal dilatation. During the time at 650 °C the sample height stays constant so no reaction or movement occurs.
- (c) finally, the temperature is decreased to the ambient one and the volume of the sample is reduced due again to the thermal relaxation.

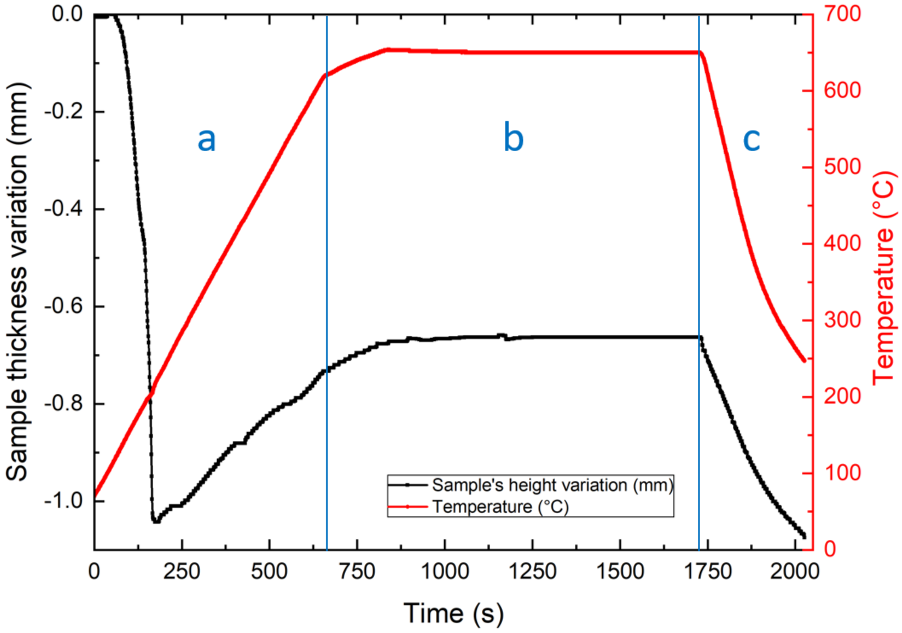

Figure III-21: SPS profile of an in-situ FeSe sample with the temperature of carbon mold close to the sample's temperature and the sample's height variation function of time. We can see the heating ramp (a), the synthesize plateau (b) and the cooling down ramp (c).

After several minutes the mold is at room temperature and its then removed from the vacuum chamber.

The reason of the brutal evolution of the sample's height was found directly on the mold itself and all over the wall of the chambers we can see on Figure III-22 and on the upper right Figure III-13. Indeed, black drops are around the mold corner and red powder is on the wall of the chamber, this is liquid selenium which escaped at 150 °C which is surprising given that the melting point of Se is 221 °C in ambient conditions. Note that the measured temperature of 150 °C corresponds to the one on the thermocouple which is located inside the mold and a few mm away from the sample, so with a high temperature rate of 50 °C.min^{-1} the real temperature of the sample should be slightly higher.

This also explains why no other reaction occurred at higher temperature as the remaining piece inside the mold is only an iron pellet.

So, we can conclude from this first in-situ test and the few other tries after that the Selenium will always go away and so the in-situ synthesis can't be done by a simple way.

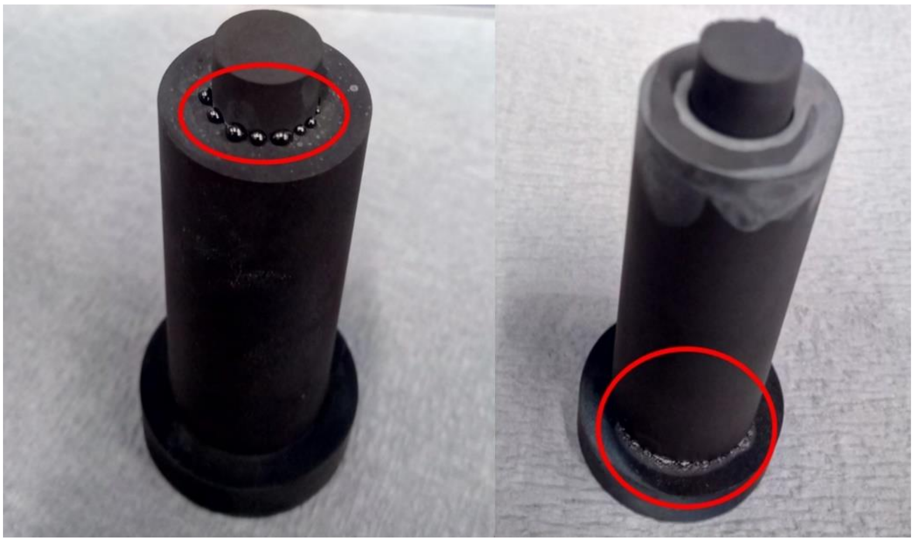

Figure III-22: Carbon molds right after the SPS sintering with an in-situ process. Selenium drops are visible outside the mold since they escaped during the synthesis process.

Following the results obtained right above, I came this time with several ideas to overcome the leak of Selenium.

The first one was to try a low temperature reaction, i.e. make the Fe and the Se react below the melting point of Se. Then by slowly increasing the temperature, the remaining Se will gently melt and react with the remaining Fe or escape. To increase the probability to react all the Iron, we tried with a 1:1 stoichiometry but also with a 1:1.3 and 1:1.5 with the hope that the extra selenium will be "burned-off" above the melting point. Also, we worked under Argon atmosphere at roughly the atmospheric pressure.

The SPS profiles for all those samples are shown on Figure III-23. Let's describe those curves step by step:

- We start by heating up at 100 °C.min^{-1} the sample until it reaches 198 °C (part a) with a small overheating follow by a temperature stabilization. We can see that the volumes of the 3 samples start by lowering when the temperature reaches 190 °C which could be either a loss of Se or a chemical reaction.
- Then the temperature slowly increases to reach 218 °C at 1 °C.min^{-1} and we can see a slow decreasing of the height of the sample with the increasing of the temperature (part b). it is greater for the 1:1 sample but this is not significant as at 218°C they have the same total variation of -0.6 mm.
- In a third part, the temperature stays at 218 °C during 20 min which is slightly below the melting point of selenium under normal atmospheric conditions (part c). During this, the variation of the height for all samples is continuing its diminution and the 1:1 sample is showing a larger variation which could indicates a better reaction as intended with a balanced stoichiometry. We can see a flattening of the height after 3000 sec at the current step for the 1:1.3 and 1:1.5 samples. This could indicate the end of the reaction.
- The temperature is then increased to 230 °C at 1 °C.min^{-1} (part d). We can clearly see the melting and the leak of Selenium on the 1:1.5 sample at around 221 °C. This phenomenon is also present but weak on the 1:1.3 sample and can be properly seen

on the 1:1 sample. This was expected as a lot of remaining Se should be in the 1:1.5 sample, less in the 1:1.3 sample and just a little in the 1:1 one.

- Now the sample can be heated up to 400 °C at 100 °C.min^{-1} with a small overeating (part e). During this step the variation of the height is "finishing" which means that the remaining Se still inside the mold is moving out and/or the last reactions occurs.
- The temperature is kept at 400 °C during 30 min (part f). Almost nothing looks to appends during this time as the sample's variation is very small.
- Finally, the sample is cooled down and so the height is reduced due to the thermal relaxation (part g).

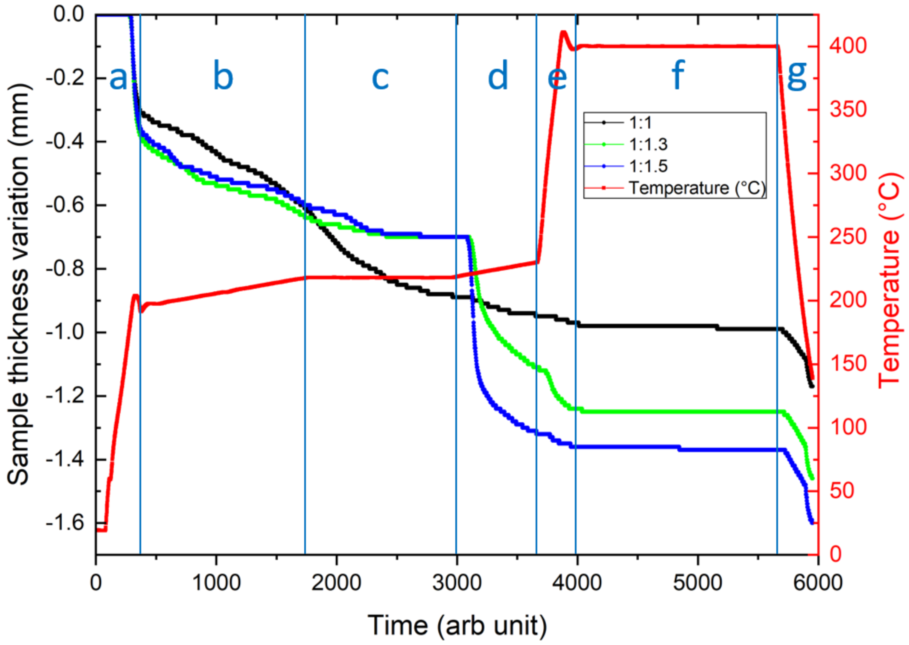

Figure III-23: SPS profile of in-situ SPS samples with the temperature of the sample and the variation of the sample's height along the experiment. Different parts of the process are showed; the fast heating (a), the slow heating (b, c, d) for the synthesis, a new fast heating (e), the plateau (f) for the annealing and the cooling down (g).

To analyze those samples, we made X-ray diffraction presented and normalized with Figure III-24. There is a huge β-FeSe phases (blue dot ●), an almost absent Fe_7Se_8 phase (red dot ●) for the 1:1 and 1:1.5 samples and completely absent one in the 1:1.3 sample (probably in the noise) but a huge presence of remaining Fe (gray dot ●) for all samples. However, the 1:1.3 sample looks a bit better as it possesses a lower quantity of remaining Iron. also, as the Fe_7Se_8 phase is weak for all sample, we decided to work with the 1:1.3 stoichiometry for the next in-situ preparation.

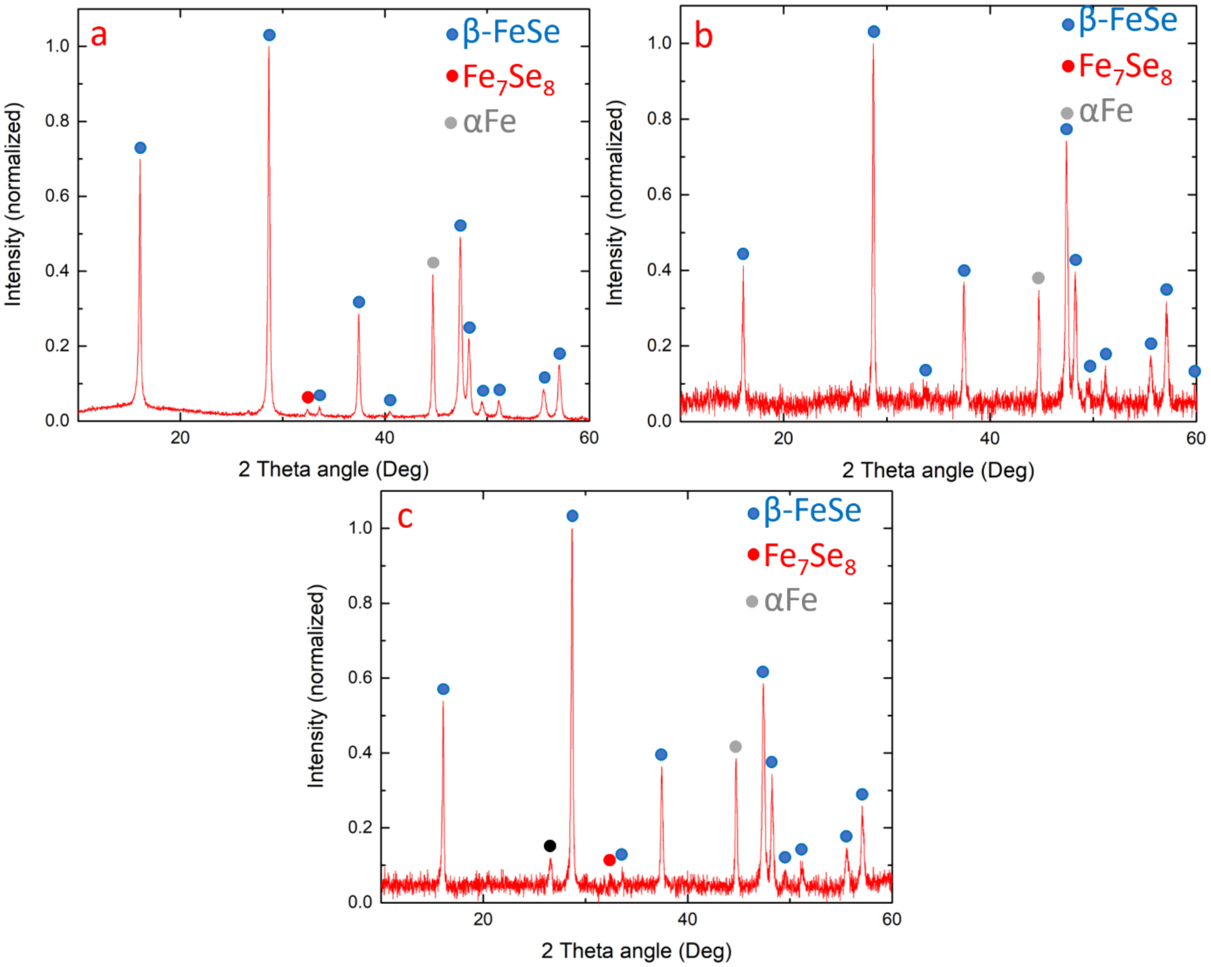

Figure III-24: X-ray pattern of FeSe samples prepared by SPS at CRISMAT with a 1:1 (a), a 1:1.3 (b) and a 1:1.5 (c) stoichiometry with the routine presented on Figure III-23. The blue (●), the red (●) and the grey (●) and the black (●) dots indicate respectively the β-FeSe, the Fe_7Se_8, the α-Fe phases and some remaining carbon. The X-ray diffraction was performed in 2 h for the (a) and only 30 min for the (b) and (c) which explains the noisy signal.

One more time, the escaped selenium is visible on the mold in Figure III-25.

Figure III-25: Picture of the carbon mold used to prepare SPS sample at CRISMAT. We can see, in the red circle, a Selenium droplet which was ejected during the in-situ process using the 1:1.5 stoichiometry.

Some other tries have been conducted with a slower routine than the one presented right above. The best result was obtained with the slow routine presented with Figure III-26. Here we opt for a fast increasing to 165 °C followed by a slow one to 218 °C and then by a stay at 218 °C during 1h, a new slow heating up to 230 °C with a stay at this temperature during 10 min which is a new step compared to before. Finally, the last part with a working temperature of 400 °C is the same as before.

The SPS profile shows a slow variation of the height of the sample, no brutal variation is present. As we worked with a 1:1.3 stoichiometry we may have an excess of Se so at least a part of the height loss comes from a leak of melted Se. However, the X-ray pattern given by Figure III-26.b, shows a very good result with a large β-FeSe phase with still an important amount of pure Fe and a tiny Fe_7Se_8 phase. So, the $m(H)$ curve of this sample was measured at 4 K, Figure III-26.c, and we can see a soft ferromagnetic curve without any sign of superconducting signal at 4 K. This is then very strange compared to the presence of a huge β-FeSe phase, but confirms the strong presence of Fe (soft ferromagnet) and the absence of Fe_7Se_8 (hard ferrimagnet).

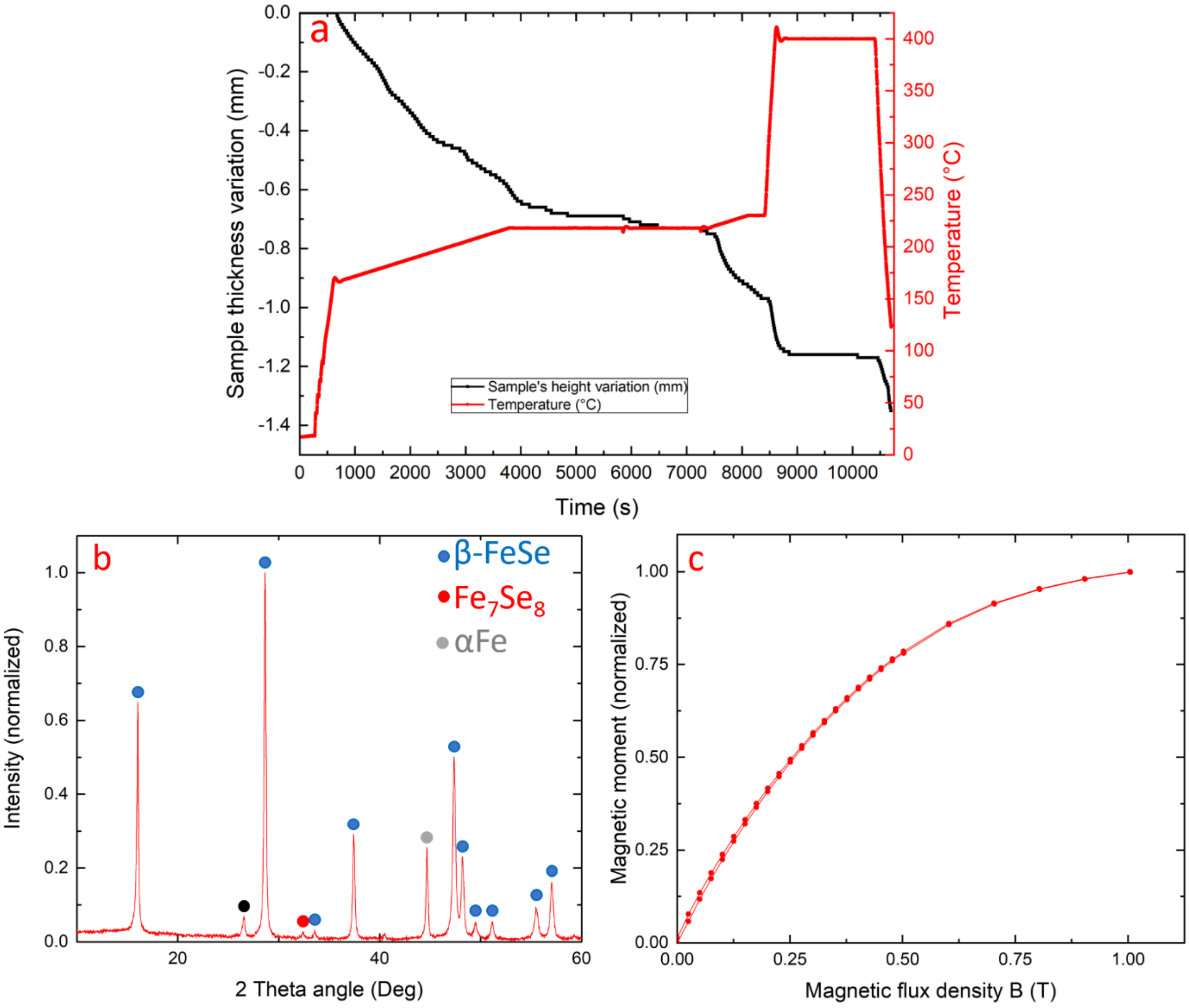

Figure III-26: (a) SPS profile of an in-situ sample with a 1:1.3 stoichiometry with a slow routine. (b) its corresponding X-ray pattern (The blue (●), the red (●) and the grey (●) and the black (●) dots indicate respectively the β-FeSe, the Fe_7Se_8, the α-Fe phases and some remaining carbon.) and (c) its magnetic moment at 4 K measured, only the 3 positive quadrants were measured.

Some last works have been done to prevent the leak of Se during the synthesis. For that, I made some wrap of Tantalum or Titanium and I placed the powder inside. The Figure III-27 show the before/after of the wrap.

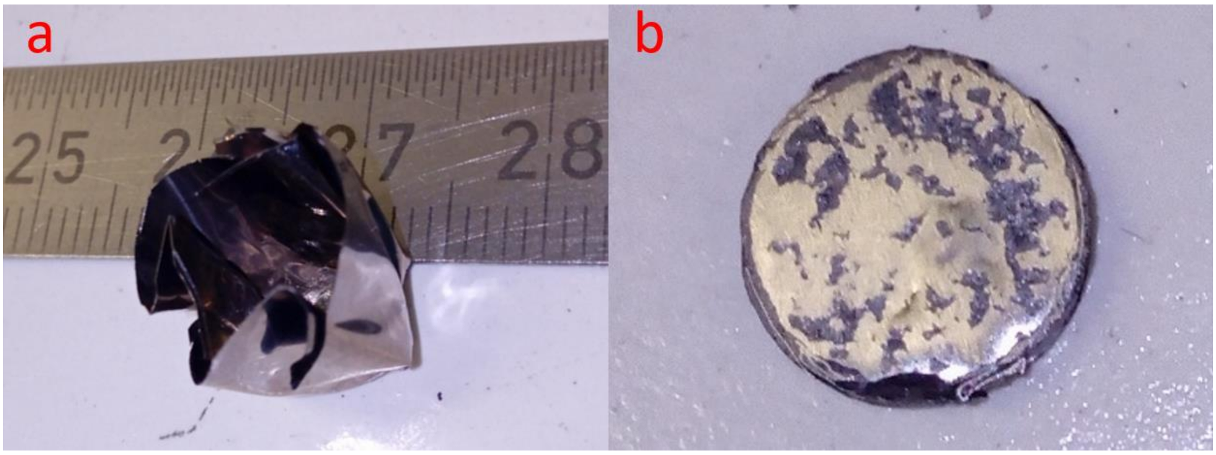

Figure III-27: Pictures of the Titanium foil used to cover the Fe and Se mixed powders and avoid the leak of Selenium. The foil was bend as a "jar" (a) then the powders is added and covered by another Ti foil then it is pressed in the mold. The results (b) shows a compact cylinder covered by the Titanium (the stain are leftover pieces of carbon sheets).

The problem wasn't completely solved as Selenium was still able to go away during the process according to the SPS profile and the X-ray pattern on Figure III-28.a,b. However, we can also see that there is less remaining Iron than for the sample presented with Figure III-26.a whereas we have a 1:1 stoichiometry so a progress has to be noted. But still no visible superconducting moment on the $m(H)$ curve of Figure III-28.c, still a superconducting transition is visible at around 8 K (insert of Figure III-28.c). So as for the work done at AIST we came back to the so-called Ex-situ synthesis method with the objective of a better superconducting moment.

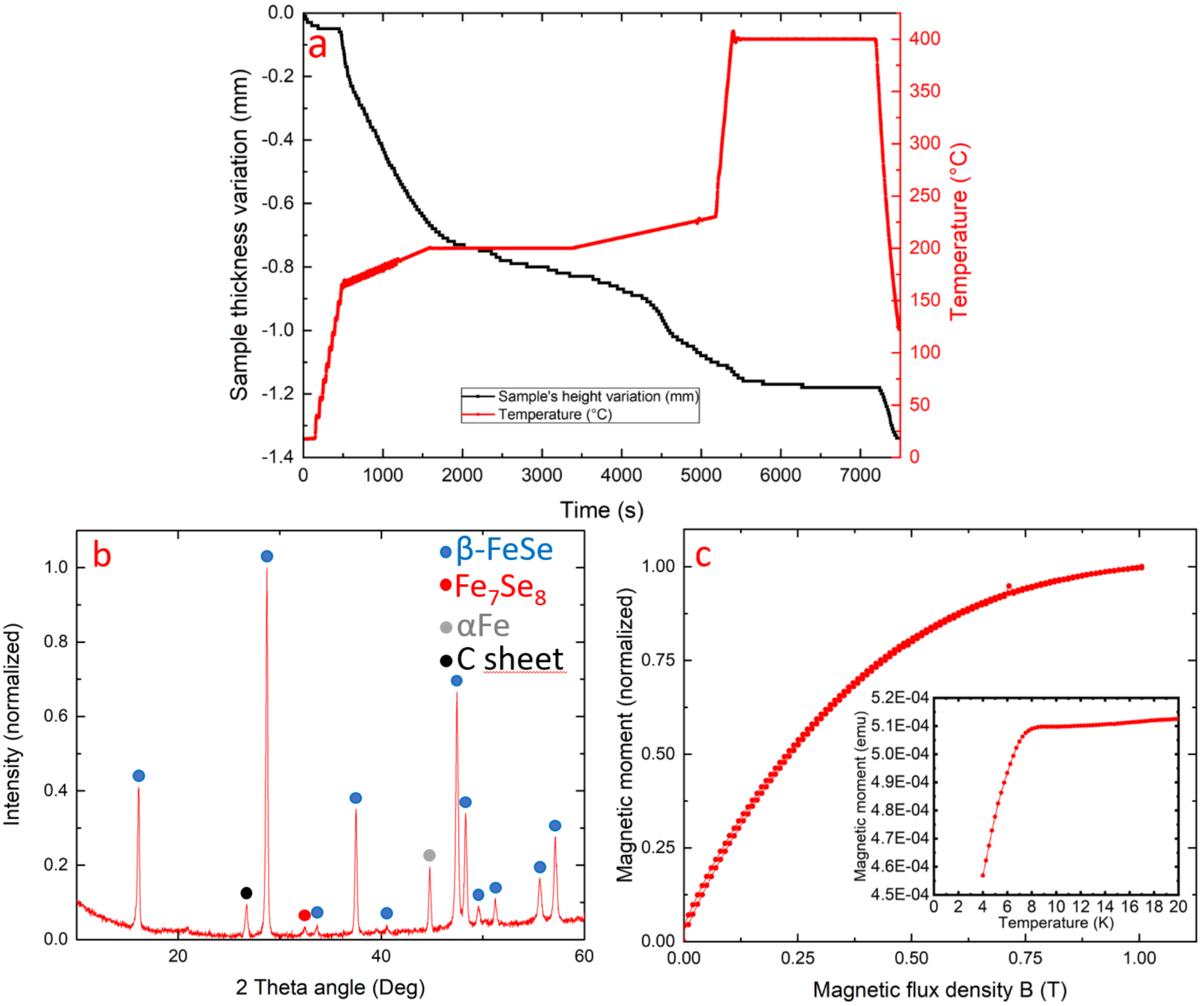

Figure III-28: (a) SPS profile of an in-situ sample with a 1:1 stoichiometry rounded by a Titanium foil. (b) its corresponding X-ray pattern (The blue (●), the red (●) and the grey (●) and the black (●) dots indicate respectively the β-FeSe, the Fe_7Se_8, the α-Fe phases and some remaining carbon.) and (c) its magnetic moment at 5 K. The insert represents the magnetic moment function of the temperature with a 20 Oe background field.

• Ex-situ SPS

We then decided to work on the ex-situ protocol. Two main results can be extracted from that work. The first one comes with the

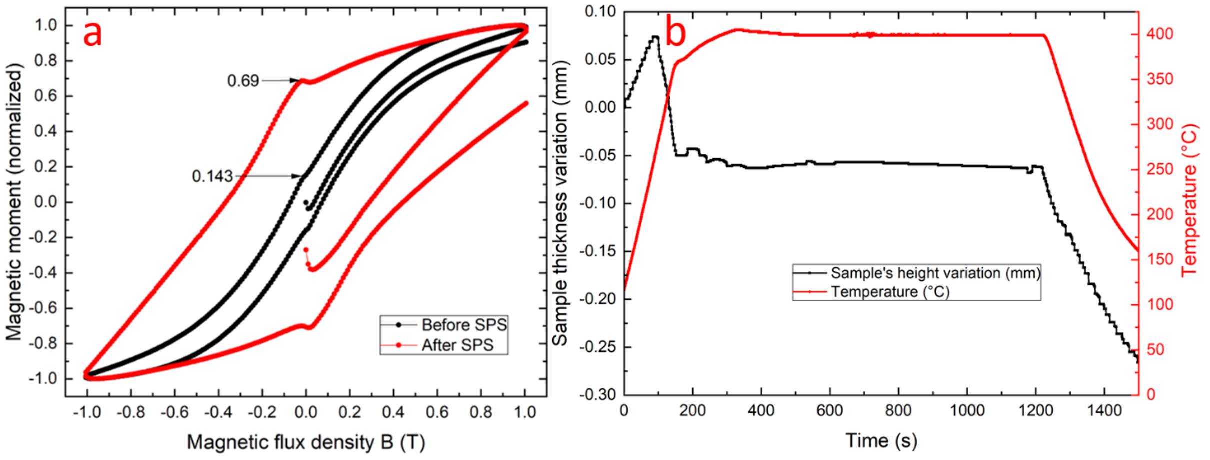

Figure III-29 which compares the $m(H)$ curve of the sample after a sintering process of 12 h at 700 °C and after its second step of 15 min at 400 °C (FeSe_700C12h_presin_400C15min_SPS). We can clearly see the benefits of the second step done by SPS as it nicely increases the ratio SC/ferri from 0.143 to 0.69. The SPS profile shows that the sample's volume starts by increasing which correspond to a thermal expansion. Then by reaching 275 °C it seems that a chemical reaction occurs until almost 400 °C so it should indicate the formation of the β-FeSe, then almost nothing new happens along the plateau.

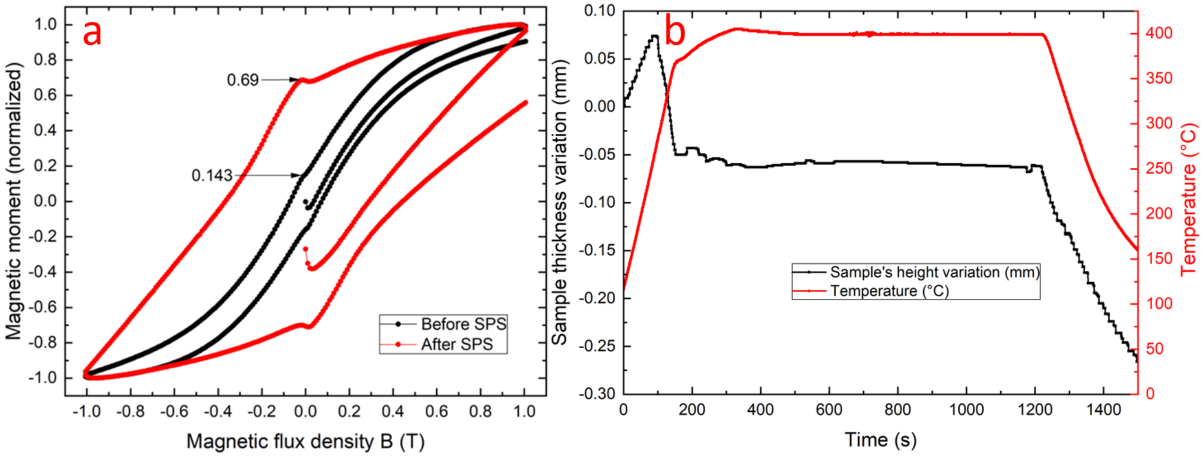

Figure III-29: Normalized magnetic moment of two FeSe samples at 2 K (b), before the SPS process (FeSe_700C24h) and after the SPS process (700C24h_presin_400C15min_SPS) with respective ratio of 0.143 and 0.69, and the corresponding SPS profile (b).

However, the result is not as good as obtained with the classic furnace routine which is in contradiction with the common idea from the literature where the superconducting properties are better with the help of hot-pressing or SPS than with classic furnace due to the increase of the density and the optimization of the grain boundary [118], [187].

Then we tried a second idea: a SPS annealing after the synthesis and annealing in furnace. This comes with the idea of maintaining the phases but increasing the density and the quality of the grain boundaries.

The resulting $m(H)$ curves are presented on Figure III-30 where we have a lower ratio after the SPS process than before (1 before and 0.47 after) so, this highlights again a negative effect of the SPS process on the magnetic properties.

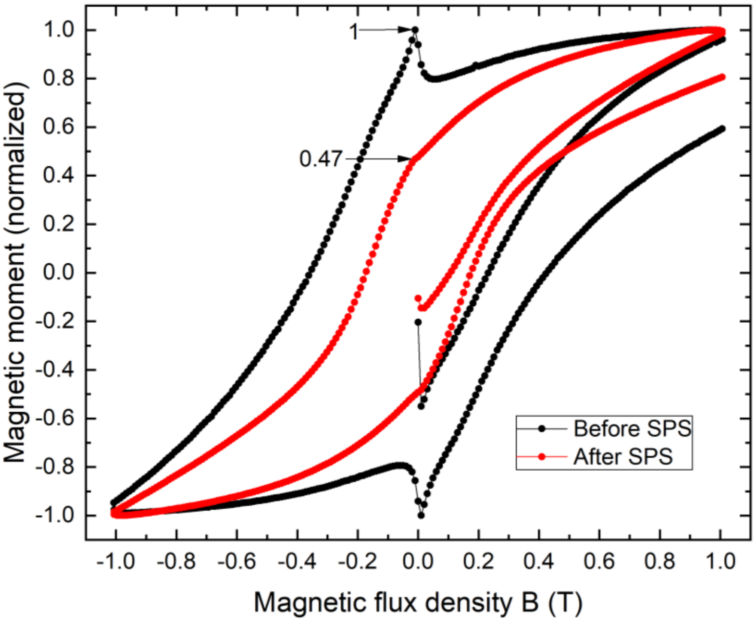

Figure III-30: Normalized magnetic moment of a FeSe samples after sintering and annealing in furnace, before a supplementary SPS annealing (FeSe_700C24h_400C40h before SPS) and after the supplementary SPS annealing (FeSe_700C24h_400C40h_presin_400C15min_SPS, after SPS) with respective ratio of 1 and 0.47.

A new sample has been prepared with a similar protocol as presented before but this time with a supplementary analysis of the sample's phases though X-ray measurements. So, a 1:1 stochiometric sample spent 24 h in the furnace at 700 °C then after an air quench and a new conditioning in the carbon mold under argon atmosphere, the sample was placed inside the SPS machine and annealed at 400 °C during half an hour. This temperature was reached in 8 min, in other words a temperature sweep rate of 50 °C.min^{-1} was used. This names the sample as FeSe_700C24h_pre-sin_400C30min_SPS.

The SPS profile, the X-ray pattern and the SQUID measurement are shown in Figure III-31. We can see on the SPS profile a very slow modification of the sample's height during the 400 °C plateau which is probably due to the densification but also a phase evolution. The absence of any variation during the heat-up process testifies to the absence of remaining Se powder.

The X-ray pattern (Figure III-31.b) is in majority displaying a β-FeSe phase but with a strong Fe_7Se_8 phase. This is confirmed by the SQUID measurement (Figure III-31.c) with a strong ferrimagnetic signal but no visible superconducting one (or almost not). It can only be seen with a $M(T)$ curve visible in the insert of Figure III-31.c with a superconducting transition temperature around 8 K. However, a comparison with the sample presented on Figure III-30, shows that even with the help of a very similar synthesis protocols, either the SPS profile and the magnetic measurements are really different. As the samples were prepared in different places: the sample of Figure III-30 was prepared at AIST and the one of Figure III-31 was prepared at CRISMAT, a difference of the calibration of the instruments or different powders (Table III-1) could explain such different. Also, as said in section III.5.b, many parameters could play a role in the lack of reproducibility. More generally those results show that the ex-situ SPS process isn't preferable to the classic furnace sintering.

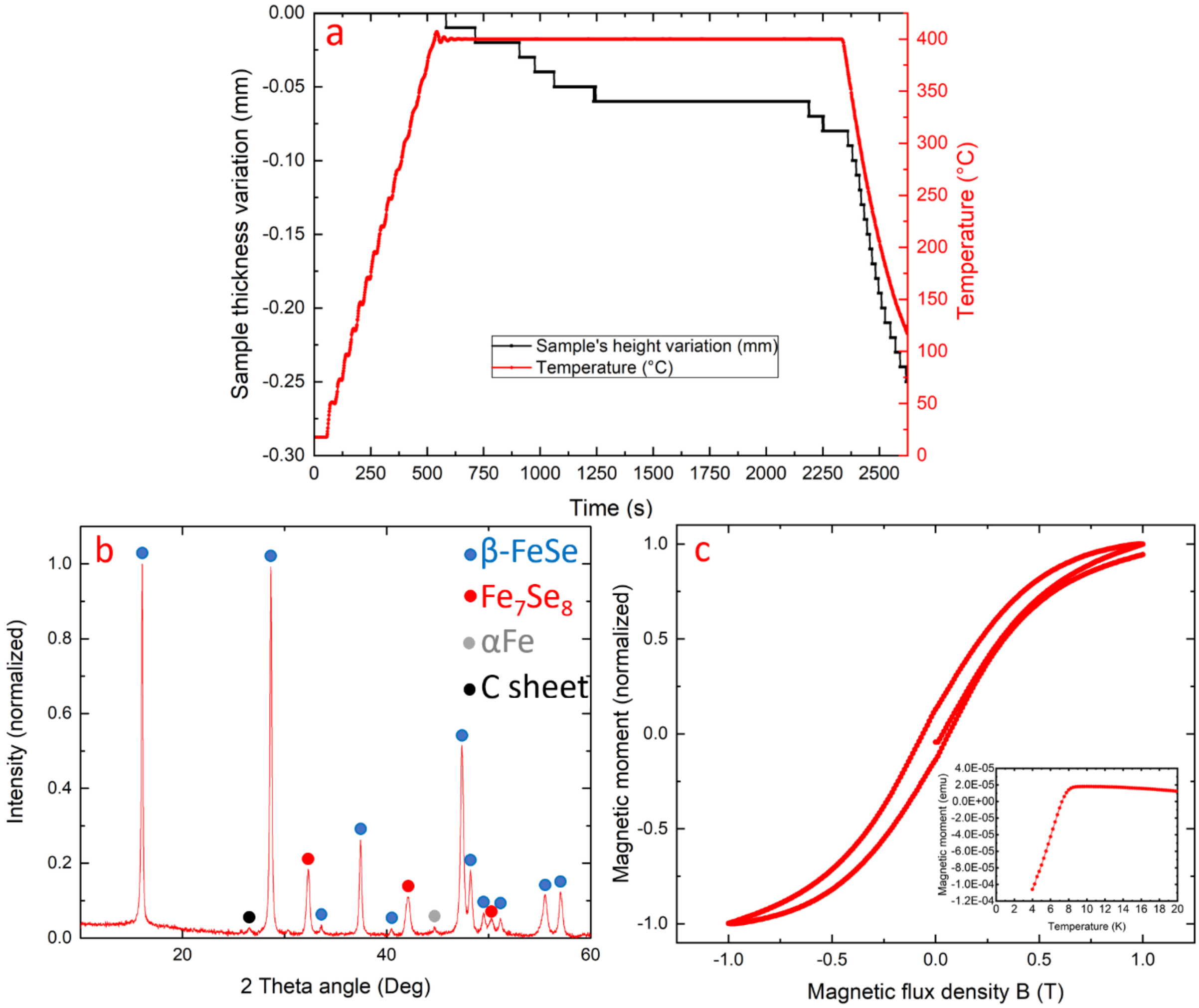

Figure III-31: (a) SPS profile of an ex-situ sample with a 1:1 stoichiometry after a furnace sintering of 24 h at 700 °C. (b) its corresponding X-ray pattern, the blue (●), the red (●), the grey (●) and the black (●) dots indicate respectively the β-FeSe, the Fe_7Se_8, the α-Fe phases and some remaining carbon, and (c) its magnetic moment at 5 K. The insert represents the magnetic moment function of the temperature with a 20 Oe background field.

III.6. New method for determining of the superconducting critical current density

In order to clearly study and compare the polycrystalline superconducting FeSe we need to extract the superconducting critical current density from the measured magnetic moment. However, the presence of the ferri/ferromagnetic signal(s) makes this work all but trivial. The first and commonly used technique is to measure the magnetic moment of the samples above the critical temperature like 15 or 20 K which is supposed to be only ferri/ferromagnetic as the superconducting moment is, by definition, null.

Then, by subtracting this moment on the one measured below T_c, this will remove the ferri/ferromagnetic moment and should isolate the superconducting one. An example is presented with Figure III-32.a where the magnetic moment at 20 and 2 K are compared and their subtraction is showed. However, the resulting $m(H)$ curve looks really bent and unusual for a superconducting hysteresis but this unusual shape is sometime "almost good" as we have presented in [39] where only a small bend can be seen. Also, by looking to the $m(T)$ curve shown as insert of Figure III-32.d, we can see that the ferrimagnetic moment is weakly evolving with the temperature compared to the superconducting signal (Zero Field Cooling). On Figure III-32.c, we can also see that the magnetic hysteresis slightly changes between 15 and 40 K (so supposed only ferrimagnetic). Those elements clearly highlight an evolution of the ferrimagnetic hysteresis with the temperature above the critical temperature. With this, the abnormal $m(H)$ hysteresis extracted on Figure III-32.b shows that the ferrimagnetic moments at 2 and 20 K should be different. So, the Figure III-32.b does not only contain a superconducting signal but also the difference on the evolution of the ferrimagnetic hysteresis.

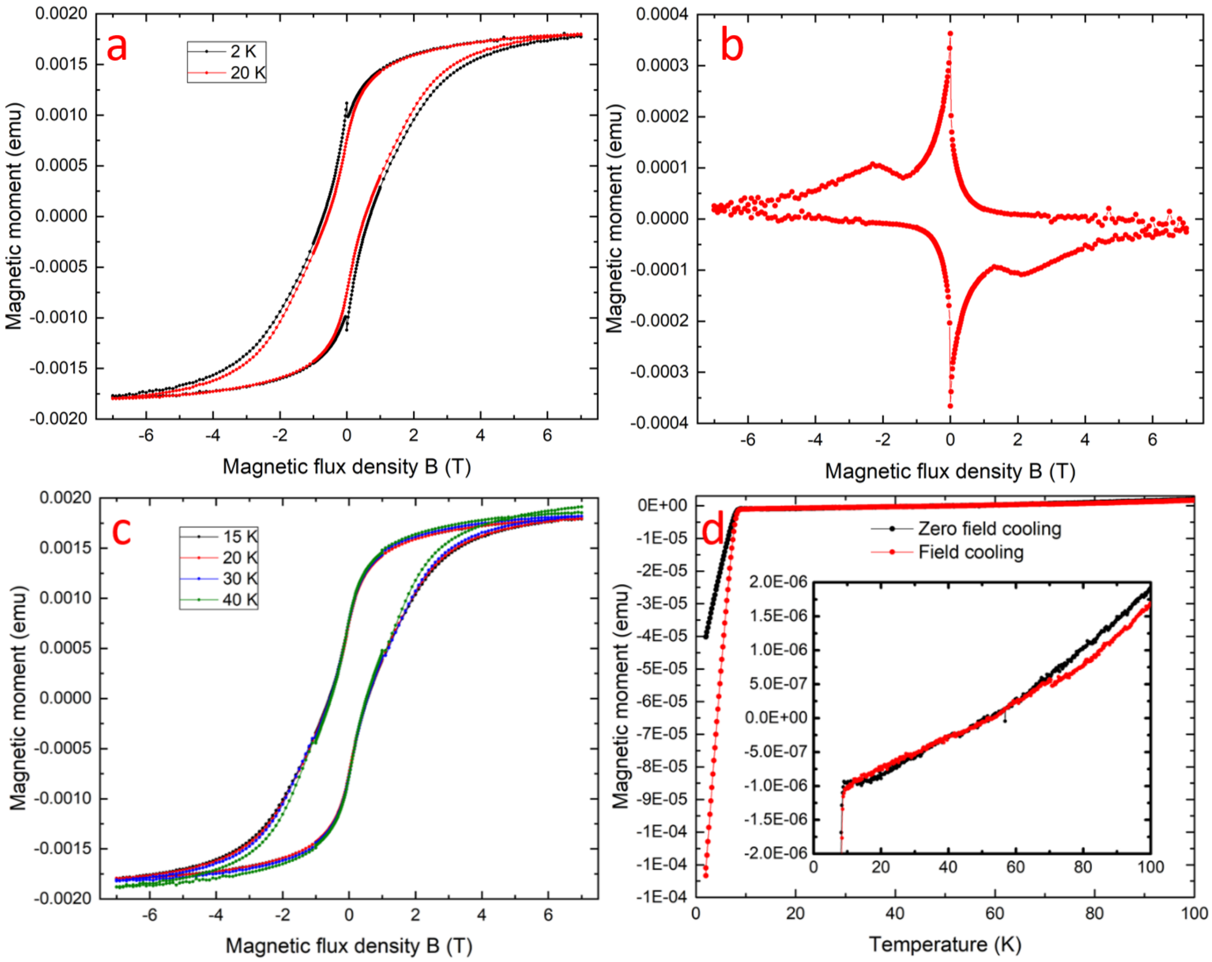

Figure III-32: Magnetic moment of a FeSe sample (FeSe_700C24h_400C40h) function of the magnetic field at 2 and 20 K (a), after subtraction of the moment between 2 and 20 K (b), the magnetic moment at 15, 20, 30 and 40 K (c) and function of the temperature (d) with a zoom on the insert.

To remove the ferrimagnetic signal at 2 K it looks necessary to extrapolate it at this temperature from the measurements above the critical temperature and in a more practical way on the extrapolation of the vertical thickness of the hysteresis curve, the so-called ΔM. The ΔM of the magnetic hysteresis was computed from 2 to 40 K as shown on Figure III-33, we can clearly see an evolution over the temperature and the hint of the superconducting signal with this sharp spike at low field on the sample below 8 K.

By looking to the evolution of the magnetic moment between 15 to 40 K (a superconducting signal may be existing at 10 K as it has already been reported [16], [39]) at different background magnetic field, Figure III-34.a (the curves have been normalized for a better comparison), we can see that the evolution of the ΔM function of the temperature is not the same for different background field. So, a simple extrapolation using the $m(T)$ of Figure III-32.d with only a very low magnetic field can't be used. A different evaluation of the ferrimagnetic moment at low temperature is needed for each value of magnetic field.

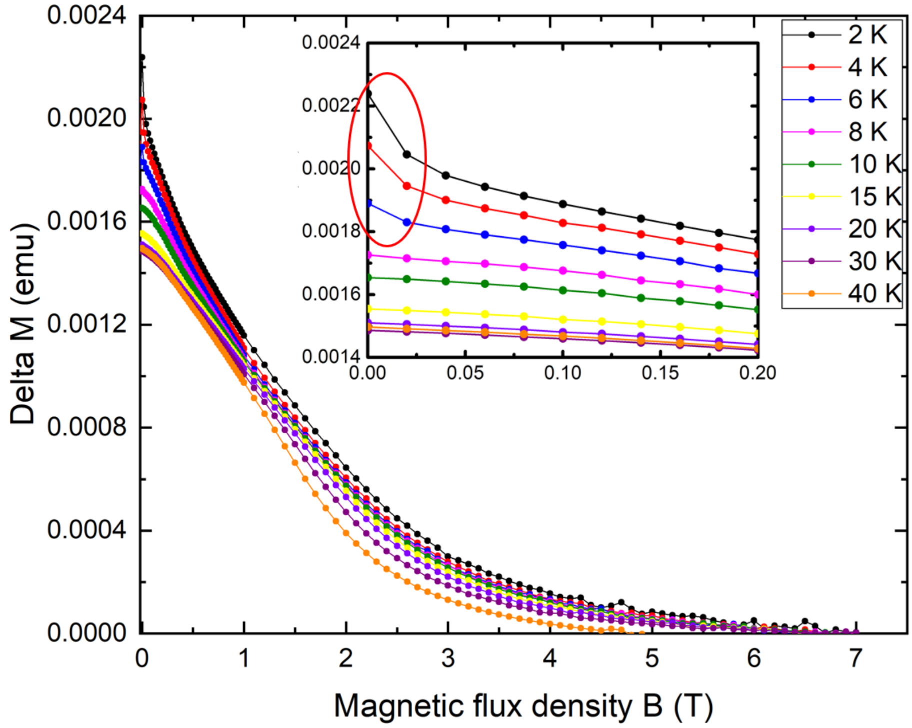

Figure III-33: Vertical thickness of the hysteresis curve (Delta M) measured on a FeSe sample (700C24h_400C40h) for various temperatures. The insert shows the moment between 0 and 0.2 T where the superconductivity is strong highlighted by the red ellipse

In this way, I used the "Fit" function of Matlab on $\Delta M\,(T)$ curves at each magnetic field using the data of Figure III-33 and it comes out that the better fitting equation is a polynomial of the third order. This has been applied for each point between 0 to 0.84 T using points from 15 to 40 K where the sample is only ferrimagnetic, Figure III-34.b. At 0.86 T the extrapolated ΔM at 10 K is equal to the measured one at the same temperature, see Figure III-34.c. This shows that the superconducting moment at 10 K is weak enough to be neglected and so the point at 10 K is now considered only ferrimagnetic and can be used to extrapolate the ferrimagnetic ΔM at lower temperature (finally fitted between 10 to 40 K).

At 1.6 T, the same phenomenon happens at 8 K, Figure III-34.d, so it is now considered only ferrimagnetic and add into the fitted points. Follows by the point at 6 K at 2.3 T, Figure III-34.e. Lastly, at 2.8 T the signal below 10 K starts to be really noisy, Figure III-34.f, and so no good extrapolation can be done, the superconducting signal is considered too weak compared to the noise produced by the ferrimagnetic part, even at 2 K.

Applied magnetic field	Temperature's interval for the fitting
0 to 0.84 T	15 to 40 K
0.86 T to 1.6 T	10 to 40 K
1.62 to 2.3 T	8 to 40 K
2.4 to 2.8 T	6 to 40 K

Table III-2: Presentation of the temperature interval of the experimental data used to fit the ferrimagnetic curves for different applied magnetic fields.

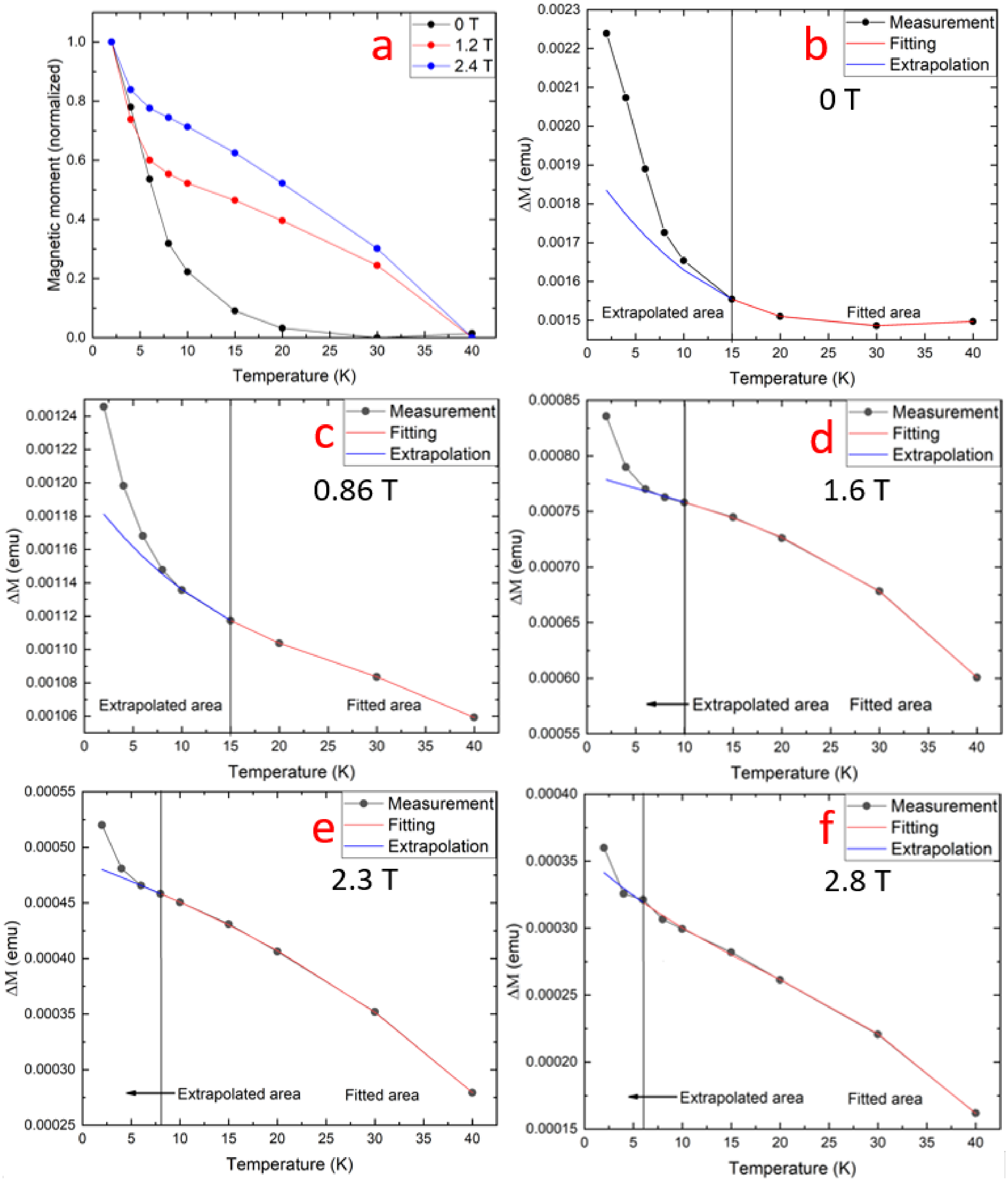

Figure III-34: (a) ΔM function of the temperature for a FeSe sample (700C20h_400C40h) under various magnetic fields and normalized. Experimental ΔM(T) curve for different applied field with a fit on the ferrimagnetic part and its extrapolation at low temperature: 15 to 40 K under self-field (b) and under 0.84 T (c), from 10 to 40 K under 1.6 T (d), from 8 to 40 K under 2.3 T (e) and from 6 to 40 K under 2.8 T (f).

All the extrapolated ferrimagnetic ΔM from 0 to 2.7 T were subtracted from the experimental curves from 2 to 10 K and the result is presented on Figure III-35.a in emu.cm^{-3} using the sample's dimension: 1.42×1.19×0.23 mm^3. With this and the help of the Chen's formula [113] the critical current density for each temperature has been extracted from 2 to 10 K and presented on Figure III-35.b.

The critical current density at 2 K does not exceed 250 A.cm^{-2} which is very low compared to the one presented in the literature [16], [18], [42]. However, the ΔM should be in the range of the one find here [16], [42], [153] even more if we considered this sample degraded of 23% (explained right below). Also, the subtraction of the 15-20 K hysteresis curve on the 2 K one is very inaccurate which artificially increase the computed superconducting moment as the ferrimagnetic hysteresis is wider at 2 K than at 20 K. Furthermore, compared to a MgB_2 sample with a J_c of 500 kA.cm^{-2} [118], a pure FeSe sample is clearly not competitive.

The evolution of the critical current density from 4 to 10 K exhibits a classic shape with no fishtail effect, that remains when a simple subtraction of the curves at 2 K and 15 or 20 K is done on the magnetic moment (Figure III-32.b). Nevertheless, the curve at 2 K shows a slowly decreasing J_c with the magnetic field and the same value than the 4 K one between 0 to 0.3 T. A possible explanation comes with the limit of the extrapolation: when the variation of the J_c is larger, in other word at low magnetic field and low temperature, the lack of accuracy of the fitting (only done between 15 to 40 K with 3 points) could have a non-negligible effect and distorts the results. At higher magnetic field, the fitting is done with more data (10 to 40 K at 0.86 T, 8 to 40 K at 1.6 T and 6 to 40 K at 2.3 T) so a better accuracy is expected. This leads to a possible underestimation of the J_c at 2 K below 0.84 T at least.

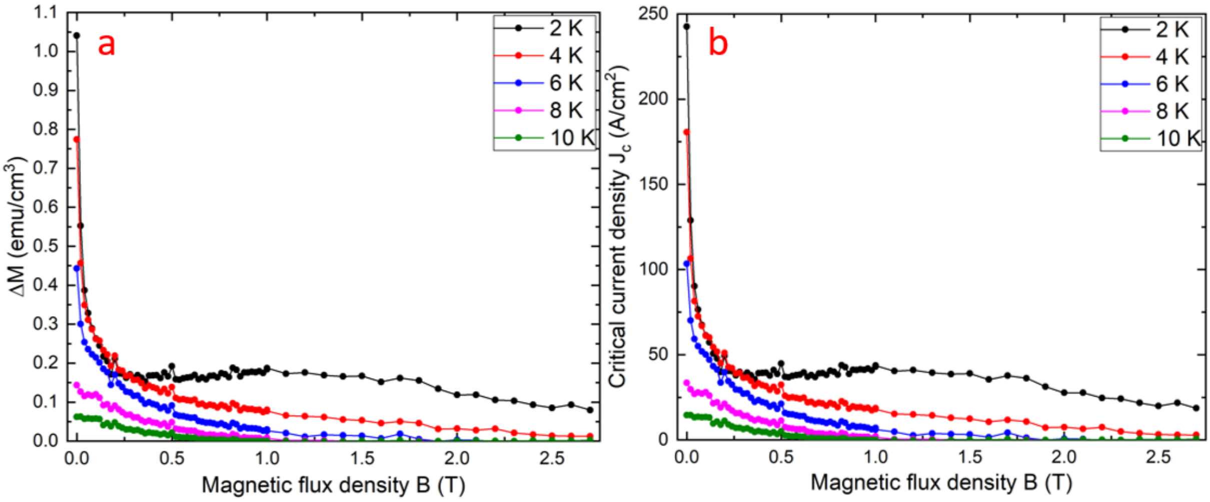

Figure III-35: Extracted superconducting vertical thickness of the ΔM (a) and critical current density J_c (b) function of the magnetic field at different temperature.

III.7. The superconductivity of the β-FeSe phase

The ferrimagnetic moment of the discussed sample right above is only of 5 emu.cm^{-3} at 7 T which is really weak compared to the ones presented in the literature [16], [18], [39], [42]. This supports the low critical current density where the magnetic moment at 2 K shows a majorly ferrimagnetic signal.

This result is itself extremely surprising considering the X-ray pattern of the sample of Figure III-20.b, shown again on Figure III-36.a, which exhibits an almost pure β-FeSe polycrystal (the supposed superconducting one) with only a very tiny ferrimagnetic Fe_7Se_8 secondary phase. This tiny Fe_7Se_8 phase is relevant with the moment at 20 K, Figure III-32.a, or at 2 K, Figure III-36.c but not the superconducting one. The same conclusion can be done on the sample with a $Fe_1Se_{0.975}$ stoichiometry where a very pure β-FeSe phase exhibit almost no superconducting signal, Figure III-36.b-d, and also a weak magnetic moment at 2 K and 7 T, Figure III-36.d, due to the remaining ferromagnetic Iron.

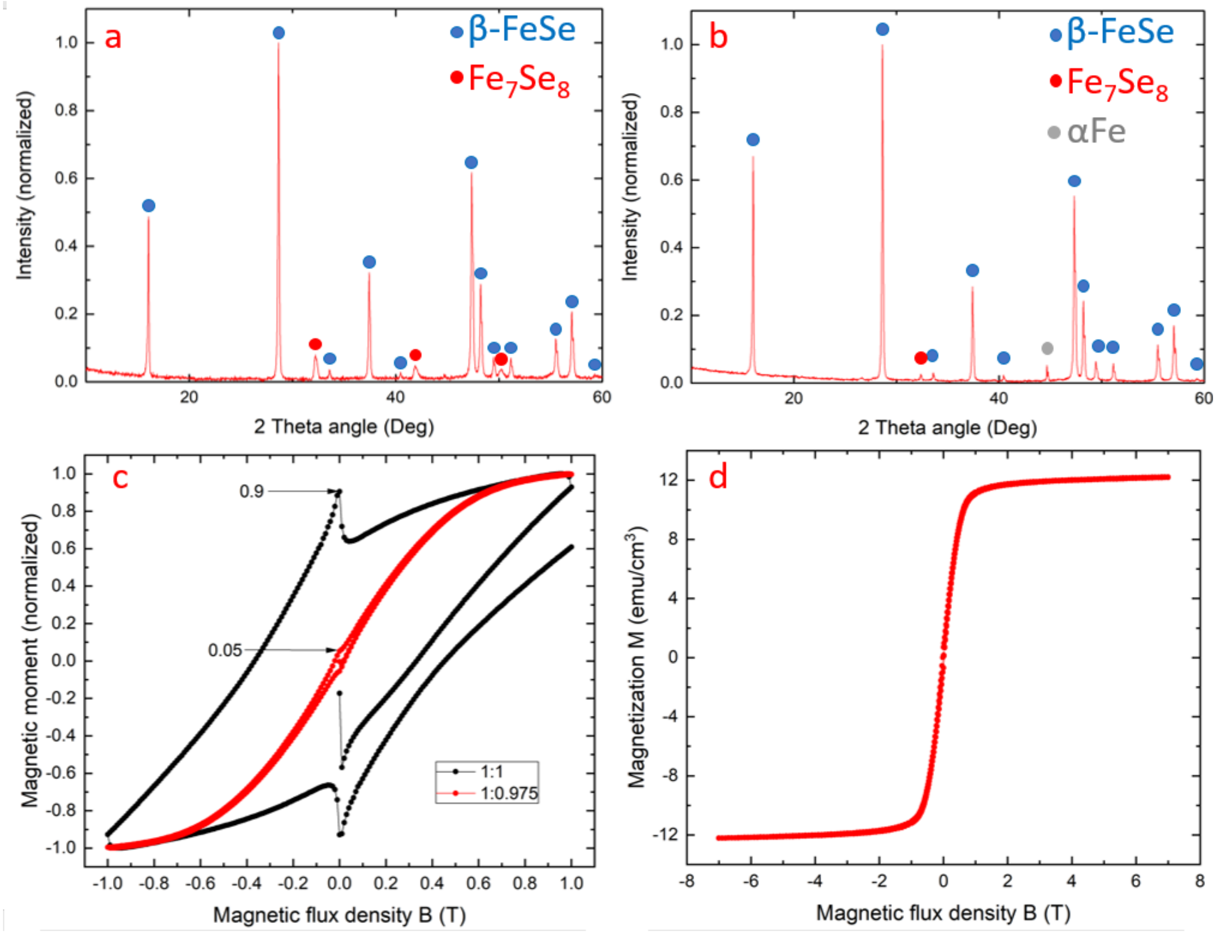

Figure III-36: X-ray pattern of the FeSe samples prepared by furnace at CRISMAT with a 1:1 (a) and a 1:0.975 stoichiometry (b) with the 700 °C 24 h 400 °C 40 h routine. The blue (●), the red (●) and the grey (●) dots indicate respectively the β-FeSe, the Fe_7Se_8 and the α-Fe phases. Magnetic moment of the 1:1 and the 1:0.975 samples (c) function of the magnetic field at 2 K and magnetization of the 1:0.975 one up to 7 T (d).

But we reported in [39] a FeSe sample with a much larger moment with a visible superconductivity and with a much bigger proportion of Fe_7Se_8: 74.2 % of β-FeSe and

25.8 % of Fe_7Se_8 evaluated by X-ray diffraction, so a 3:1 ratio. Compared to a 20:1 ratio with the sample presented before, Figure III-36.a. This again explains the big difference of ferrimagnetic moment (one is 25 % of the sample where the other is around 4.8 %). But this still shows that the amount of β-FeSe can't be directly linked with the amount of superconducting signal.

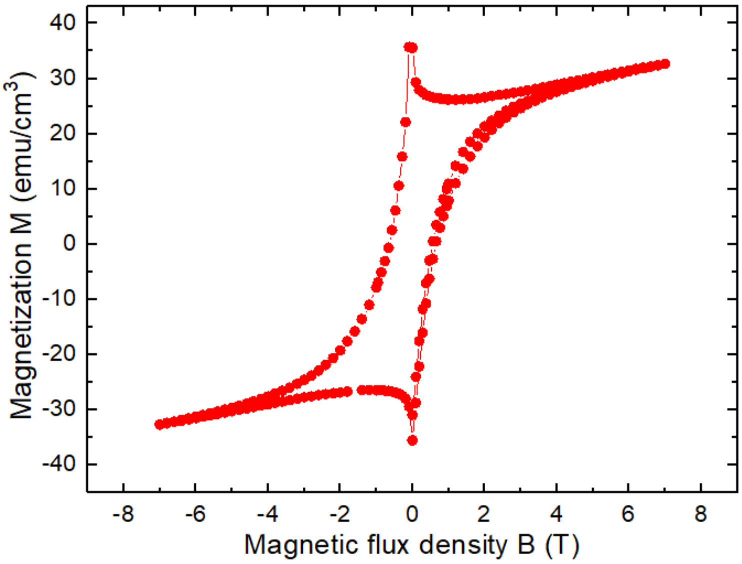

Figure III-37: Magnetization of a FeSe sample with a 1:1 stoichiometry (ball_milled_FeSe_700C1h_400C40h) function of the magnetic field at 4 K [39].

A possible explanation was presented by K. W. Lee et al. in [32] were the superconductivity of FeSe is expected to appears in the β-FeSe phase with a tiny deficiency of Se atoms of typically one for eight:

$$\mathrm{Fe1Se_{1-x}}, x = \frac{1}{8} \tag{III.1}$$

As this particularity isn't detected using X-ray diffraction or SEM-EBSD on large areas (as done here), we can't know if we have a β-FeSe with or without Se deficiency.

However, with the help of the Fe_7Se_8 or the α-Fe secondary phases we could qualitatively detect the presence of Se deficiency in the β-FeSe phase with the approximation of a good precision on the stoichiometry during the preparation and the synthesis. Indeed, an almost pure β-FeSe phase should be expected in the 1:1 sample (Figure III-36.a) but a Fe_7Se_8 phase is present which shows that an excess of Se is present as no α-Fe was detected. This led to the conclusion that a small deficiency of Fe is present in the β-FeSe phase, which explains the weak but measurable superconducting signal. Also, as Fe_7Se_8 is the exact complement with Fe_8Se_7 (supposed to be the stoichiometry of the superconducting β-FeSe), the amount of Fe_7Se_8 should be the amount of superconducting β-FeSe for a 1:1 stoichiometry without α-Fe.

On the other hand, the second sample with a 1:0.975 stoichiometry should have the good stoichiometry for having a pure β-FeSe with a good amount of Se deficiency. However, the exceeding iron is partly staying alone and the Fe_7Se_8 phase is even weaker, Figure III-36.b, so the deficiency of Se is expected to be not enough which is confirmed by the $M(H)$ curve, Figure III-36.d.

More generally, in all samples presented above (excepted the ones with a specified stoichiometry different to 1:1) we always have a ferrimagnetic signal, supported by the presence of Fe_7Se_8 on the X-ray pattern or by SEM. This ferrimagnetic signal is too big for being attributed only to the lack of precision during the weight and the preparation of the samples. This leads to the conclusion that we always have a deficiency of Se in the β-feSe phase which explains the apparition of superconductivity, but when we reduced the amount of Se by an unbalanced stoichiometry, the secondary α-Fe phase will appear and the β-FeSe phase will conserve a 1:1 stoichiometry. The consequence is a huge difficulty to get a pure β-feSe with a good superconductivity in a polycrystal.

III.8. Doping and chemical stability of FeSe

III.8.a. Doping of FeSe

We have seen before that, even by assuming the possibility of preparing a pure FeSe polycrystalline phase with a good grain connectivity, the Iron-Selenide complex will still have a critical temperature below 15 K and a critical current density bellow 10^5 A.cm^{-2} [180] which makes FeSe far from being competitive with MgB_2, already disponible as polycrystalline bulks prepared by SPS.

The solution may come with the large number of doping elements:

- Tellurium: Many works have been done on the FeSeTe complex which increases the critical temperature to 15 K and a bit the critical current density [160], [187], [191]–[193] but not at the point of being competitive or even the possibility of the use with liquid Hydrogen. Also, the rareness of Tellurium does not match with an industrial production.
- Sulfur: Gives similar result as for Tellurium addition on the critical current and a superconducting transition at 9-11 K [194], [195] but despite the abundance of the Sulfur on earth, the limitations are the same as for Tellurium.
- Silver: Slightly increases the superconducting properties [42], [159], [196] but still not enough.
- Alkali and alkali-earth metal: Several elements (Li, Na, K, Cs, Ca, Sr and Ba) have been tested with FeSe [27] with various T_c= 30 to 46 K. A particular attention have been done on the KFeSe [17], [164], [165], [197], [198] with very promising superconducting properties [167] but the most interesting properties comes from the NaFeSe complex [28], [199]. Looking to the literature those elements could makes Iron-selenide competitive with MgB_2.

I naturally choose to work on alkali elements and in particular with Na and Sr elements (disponible in the laboratory) for a furnace as well as a SPS sintering.

Both materials have been used for furnace sintering with the routines and stoichiometry as $Sr_{0.4}Fe_1Se_1$_800C10h_400C2h, $Na_{0.5}Fe_1Se_1$_700C10h_400C2h which were chosen from [27] and the synthesis was chosen to be quick as we intended to see if a possible superconducting phase could be prepared.

The Na element is very hard to handle in pure form (very soft and gummy) and has a very low fusion temperature (97.8 °C) and the fusion temperature of strontium (777 °C) does not allows a good repartition of the Se and Sr before losing all the Selenium, so, the in-situ sintering with doping elements wasn't considered. However, for the Strontium, Ex-situ synthesis of Sr doped FeSe was tried:

A furnace sintering has been done at 800 °C during 10 h as the fusion temperature of Strontium is 777 °C, follows by an annealing at 400 °C during 2 h. The result wasn't very great, the Figure III-38.a is presenting the quartz tube containing the Sr doped samples and we can see that the powders react and/or went out of the Tantalum foil and react with the quartz tube itself. We were able to handle an X-ray measurement of the Sr doped sample, Figure III-38.b, where we can see the presence of a dominant β-FeSe phase, the Fe_7Se_8 one as well as a SrSe phase.

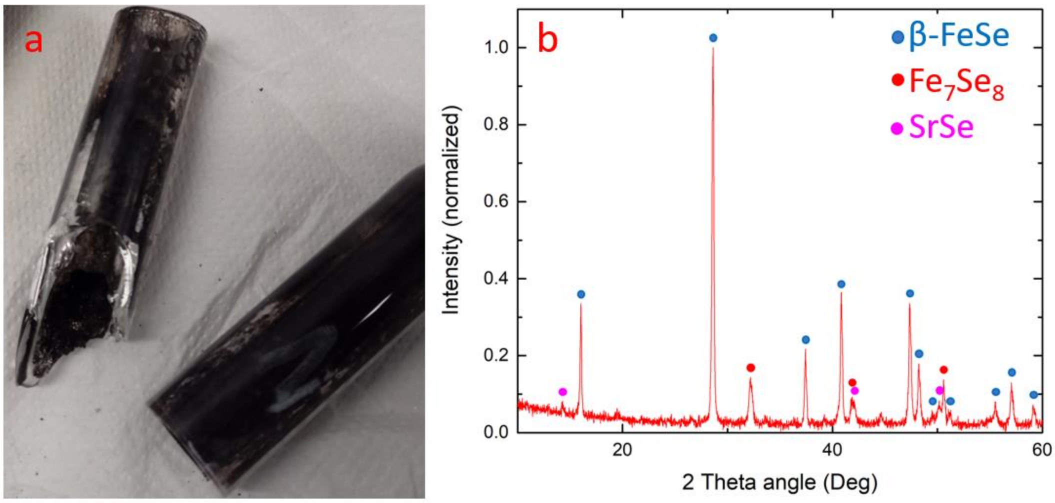

Figure III-38: X-ray diffraction pattern of a Strontium doped FeSe prepared by classic furnace sintering ($Sr_{0.4}Fe_1Se_1$_800C10h_400C2h) the blue (●), the red (●) and the violet (●) dots indicate respectively the β-FeSe, the Fe_7Se_8 and the SrSe (Strontium-Selenium) phases.

On another sample, we followed the same furnace sintering process and as a second step a SPS annealing of 30 min at 400 °C was done, so an ex-situ sintering, the SPS profile is showed with Figure III-39.a. We can see that we have a diminution of the sample's height during the heating process which is unexpected as the reaction should have been done during the

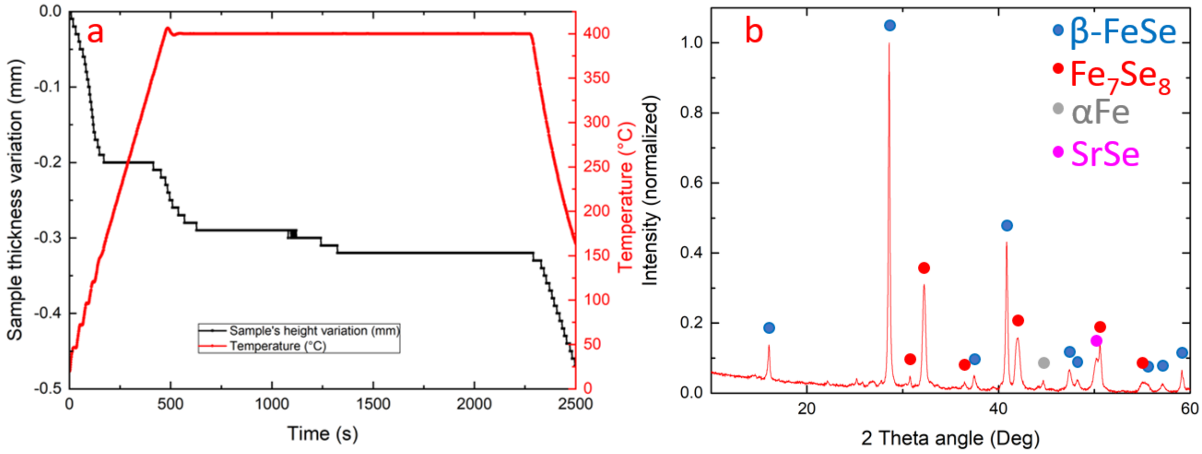

furnace sintering/annealing like for the ex-situ samples prepared when the volume increases with the temperature due to thermal expansion (Figure III-23) or no evolution until 400 °C is reached (Figure III-31). This highlights a possible chemical reaction or leaking. Then at 400 °C a similar evolution as for the ex-situ sample, Figure III-31. So, to figure out what happens, the result was prepared for X-ray measurement and after the measurement, most of the powder has disappeared so a reaction with the oxygen of air may has occurred. The X-ray can be seen on Figure III-39.b with a dominant β-FeSe phase, a non-negligible Fe_7Se_8 phase with some remaining content of iron and a Strontium-Selenium (SrSe) complex.

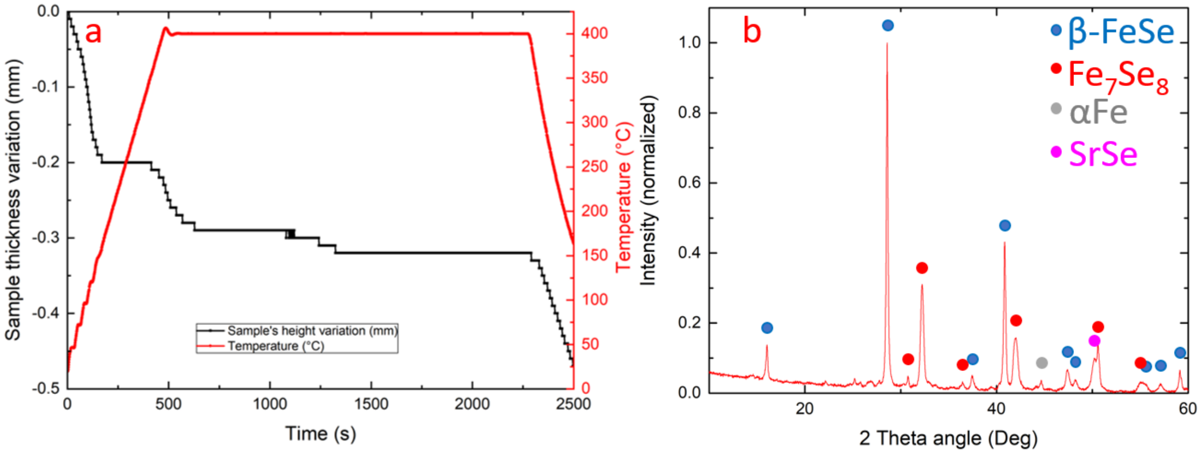

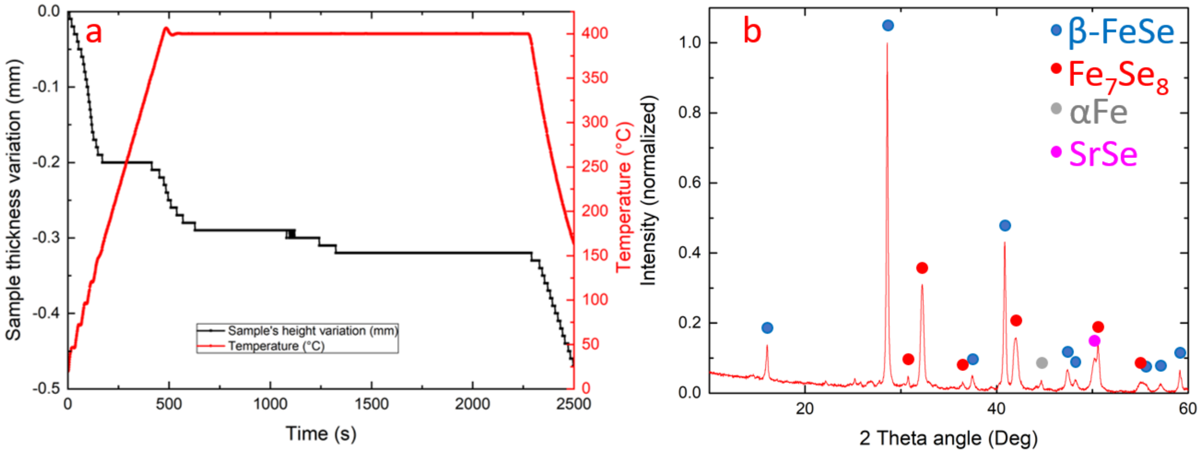

Figure III-39: SPS profile (a) and X-ray diffraction pattern (b) of a Strontium doped FeSe with an ex-situ synthesis routine ($Sr_{0.4}Fe_1Se_1$_800C10h_400C2h_pre-sin_400C30min_SPS). For the X-ray patern, the blue (●), the red (●), the grey (●) and the violet (●) dots indicate respectively the β-FeSe, the Fe_7Se_8, the α-Fe and the SrSe (Strontium-Selenium) phases.

In both cases a very strong smell comes out form the sample and a long (over a day) but observable reaction shows that the samples was reacting with air and particularly with oxygen as alkali and alkali-earth metal usually do. Also, a more violent reaction occurs in contact with ethanol indicating the resulting sample with Na and Sr looks to be highly unstable in contact with oxygen. The consequence is the impossibility of performing MPMS measurement because a day after the synthesis the sample seems to have reacted with air.
This leads to the conclusion that preparing doped FeSe with alkali or alkali-earth metals makes it very hard to handle and potentially dangerous when MgB_2 looks to be really stable in atmosphere, even over several years.

III.8.b. Chemical stability and aging of FeSe

One of the key points for an industrial and usable material is the conservation of its chemical and physical property over time and in contact with its environment of use (air, vacuum, liquid hydrogen/helium…).

In this way, the stability of the FeSe samples I prepared (FeSe_700C24h_400C40h) has been verified as we can see on Figure III-40 where the normalized magnetic moment of a sample was measured before and after 5 months. We can see that a degradation of the ratio is measured as it has been divided by 2.7.

A possible explanation comes with the SEM analysis done on the samples 6 months after its synthesis with an EBDS analysis to determine the different phases in presence. The result is presented on Figure III-40.c, as expected a β-FeSe phase is dominant, follows by the Fe_7Se_8 phase but surprising is the presence of pure Fe as this phase was absent during the X-ray analysis of the same sample right after its synthesis presented above with Figure III-40.b. Also, it is very interesting to see that the Fe looks to be agglomerated and surrounded by Fe_7Se_8 structures. This could indicate a potential transformation of the β-FeSe into Fe_7Se_8 and α-Fe as follow:

$$8Fe_1Se_1 \rightarrow Fe_7Se_8 + Fe \qquad (III.2)$$

This possible transformation is problematic as it highlights the instability of the β-FeSe phase and also explains the reduction of the ratio as superconducting parts become ferri/ferromagnetic.

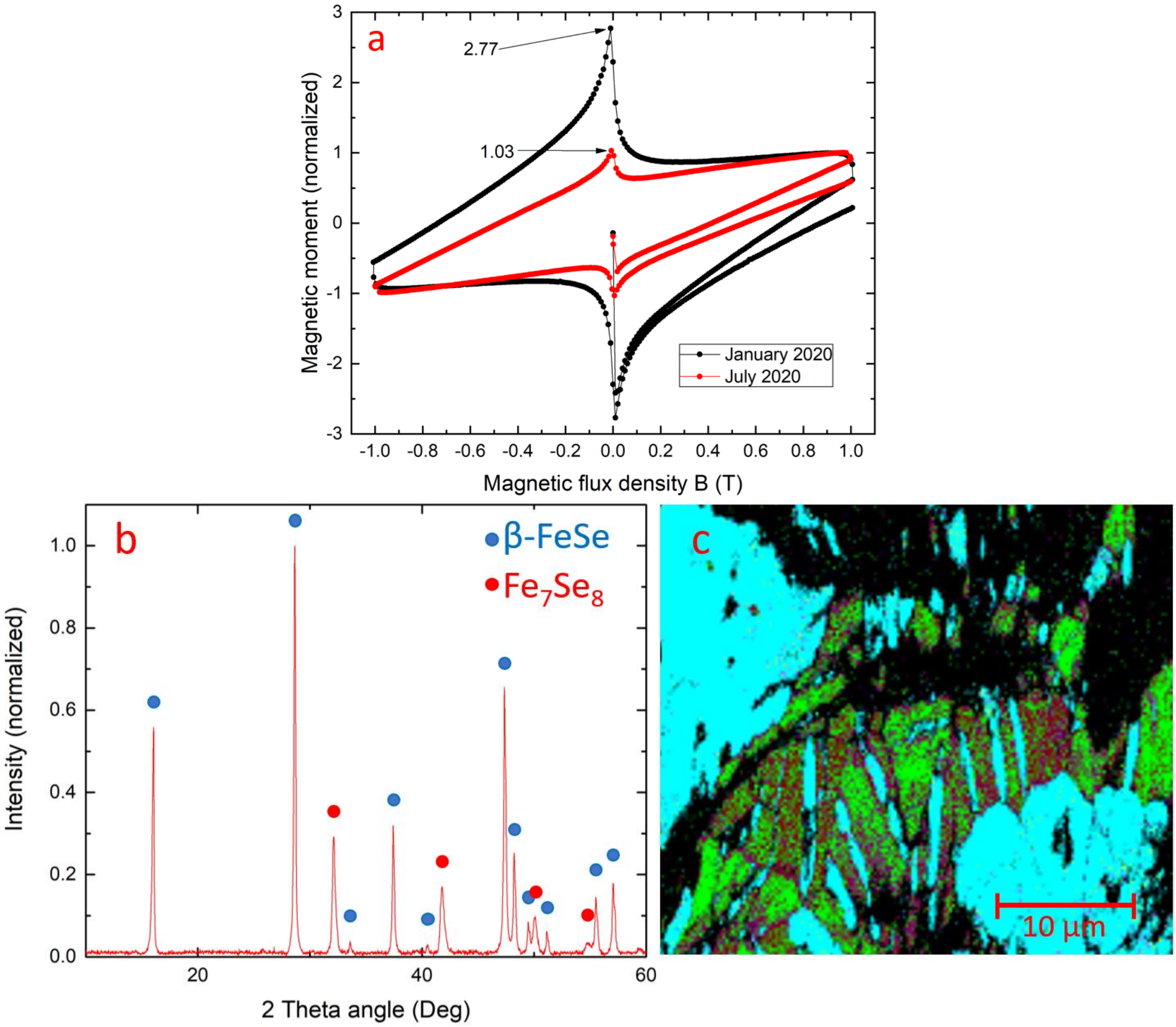

Figure III-40: (a) comparison of the magnetic moment measured on the FeSe_700C24h_400C40h with a 6 months interval. (b) is the X-ray diffraction pattern done in January 2020 right after the synthesis, the blue (●) and the red (●) dots indicate respectively the β-FeSe and the Fe_7Se_8 *phases. (c) presents the SEM-EBSD analysis done in July 2020, 6 months after the synthesis, the cyan (●), the violet (●) and the green (●) colors are respectively the β-FeSe, the* Fe_7Se_8 *and the α-Fe phases.*

Also, really surprising is the total absence of oxygen atoms which makes this material stable with air but also support the theory of an unstable β-FeSe phase as no help of external material was needed for the degradation.

This degradation has been previously observed in Literature with a decreasing of the β-FeSe phase and an increasing of the Fe content and highlight a possible role of the air in the degradation [169] but this was also seen after 70 days of storage in a Free-oxygen glovebox [200] with an obvious apparition of a ferrimagnetic moment. Also, In our publications, the SEM measurements done several time after the synthesis also point out the presence of iron which was absent of the X-ray measurement done right after the synthesis [39].

III.9. Conclusion

Along this chapter we have seen how to prepare, synthetize and anneal a FeSe bulk polycrystal either using classic sintering, Spark Plasma Sintering or both processes one after the other. Then a characterization of its magnetic and crystallographic properties has been done in order to identify and discriminate the phases.

Three main different phases have been observed: the β-FeSe supposed to be responsible of the superconductivity, the Fe_7Se_8 phase associated with the hard ferrimagnetic moment and the α-Fe phase responsible of a soft ferromagnetic signal.

Along the exploration of the synthesis and annealing temperatures or the stoichiometry of Iron and Selenium, we identify the magnetic properties as well as the x-ray pattern of each phases.

However, despite having an almost pure β-FeSe sample either with the help of classic furnace sintering or SPS sintering, the superconductivity remains very weak even more compare with the magnetism of the secondary phases. A possible explanation of those observations comes with a possible lack of Selenium vacancies, possibly responsible of the superconductivity in the β-FeSe phase [32]. This Se deficiency is present in 1:1 stoichiometry when the secondary Fe_7Se_8 phase is also present but with an unbalanced stoichiometry like 1:0.975 the exceeding Iron forms a α-Fe ferromagnetic phase and almost no superconductivity appears in the β-FeSe phase.

The huge sensibility of the magnetic properties and the ratio of the phases on the stoichiometry also leads to a lack of reproducibility due to the precision of the measurement during each step of the preparation process and of the calibration of each instrument.

Important degradations have been observed on the FeSe samples after few months, with a diminution of the ratio superconductivity/ferrimagnetism, confirmed by the apparition of α-Fe after months around Fe_7Se_8 explained by a degradation of the β-FeSe phase into the ferri and ferromagnetic phases. The non-stability of the β-FeSe phase over the Fe_7Se_8 and the α-Fe is a possible explanation of the difficulty of synthetize Se deficient β-FeSe, in other words it is easier to form α-Fe and Fe_7Se_8 with no Se deficient β-FeSe than superconducting β-FeSe. Furthermore, the several try of in-situ synthesis as well as doping with alkaline elements were unsuccessful due to the reaction temperatures or reactivity with the samples older (quartz tube, …) or the atmosphere. So, a fast synthesis routine looks really challenging for the preparation of a pure, superconducting and stable β-FeSe phase over a large polycrystalline bulk, even more with the addition of doping elements.

After supplementary measurements I was able to extract the critical current density J_c of the superconducting phase which is about 10^2 A.cm^{-2}, lower than compared to other materials such as MgB_2 (above 10^5 A.cm^{-2} at 4.2 K). It also highlights the complexity of the ferrimagnetic moment function of the temperature and/or the external magnetic field.

All those elements allow me to conclude about the potential of FeSe superconductors for electrical engineering applications. the difficulty of synthesis and the very limited superconducting properties does not bring the FeSe as a serious competitor with other materials such as MgB_2. Also, the difficulty of doping greatly limits the possibility of enhancement of the superconducting properties at an acceptable level.

Chapter IV: Characterization of YBaCuO superconductors prepared by Infiltration Growth process

IV.1. Introduction

In the previous chapters of this manuscript we have seen how and why characterizing superconducting bulk materials for electrical engineering applications. Then we took the example of a relatively new superconductors with still misunderstood properties and with a low level of readiness.

In this chapter we will work on much more mature materials, the famous $Y_1Ba_2Cu_3O_y$ complex where large size bulks (>cm) can be prepared and used for Trapped Field (TF) experiments and/or magnetic shielding and particularly on a synthesis protocol: the so-called infiltration Growth process (IG).

This kind of synthesis technique used on REBaCuO materials is well known [26], [120], [201]–[204] and is now ready for further improvement of the resulting superconducting properties and a characterization in more specific environment such as at lower temperature than 77 K or under higher magnetic field than usually used in MPMS machines (<10 T).

In this way, S. Pavan et al. managed the synthesis of a $Y_1Ba_2Cu_3O_y$ bulk crystal using IG process using precursors powders submitted to an ultrasonication pre-treatment [104].

Then using the high field magnet platform of the High Field Magnet Laboratory, Nijmegen, Netherland, with the help of MPMS-SQUID measurement, I was able to characterize the superconducting properties, i.e. J_c and $\mu_0 H_{irr}$ of the IG-YBaCuO samples at up to 33 T and down to 40 K.

In a second part, we will explore an exotic design of superconducting bulks possible with the IG process: superconducting foams. Despite having been prepared years ago [97], [205] the original design is only at its first steps of development. To study it, as for a classic bulk sample, magnetic measurement using MPMS-SQUID and microscopy analysis of its structure were carried out to described its superconducting properties and crystallographic structure.

IV.2. Infiltration Growth (IG) YBCO with ultrasonication pre-treatment

IV.2.a. Pre-treatment and synthesis process

The Infiltration Growth processes done on the YBaCuO complex consists of using 2 different precursors, the so-called green Y-211 $Y_2Ba_1Cu_1O_5$ and $Ba_3Cu_5O_8$. The Y-211 is pressed as a pellet and placed on the $Ba_3Cu_5O_8$. Then the sample is heated up at roughly 1000-1050 °C depending on the protocol [203] in order to liquify the $Ba_3Cu_5O_8$ and let it diffuse though the Y-211 then it reacts and formed the $Y_1Ba_2Cu_3O_y$ with a slow cooling . The crystal coherence is ensured by the seed placed at the top of the Y-211 bulk, this seed is generally made of NdBaCuO or SmBaCuO because of their higher fusion temperatures [206]. A schematic drawing of the IG-process is presented on Figure IV-1.

The preparation of top seeded Infiltration Growth method YBCO (IG-YBCO) bulks requires Y211 powder pressed as a pellet which reacts with a liquid $Ba_3Cu_5O_8$ phase. The size of the grain is essential to ensure a good reaction with the liquid phase, a high density, good pinning site with unreacted particles and so the best superconducting performances [104], [207].

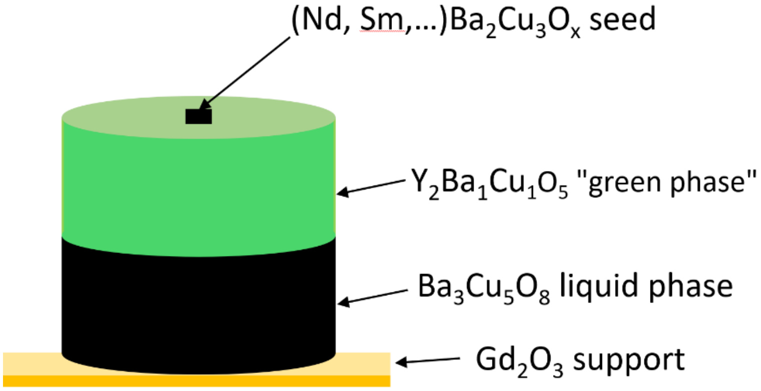

Figure IV-1: Drawing of the Infiltration Growth (IG) process. The Green Y211 bulk is placed above a $Ba_3Cu_5O_8$, the liquid phase at high temperature which infiltrate the green phase and react with it according to the crystal orientation given by the seed at the top of the green Y211.

Comparing to the so-called Top Seeded Melt Growth (TSMG) method, which allows the preparation of YBCO single crystal with very good properties and relatively large sizes [38], [127], [206], [208], the IG method as the advantage of a better shape and density control which allows the preparation of various design such as middle seeded or foams [97], [119], [209], [210]

In this way, IG-YBCO were prepared by colleagues, Dr. S. Pavan Kumar Naik et al. [104], with a special focus on the precursor powders on which an ultrasonication pre-treatments were done. The powder is placed inside acetone as liquid medium, then ultrasonic wave with a power of 300 W is applied on the powder. Different treatments time were applied: 15, 30, 45 and 60 min and all results were compared regarding microscopic aspect and trapped magnetic field and critical current density at 77 K.

However, it is clear that larger magnetic fields are needed to have a complete picture of the magnetic properties at temperature below 77 K where the irreversible magnetic field $\mu_0 H_{irr}$ is already almost at 7 T. This will of course support a potential use in applications working below 77 K [87], [211] but will also give a more complete idea of the sample's performance and allows a deeper comparison with the TSMG ones.

Thus, we decided to do high field measurements (HF measurements) of up to 33 T using high field magnets of the European Magnetic Field Laboratory (EMFL) for two samples at 77 K. According to the measurements done by S. Pavan et al. (Fig. 10 of [104]), the samples with respectively the highest and the lowest critical current are the samples with 45 and 60 min of ultrasonication, hereinafter S-45 and S-60 samples.

IV.3. High Field Cantilever Magnetometry

IV.3.a. The High Field Magnet Laboratory

EMFL is a group of 4 different laboratories in Europe with a common goal of working on high magnetic field and magnets:

- The Hochfeld-Magnetlabor Dresden (HLD) in Germany, focused on the production of pulsed field (such as 95 T during 10 ms)
- The Laboratoire National des Champs Magnétiques Intenses (LNCMI) situated in France at both Toulouse for pulsed field (up to 150 T using semi-destructive method where the coil is destroyed) and Grenoble for continuous magnetic field (up to 35 T using resistive or superconducting magnets)
- The High Field Magnet Laboratory (HFML) in Netherland at Nijmegen, focused on the production of continuous high magnetic field (up to 45 T using a hybrid resistive/superconducting magnet).

Each of those centers have different equipment, in this way only the HFML can perform cantilever magnetometry at up to 33 T [136].

The 33 T are generated in a 32 mm inner bore at room temperature using a resistive electromagnet made of pure copper with the so-called Bitter magnet configuration and the help of a high power of 20 MW (40 kA, 500V) [212]. It consists of a multilayer magnet made of stacked copper and isolating leaves with holes for the water cooling (240 l/s) [213], as it can be seen on Figure IV-2.

Also, the magnetic field gradient as well as the field center are known and given in [214] which is important for the chosen measurement technique, force magnetometry, as the sample must be in a field gradient outside the center. Finally, the magnet is controlled via a computer where the value of the magnetic field as well as the field sweep rate (up to 2 T/min) and the temperature in the magnet can be controlled.

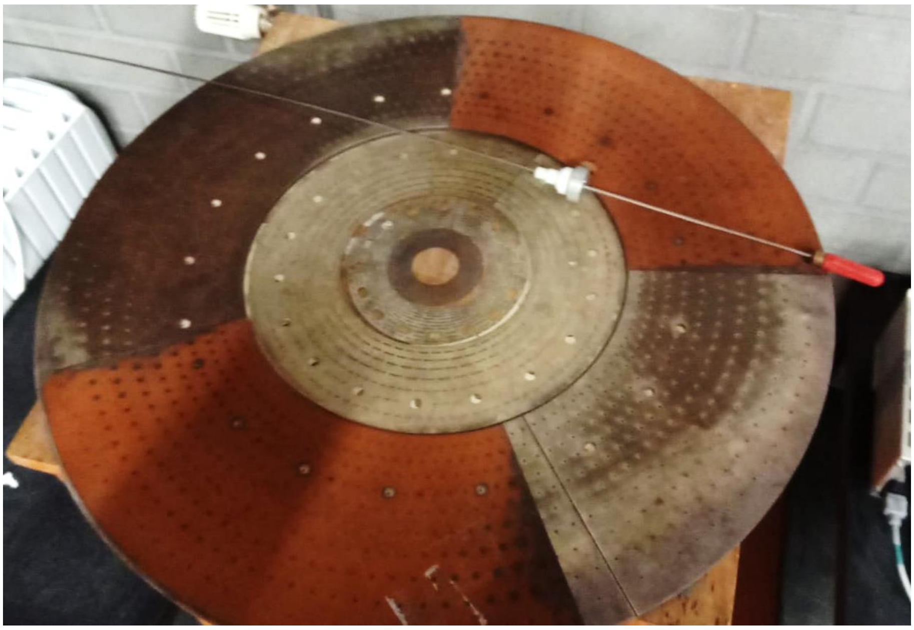

Figure IV-2: Picture of Bitter magnet's layers used for high field generation. It is made of copper and isolating plates pierced of small holes filled by the demineralized water, each section is generating more than 8 T and so the 4 different discs are then giving the 33 T magnetic field. The bigger holes are used for the mechanical reinforcement by using stainless-steel rods.

IV.3.b. Experimental setup for high magnetic field measurement

One of the main limitations of high field magnets is the available space for the experimental setup and the sample. Indeed, the inner bore is of 32 mm of diameter at room temperature and 1 cm inside the cryostat. So as every component of the experiment (cooling an isolating system, measurement systems and the samples) have to be contained in this limited diameter and work under hard condition, such as a 33 T magnet, a measurement of the magnetic force has been chosen to characterize the critical current density of the sample.
As said in section II.3.c, the magnetic force can be measured with the help of the Cantilever magnetometry technique either by a measure of the force in a magnetic gradient (Force magnetometry) or with an angle between the sample's magnetic field and the external magnetic field (torque magnetometry) [137], [138], [215]–[217]. The force magnetometry technique has been chosen as the torque magnetometry is adapted for anisotropic sample and easier to set-up. When for the force magnetometry, the measurement probe is adjusted one for all at the beginning of the measurement campaign and so it is rigorously the same for each sample and each temperature. More details are presented in section II.3.c.

- ### Cooling and temperature control system

a) Description

All the system was cooled down using gaseous/liquid helium and the cryostat was using a nitrogen shield inside the room temperature inner bore.

A basic drawing of the cooling system is proposed on Figure IV-3 where a helium tank is connected to a closed circuit. The helium flow is ensured by a pump and can be controlled both by the pump or a needle controlling the openness of a nozzle placed at the bottom of the cryostat from where the helium enter into the cryostat. The helium is evacuated at the top of the cryostat and through the helium recuperation system for a new liquefaction. Note that, the lowest measured temperature was 40 K so the helium was always in gaseous state during the experiment.

The temperature is controlled by, of course, the helium flow at the nozzle but also by a heater based on the nozzle as well. Associated with a thermometer placed close to the heater, the temperature of the incoming helium is then well controlled.

Also, the temperature on the sample is obviously measured by a thermometer placed closed to the sample. The two thermometers are connected to a LakeShore controller 250.

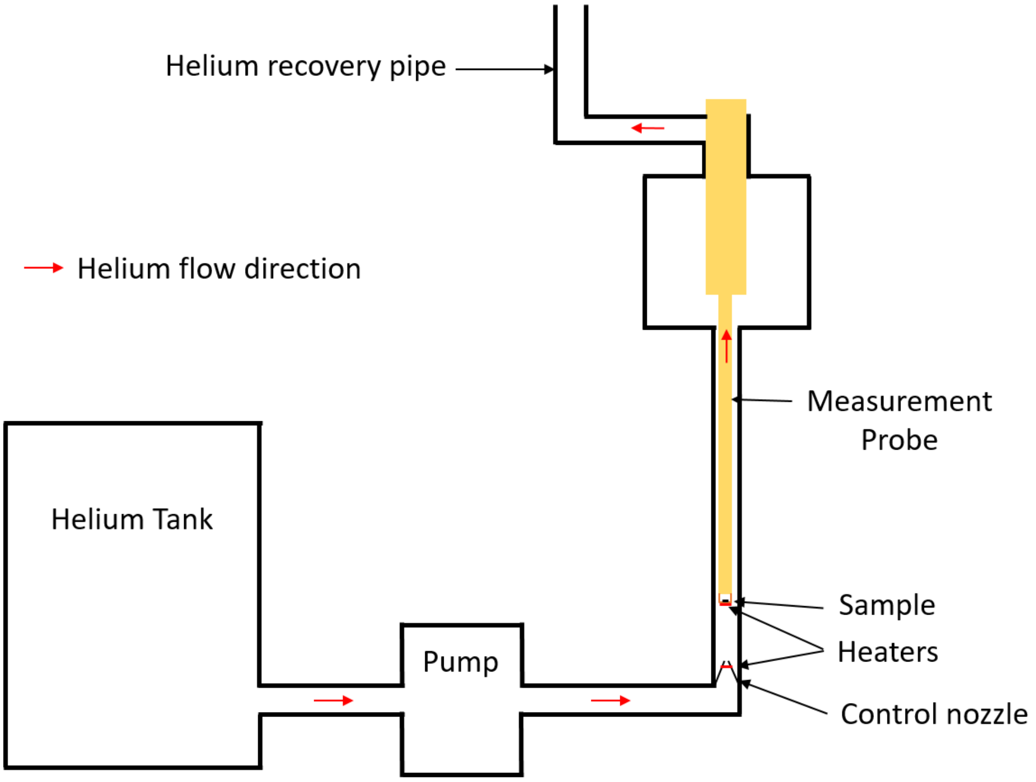

Figure IV-3: Schematic drawing of the cooling system used to cooldown the sample during the high field measurement. A helium tank is providing the helium at 4.2 K then its flow is controlled via a pump and the nozzle. Heaters are here to control the temperature of the incoming Helium and on the sample. Then the laboratory is equipped of a recovery system.

b) Limits

However, managing the temperature is quite challenging and time consuming, change the temperature can be really fast (up to 5 K/min) but fixing it is very long due to the inertia of the system and the difficulty for matching the flow and the heat on the nozzle. So, it can take more than half an hour for changing the temperature and fixing it with a precision of 0.2 K. Also, along the experiments the temperature can shift due to the difficulty to fix it and noise is generated by the high fields on the thermometer. This is illustrated by Figure IV-4 where over an experiment the measured temperature artificially increases and hides the true variation of temperature. But, as we can see at the end of the experiment, the temperature has moved from 49.8 to 50.1 K so a variation of 0.3 K which is sufficiently low to be neglected.

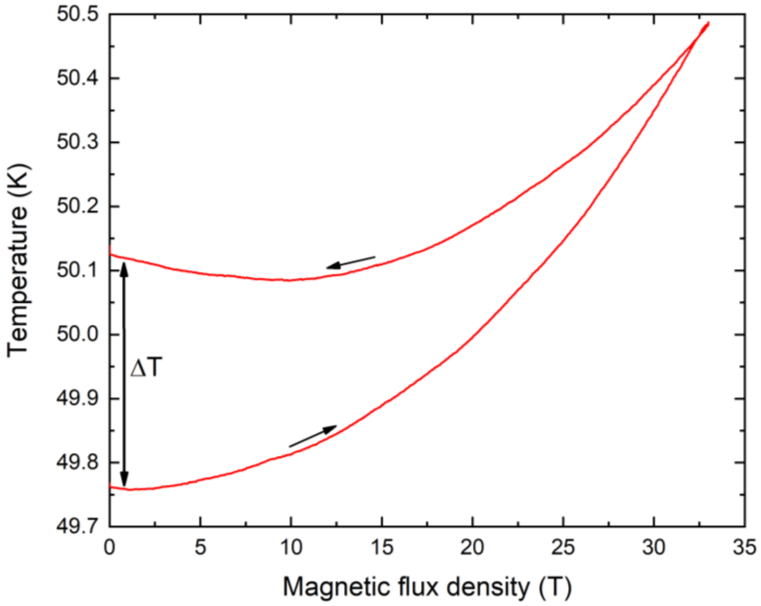

Figure IV-4: Variation of the temperature over a HF run. The external field is looping from 33 to 0 T in about 35 min and a shift of ΔT=0.36 K is observed. Also, we can see the shift of the temperature given by the thermometer due to the effect of the magnetic field on it.

- Field detection and sample positioning

Before starting the experiment, it is necessary to place the sample slightly above or below the field center, which is well known for each magnet at HFML [214]. This assures a magnetic field as closed as possible to the maximal one (present at the field center) but also a magnetic gradient, essential for the cantilever magnetometry based on magnetic force A Hall sensor, plugged on a voltmeter, is placed 2 cm below the sample, so placing the sensor on the field center (where the field is maximal) will place the sample 2 cm above it which is enough to guarantee a gradient all along the experiment with a magnetic field almost maximal.

Then the probe with the sample holder is fixed using rings of different heights, so for all the experiment the position of the setup is fixed and samples are always placed 2 cm above the field center.

- Cantilever magnetometry

As explained before the chosen method for measuring the magnetic properties of IG-YBCO bulks is the so-called cantilever magnetometry.

The setup used to determine the superconducting properties, presented on Figure IV-5, is as follow:

- (1) the cantilever made of pure copper, fixed on the sample holder at the extremity with an electrode placed at the bottom and placed strictly perpendicular to the external magnetic field (to avoid any torque).
- (2) the IG-YBCO sample is glue using a G01 glue on the cantilever.
- (3) The sample holder, fixed on the cryogenic probe, with the second electrode, facing the first one at a distance "d".

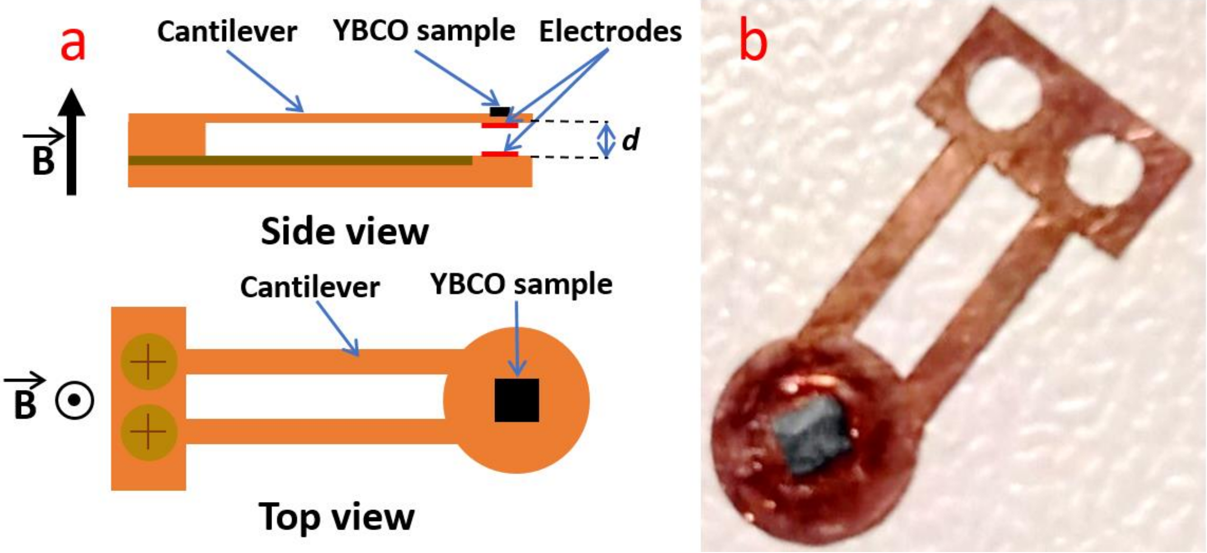

Figure IV-5: (a) Schematic drawing of the cantilever with a side and a top view. We can see the sample placed at the center of the cantilever. The cantilever is perpendicular with the external magnetic field and at a distance d of the second electrode (the first one is placed right below the cantilever). (b) Picture of the actual cantilever with a sample glued on it.

Along the experiment, the capacitance between the 2 facing electrodes is measured using a capacitance bridge (model AH 2700A from Lakeshore).

Major drawbacks have to be highlighted:

- It is necessary to calibrate the cantilever before starting the measurement in order to determine its bending coefficient *K* which is difficult and very time consuming for a one-week experiment campaign.
- The lack of knowledge concerning the *K* factor of the cantilever can also lead to irreversible deformations of it if the mechanical stress is too high. The consequence is the irreversibility of the measured capacitance. At the end of the run, the cantilever doesn't go back to its original place.

Figure IV-6 is giving an example of a plastic deformation event, when the external field is increasing (from "Starting point"), as showed by the arrows, the measured capacitance is lowering due to the repulsion force generated by the sample in a magnetic gradient. However, a plastic deformation occurred between 17 to 30 T with an increasing magnetic field as the evolution of the capacitance is almost flat which is unexpected compared to all other measurements (Figure IV-8). With this, a to high deformation induces an angle between the two electrodes which are no more facing each other's and distorts the measured value.

Finally, when the external magnetic field is reduced to zero, at which the relative capacitance is not null which means that the cantilever isn't back to its starting position. The cantilever is now slightly further from the other electrodes than before the beginning of the experiment and the measured evolution of the capacitance during the experiment is completely unusable. This deformation leads to a shift of the capacitance from the beginning to the end of the measurement of around $\Delta C = -0.15$ pF as it can be seen on Figure IV-6.

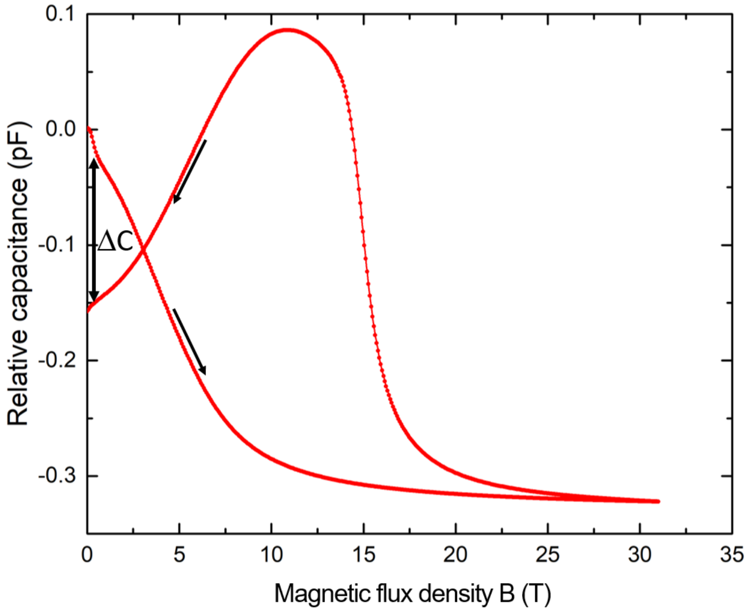

Figure IV-6: Relative capacitance measured on the S-45 sample at 50 K, the arrows are showing the variation over time with the external magnetic field. We can see that a plastic deformation of $\Delta C = -0.15$ pF is occurring above 20 T as the relative capacitance never go back to 0. Finally, when the field is reduced the effect of the plastic deformation is visible by the remaining relative capacitance ΔC.

Following those drawbacks, it is necessary to settle approximations:

- the airgap d of the capacitance is always small enough compared to the dimensions of the section of both electrodes ($d = 1$ mm electrode = 3 mm of diameter).
- the variation of the bending angle of the cantilever during the experiment is small enough to have $\sin(\theta) = \theta$, with θ the angle, so the variation of d is also linear with θ and the electrodes are always considered face to face. This approximation is of course no more valid when plastic deformation occurs.
- the variation of d is small enough to have a linear elasticity for the cantilever (fully reversible) so the force is linearly linked with the variation of d over a run.
- the shapes of the different samples are considered equivalent so we assume that the demagnetization factor is the same for both samples.

IV.4. Experimental characterization of IG YBaCuO with ultrasonication pretreatment

IV.4.a. Sample preparation

The limited size of the cantilever (9 mm of diameter) is similar with the disponible space inside a MPMS-SQUID, also as the sample have to be characterized on such machine after the HF campaign, I prepared sample with the typical mm size range as presented on II.2.e Consequently, the two IG-YBCO selected for HF, S-45 and S-60, were cut from each bulk with the following dimensions:

- 1.63 × 1.55 × 0.34 mm^3 (5.1 mg so 5.93 $g.cm^{-3}$, 94 % of the theoretical density) for the S-45 sample, visible on Figure IV-7.a.
- 1.03 × 1.02 × 0.33 mm^3 (1.9 mg so 5.48 $g.cm^{-3}$, 87 % of the theoretical density) for the S-60 sample, visible on Figure IV-7.b.

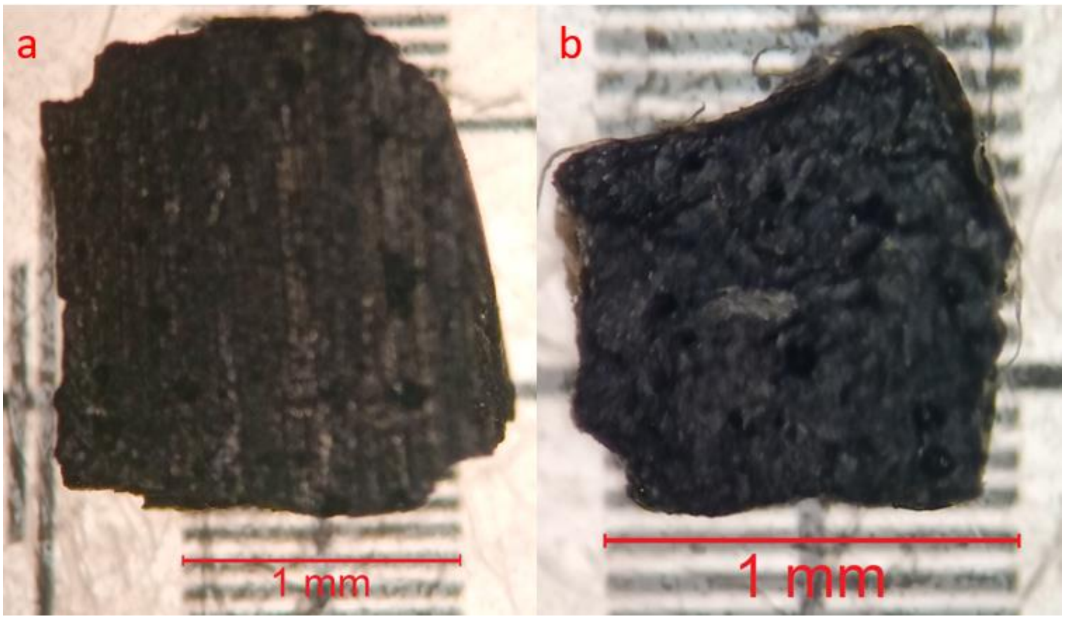

Figure IV-7: Picture of the samples S-45 (a) and S-60 (b) characterized with the HF measurements.

IV.4.b. High magnetic field measurement

The two samples, S-60 and S-45, (described right above) were then prepared and installed on the cantilever and placed 2 cm above the field center.

The resulting measurement for the sample S-60 is presented on Figure IV-8.b where the variation of the capacitance is presented for temperature from 70 K and 40 K. The arrows show the change of variations, so the capacitance starts by lowering as the sample is trying to moved out from the magnet field which is maximum in the field center, right below the cantilever, so the distance between the electrodes increases. As the external magnetic field is increasing, the magnetic force is also increasing but at a point (such as 16 T at 40 K) it starts to decrease until going back to its original value, which correspond to the irreversible magnetic field. When the Magnetic field is reversed, the cantilever is bending in the other way as now the magnetic field is decreasing and inverts the magnetic moment of the sample. The result of the S-45 sample is shown on Figure IV-8.a with similar results but with a sharper variation than for the S-60 (Figure IV-8.b) sample and for temperatures only between 70 to 60 K.

Partly explained by the size of the sample, the too high performances below 60 K, exacerbate by a fishtail effect, induced a plastic deformation on the cantilever during the measurement and so inconsistent and unusable results. This limit was reached at 40 K for the S-60 sample. Such event was presented on Figure IV-6 with the measured variation of the capacitance at 50 K using the S-45 sample where the arrows indicate the direction of the variation. When the magnetic field increases, the sample is moving out from the field center and so the cantilever is bent. But for fields above 15 T, the cantilever does not go back as the critical current inside the bulks should be decreasing and the variation of the capacitance stays high even at 33 T. This clearly indicates that the capacitance had a plastic deformation and so there is no elastic force to push-back the sample at its original position when the irreversible magnetic field is reached.

In a second time, when the magnetic field is going down, we recognize a similar shape as for the higher temperatures with the bump follows by a decreasing of the capacitance until it reaches its final position. This final position is very different of the original one which is another evidence of a plastic deformation. The cantilever is now slightly further from the other electrodes than before the beginning of the experiment and the measured evolution of the capacitance during the experiment is completely unusable.

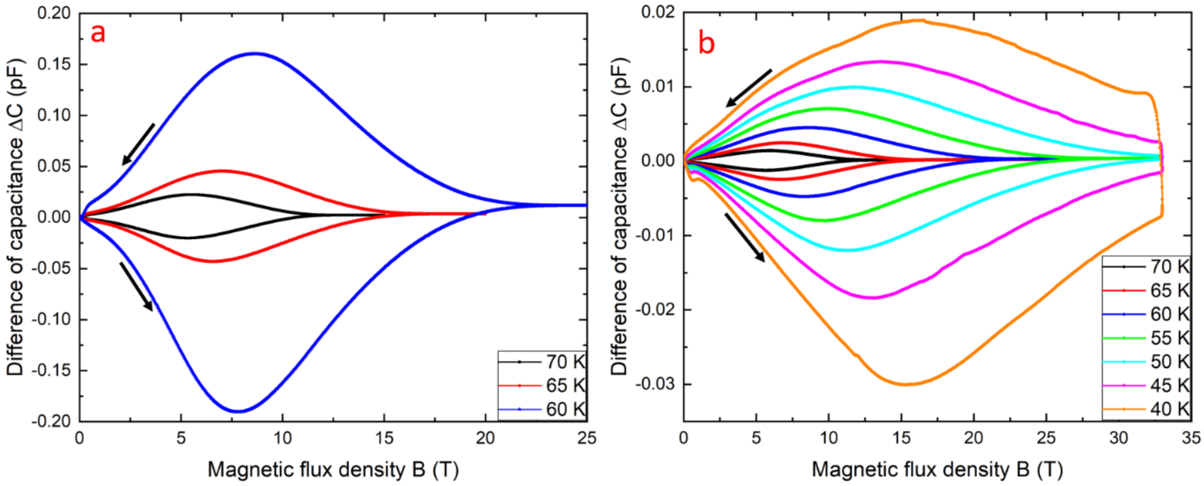

Figure IV-8: Variation of the capacitance measured with the sample S-45 from 70 to 60 K (a) and with the sample S-60 from 70 to 40 K (b).

As we have now measured the capacitance function of the applied magnetic field on ours superconducting samples and in order to confront the samples and extract their superconducting properties such as the critical current or the irreversible magnetic field, we will use EQ. II.33 where the critical current density J_c is linked to the measured capacitance C:

$$J_c = k\frac{d_1|\Delta C|}{C_2 B_r ABC} \qquad (\mathrm{IV.1})$$

with J_c the critical current density in the sample, K the elastic coefficient, d_1 the starting distance between the 2 electrodes of the capacitance, $\Delta C = C_2 - C_1$ the difference of capacitance, C_2 the capacitance measured, $B_r = \alpha B_z$ the radial component of the magnetic field and ABC the sample volume.

To be able to apply this formula on our experimental results, it is important to point out several points. The radial magnetic field wasn't measured during the experiment, only the axial magnetic field B_z at the center of the magnet was clearly measured. To give an idea of the radial magnetic field some considerations have to be done:

- The shift of the cantilever is considered small enough for having a linear variation of the radial magnetic field in both senses as well as the elastic coefficient k, in other words, either the cantilever goes away or gets closer to the magnetic field center, the radial magnetic field is always linearly variating.
- As the sample is small compared to the magnet, the radial as well as the axial magnetic field are considered constant all along the sample.
- Finally, the samples are always considered fully penetrated and, according to the Bean model [105], [106], [113], the critical current density is everywhere the same and so the magnetic field lines are unaffected by the sample (the bending field lines below the samples are completely compensate by the opposite bedding above the sample).

During ramping of the magnetic field, the sample move away from the field center… The displacement of the sample during the experiment can induce a variation of the difference of the capacitance ΔC due to the variation of the magnetic field along this displacement as it can be seen on Figure IV-8. Computing the average of the capacitance in both cases at the same magnetic field allows to compensate this variation.

Finally, by substituting the constants with the factor β and including the capacitance free of the variation of the radial field:

$$J_c = \beta \frac{|\Delta C|}{B_z} \quad \text{with} \quad \beta = \frac{k d_1}{C_2 \alpha ABC} \tag{IV.2}$$

The factor β contains undetermined constant so the critical current density can only be computed with arbitrary unit and then "rescaled" using other measurements where the critical current density can be measured.

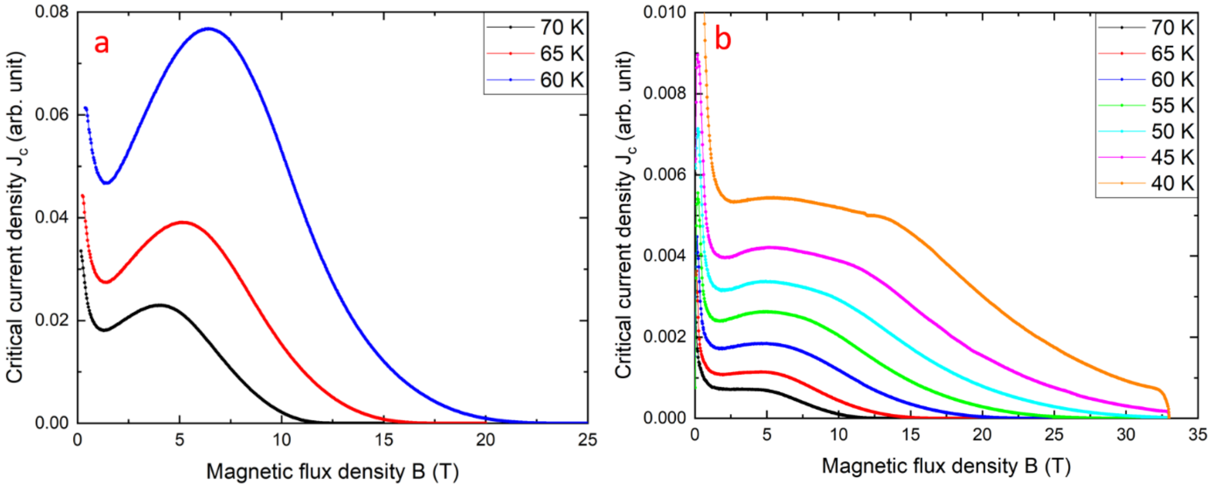

Figure IV-9: Critical current density Jc in arbitrary unit vs external magnetic field (T) for the S-45 (a) and the S-60 (b) samples.

Therefore, the critical current density in arbitrary unit is presented on Figure IV-9.a for the S-45 and Figure IV-9.b for the S-60 sample. As we can see, the fishtail effect is present on both sample but the S-45 is showing a very large one, also reported in [104]. As expected from Figure IV-8.b , 33 T looks not enough to get the full picture of the critical current density at 45 and 40 K in the condition the experiments were done (under a constant variable magnetic field of 33 mT.s^{-1}). However, the shapes of the curves are very similar with the ones of other YBaCuO superconductor measured by SQUID (as seen before with Figure II-16) as the J_c and the H_{irr} are both increasing by lowering the sample's temperature for both curves.

Now it seems necessary to find a way to "rescale" the arbitrary J_c on its real value for each temperature and applied field.

IV.4.c. Comparison with critical current measured by SQUID magnetometry

SQUID measurements have now to be done on the same sample for the same temperature, then the high field measurements could be rescaled on the SQUID ones.

Those measurements have been carried-out using the same set-up as presented before, the ±7 T Quantum Design's MPMS-SQUID 3 of Jean Lamour Institute with the same samples as for HF measurements (the weight and the size of the samples have been verified).

The Figure IV-10.a,b are showing, respectively for the S-45 and S-60 samples, the critical current density at the temperature showed on Figure IV-9. Also, Figure IV-10.c shows both curves at 77 K which let us compare them. So as expected, the S-45 sample is showing a slightly higher J_c.

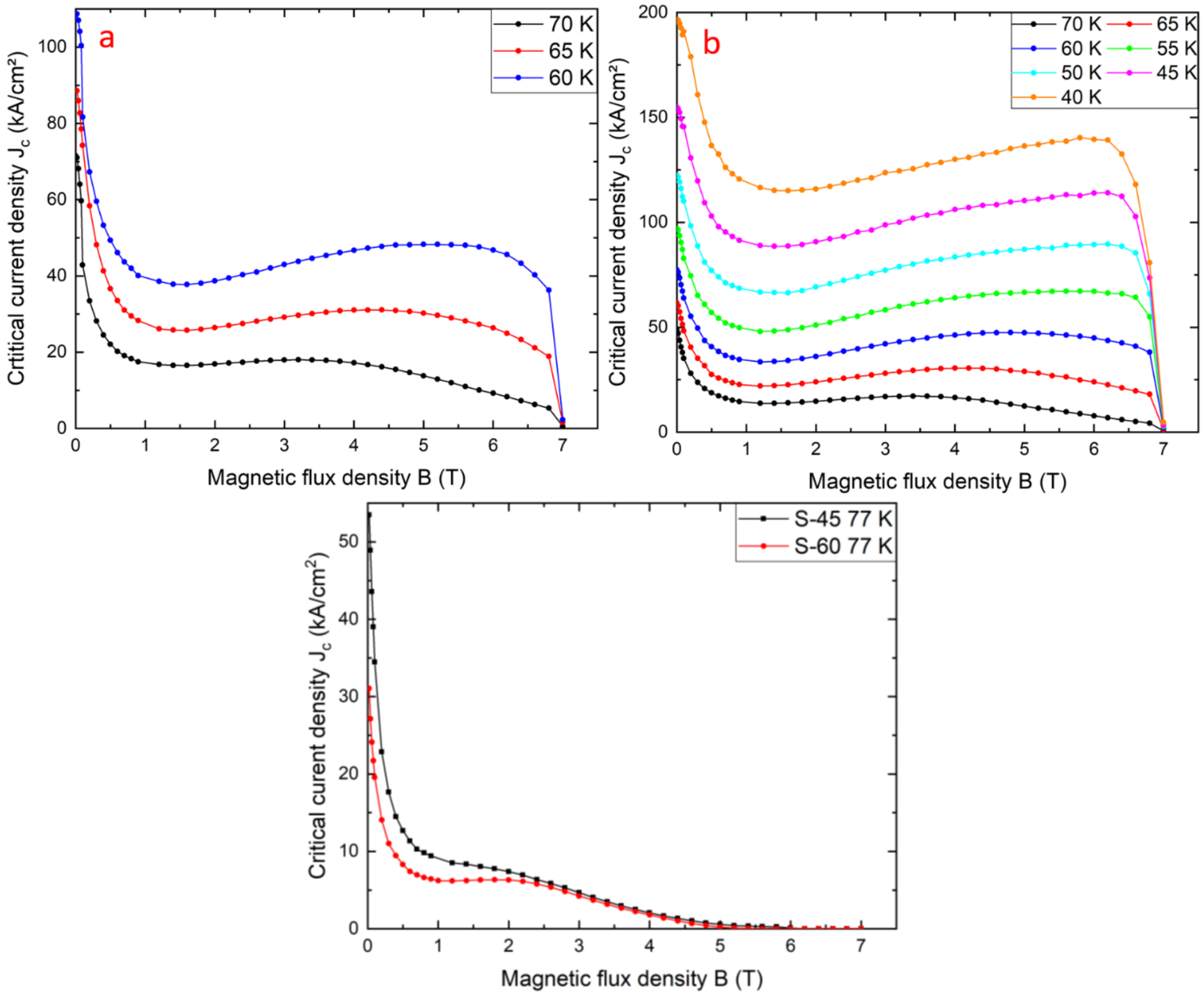

Figure IV-10: Critical current density versus applied magnetic field for various temperatures measured by SQUID magnetometry for the samples S-45 (a) and S-60 (b) and the curve at 77 K for both samples (c).

The measurements of the magnetic moments with the help of a MPMS-SQUID allows a brief comparison with the first study using force magnetometry done on those samples, however, the high field measurements were done "on-the-fly", with a constant magnetic field sweep rate of 33 mT.s^{-1}. On Figure IV-11, where the J_c measured by SQUID is compared with the J_c of the high field measurement for the S-60 sample, we can see that their shapes are really different, the top of the fishtail is at a different place and it seems that a simple factor between both measurements can't be applied to obtain the critical current density at magnetic fields up to 33 T.

This effect is maybe linked with the magnetic field sweep rate present during the measurement through the effect of the dynamic relaxation rates on J_c [137] and the flux creep process [218]. So, to explain those results and then to extract the superconducting properties, we firstly need to study the effect of a variable magnetic field on the critical current density and the associated irreversible magnetic fields.

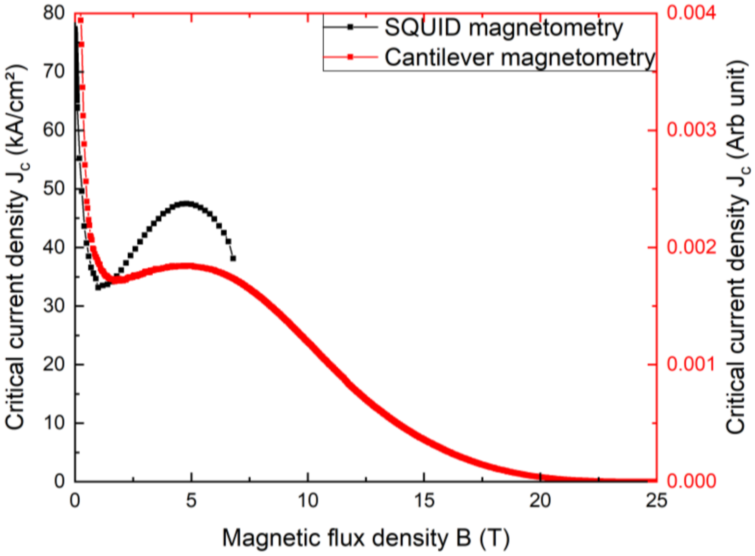

Figure IV-11: Comparison of the critical current density extracted from SQUID magnetometry measurement in A.cm^{-2} with HF cantilever magnetometry in arbitrary unit for the S-60 sample at 60 K.

IV.5. Critical current density under High and variable magnetic field

IV.5.a. Impact of the magnetic field sweep rate

As a MPMS-3 SQUID from Quantum design allows a magnetic field sweep rate up to 70 mT.s^{-1}, I measured the magnetic moment and so the critical current density at 77 K for different magnetic field sweep rate up to 40 mT.s^{-1} on the S-60 sample. The resulting measurement is presented on Figure IV-12. We can see that higher the sweep rate, higher the critical current and its associated irreversible magnetic field which is supported by the insert of Figure IV-12 where the J_c at 2 T is presented function of the field sweep rate. It seems that the effect of the sweep rate on the critical current density saturates at value over 40 mT.$^{-1}$.

The influence of the magnetic field sweep rate has been study in the past [137] where the critical current with a continuous sweep rate is described as the “true” critical current. Then when the sweep rate is no more, a relaxation processes occurs in the superconductors leading to the “habitual” J_c. However, it only covers a part of the problem as only a part of the $J_c(B)$ was studied.

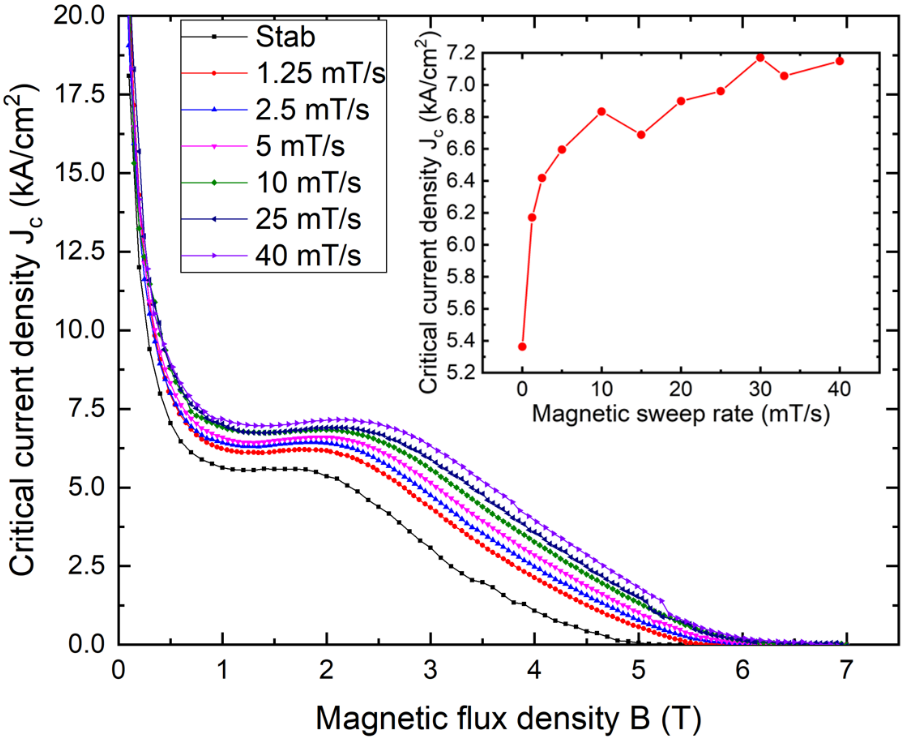

Figure IV-12: Critical current density of the S-60 sample measured with different magnetic field sweep rate at 77 K. The insert is comparing this critical current density at 2 T for the different sweep rate.

As our samples possess a strong fishtail effect and are orthorhombic-shaped bulks, another model should be developed to extract the J_c after relaxation and much more measurements are needed to support a potential new model. Such kind of model is presented in several papers like the Anderson model [218] and gives a way to study the thermally activated flux/vortex motion in superconductors. When the external magnetic field is sweeping, the vortex motion induces an electrical field and it comes out a magnetization relaxation rate and a way to explains this phenomenon [191], [219]–[221].

This model needs a complete study of the vortex dynamic and so of the sweeping rate of the sample at different magnetic fields as it is really field sensitive [191], [221]. Also, as we are comparing data measured by two very different ways, giving a detail study of this phenomenon is a non-sense if not all parameters are nicely controlled. This is why, in this manuscript, I will firstly produce and apply a simple empiric computation using measurement of the magnetization, and so the J_c, for various temperatures either with a 33 mT.s^{-1} sweep rate and stabilized magnetic fields. Then, I will apply this method on the HF measurement for a rescaling on the SQUID's ones.

IV.5.b. Critical current density under a variable and stable magnetic field

Figure IV-13.a,b are respectively showing the magnetization measured for a stabilized magnetic field at each point (the "SQUID Stab" curve) and during a constant sweep rate of 33 mT.s^{-1} (the "SQUID 33 mT.s^{-1}" curve) of the S-60 sample obtained via the same MPMS SQUID as before. In this section, we will only explain the method on the S-60 sample but the same method was used for the S-45 sample.

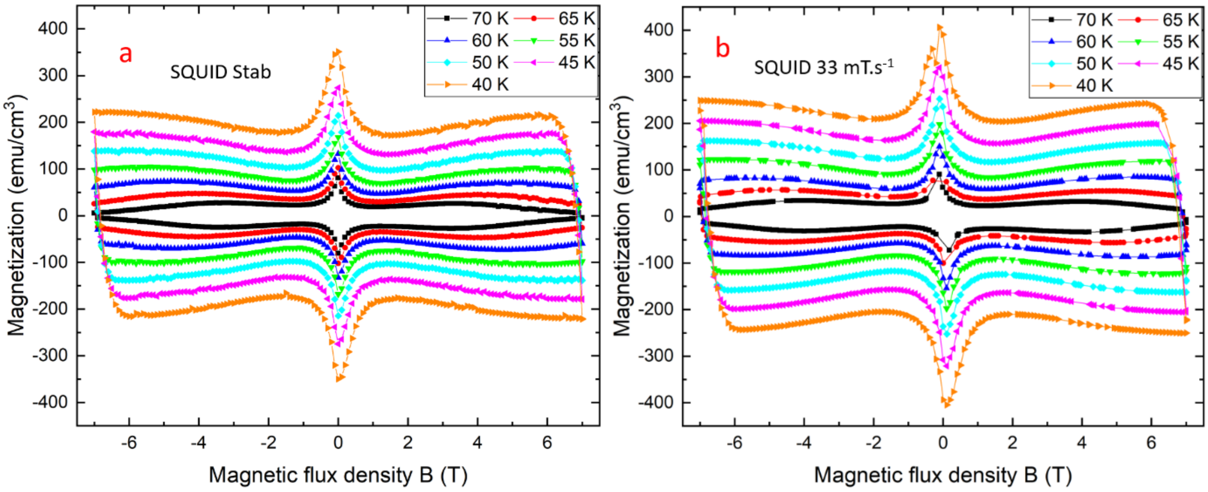

Figure IV-13: Magnetization measured with the help of a MPMS SQUID with a stabilized magnetic field (a), and a constantly sweeping field of 33 mT.s^{-1} (b) at the same temperature used for the HF measurement of the S-60 sample.

First of all, the curves of Figure IV-13 are fitted and smoothed from 0.7 to 5.8-6.3 T, using the Smoothing spline function of MATLAB which consists of a series of polynomials, in order to have a regular repartition of the point and without the extremity where the Bean's model is no more valid (due to the penetration field). We can see that when the SQUID Stab moment is showing a noisy signal, the SQUID 33 mT.s^{-1} moment displays missing point for all temperatures. This comes from the difficulty for the machine to measure the magnetic moment with a sweeping magnetic field: the SQUID Stab moment is measured with a regular step of field while for the dynamic one it is done "on the fly" so the measured steps are irregular. The smoothing as well as the fitting function from MATLAB softens or eliminates those issues.

Their respective critical currents densities were then determined with the help of the Chen's Formula presented in section II.2.d and displayed on Figure IV-14. Where the missing points of the SQUID 33 mT.s^{-1} curves are nicely corrected by the fitting, the SQUID Stab ones is still showing a noisy signal even after a smoothing/fitting correction.

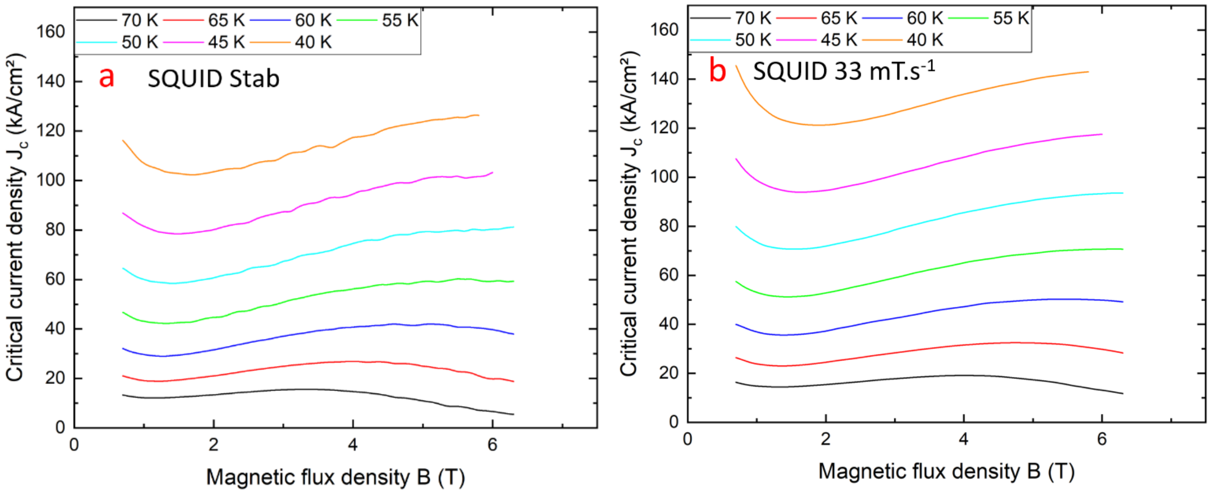

Figure IV-14: Fitted critical current density computed from the SQUID Stab (a) and SQUID 33 mT.s-1 (b) fitted magnetization of the S-60 sample.

On all curves of Figure IV-14, two characteristic points are present: the minimum of J_c in the "valley" and the maximum of the "hill" of the curve, an example is presented on Figure IV-15: Fitted critical current density at 70 K either with a fixed or sweeping magnetic field (33 mT.s-1) with the characteristic points of the S-60 sample. with both curves at 70 K. Those points are extracted and presented as follow:

SQUID Stab curve: $P_{min,0}(J_{cmin,0};B_{min,0})$, $P_{max,0}(J_{cmax,0};B_{max,0})$.

SQUID 33 mT.s^{-1} curve: $P_{min,33}(J_{cmin,33};B_{min,33})$, $P_{max,33}(J_{cmax,33};B_{max,33})$.

where, as example, $P_{min,0}$ is the point in the minimum of the valley for the SQUID Stab curve of coordinate $J_{cmin,0}$ and $B_{min,0}$.

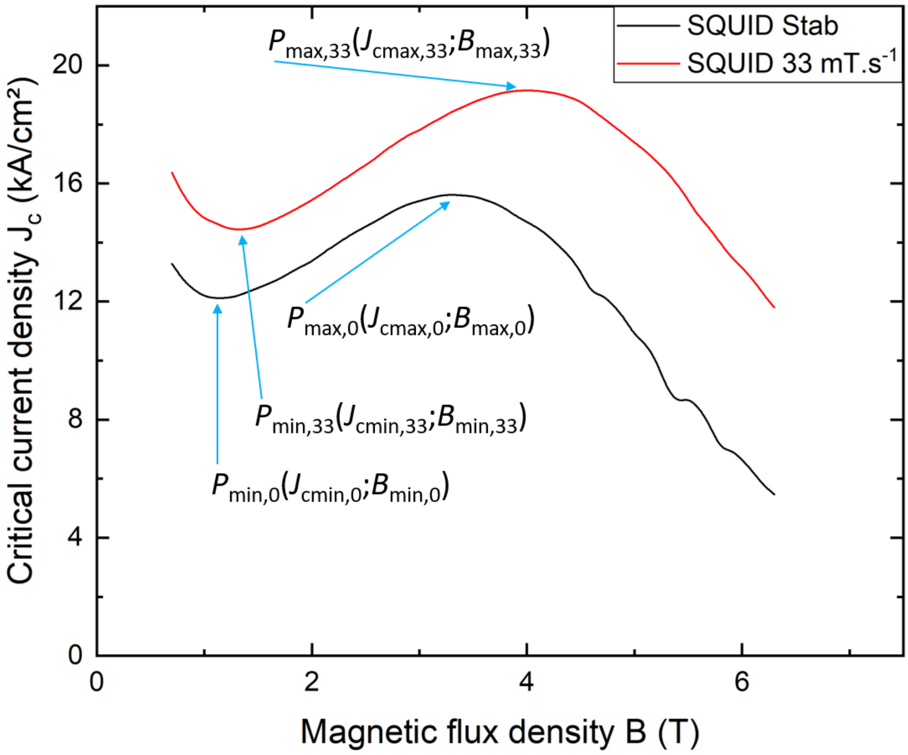

Figure IV-15: Fitted critical current density at 70 K either with a fixed or sweeping magnetic field (33 mT.s^{-1}) with the characteristic points of the S-60 sample.

The idea is to compute the corrective ratio between the critical current of the points at the minimum of each curve as well as for their maximum. Let's take an example with the curves at 70 K, those ratios are:

$$R_{1,min} = \frac{Jc_{min,33}}{Jc_{min,0}} = \frac{14445}{12118} = 1.192 \qquad (IV.6)$$

$$R_{1,max} = \frac{Jc_{max,33}}{Jc_{max,0}} = \frac{19150}{15613} = 1.227 \qquad (IV.7)$$

As we can see those ratios are different, which means that the ratio is evolving with the magnetic field. We will consider this evolution as linear with the surrounding magnetic field, consequently, the characteristics of the correcting curves are determined:

$$R(B) = f \times B + g \qquad (IV.8)$$

where:

$$f = \frac{R_{1,min} - R_{1,max}}{B_{min,0} - B_{max,0}} = 1.6x10^{-2} \qquad (IV.8)$$

$$g = R_{1,max} - d \times B_{max,0} = 1.174 \qquad (IV.9)$$

Thus, a corrective factor is computed for each magnetic field step used in the fit and used on the SQUID 33 mT.s^{-1} curve which finally rescaled it on the critical current value of the SQUID Stab curve. The result is shown on Figure IV-16.

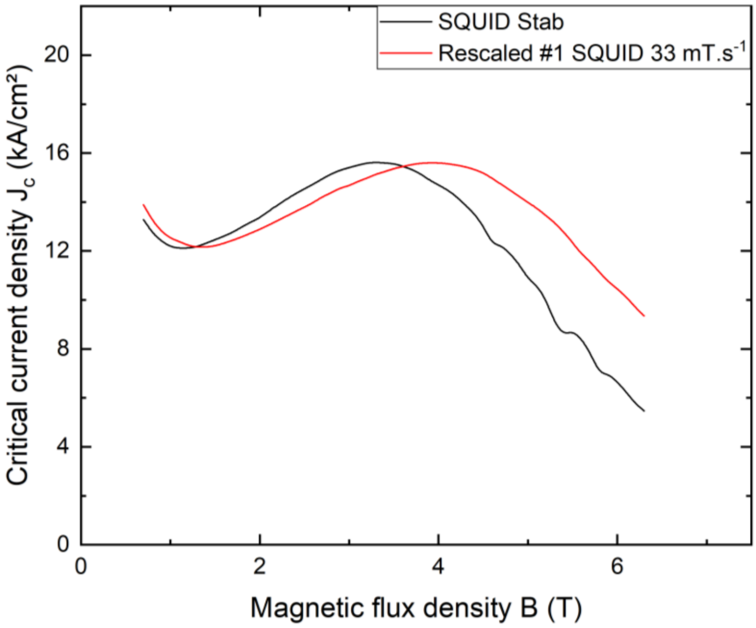

Figure IV-16: SQUID Stab curve number 1 of the critical current density and SQUID 33 mT.s-1 curve after the "rescaling" of the critical current density of the S-60 sample.

However, the curve still looks “stretch” along the magnetic field’s axis as only the value of the critical current is corrected. In this way, the same protocol is applied to compute the correcting ratio but this time on the magnetic field:

$$R_{2,min} = \frac{B_{min,33}}{B_{min,0}} = \frac{1.36}{1.15} = 1.18 \qquad (IV.10)$$

$$R_{2,max} = \frac{\mathrm{B}_{\mathrm{max,33}}}{\mathrm{B}_{\mathrm{max,0}}} = \frac{3.93}{3.3} = 1.19 \qquad (IV.11)$$

With this, the correcting coefficient of Eq. IV.8 is computed for the magnetic field using Eq. IV.10 and Eq IV.11 and then applied on the “Rescaled #1 SQUID 33 mT.s^{-1}” curve of Figure IV-16.

Finally, the Figure IV-17 shows the result after the second successive rescaling. We can see that the rescaling is not perfect because of the noise but I will consider it as acceptable regarding the precision of the measured data and the successive approximations of the models.

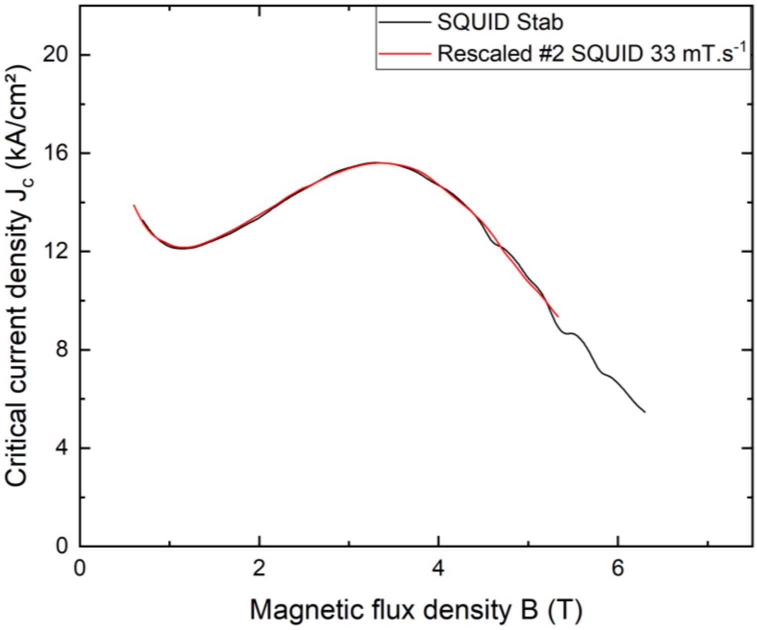

Figure IV-17: SQUID Stab curve of the critical current density and SQUID 33 mT.s-1 curve after the “rescaling” of both the critical current density and magnetic field of the S-60 sample.

This method was used on all the other temperatures, i.e. 65, 60, 55, 50, 45 and 40 K for the S-60 sample and 70, 65 and 60 K for the S-45 one. For temperatures below 55 K the top of the “hill” is above 7 T so the *J*c as well as the magnetic field were extrapolated using the points at higher temperature. Then all correcting coefficients were computed and applied on the SQUID 33 mT.s^{-1} critical current density which was successfully rescaled on the SQUID Stab one as displayed on Figure IV-18. We can see that the fitting, as observed on Figure IV-17, is not perfect but acceptable facing the noisy signal and global measurement incertitude. But at low field (typically below 1 T) the curves start to be different, this comes from the penetration magnetic field which is equal, as example, to 1 T for the *J*c of the

SQUID 33 mT.s^{-1} at 40 K so it is obvious that the fitting is no longer good as the result is outside of the Bean's model limits.

As this method is using extremes values, it is really sensitive to the noise and on the precision of their position, so the parameters may require some readjustment until the fit is acceptable, i.e. when the general shape of both curves are the same. In conclusion to this part, the quality of the rescaling is good enough to be considered as a solution to extract the critical current density from the HF measurements.

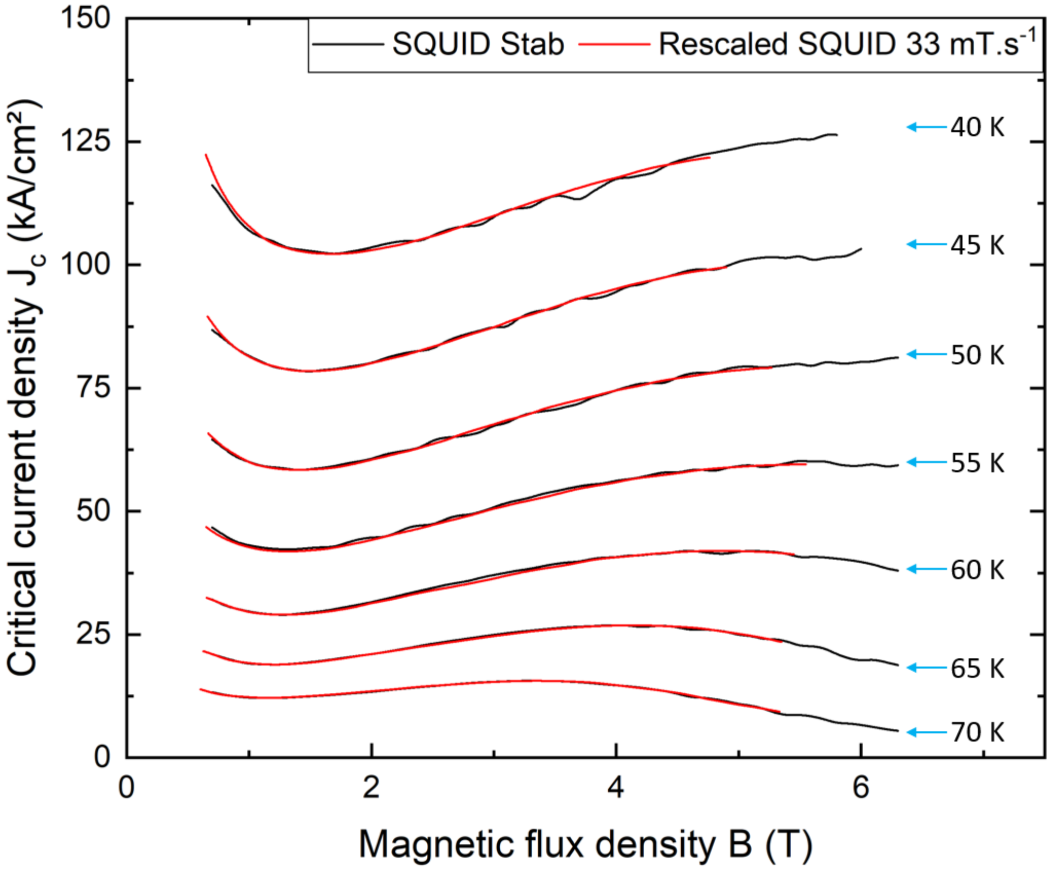

Figure IV-18: Comparison of the critical current density of the SQUID Stab curve and the SQUID 33 mT.s-1 one after rescaling of its current and magnetic field for all temperature of the S-60 sample.

IV.5.c. The problematic effect of time on superconducting properties of IG-YBCO

As the high fields measurement have been done with the same sweep rate and the same sample than for the SQUID measurement with a 33 mT.s^{-1} sweep rate, a simple ratio could give the factor between those two measurement and then gives the critical current density J_c at up to 33 T. However, as highlighted by Figure IV-11 the 2 curves have a really different shape that can't be explain only because of a ratio but also by the effect of aging.

It is well known that, after a long time, materials could suffer of degradation due to various processes, some example and effects has been presented over section III.8.b. This phenomenon wasn't expected with YBaCuO bulks as they are highly stable over time and even an increasing of J_c was measured with time [132]. However, as the IG YBaCuO hasn't the density or is simply not as known as the MG ones and because the samples were cut in small millimeter pieces (Figure IV-7), a much faster degradation can occur.

High field measurements were done during October 2019, right after, along November 2019, I made SQUID measurement but with a fix magnetic field during each measurement. A 4 months trip to Japan for working on FeSe superconductor presented in Chapter II:, follows by the sanitary lockdown due to Covid-19 push the next measurement to September 2020 so up to one year later. At that time, measurements with a constant sweep rate of 33 mT.s^{-1} were carried out. This is where I found out that the shape of the high field measurement was really different from the one measured by SQUID. So, the measurement done with and without sweep rate (field stabilized at each point) can't be compared and new measurement with/without sweep rate as to be done at the same time.

However, a new lockdown as well as a breakdown of the Helium liquefactor providing the liquid Helium for the SQUID shutdown the magnetic platform of the Jean Lamour Institute where I was performing my measurements. New measurements weren't possible until autumn 2021 where I finally made a complete evaluation of the superconducting properties with and without the magnetic field sweep rate.

A summary of the measurement schedule is presented with Figure IV-19.

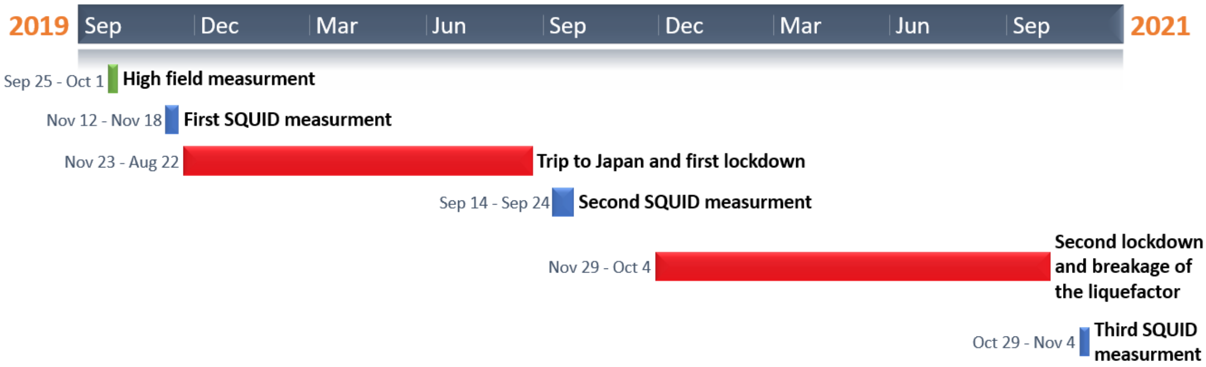

Figure IV-19: Schedule of the magnetic measurements done over 2 years on the IG-YBaCuO samples.

This allows to compare the J_c between the first and the third measurement so spaced by 2 years, the comparison is given on Figure IV-20 at 77 K. This clearly highlights the degradation of the properties which can be evaluated as a loss of roughly 15% of the J_c over 2 years for the value at 2 T.

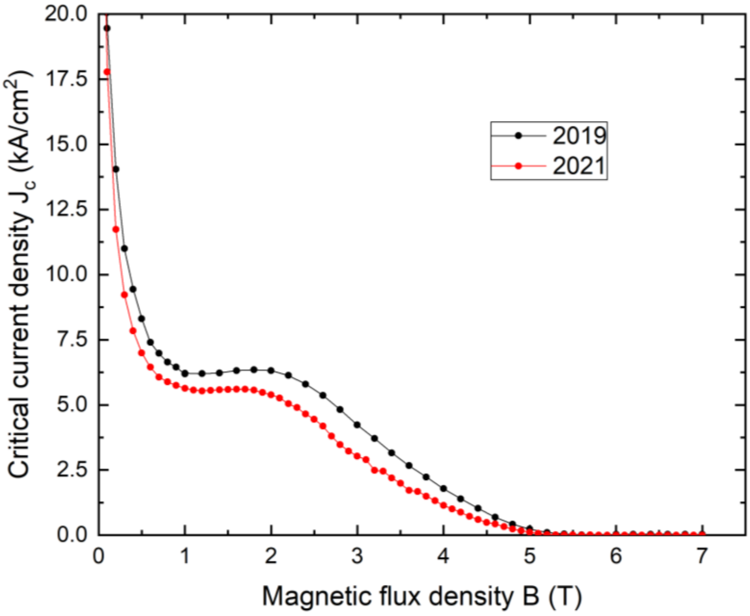

Figure IV-20: Critical current density measured in 2019 and in 2021 at 77 K of the S-60 sample.

So, to rescaled the HF measurements, we will use the curves of the 2019 campaign with a stable magnetic field using the same technique as for rescaling the SQUID 33 mT.s^{-1} J_c on the SQUID Stab one for the 2021 campaign.

IV.5.d. Rescaling of the high field critical current density

The same method with two iterations was then applied for the correction of the magnetic field of the extremum. For the generalization over all the temperature and for both samples, I used a MATLAB program which is able to rapidly iterates this kind of computation.

Finally, the result of the correction on respectively the HF measurement of S-45 and S-60 sample are presented on Figure IV-21. We can see that, as for Figure IV-18, the fit is not perfect due to the lack of precision during the measurement and/or the penetration field, particularly at 70 K for the S-60.

However, it finally gives an opportunity to study the performances of IG-YBCO with ultrasonication pre-treatment above 7 T.

In this way the irreversible magnetics field of both samples are summarized on Table III-1.

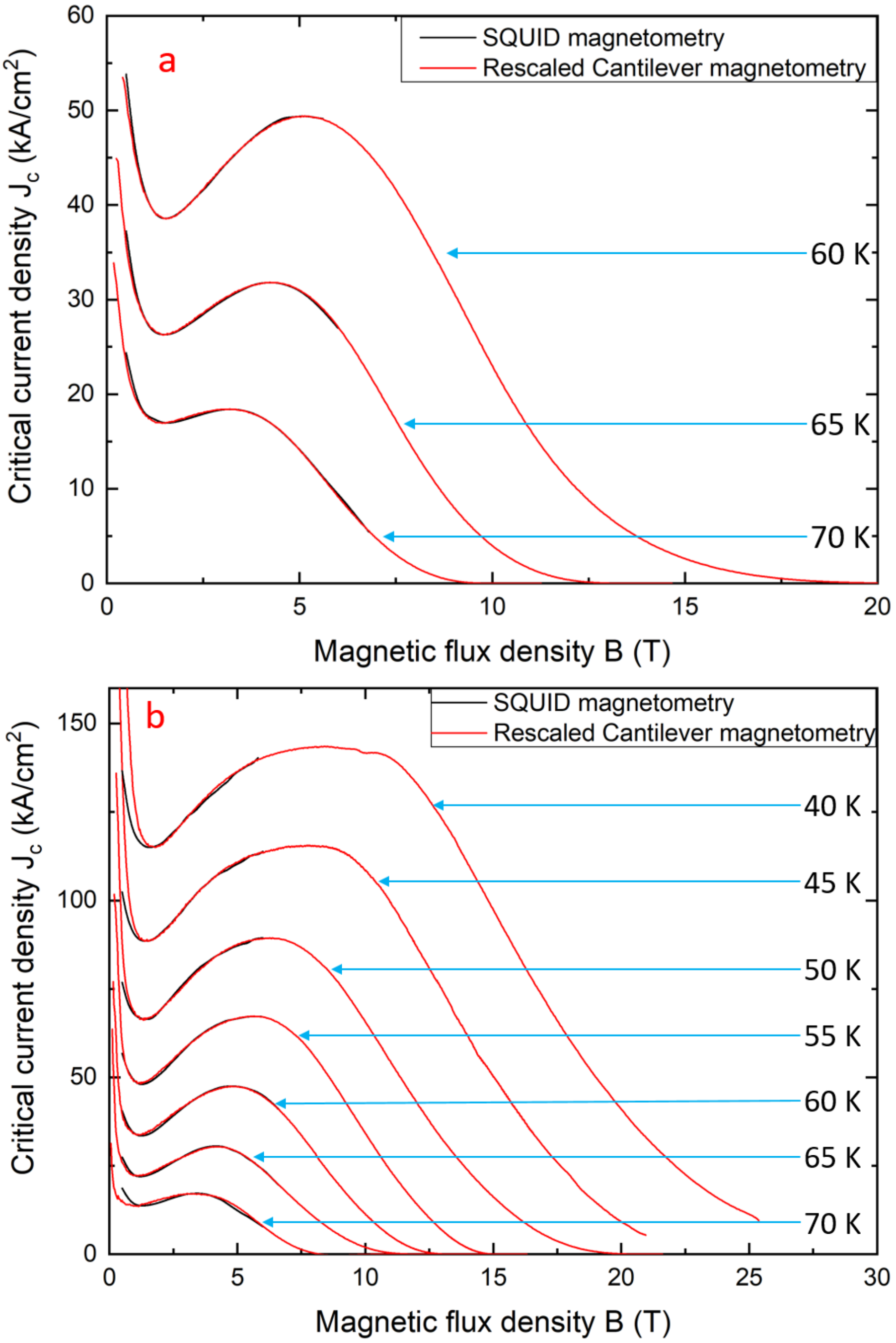

Figure IV-21: Comparison of the critical current density of the relaxed curve measured by SQUID magnetometry and the rescaled high field cantilever magnetometry for the S-45 (a) and S-60 (b) samples.

Temperature	70 K	65 K	60 K	55 K	50 K	45 k	40 K
S-45	9.3 T	12.6 T	19.2 T				
S-60	8.1 T	11.5 T	12.8 T	14.8 T	20 T	21 T	25 T

Table IV-1: Irreversible magnetic flux density B_{irr} of the S-45 and S-60 samples after the rescaling of the high field measurement.

IV.5.e. The critical current density of IG YBaCuO under high fields

As we can see on Figure IV-22 where the critical current of the S-45 and S-60 are presented and compared. The samples S-45 shows better superconducting properties as its critical current density is 7 % larger than of the S-60 at 60 K and 2 T and 2 times higher at 10 T. The same observation can be done with the irreversible magnetic field, higher for the S-45 samples than for the S-60 one. It is interesting to note that the shape of the curve at 60 K of both samples is really different where at higher temperature it's a very similar shape particularly at high fields. This appears not to be linked to a potential bad fitting, as both curves at 60 K are nicely fitting their respective SQUID measurement (see Figure IV-21), it is also supported by the insert of Figure IV-22 where the SQUID measurement of both samples at 60 K are showing a diverging shape above the maximum of the Fishtail.

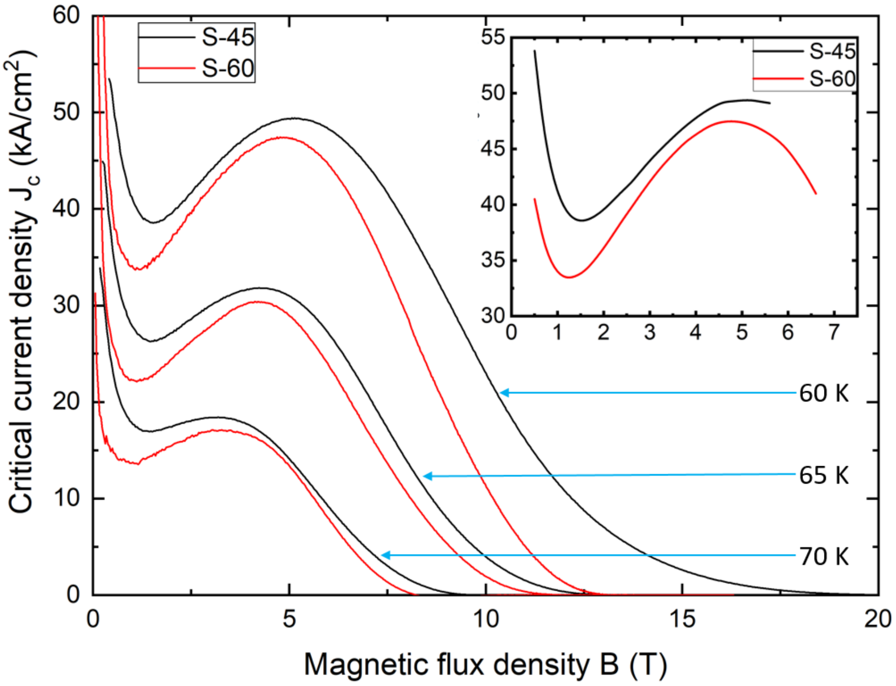

Figure IV-22: Comparison of the rescaled HF critical current density of the S-45 and the S-60 sample for temperatures between 70 to 60 K. The insert is showing the fitted SQUID measurement of both S-45 and S-60 samples at 60 K.

Besides, in the literature there is still no measurement of the *J_c* for superconducting bulks at low temperature as the majority of the equipment (MPMS, PPMS) rarely exceeded 9 T. We can still figure out the performances at 77 K as the one done on a classic TSMG-YBCO made by a company called Can superconductors, a reference for high performance YBCO bulks. Their critical current density is between 10 to 25 kA.cm^{-2} at 77 K and 2 T of background field using a MPMS-SQUID [127]. The same kind of samples were presented as example in section II.2.e with Figure II-16 where I found a *J_c* of 16.7 kA.cm^{-2} for the same temperature and external magnetic field. So, according to the literature and the data I was able to compute, IG YBCO are showing a similar critical current density after ultrasonication process. This highlights the readiness of the IG process associate with ultrasonication.

Also, very interesting is the presence of a Fishtail effect as for the TSMG-YBCO presented in section II.2.e with Figure II-16 which confirms again that fishtail effect can appear nearly in every superconducting material.

IV.6. Computation of the trapped field in IG YBCO

However, it seems that nobody before us were able to measure and evaluate the critical current density of superconducting bulks using HF as high as 33 T and down to 40 K. An experiment on similar samples (IG-YBCO) were done at up to 14 T [120] and exposes a J_c slightly lower than the one found with the S-60 sample at 50 K which should comfort the efficiency of the ultrasonication but according to the precision of the presented work as well as the general precision of a SQUID measurement, the difference isn't so significant.

However, it is not enough to compare the J_c at lower temperature and higher magnetic field. A possible comparison comes with the measurement of the trapped field for a standard cylindrical bulk of 3×1 cm of respective diameter and height which was done with the help of high fields magnets [140], [208]. As we haven't the complete bulk to magnetize, we decided to use a numerical simulation of a high field magnetization by using COMSOL Multiphysics software, then evaluate the trapped field at 40 K under 20 T. For that we compute the trapped field of two bulks supposed perfectly homogeneous and cylindrical (3×1 cm of diameter and height each), stacked together with a negligible distance. We considered the J_c presented above and we used the so called "H-formulation" to compute the electromagnetic quantities [144], [222] for each temperatures. Of course, here we completely neglect the mechanical stress as well as the flux jump potential, the goal is only to compare the computed J_c with other experimental data.

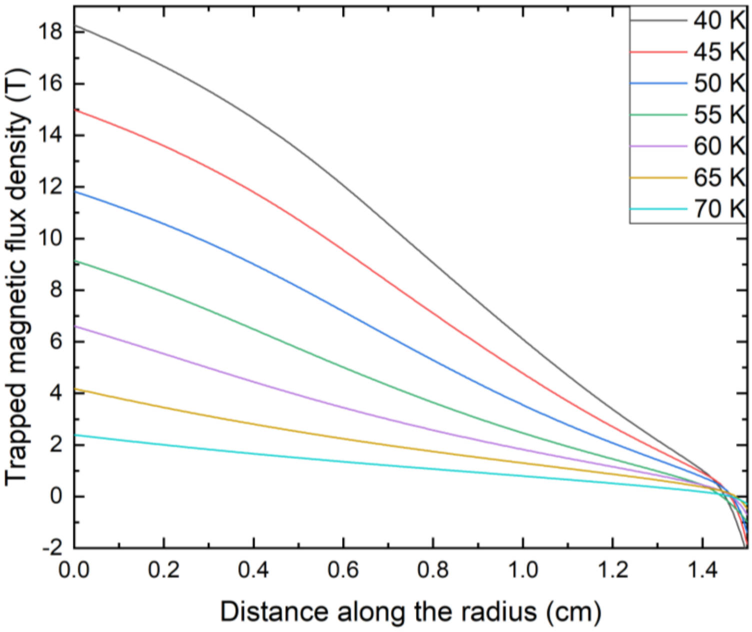

Figure IV-23: Simulation of the axial trapped field B_z between two 3 cm wide and 1 cm height superconducting bulk function of the distance from the sample's center at different temperatures.

The computed trapped field function of the position over the sample radius is shown on Figure IV-23. This shows that, in theory, more than 18 T can be trapped on this kind of IG-YBCO at 40 K which is more than results presented on a paper at a similar temperature [223] or at lower temperature [140], [208]. Of course, according to the approximations on the homogeneity and the absences thermal/mechanical issues our simulation is giving the theoretical maximal trapped field but this however shows that IG YBaCuO can possess competitive superconducting properties for application.

IV.7. Future development using the infiltration Growth process and YBaCuO foams

We have seen that, despite having improving superconducting properties associated with promising methods such as ultrasonication of the precursors Y-211 powder, the IG-YBCO samples I characterized still possess similar superconducting properties.

However, this technique offers many possibilities such as a better shape control as the shape of the sample after the IG process is close to the starting one and we can use different preparation processes on the precursor. This has been done by preparing foam's shape precursors (Figure IV-24.a) with the help of a polyurethane foam used to produce, after infiltration growth process, a superconducting foam (Figure IV-24.b) [97], [209]. This new design allows a very high porosity, a huge advantage for cooling the bulk as the surface in contact with the cooling fluid is much greater than with a classic bulk. Also, for applications when the weight is a central concern such as for space applications, its low density is appreciated and a potential use as permanent magnet with in-situ magnetization for aircraft application or for docking system of satellite is studied [88], [119].

Although, the random size and orientation of the struts, Figure IV-24.c-d, highly limits the generation of a good crystal during the IG process. The consequence is a polycrystal (Figure IV-24.e) with a relatively weak grain boundary and so a limited critical current density as well as irregular performances. Indeed, we determined the magnetization, the critical current density of different samples and the general trapped field profile of a YBaCuO foam [119], [210]. The J_c is about 5.5 kA.cm^{-2} at 60 K and under 1 T in [210] which is much lower than the 34 kA.cm^{-2} of the S-60 sample at 1 T.

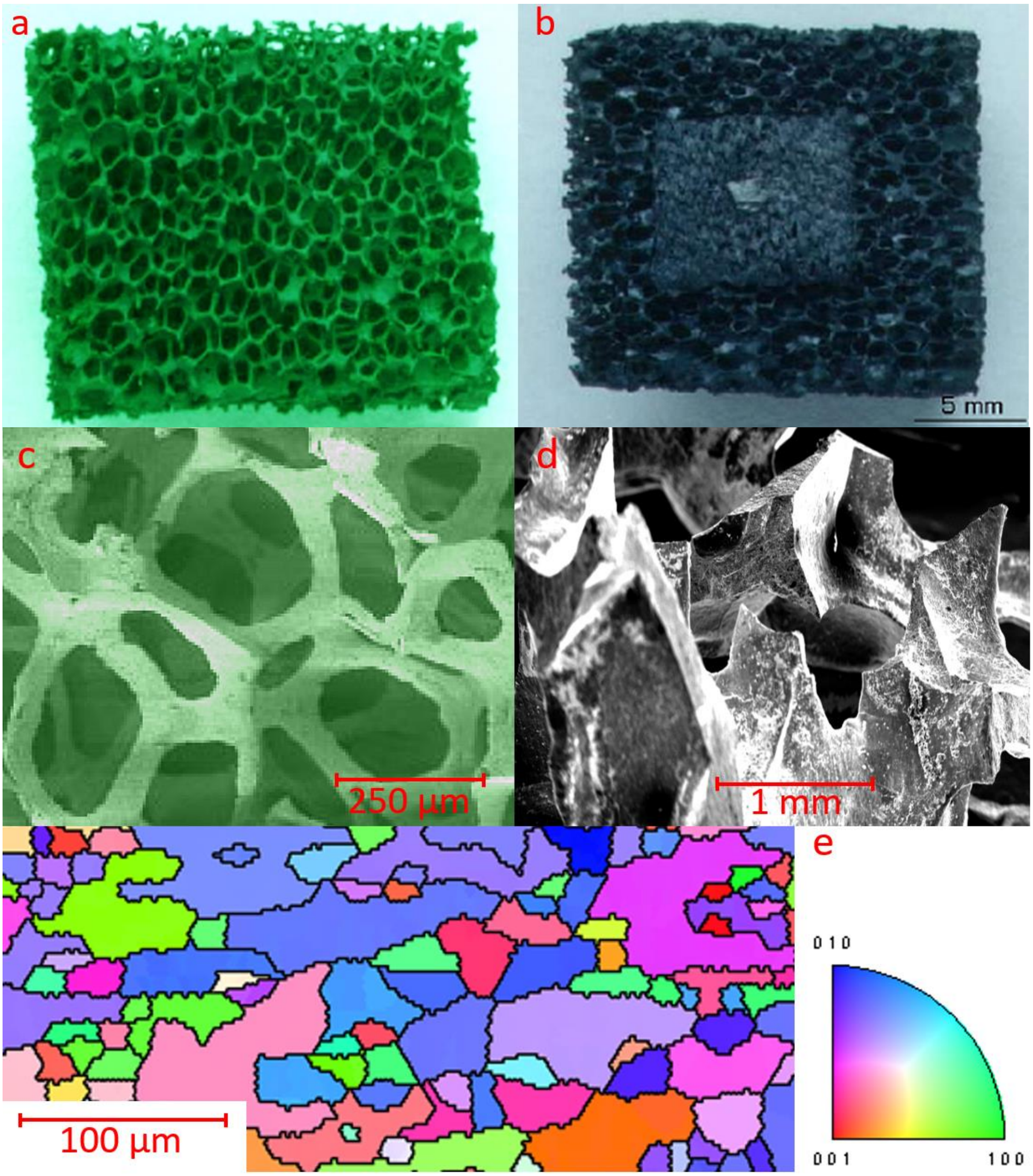

Figure IV-24: Picture of the foam before the Infiltration growth with the Y211 green precursor (a) and after with the superconducting Y123 phase (b). Also, there is a picture done by SEM on the Y211 foam (c) and after the synthesis (d). Finally using SEM-EBSD, an IPF was done on one of the Y123 strut (e) where we can see a random orientation, reporting a polycrystalline nature.

Measurements of the magnetization are shown with Figure IV-25.a between 77 to 60 K. It is expressed in emu.g^{-1} because of the complex shape of the strut used for the measurement which also does not allow to extract the critical current density without a huge approximation on the sample's shape, Figure IV-25.c.

The Figure IV-25.b where the magnetic moment is measured at 85 K, shows a paramagnetic signal present on the sample but weak for lower temperatures. Finally, the insert is highlighting the presence of a weak but existing superconducting hysteresis even at 85 K.

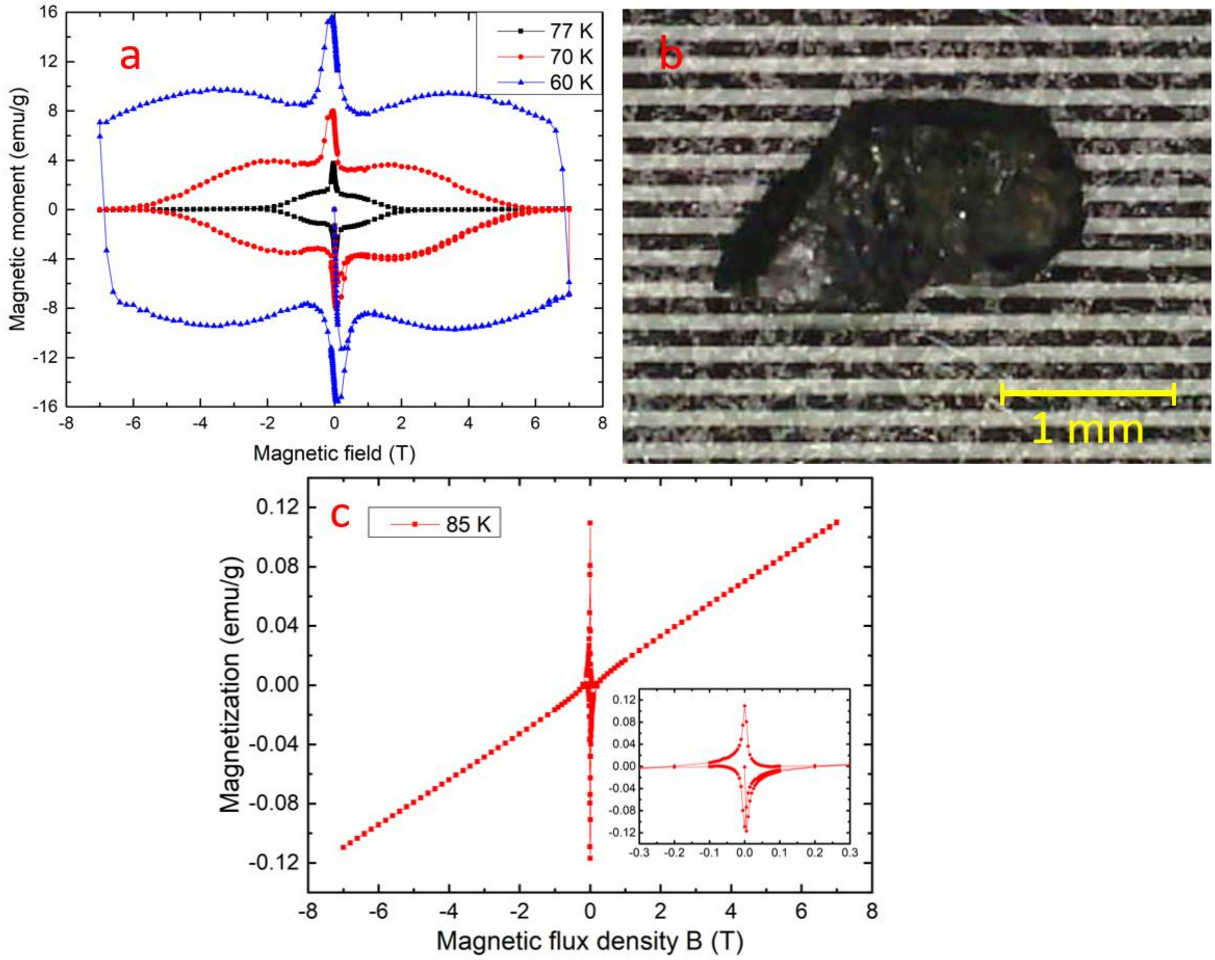

Figure IV-25: Magnetization in emu.g^{-1} of a superconducting strut extracted from the YBaCuO foam for temperature between 77 to 60 K expressed in emu.g^{-1} (a). Those measurement where done with the small strut on the picture (b). The magnetization is also evaluated at 85 K with a visible paramagnetic signal (c). The inert is highlighting the superconducting moment between -0.3 to +0.3 T.

Nevertheless, the magnetization is enough to give an idea of the superconducting properties. So, we can compare it with the ones of the samples prepared with ultrasonication, here the S-60 sample, with its magnetization in emu.g^{-1}, such comparison is presented on Figure IV-26. We can see that the magnetization is lower but not that much: 25 emu.g^{-1} for the S-60 and 16 emu.g^{-1} for the foam at 60 K and self-field. The difference is even larger at 77 K (10 versus 4 emu.g^{-1}). Also, the irreversible magnetic field is lower. Nevertheless, the properties are of the same order of magnitude and we have to underline that the difference of shape and so shape factor may play a role in the difference between those two samples.

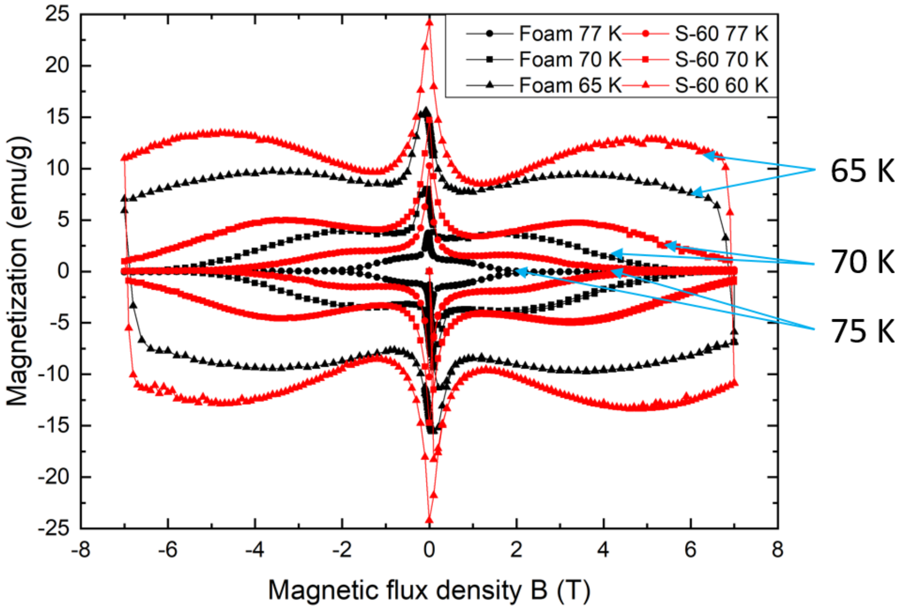

Figure IV-26: Magnetization per gram of the S-60 sample and the foam, both prepared by IG, at 77, 70 and 60 K function of the magnetic field.

Let's make a focus on the trapped field measurement at 77 K of the foam done with a 0.3 T permanent magnet. The result is presented on Figure IV-27 with the measured trapped field 1 cm above the top of the foam on which the magnet was on. We can see that the higher value of trapped field we measured is only 0.023 T which is really low compared to the 0.3 T of the applied field for the FC process. This is partly due to the bad crystal quality, where the superconducting phase is evenly distributed over the sample and the secondary phase Y211 is widely represented. But we can also see huge irregularities in the trapped field profile with multiple "spikes". They are a direct hint of the topology of the foam as the distance between the measurement probe and the struts is varying, sometimes the probe is close to a strut, sometimes the probe is above a hole. So, of course, this also plays a role in the limited trapped field.

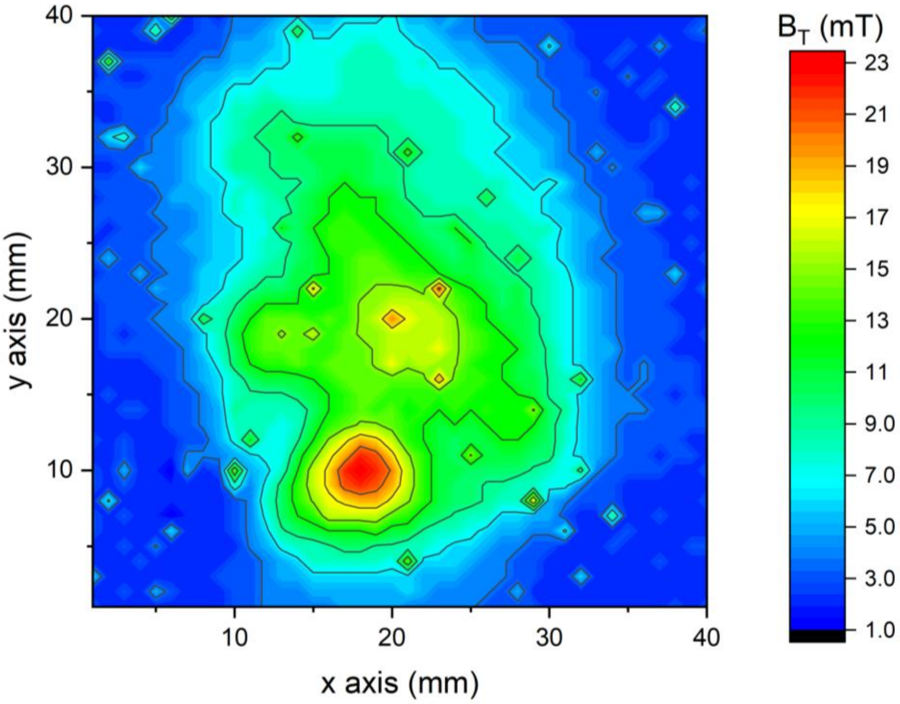

Figure IV-27: Trapped field measurement done on the superconducting foam using a 0.3 T permanent magnet at 77 K. We can see a large irregularity of the trapped field distribution and less than 10 % of the applied field is trapped.

Those problematic properties are now highly restraining the potential use of an HTS superconducting foam in practical applications. But recent development of the 3D printing of ceramics and particularly the work done on 3D printed YBaCuO could allow the synthesis of a new generation of superconducting foam with the Y123 powder to make a polycrystalline YBaCuO [224]–[226]. Or we can bring together a 3D printed green foam/bulk of Y211 powder with an optimized IG process to get the desirable shape or density on a single-crystal or a polycrystal with superconducting grain boundaries.

IV.8. Conclusion

With this chapter, we have seen that force magnetometry, associated with a cantilever and a capacitive measurement, allow a measurement of the critical current density generated by a superconducting sample in a magnetic gradient for various temperature and magnetic fields as high as 33 T.

This was done on a IG-YBaCuO prepared with ultrasonication pre-treatment on the precursor powder but with a constant sweep rate of 33 mT.s^{-1}. This particularity required a deeper study of the samples properties such as the impact of the magnetic field sweep rate on the critical current density J_c and the irreversible magnetic field H_{irr}.

Following this I used a method I developed to rescaled the J_c measured with a constant field sweep rate of 33 mT.s^{-1} on the J_c measured with a stabilized external field.

The result was good enough to be considered convenient for rescaling the HF measurement which has been done with success.

Finally, the evaluation of the J_c under high magnetic field and down to 40 K gives us information about the performances of such material and shows its competitivity with classic melt growth bulks.

So, this study highlights the potential of IG-YBaCuO bulks supported by many innovation and advantages such as using a foam shape or 3D printing. But, also of the cantilever measurement to determine the superconducting properties of small or large size bulks, of course when all the calibrations are properly done first.

Chapter V: General Conclusion

As a first part, a focus on the characterization technique was done either to determine the material such as with the X-ray diffraction or the help of a Scanning Electron or Optic Microscope. But also, the magnetic properties with Magnetic Property Measurement Systems, cantilever magnetometry or trapped field experiments. This allows to clearly define the limits and the precision of each methods I used in order to produce a reliable work and to be able to compare each measurement. With this, the Bean model and its extensions, the Kim's model and the Chen formula [105], [106], [113] have been detailed and used with proper approximations.

Two types of superconducting bulk materials have been studies: the polycrystalline Iron-Selenide, FeSe and the Infiltration Growth YBaCuO compounds.

The polycrystalline FeSe superconductors with the β-FeSe phase is still at its early stage of development and the presence of ferromagnetic α-Fe and ferrimagnetic Fe_7Se_8 secondary phases lead to a focus on the synthesis techniques and the characterization of its phases and magnetic properties.
Two synthesis techniques have been chosen: the classic furnace sintering and the Spark Plasma Sintering. The optimization of the synthesis parameters such as the synthesis and annealing temperatures/durations or the stoichiometry lead to an improvement of the ratio of superconducting magnetic moment against the ferro/ferrimagnetic ones with the classic furnace sintering but still an important of Fe_7Se_8 secondary phase is present.
SPS process was done with in-situ and ex-situ protocols to obtain a fast sintering routine. Due to the low melting temperature of selenium, the in-situ process gives a very weak superconducting magnetic moment but an almost pure β-FeSe phase. The ex-situ process gives a worse ratio of superconducting moment than with furnace sintering.
With this, a comparison between the ratio of the supposed superconducting β-FeSe phase with the ferromagnetic α-Fe phase and the ferrimagnetic Fe_7Se_8 phase and the ratio of their respective magnetic moment support the theory in which superconductivity appears in the β-FeSe only with a deficiency of selenium [32].
Secondary, the superconducting critical current density has been extracted and is 50 $A.cm^{-2}$ at 2 K and under 1 T. To boost this low critical current density, doping FeSe samples with alkali earth elements have been tried but the unstable resulting samples didn't exhibit any amelioration of superconducting properties.
Finally, the observation of important degradation of the superconducting phase into the ferromagnetic and ferrimagnetic one lead to the conclusion that producing a pure superconducting β-FeSe polycrystalline phase is extremely difficult and its instability over time and low superconducting properties make it uncompetitive with other comparable materials such as the MgB_2 produced by very short SPS process [118].

YBaCuO samples prepared by Infiltration Growth and with an ultrasonication treatment on the precursor powder have been characterized under high magnetic field (up to 33 T) and for various temperatures from 77 to 40 K. For this the magnetic force was measured with a cantilever under a constant magnetic field sweep rate of 33 $mT.s^{-1}$ and in a magnetic gradient and the data were rescaled on SQUID measurements done at up to 7 T with no magnetic field sweep rate.

Consequently, we study the impact on the field sweep rate on the critical current density and the irreversible magnetic field and we tested the use of the force magnetometry to determine the superconducting properties.

From the critical current density, we were able to compute a theoretical trapped field of 18 T at 40 K which is similar to the performance of a classic Melt Growth YBaCuO and so gives information about the readiness of YBaCuO prepared by infiltration growth.

To go further with the Infiltration growth method, I presented the characterization of a YBaCuO foam with lower superconducting properties than for the others IG-YBCO partly due to the polycrystalline aspect but encouraging for further investigation such as 3D printing.

More generally, this PhD thesis was focused on the characterization of innovative or new superconducting materials or superconductors with original designs and compared them regarding electrical engineering applications. However, the synthesis, the characterization and the application of new superconductors is done by distinct communities with different skills, objectives and characterization technique. This leads to misunderstanding in the communication: the competitivity of a material is determined by its critical current density, critical temperature measured on small samples and its crystallographic phase purity for material scientists. One the other hand, it's more defined by its readiness for industrial production (low cost, fast and reliable), magnetic performance of large size bulks and reliability over time for engineers. Those differences make the communication sometimes hard and motivate me to work on the synthesis and the characterization of the Iron-Selenide superconductors according to the electrical application needs. This led to the use of a fast and low-cost sintering process for the industrialization, the SPS, a simple material with disponible element, free of rare earth and toxic elements such as the arsenide. And finally, with lots of possible optimization with the alkaline earth doping for a use at 20 K and below 10 T. Despite obtaining limited properties with FeSe, working on each steps of development of a superconducting material and also working on a more developed one with the IG-YBCO bulks give me the opportunity to learn and show the possibilities and limitations of each of those steps.

Nomenclature

Symbol	Unit	Name
α		Constant to compute the radial magnetic field
a	[m]	Sample half width
β	[A^2.m^4]	Constant to compute the critical current density
B	[T]	Magnetic flux density
B_T	[T]	Trapped magnetic flux density
B_r	[T]	Radial component of the magnetic field
B_z	[T]	Axial component of the magnetic field
b	[m]	Sample half length
C	[F]	Capacitance
c	[m]	Sample thickness
ΔC	[F]	Relative capacitance
Δd	[m]	Distance variation
ΔM	[A.m^{-1}], [emu.cm^{-3}]	Thickness of the magnetization hysteresis
ΔT	[K]	Temperature variation
D	[kg.m^{-3}]	Density
d	[m]	Thickness
e	[A.s]	Elementary charge
F_p	[N], [N.m^{-3}]	Pinning force
F_{Lorentz}	[N], [N.m^{-3}]	Lorentz force
f	[T^{-1}]	Constant to compute the ratio of critical current density
g		Constant to compute the ratio of critical current density
θ	[°]	Diffraction angle
θ_{Torque}	[°]	Torque angle
H	[A.m^{-1}]	Magnetic field
H_{c1}	[A.m^{-1}]	First critical magnetic field
H_{c2}	[A.m^{-1}]	Second critical magnetic field
H_p	[A.m^{-1}]	Penetration field
h	[J.s]	Plank constant
I_c	[A]	Critical current
J_c	[A.m^{-2}]	Critical current density
J_e	[A.m^{-2}]	Engineering critical current density
K		Ginzburg–Landau parameter
k	[N.m^{-1}]	Linear elastic coefficient
λ_L	[m]	London penetration length
L	[m]	Sample length
μ_0	[H.m^{-1}]	Vacuum permeability
$\mu_0 M$	[T]	Magnetic polarization
M	[A.m^{-1}], [emu.cm^{-3}], [emu.g^{-1}]	Magnetization

m	[A.m^2], [emu]	Magnetic moment
m_e	[Kg]	Mass of electron
n_s		Number of charge carrier
ξ	[m]	Coherence length
Φ_0	[V.s]	Magnetic flux quantum
V	[V]	Voltage
V_B	[T.s^{-1}], [mT.s^{-1}]	Magnetic flux density sweep rate
R_1		Ratio of critical current densities
R_2		Ratio of magnetic flux densities
T	[K]	Temperature
W	[m]	Sample width

Bibliography

[1] R. Abd-shukor, *ASM Inaugural Lecture 2009 High Temperature Superconductors: Materials, Mechanisms and Applications*. Percetakan J. R., 2009.

[2] P. Mangin and R. Kahn, *Superconductivity: An introduction*. Springer International Publishing, 2017. doi: 10.1007/978-3-319-50527-5.

[3] N. E. Phillips, *Heat Capacity of Aluminum between 0.1°K and 4.0°K*, Phys. Rev., vol. 114, no. 3, pp. 676–685, May 1959, doi: 10.1103/PhysRev.114.676.

[4] A. A. Abrikosov, *Nobel Lecture: Type-II superconductors and the vortex lattice*, Rev. Mod. Phys., vol. 76, no. 3, pp. 975–979, Dec. 2004, doi: 10.1103/RevModPhys.76.975.

[5] K. Berger, *Etude des phénomènes couplés magnétothermiques dans les Supraconducteurs à Haute Température*, phdthesis, Université Henri Poincaré - Nancy 1, 2006.

[6] P. Ray, *Structural investigation of La(2-x)Sr(x)CuO(4+y) - Following staging as a function of temperature*, 2015.

[7] T. Benkel *et al.*, *REBCO Performance at High Field With Low Incident Angle and Preliminary Tests for a 10-T Insert*, IEEE Trans. Appl. Supercond., vol. 26, no. 3, pp. 1–5, Apr. 2016, doi: 10.1109/TASC.2016.2540158.

[8] L. Kopera, P. Kováč, I. Hušek, and T. Melišek, *Rutherford cable made of single-core MgB_2 wires*, Supercond. Sci. Technol., vol. 26, no. 12, p. 125007, Dec. 2013, doi: 10.1088/0953-2048/26/12/125007.

[9] P. Kov c *et al.*, *Magnetic interaction of an iron sheath with a superconductor*, Supercond. Sci. Technol., vol. 16, no. 10, pp. 1195–1201, Oct. 2003, doi: 10.1088/0953-2048/16/10/312.

[10] W. Borchardt-Ott, Ed., *Crystallography*, 2nd ed. Berlin Heidelberg: Springer-Verlag, 1995. doi: 10.1007/978-3-642-57754-3.

[11] E. W. Abel, Ed., *Metallic and ionic bonding*, in *Tutorial Chemistry Texts*, Cambridge: Royal Society of Chemistry, 2007, pp. 145–166. doi: 10.1039/9781847551955-00145.

[12] E. W. Abel, Ed., *Covalent bonding I: The dihydrogen molecule-ion, $H2^+$, and the dihydrogen molecule*, in *Tutorial Chemistry Texts*, Cambridge: Royal Society of Chemistry, 2007, pp. 34–58. doi: 10.1039/9781847551955-00034.

[13] C. Kittel, *Introduction to solid state physics*, 8th ed. Hoboken, NJ: Wiley, 2005.

[14] B. A. Averill, *12.4: Defects in Crystals*, *Chemistry LibreTexts*, Nov. 24, 2013.

[15] A. G. Bhagurkar, A. Yamamoto, N. H. Babu, J. H. Durrell, A. R. Dennis, and D. A. Cardwell, *Synthesis of dense bulk MgB_2 by an infiltration and growth process*, Supercond. Sci. Technol., vol. 28, no. 1, p. 015012, Jan. 2015, doi: 10.1088/0953-2048/28/1/015012.

[16] A. Galluzzi, M. Polichetti, K. Buchkov, E. Nazarova, D. Mancusi, and S. Pace, *Evaluation of the intragrain critical current density in a multidomain FeSe crystal by means of dc magnetic measurements*, Supercond. Sci. Technol., vol. 28, no. 11, p. 115005, Sep. 2015, doi: 10.1088/0953-2048/28/11/115005.

[17] Y. Cui, X. Wang, P. Li, Y. Chen, and Y. Zhao, *Effect of the FeSe Precursor on the Superconductivity of KxFe2–ySe2*, J. Supercond. Nov. Magn., vol. 29, no. 11, pp. 2771–2775, Nov. 2016, doi: 10.1007/s10948-016-3606-z.

[18] M. Muralidhar, K. Furutani, D. Kumar, M. R. Koblischka, M. S. R. Rao, and M. Murakami, *Improved critical current densities in bulk FeSe superconductor using ball milled powders and high temperature sintering*, Phys. Status Solidi A, vol. 213, no. 12, pp. 3214–3220, 2016, doi: 10.1002/pssa.201600299.

[19] T. D. Dzhafarov, H. Cömert, M. Altunbaş, Ü. Alver, T. Küçükömeroğlu, and A. İ. Kopya, *Diffusion of Ag in Bi(Pb)-Sr-Ca-Cu-O superconductors*, J. Alloys Compd., vol. 221, no. 1–2, pp. 264–266, Apr. 1995, doi: 10.1016/0925-8388(94)01472-8.

[20] T. D. Dzhafarov, M. Altunbaş, A. Varilci, and T. Küçükömeroğlu, *The effect of Au diffusion on structural and superconducting properties of YBaCuO*, Mater. Lett., vol. 25, no. 3–4, pp. 81–86, Nov. 1995, doi: 10.1016/0167-577X(95)00141-7.

[21] M. Eisterer *et al.*, *Neutron irradiation of MgB $_2$ bulk superconductors*, Supercond. Sci. Technol., vol. 15, no. 2, pp. L9–L12, Feb. 2002, doi: 10.1088/0953-2048/15/2/101.

[22] R. V. Vovk, G. Ya. Khadzhai, and O. V. Dobrovolskiy, *Effect of electron irradiation and Pr doping on the charge transport in YBCO single crystals*, Solid State Commun., vol. 282, pp. 5–8, Oct. 2018, doi: 10.1016/j.ssc.2018.07.005.

[23] H. W. Weber, *Irradiation Damage in Superconductors*, in *Advances in Cryogenic Engineering Materials*, R. P. Reed and A. F. Clark, Eds. Boston, MA: Springer US, 1986, pp. 853–864. doi: 10.1007/978-1-4613-9871-4_102.

[24] L. Civale, *Vortex pinning and creep in high-temperature superconductors with columnar defects*, Supercond. Sci. Technol., vol. 10, no. 7A, pp. A11–A28, Jul. 1997, doi: 10.1088/0953-2048/10/7A/003.

[25] M. D. Ainslie *et al.*, *Numerical modelling of mechanical stresses in bulk superconductor magnets with and without mechanical reinforcement*, Supercond. Sci. Technol., vol. 32, no. 3, p. 034002, Mar. 2019, doi: 10.1088/1361-6668/aaf851.

[26] D. K. Namburi *et al.*, *Pulsed-field magnetisation of Y-Ba-Cu-O bulk superconductors fabricated by the infiltration growth technique*, Supercond. Sci. Technol., vol. 33, no. 11, p. 115012, Oct. 2020, doi: 10.1088/1361-6668/abb590.

[27] T. P. Ying *et al.*, *Observation of superconductivity at 30~46K in AxFe2Se2 (A = Li, Na, Ba, Sr, Ca, Yb and Eu)*, Sci. Rep., vol. 2, no. 1, Art. no. 1, May 2012, doi: 10.1038/srep00426.

[28] S. Jin *et al.*, *Two new parent compounds for FeSe-based superconducting phases*, ArXiv160701103 Cond-Mat, Jul. 2016, Accessed: Apr. 27, 2021. [Online]. Available: http://arxiv.org/abs/1607.01103

[29] G. R. Stewart, *Superconductivity in iron compounds*, Rev. Mod. Phys., vol. 83, no. 4, pp. 1589–1652, Dec. 2011, doi: 10.1103/RevModPhys.83.1589.

[30] Y. Zhao, C. H. Cheng, and J. S. Wang, *Roles of silver doping on joins and grain boundaries of melt-textured YBCO superconductor*, Supercond. Sci. Technol., vol. 18, no. 2, pp. S34–S37, Feb. 2005, doi: 10.1088/0953-2048/18/2/008.

[31] H. Salamati, A. A. Babaei-Brojeny, and M. Safa, *Investigation of weak links and the role of silver addition on YBCO superconductors*, Supercond. Sci. Technol., vol. 14, no. 10, pp. 816–819, Oct. 2001, doi: 10.1088/0953-2048/14/10/302.

[32] K.-W. Lee, V. Pardo, and W. E. Pickett, *Magnetism driven by anion vacancies in superconducting* α *-FeSe 1 − x*, Phys. Rev. B, vol. 78, no. 17, p. 174502, Nov. 2008, doi: 10.1103/PhysRevB.78.174502.

[33] J. L. Routbort and S. J. Rothman, *Oxygen diffusion in cuprate superconductors*, J Appl Phys, vol. 76, no. 10, p. 15, 1994.

[34] J. S. Higgins, Y. Dagan, M. C. Barr, B. D. Weaver, and R. L. Greene, *Role of oxygen in the electron-doped superconducting cuprates*, Phys. Rev. B, vol. 73, no. 10, p. 104510, Mar. 2006, doi: 10.1103/PhysRevB.73.104510.

[35] T. Yagi, M. Domon, Y. Okajima, and K. Yamaya, *Effect of oxygen deficiency on the normal and superconducting properties of CaLaBaCu3Oy*, Phys. C Supercond., vol. 173, no. 5, pp. 453–457, février 1991, doi: 10.1016/0921-4534(91)90747-M.

[36] A. Erb, J.-Y. Genoud, F. Marti, M. Daumling, E. Walker, and R. Flükiger, *Reversible Suppression of the so-called Fishtail Effect in ultra pure Single Crystals of YBa2Cu307_~ achieved by proper Oxygenation*, J. Low Temp. Phys., vol. 105, no. 314, p. 6, 1996.

[37] M. Suyama, S. Pyon, Y. Iijima, S. Awaji, and T. Tamegai, *Trapping a magnetic field of 17.89 T in stacked coated conductors by suppression of flux jumps*, Supercond. Sci. Technol., vol. 35, no. 2, p. 02LT01, Feb. 2022, doi: 10.1088/1361-6668/ac4560.

[38] M. Murakami, *Processing of bulk YBaCuO*, Supercond. Sci. Technol., vol. 5, no. 4, pp. 185–203, Apr. 1992, doi: 10.1088/0953-2048/5/4/001.

[39] Q. Nouailhetas *et al.*, *Magnetic phases in superconducting, polycrystalline bulk FeSe samples*, AIP Adv., vol. 11, no. 1, p. 015230, Jan. 2021, doi: 10.1063/9.0000167.

[40] A. Koblischka-Veneva, M. r. Koblischka, J. Schmauch, J. Noudem, and M. Murakami, *Analysis of the microstructure of bulk MgB2 using TEM, EBSD and t-EBSD*, J. Microsc., vol. 274, no. 3, pp. 123–131, 2019, doi: 10.1111/jmi.12790.

[41] D. M. Gokhfeld, *An extended critical state model: Asymmetric magnetization loops and field dependence of the critical current of superconductors*, Phys. Solid State, vol. 56, no. 12, pp. 2380–2386, Dec. 2014, doi: 10.1134/S1063783414120129.

[42] A. Galluzzi, M. Polichetti, K. Buchkov, E. Nazarova, D. Mancusi, and S. Pace, *Critical current and flux dynamics in Ag-doped FeSe superconductor*, Supercond. Sci. Technol., vol. 30, no. 2, p. 025013, Feb. 2017, doi: 10.1088/1361-6668/30/2/025013.

[43] J. E. Evetts and B. A. Glowacki, *Relation of critical current irreversibility to trapped flux and microstructure in polycrystalline YBazCu3OT*, p. 9.

[44] E. Zeldov *et al.*, *Geometrical Barriers in High-Temperature Superconductors*, Phys. Rev. Lett., vol. 73, no. 10, pp. 1428–1431, Sep. 1994, doi: 10.1103/PhysRevLett.73.1428.

[45] D. Gokhfeld, *Critical current density and trapped field in HTS with asymmetric magnetization loops*, J. Phys. Conf. Ser., vol. 695, p. 012008, Mar. 2016, doi: 10.1088/1742-6596/695/1/012008.

[46] D. M. Gokhfeld, D. A. Balaev, M. I. Petrov, S. I. Popkov, K. A. Shaykhutdinov, and V. V. Val'kov, *Magnetization asymmetry of type-II superconductors in high magnetic fields*, J. Appl. Phys., vol. 109, no. 3, p. 033904, Feb. 2011, doi: 10.1063/1.3544038.

[47] D. Boussard *et al.*, *The LHC superconducting cavities*, in, Mar. 1999, vol. 2, pp. 946–948 vol.2. doi: 10.1109/PAC.1999.795409.

[48] L. Rossi, *The LHC superconducting magnets*, in, May 2003, vol. 1, pp. 141-145 Vol.1. doi: 10.1109/PAC.2003.1288863.

[49] N. Mitchell, A. Devred, P. Libeyre, B. Lim, and F. Savary, *The ITER Magnets: Design and Construction Status*, IEEE Trans. Appl. Supercond., vol. 22, no. 3, pp. 4200809–4200809, Jun. 2012, doi: 10.1109/TASC.2011.2174560.

[50] J. L. Duchateau, J. Y. Journeaux, and B. Gravil, *Tore Supra Superconducting Toroidal Magnetic Field System*, Fusion Sci. Technol., vol. 56, no. 3, pp. 1092–1123, Oct. 2009, doi: 10.13182/FST09-A9170.

[51] W. Abdel Maksoud *et al.*, *Results of the first JT-60 SA toroidal field coils tests in the cold test facility*, Fusion Eng. Des., vol. 124, pp. 14–17, Nov. 2017, doi: 10.1016/j.fusengdes.2017.02.009.

[52] Z. Melhem *et al.*, *High Temperature Superconducting (HTS) Coils for a Compact Spherical Tokamak*, IEEE Trans. Appl. Supercond., vol. 25, no. 3, pp. 1–4, Jun. 2015, doi: 10.1109/TASC.2014.2375512.

[53] K. Kim *et al.*, *Status of the KSTAR superconducting magnet system development*, Nucl. Fusion, vol. 45, no. 8, pp. 783–789, Aug. 2005, doi: 10.1088/0029-5515/45/8/003.

[54] T. Rummel *et al.*, *The Superconducting Magnet System of the Stellarator Wendelstein 7-X*, IEEE Trans. Plasma Sci., vol. 40, no. 3, pp. 769–776, Mar. 2012, doi: 10.1109/TPS.2012.2184774.

[55] T. Satow *et al.*, *Results on the superconducting magnet system for the Large Helical Device*, IEEE Trans. Appl. Supercond., vol. 10, no. 1, pp. 600–605, Mar. 2000, doi: 10.1109/77.828306.

[56] M. Parizh, Y. Lvovsky, and M. Sumption, *Conductors for commercial MRI magnets beyond NbTi: requirements and challenges*, Supercond. Sci. Technol., vol. 30, no. 1, p. 014007, Jan. 2017, doi: 10.1088/0953-2048/30/1/014007.

[57] S. Awaji *et al.*, *Field Stability Analysis of 25 T Cryogen-Free Superconducting Magnet and Upgrade Plans for 30 T System at HFLSM, IMR, Tohoku University*, IEEE Trans. Appl. Supercond., vol. 29, no. 5, pp. 1–5, Aug. 2019, doi: 10.1109/TASC.2019.2898699.

[58] N. Mitchell, *Analysis of the effect of Nb3Sn strand bending on CICC superconductor performance*, Cryogenics, vol. 42, no. 5, pp. 311–325, May 2002, doi: 10.1016/S0011-2275(02)00041.

[59] C. Adolphsen *et al.*, *The International Linear Collider Technical Design Report - Volume 3.I: Accelerator R&D in the Technical Design Phase*, ArXiv13066353 Phys., Jun. 2013, Accessed: Nov. 10, 2021. [Online]. Available: http://arxiv.org/abs/1306.6353

[60] D. U. Gubser, *Superconducting homopolar motor and conductor development*, JOM, vol. 48, no. 10, pp. 30–34, Oct. 1996, doi: 10.1007/BF03223098.

[61] P. Masson, J. Leveque, D. Netter, and A. Rezzoug, *Experimental study of a new kind of superconducting inductor*, IEEE Trans. Appl. Supercond., vol. 13, no. 2, pp. 2239–2242, Jun. 2003, doi: 10.1109/TASC.2003.813055.

[62] M. K. Wu *et al.*, *Superconductivity at 93 K in a new mixed-phase Y-Ba-Cu-O compound system at ambient pressure*, Phys. Rev. Lett., vol. 58, no. 9, pp. 908–910, Mar. 1987, doi: 10.1103/PhysRevLett.58.908.

[63] H. Maeda, Y. Tanaka, M. Fukutomi, and T. Asano, *A New High-Tc Oxide Superconductor without a Rare Earth Element*, Jpn. J. Appl. Phys., vol. 27, no. 2A, p. L209, Feb. 1988, doi: 10.1143/JJAP.27.L209.

[64] M. Moyzykh *et al.*, *First Russian 220 kV Superconducting Fault Current Limiter (SFCL) For Application in City Grid*, IEEE Trans. Appl. Supercond., vol. 31, no. 5, pp. 1–7, Aug. 2021, doi: 10.1109/TASC.2021.3066324.

[65] G. B. Huang, B. Douine, K. Berger, G. Didier, I. Schwenker, and J. Lévêque, *Increase of Stability Margin in Embedded DC Electric Grid With Superconducting Stabilizer*, IEEE Trans. Appl. Supercond., vol. 26, no. 4, pp. 1–4, Jun. 2016, doi: 10.1109/TASC.2016.2543963.

[66] J. Bock, A. Hobl, J. Schramm, S. Krämer, and C. Jänke, *Resistive Superconducting Fault Current Limiters Are Becoming a Mature Technology*, IEEE Trans. Appl. Supercond., vol. 25, no. 3, pp. 1–4, Jun. 2015, doi: 10.1109/TASC.2014.2364916.

[67] F. Trillaud, B. Douine, and L. Quéval, *Superconducting Power Filter for Aircraft Electric DC Grids*, IEEE Trans. Appl. Supercond., vol. 31, no. 5, pp. 1–5, Aug. 2021, doi: 10.1109/TASC.2021.3060682.

[68] M. Tomita, K. Suzuki, Y. Fukumoto, A. Ishihara, T. Akasaka, and Y. Kobayashi, *Energy-saving railway systems based on superconducting power transmission*, Energy, vol. 122, pp. 579–587, Mar. 2017, doi: 10.1016/j.energy.2017.01.099.

[69] H. Yumura *et al.*, *Update of YOKOHAMA HTS Cable Project*, IEEE Trans. Appl. Supercond., vol. 23, no. 3, pp. 5402306–5402306, Jun. 2013, doi: 10.1109/TASC.2013.2245931.

[70] M. Stemmle, F. Merschel, M. Noe, and A. Hobl, *AmpaCity — Advanced superconducting medium voltage system for urban area power supply*, in, Apr. 2014, pp. 1–5. doi: 10.1109/TDC.2014.6863566.

[71] K.-P. Weiss, W. H. Fietz, M. Heiduk, C. Lange, A. Preuß, and M. J. Wolf, *Development and test of a 35 kA - HTS CroCo cable demonstrator*, J. Phys. Conf. Ser., vol. 1559, p. 012082, Jun. 2020, doi: 10.1088/1742-6596/1559/1/012082.

[72] V. E. Sytnikov *et al.*, *The 5 m HTS Power Cable Development and Test*, IEEE Trans. Appl. Supercond., vol. 17, no. 2, pp. 1684–1687, Jun. 2007, doi: 10.1109/TASC.2007.899980.

[73] G. Hajiri, K. Berger, R. Dorget, J. Lévêque, and H. Caron, *Thermal and Electromagnetic Design of DC HTS Cables for the Future French Railway Network*, IEEE Trans. Appl. Supercond., vol. 31, no. 5, pp. 1–8, Aug. 2021, doi: 10.1109/TASC.2021.3059598.

[74] J. Ciceron, A. Badel, P. Tixador, and F. Forest, *Design Considerations for High-Energy Density SMES*, IEEE Trans. Appl. Supercond., vol. 27, no. 4, pp. 1–5, Jun. 2017, doi: 10.1109/TASC.2017.2655627.

[75] W. Yuan *et al.*, *Design and Test of a Superconducting Magnetic Energy Storage (SMES) Coil*, IEEE Trans. Appl. Supercond., vol. 20, no. 3, pp. 1379–1382, Jun. 2010, doi: 10.1109/TASC.2010.2041201.

[76] A. Colle, T. Lubin, S. Ayat, O. Gosselin, and J. Leveque, *Test of a Flux Modulation Superconducting Machine for Aircraft*, J. Phys. Conf. Ser., vol. 1590, p. 012052, Jul. 2020, doi: 10.1088/1742-6596/1590/1/012052.

[77] A. Colle, T. Lubin, S. Ayat, O. Gosselin, and J. Lévêque, *Analytical Model for the Magnetic Field Distribution in a Flux Modulation Superconducting Machine*, IEEE Trans. Magn., vol. 55, no. 12, pp. 1–9, Dec. 2019, doi: 10.1109/TMAG.2019.2935696.

[78] R. Dorget, T. Lubin, S. Ayat, and J. Lévêque, *3-D Semi-Analytical Model of a Superconducting Axial Flux Modulation Machine*, IEEE Trans. Magn., vol. 57, no. 11, pp. 1–15, Nov. 2021, doi: 10.1109/TMAG.2021.3108632.

[79] M. Miki *et al.*, *Development of a synchronous motor with Gd–Ba–Cu–O bulk superconductors as pole-field magnets for propulsion system*, Supercond. Sci. Technol., vol. 19, no. 7, pp. S494–S499, Jul. 2006, doi: 10.1088/0953-2048/19/7/S14.

[80] Z. Huang, M. Zhang, W. Wang, and T. A. Coombs, *Trial Test of a Bulk-Type Fully HTS Synchronous Motor*, IEEE Trans. Appl. Supercond., vol. 24, no. 3, pp. 1–5, Jun. 2014, doi: 10.1109/TASC.2013.2296142.

[81] F. Grilli *et al.*, *Superconducting motors for aircraft propulsion: the Advanced Superconducting Motor Experimental Demonstrator project*, J. Phys. Conf. Ser., vol. 1590, no. 1, p. 012051, Jul. 2020, doi: 10.1088/1742-6596/1590/1/012051.

[82] G. Snitchler, B. Gamble, and S. S. Kalsi, *The performance of a 5 MW high temperature superconductor ship propulsion motor*, IEEE Trans. Appl. Supercond., vol. 15, no. 2, pp. 2206–2209, Jun. 2005, doi: 10.1109/TASC.2005.849613.

[83] T. Winkler and EcoSwing Consortium, *The EcoSwing Project*, IOP Conf. Ser. Mater. Sci. Eng., vol. 502, p. 012004, Apr. 2019, doi: 10.1088/1757-899X/502/1/012004.

[84] Z. Deng *et al.*, *A High-Temperature Superconducting Maglev Ring Test Line Developed in Chengdu, China*, IEEE Trans. Appl. Supercond., vol. 26, no. 6, pp. 1–8, Sep. 2016, doi: 10.1109/TASC.2016.2555921.

[85] H.-W. Lee, K.-C. Kim, and J. Lee, *Review of maglev train technologies*, IEEE Trans. Magn., vol. 42, no. 7, pp. 1917–1925, Jul. 2006, doi: 10.1109/TMAG.2006.875842.

[86] M. Ono, S. Koga, and H. Ohtsuki, *Japan's superconducting Maglev train*, IEEE Instrum. Meas. Mag., vol. 5, no. 1, pp. 9–15, Mar. 2002, doi: 10.1109/5289.988732.

[87] R. Dorget *et al.*, *Review on the Use of Superconducting Bulks for Magnetic Screening in Electrical Machines for Aircraft Applications*, Materials, vol. 14, no. 11, Art. no. 11, Jan. 2021, doi: 10.3390/ma14112847.

[88] M. R. Koblischka *et al.*, *Flux Pinning Docking Interfaces in Satellites Using Superconducting Foams as Trapped Field Magnets*, IEEE Trans. Appl. Supercond., vol. 32, no. 4, pp. 1–5, Jun. 2022, doi: 10.1109/TASC.2022.3147734.

[89] Y. Takahashi, T. Naito, T. Nakamura, and M. Takahashi, *Detection of ^{1} H NMR signal in a trapped magnetic field of a compact tubular MgB_2 superconductor bulk*, Supercond. Sci. Technol., vol. 34, no. 6, p. 06LT02, Jun. 2021, doi: 10.1088/1361-6668/abf66e.

[90] J. Nagamatsu, N. Nakagawa, T. Muranaka, Y. Zenitani, and J. Akimitsu, *Superconductivity at 39 K in magnesium diboride*, Nature, vol. 410, no. 6824, Art. no. 6824, Mar. 2001, doi: 10.1038/35065039.

[91] Z. Q. Ma and Y. C. Liu, *Low-temperature synthesis of MgB_2 superconductors*, Int. Mater. Rev., vol. 56, no. 5–6, pp. 267–286, Nov. 2011, doi: 10.1179/1743280411Y.0000000002.

[92] M. Eisterer, J. Emhofer, S. Sorta, M. Zehetmayer, and H. W. Weber, *Connectivity and critical currents in polycrystalline MgB_2*, Supercond. Sci. Technol., vol. 22, no. 3, p. 034016, Mar. 2009, doi: 10.1088/0953-2048/22/3/034016.

[93] A. Yamamoto, A. Ishihara, M. Tomita, and K. Kishio, *Permanent magnet with MgB_2 bulk superconductor*, Appl. Phys. Lett., vol. 105, no. 3, p. 032601, Jul. 2014, doi: 10.1063/1.4890724.

[94] J. H. Durrell *et al.*, *Bulk superconductors: a roadmap to applications*, Supercond. Sci. Technol., vol. 31, no. 10, p. 103501, Oct. 2018, doi: 10.1088/1361-6668/aad7ce.

[95] Y. Iwasea, J. Bascunan, S.-Y. Hahn, and W. Yao, *High-temperature superconductors for NMR/MRI magnets:opportunities and challenges*, Prog. Supercond. Cryog., vol. 11, no. 4, pp. 1–7, 2009.

[96] M. Tomsic *et al.*, *Overview of MgB2 Superconductor Applications*, Int. J. Appl. Ceram. Technol., vol. 4, no. 3, pp. 250–259, 2007, doi: 10.1111/j.1744-7402.2007.02138.x.

[97] E. S. Reddy and G. J. Schmitz, *Superconducting foams*, Supercond. Sci. Technol., vol. 15, no. 8, pp. L21–L24, Jun. 2002, doi: 10.1088/0953-2048/15/8/101.

[98] *Materials Characterization de Yang Leng - Livre électronique | Scribd.*

[99] M. Dunlap and J. E. Adaskaveg, *Introduction to the Scanning Electron Microscope*. the Facility for Advanced Instrumentation: U. C. Davis, 1997.

[100] W. Zhou and Z. L. Wang, Eds., *Scanning microscopy for nanotechnology: techniques and applications*. New York: Springer, 2007.

[101] J. L. Smith *et al.*, *Low-temperature critical field of YBCO*, J. Supercond., vol. 7, no. 2, pp. 269–270, Apr. 1994, doi: 10.1007/BF00724550.

[102] T. Sekitani, N. Miura, S. Ikeda, Y. H. Matsuda, and Y. Shiohara, *Upper critical field for optimally-doped YBa2Cu3O7–δ*, Phys. B Condens. Matter, vol. 346–347, pp. 319–324, Apr. 2004, doi: 10.1016/j.physb.2004.01.098.

[103] T. Karwoth *et al.*, *Electrotransport and magnetic measurements on bulk FeSe superconductors*, J. Phys. Conf. Ser., vol. 1054, p. 012018, Jul. 2018, doi: 10.1088/1742-6596/1054/1/012018.

[104] S. Pavan Kumar Naik, M. Miryala, M. R. Koblischka, A. Koblischka-Veneva, T. Oka, and M. Murakami, *Production of Sharp-Edged and Surface-Damaged Y2BaCuO5 by Ultrasound: Significant Improvement of Superconducting Performance of Infiltration Growth-Processed YBa2Cu3O7–δ Bulk Superconductors*, ACS Omega, vol. 5, no. 12, pp. 6250–6259, Mar. 2020, doi: 10.1021/acsomega.9b02816.

[105] C. P. Bean, *Magnetization of Hard Superconductors*, Phys. Rev. Lett., vol. 8, no. 6, pp. 250–253, Mar. 1962, doi: 10.1103/PhysRevLett.8.250.

[106] C. P. Bean, *Magnetization of High-Field Superconductors*, Rev. Mod. Phys., vol. 36, no. 1, pp. 31–39, Jan. 1964, doi: 10.1103/RevModPhys.36.31.

[107] Y. B. Kim, C. F. Hempstead, and A. R. Strnad, *Critical Persistent Currents in Hard Superconductors*, Phys. Rev. Lett., vol. 9, no. 7, pp. 306–309, Oct. 1962, doi: 10.1103/PhysRevLett.9.306.

[108] Y. B. Kim, C. F. Hempstead, and A. R. Strnad, *Magnetization and Critical Supercurrents*, Phys. Rev., vol. 129, no. 2, pp. 528–535, Jan. 1963, doi: 10.1103/PhysRev.129.528.

[109] W. A. Fietz, M. R. Beasley, J. Silcox, and W. W. Webb, *Magnetization of Superconducting Nb-25%Zr Wire*, Phys. Rev., vol. 136, no. 2A, pp. A335–A345, Oct. 1964, doi: 10.1103/PhysRev.136.A335.

[110] W. I. Dunn and P. Hlawiczka, *Generalized critical-state model of type II superconductors*, J. Phys. Appl. Phys., vol. 1, no. 11, pp. 1469–1476, Nov. 1968, doi: 10.1088/0022-3727/1/11/311.

[111] J. A. Hulbert, *Magnetization of a cylindrical hard superconductor*, Br. J. Appl. Phys., vol. 16, no. 11, pp. 1657–1666, Nov. 1965, doi: 10.1088/0508-3443/16/11/306.

[112] G. R. Kumar and P. Chaddah, *Extension of Bean's model for high- T_c superconductors*, Phys. Rev. B, vol. 39, no. 7, pp. 4704–4707, Mar. 1989, doi: 10.1103/PhysRevB.39.4704.

[113] D. -X. Chen and R. B. Goldfarb, *Kim model for magnetization of type-II superconductors*, J. Appl. Phys., vol. 66, no. 6, pp. 2489–2500, Sep. 1989, doi: 10.1063/1.344261.

[114] A. Sanchez and C. Navau, *Critical-current density from magnetization loops of finite high- T_c superconductors*, Supercond. Sci. Technol., vol. 14, no. 7, pp. 444–447, Jul. 2001, doi: 10.1088/0953-2048/14/7/304.

[115] M. Sawicki, W. Stefanowicz, and A. Ney, *Sensitive SQUID magnetometry for studying nanomagnetism*, Semicond. Sci. Technol., vol. 26, no. 6, p. 064006, Jun. 2011, doi: 10.1088/0268-1242/26/6/064006.

[116] D.-X. Chen, C. Prados, E. Pardo, A. Sanchez, and A. Hernando, *Transverse demagnetizing factors of long rectangular bars: I. Analytical expressions for extreme values of susceptibility*, J. Appl. Phys., vol. 91, no. 8, pp. 5254–5259, Apr. 2002, doi: 10.1063/1.1459745.

[117] B. Douine, *Caractérisation des supraconducteurs et pertes en régime variable*, HDR.

[118] J. G. Noudem *et al.*, *Improvement of critical current density of MgB2 bulk superconductor processed by Spark Plasma Sintering*, J. Am. Ceram. Soc., vol. 103, no. 11, pp. 6169–6175, 2020, doi: https://doi.org/10.1111/jace.17366.

[119] M. R. Koblischka *et al.*, *Superconducting YBCO Foams as Trapped Field Magnets*, Materials, vol. 12, no. 6, Art. no. 6, Jan. 2019, doi: 10.3390/ma12060853.

[120] N. Devendra Kumar, T. Rajasekharan, K. Muraleedharan, A. Banerjee, and V. Seshubai, *Unprecedented current density to high fields in $YBa_2Cu_3O_{7-\delta}$ superconductor through nano-defects generated by preform optimization in infiltration growth process*, Supercond. Sci. Technol., vol. 23, no. 10, p. 105020, Oct. 2010, doi: 10.1088/0953-2048/23/10/105020.

[121] H. Le Trong *et al.*, *Paramagnetic behaviour of silver nanoparticles generated by decomposition of silver oxalate*, Solid State Sci., vol. 69, pp. 44–49, Jul. 2017, doi: 10.1016/j.solidstatesciences.2017.05.009.

[122] P. Vanderbemden, *Determination of Critical Current in Bulk High-Temperature Superconductors by Magnetic Flux Profile Measuring Methods*, Université de Liège, 1999.

[123] M. Daeumling, M. Seuntjens, and D. C. Larbalestier, *Oxygen-defect flux pinning, anomalous magnetization and intra-grain granularity in YBa2Cu301-s*, vol. 346, p. 4, 1990.

[124] L. F. Cohen, J. R. Laverty, G. K. Perkins, A. D. Caplin, and W. Assmus, *Fishtails, scales and magnetic fields*, Cryogenics, vol. 33, no. 3, pp. 352–356, Jan. 1993, doi: 10.1016/0011-2275(93)90058-V.

[125] M. Jirsa, L. Půst, D. Dlouhý, and M. R. Koblischka, *Fishtail shape in the magnetic hysteresis loop for superconductors:Interplay between different pinning mechanisms*, Phys. Rev. B, vol. 55, no. 5, pp. 3276–3284, Feb. 1997, doi: 10.1103/PhysRevB.55.3276.

[126] M. Ullrich, D. Müller, K. Heinemann, L. Niel, and H. C. Freyhardt, *Possible origin of the anomalous magnetization behavior in melt-textured* $Y_1 Ba_2 Cu_3 O_{7-\delta}$ *crystallites*, Appl. Phys. Lett., vol. 63, no. 3, pp. 406–408, Jul. 1993, doi: 10.1063/1.110033.

[127] V. Antal *et al.*, *Relationship between local microstructure and superconducting properties of commercial YBa2Cu3O7-δ bulk*, Supercond. Sci. Technol., vol. 33, no. 4, p. 044004, Feb. 2020, doi: 10.1088/1361-6668/ab714f.

[128] M. McElfresh, *Fundamentals of Magnetism And Magnetic Measurments Featuring Quantum Design's Magnetic Property Measurment System*, Purdue University, Quantum Design, 1994.

[129] H. Weinstock, Ed., *SQUID Sensors: Fundamentals, Fabrication and Applications*. Dordrecht: Springer Netherlands, 1996. doi: 10.1007/978-94-011-5674-5.

[130] A. Kraft, C. Rupprecht, and Y.-C. Yam, *Superconducting Quantum Interference Device*, p. 6, 2017.

[131] S. Diego, *Magnetic Property Measurement System*, p. 82.

[132] Q.-R. Feng, X. Zhu, S.-Q. Feng, H. Zhang, and Z.-Z. Gan, *Effect of time aging on the properties of Ag-doped YBaCuO superconductors*, Supercond. Sci. Technol., vol. 6, no. 10, pp. 715–720, Oct. 1993, doi: 10.1088/0953-2048/6/10/002.

[133] R. Egan *et al.*, *A flux extraction device to measure the magnetic moment of large samples; application to bulk superconductors*, Rev. Sci. Instrum., vol. 86, no. 2, p. 025107, Feb. 2015, doi: 10.1063/1.4907903.

[134] M. Philippe, *Magnetic properties of structures combining bulk high temperature superconductors and soft ferromagnetic alloys*, Univ. Liège, 2015, Accessed: Jul. 25, 2022. [Online]. Available: https://www.semanticscholar.org/paper/Magnetic-properties-of-structures-combining-bulk-Philippe/7f9ba88e05203dea617c7235d65cca7dbc9328e1

[135] M. P. Philippe *et al.*, *Magnetic characterisation of large grain, bulk Y–Ba–Cu–O superconductor–soft ferromagnetic alloy hybrid structures*, Phys. C Supercond., vol. 502, pp. 20–30, Jul. 2014, doi: 10.1016/j.physc.2014.04.025.

[136] F. Martín-Hernández, I. M. Bominaar-Silkens, M. J. Dekkers, and J. K. Maan, *High-field cantilever magnetometry as a tool for the determination of the magnetocrystalline anisotropy of single crystals*, Tectonophysics, vol. 418, no. 1, pp. 21–30, May 2006, doi: 10.1016/j.tecto.2005.12.011.

[137] A. J. J. van Dalen, M. R. Koblischka, R. Griessen, M. Jirsa, and G. Ravi Kumar, *Dynamic contribution to the fishtail effect in a twin-free DyBa2Cu3O7–δ single crystal*, Phys. C Supercond., vol. 250, no. 3, pp. 265–274, Aug. 1995, doi: 10.1016/0921-4534(95)00363-0.

[138] T. Schuster, H. Kuhn, E. H. Brandt, M. Indenbom, M. R. Koblischka, and M. Konczykowski, *Flux motion in thin superconductors with inhomogeneous pinning*, Phys. Rev. B, vol. 50, no. 22, pp. 16684–16707, Dec. 1994, doi: 10.1103/PhysRevB.50.16684.

[139] S. Brialmont, J. F. Fagnard, and P. Vanderbemden, *A simple torque magnetometer for magnetic moment measurement of large samples: Application to permanent magnets and bulk superconductors*, Rev. Sci. Instrum., vol. 90, no. 8, p. 085101, Aug. 2019, doi: 10.1063/1.5111399.

[140] J. H. Durrell *et al.*, *A trapped field of 17.6 T in melt-processed, bulk Gd-Ba-Cu-O reinforced with shrink-fit steel*, Supercond. Sci. Technol., vol. 27, no. 8, p. 082001, Aug. 2014, doi: 10.1088/0953-2048/27/8/082001.

[141] M. Tomita and M. Murakami, *High-temperature superconductor bulk magnets that can trap magnetic fields of over 17 tesla at 29 K*, Nature, vol. 421, no. 6922, pp. 517–520, Jan. 2003, doi: 10.1038/nature01350.

[142] H. Fujishiro and T. Naito, *Simulation of temperature and magnetic field distribution in superconducting bulk during pulsed field magnetization*, Supercond. Sci. Technol., vol. 23, no. 10, p. 105021, Oct. 2010, doi: 10.1088/0953-2048/23/10/105021.

[143] K. Berger, J. Leveque, D. Netter, B. Douine, and A. Rezzoug, *Influence of Temperature and/or Field Dependences of the E-J Power Law on Trapped Magnetic Field in Bulk YBaCuO*, IEEE Trans. Appl. Supercond., vol. 17, no. 2, pp. 3028–3031, Jun. 2007, doi: 10.1109/TASC.2007.902095.

[144] M. D. Ainslie and H. Fujishiro, *Modelling of bulk superconductor magnetization*, Supercond. Sci. Technol., vol. 28, no. 5, p. 053002, May 2015, doi: 10.1088/0953-2048/28/5/053002.

[145] G. Fuchs, W.-R. Canders, H. May, R. Palka, and G. Krabbes, *High Temperature Superconductor Bulk Materials: Fundamentals, Processing, Properties Control, Application Aspects*. John Wiley & Sons, 2006.

[146] B. Douine, C.-H. Bonnard, F. Sirois, K. Berger, A. Kameni, and J. Lévêque, *Determination of Jc and n-Value of HTS Pellets by Measurement and Simulation of Magnetic Field Penetration*, IEEE Trans. Appl. Supercond., vol. 25, no. 4, pp. 1–8, Aug. 2015, doi: 10.1109/TASC.2015.2409201.

[147] B. Douine, K. Berger, F. Trillaud, M. Elbaa, and E. H. Ailam, *Determination of the Complete Penetration Magnetic Field of a HTS Pellet From the Measurements of the Magnetic Field at Its Top-Center Surface*, IEEE Trans. Appl. Supercond., vol. 28, no. 4, pp. 1–4, Jun. 2018, doi: 10.1109/TASC.2018.2796380.

[148] S. C. Wimbush and N. M. Strickland, *A Public Database of High-Temperature Superconductor Critical Current Data*, IEEE Trans. Appl. Supercond., vol. 27, no. 4, pp. 1–5, Jun. 2017, doi: 10.1109/TASC.2016.2628700.

[149] K. Maehata *et al.*, *High current transport test of a YBCO bulk conductor up to 25 kA*, IEEE Trans. Appl. Supercond., vol. 9, no. 2, pp. 1281–1284, Jun. 1999, doi: 10.1109/77.783535.

[150] R. Heller, G. Friesinger, A. M. Fuchs, and R. Wesche, *Development of high temperature superconductor current leads for 70 kA [ITER-FEAT coil system]*, IEEE Trans. Appl. Supercond., vol. 12, no. 1, pp. 1285–1288, Mar. 2002, doi: 10.1109/TASC.2002.1018637.

[151] Y. Kamihara *et al.*, *Iron-Based Layered Superconductor: LaOFeP*, J. Am. Chem. Soc., vol. 128, no. 31, pp. 10012–10013, Aug. 2006, doi: 10.1021/ja063355c.

[152] Y. Kamihara, T. Watanabe, M. Hirano, and H. Hosono, *Iron-Based Layered Superconductor* $La[O_{1-x}F_x]FeAs$ (x= *0.05–0.12) with* T_c= *26 K*, J. Am. Chem. Soc., vol. 130, no. 11, pp. 3296–3297, Mar. 2008, doi: 10.1021/ja800073m.

[153] F.-C. Hsu *et al.*, *Superconductivity in the PbO-type structure ␣-FeSe*, p. 3.

[154] D. C. Johnston, *The puzzle of high temperature superconductivity in layered iron pnictides and chalcogenides*, Adv. Phys., vol. 59, no. 6, pp. 803–1061, Nov. 2010, doi: 10.1080/00018732.2010.513480.

[155] J. Paglione and R. L. Greene, *High-temperature superconductivity in iron-based materials*, Nat. Phys., vol. 6, no. 9, Art. no. 9, Sep. 2010, doi: 10.1038/nphys1759.

[156] G. Wu *et al.*, *Superconductivity at 56 K in samarium-doped SrFeAsF*, J. Phys. Condens. Matter, vol. 21, no. 14, p. 142203, Mar. 2009, doi: 10.1088/0953-8984/21/14/142203.

[157] S. Margadonna *et al.*, *Pressure evolution of the low-temperature crystal structure and bonding of the superconductor FeSe (* T_c *= 37 K)*, Phys. Rev. B, vol. 80, no. 6, p. 064506, Aug. 2009, doi: 10.1103/PhysRevB.80.064506.

[158] J.-F. Ge *et al.*, *Superconductivity above 100 K in single-layer FeSe films on doped SrTiO3*, Nat. Mater., vol. 14, no. 3, pp. 285–289, Mar. 2015, doi: 10.1038/nmat4153.

[159] M. R. Koblischka *et al.*, *Excess Conductivity Analysis of Polycrystalline FeSe Samples with the Addition of Ag*, Materials, vol. 13, no. 21, Art. no. 21, Jan. 2020, doi: 10.3390/ma13215018.

[160] K.-W. Yeh *et al.*, *Tellurium substitution effect on superconductivity of the α-phase iron selenide*, EPL Europhys. Lett., vol. 84, no. 3, p. 37002, Nov. 2008, doi: 10.1209/0295-5075/84/37002.

[161] D. Croitori *et al.*, *Structure, superconductivity, and magnetism in Rb 1 − x Fe 1.6 Se 2 − z S z*, Phys. Rev. B, vol. 101, no. 5, p. 054516, Feb. 2020, doi: 10.1103/PhysRevB.101.054516.

[162] E.-W. Scheidt *et al.*, *Superconductivity at Tc = 44 K in LixFe2Se2(NH3)y*, Eur. Phys. J. B, vol. 85, no. 8, p. 279, Aug. 2012, doi: 10.1140/epjb/e2012-30422-6.

[163] A. Krzton-Maziopa, E. V. Pomjakushina, V. Y. Pomjakushin, F. von Rohr, A. Schilling, and K. Conder, *Synthesis of a new alkali metal–organic solvent intercalated iron selenide superconductor with* $T_c \approx 45$ *K*, J. Phys. Condens. Matter, vol. 24, no. 38, p. 382202, Sep. 2012, doi: 10.1088/0953-8984/24/38/382202.

[164] T. Ying *et al.*, *Superconducting Phases in Potassium-Intercalated Iron Selenides*, J. Am. Chem. Soc., vol. 135, no. 8, pp. 2951–2954, Feb. 2013, doi: 10.1021/ja312705x.

[165] J. Guo *et al.*, *Superconductivity in the iron selenide KxFe2Se2 (0 ≤ x ≤ 1.0)*, Phys. Rev. B, vol. 82, no. 18, p. 180520, Nov. 2010, doi: 10.1103/PhysRevB.82.180520.

[166] H. Lei and C. Petrovic, *Giant increase in critical current density of KxFe2−ySe2 single crystals*, Phys. Rev. B, vol. 84, no. 21, p. 212502, Dec. 2011, doi: 10.1103/PhysRevB.84.212502.

[167] T. Ozaki *et al.*, *One-step synthesis of* $K_xFe_{2-y}Se_2$ *single crystal for high critical current density*, EPL Europhys. Lett., vol. 98, no. 2, p. 27002, Apr. 2012, doi: 10.1209/0295-5075/98/27002.

[168] H. Okamoto, *The fese (ironselenium) system*, J. Phase Equilibria, vol. 12, no. 3, pp. 383–389, Jun. 1991, doi: 10.1007/BF02649932.

[169] E. Pomjakushina, K. Conder, V. Pomjakushin, M. Bendele, and R. Khasanov, *Synthesis, crystal structure, and chemical stability of the superconductor FeSe 1 − x*, Phys. Rev. B, vol. 80, no. 2, p. 024517, Jul. 2009, doi: 10.1103/PhysRevB.80.024517.

[170] L. J. Swartzendruber, *The Fe (Iron) system*, Bull. Alloy Phase Diagr., vol. 3, no. 2, pp. 161–165, Sep. 1982, doi: 10.1007/BF02892374.

[171] J. Serre, P. Gibart, and J. Bonnerot, *Propriétés physiques de Fe7Se8*, J. Phys., vol. 30, no. 1, pp. 93–96, 1969, doi: 10.1051/jphys:0196900300109300.

[172] I. Radelytskyi *et al.*, *Structural, magnetic, and magnetocaloric properties of* Fe_7Se_8 *single crystals*, J. Appl. Phys., vol. 124, no. 14, p. 143902, Oct. 2018, doi: 10.1063/1.5042344.

[173] M. Ghalawat and P. Poddar, *Remarkable Effect of Fe and Se Composition on Magnetic Properties—Comparative Study of the Fe–Se System at the Nanoscale*, J. Phys. Chem. C, vol. 126, no. 9, pp. 4655–4663, Mar. 2022, doi: 10.1021/acs.jpcc.1c10286.

[174] P. Terzieff and K. L. Komarek, *The paramagnetic properties of iron selenides with NiAs-type structure*, Monatshefte Chem., vol. 109, no. 3, pp. 651–659, 1978, doi: 10.1007/BF00912781.

[175] P. Terzieff and K. L. Komarek, *The antiferromagnetic and ferrimagnetic properties of iron selenides with NiAs-type structure*, Monatshefte Chem., vol. 109, no. 5, pp. 1037–1047, 1978, doi: 10.1007/BF00913006.

[176] Y. Mizuguchi, F. Tomioka, S. Tsuda, T. Yamaguchi, and Y. Takano, *Superconductivity at 27K in tetragonal FeSe under high pressure*, Appl. Phys. Lett., vol. 93, no. 15, p. 152505, Oct. 2008, doi: 10.1063/1.3000616.

[177] M. Ma, D. Yuan, Y. Wu, H. Zhou, X. Dong, and F. Zhou, *Flux-free growth of large superconducting crystal of FeSe by traveling-solvent floating-zone technique*, Supercond. Sci. Technol., vol. 27, no. 12, p. 122001, Dec. 2014, doi: 10.1088/0953-2048/27/12/122001.

[178] H. Lei, R. Hu, and C. Petrovic, *Critical fields, thermally activated transport, and critical current density of β -FeSe single crystals*, Phys. Rev. B, vol. 84, no. 1, p. 014520, Jul. 2011, doi: 10.1103/PhysRevB.84.014520.

[179] S. I. Vedeneev, B. A. Piot, D. K. Maude, and A. V. Sadakov, *Temperature dependence of the upper critical field of FeSe single crystals*, Phys. Rev. B, vol. 87, no. 13, p. 134512, Apr. 2013, doi: 10.1103/PhysRevB.87.134512.

[180] Y. Sun *et al.*, *Critical current density, vortex dynamics, and phase diagram of single-crystal FeSe*, Phys. Rev. B, vol. 92, no. 14, p. 144509, Oct. 2015, doi: 10.1103/PhysRevB.92.144509.

[181] M. Miryala *et al.*, *Complex pulse magnetization process and mechanical properties of spark plasma sintered bulk MgB2*, Mater. Sci. Eng. B, vol. 273, p. 115390, Nov. 2021, doi: 10.1016/j.mseb.2021.115390.

[182] G. Z. Li *et al.*, *The critical current density of advanced internal-Mg-diffusion-processed* MgB_2 *wires*, Supercond. Sci. Technol., vol. 25, no. 11, p. 115023, Nov. 2012, doi: 10.1088/0953-2048/25/11/115023.

[183] M. Bendele *et al.*, *Anisotropic superconducting properties of single-crystalline FeSe 0.5 Te 0.5*, Phys. Rev. B, vol. 81, no. 22, p. 224520, Jun. 2010, doi: 10.1103/PhysRevB.81.224520.

[184] T. M. McQueen *et al.*, *Extreme sensitivity of superconductivity to stoichiometry in Fe 1 + δ Se*, Phys. Rev. B, vol. 79, no. 1, p. 014522, Jan. 2009, doi: 10.1103/PhysRevB.79.014522.

[185] A. J. Williams, T. M. McQueen, and R. J. Cava, *The stoichiometry of FeSe*, Solid State Commun., vol. 149, no. 37–38, pp. 1507–1509, Oct. 2009, doi: 10.1016/j.ssc.2009.07.011.

[186] J.-C. Grivel, *A simple method for preparing superconducting FeSe pellets without sealing in evacuated silica tubes*, Ceram. Int., vol. 43, no. 14, pp. 11474–11480, Oct. 2017, doi: 10.1016/j.ceramint.2017.05.280.

[187] J.-H. Ahn and S. Oh, *Effect of hot-consolidation method on the superconducting properties of B- and C-doped FeSe0.5Te0.5*, Curr. Appl. Phys., vol. 13, no. 6, pp. 1096–1100, Aug. 2013, doi: 10.1016/j.cap.2013.02.019.

[188] X. Li, Z. Ma, Y. Liu, M. Dong, and L. Yu, *The Sintering Process and Superconductivity of Polycrystalline Milled Fe–Se*, IEEE Trans. Appl. Supercond., vol. 23, no. 2, pp. 7000405–7000405, Apr. 2013, doi: 10.1109/TASC.2013.2246159.

[189] Y. Xia, F. Huang, X. Xie, and M. Jiang, *Preparation and superconductivity of stoichiometric β-FeSe*, EPL Europhys. Lett., vol. 86, no. 3, p. 37008, May 2009, doi: 10.1209/0295-5075/86/37008.

[190] M. Shahbazi, H. E. Cathey, and I. D. R. Mackinnon, *Stoichiometry of tetragonal and hexagonal* Fe_x *Se: phase relations*, Supercond. Sci. Technol., vol. 33, no. 7, p. 075003, Jul. 2020, doi: 10.1088/1361-6668/ab89ec.

[191] A. Galluzzi, K. Buchkov, and E. Nazarova, *Magnetic field sweep rate influence on the critical current capabilities of a Fe(Se,Te) crystal*, Appl. Phys., p. 8, 2020.

[192] C. Fiamozzi Zignani *et al.*, *Improvements of high-field pinning properties of polycrystalline Fe(Se,Te) material by heat treatments*, J. Mater. Sci., vol. 54, no. 6, pp. 5092–5100, Mar. 2019, doi: 10.1007/s10853-018-03218-5.

[193] A. Masi *et al.*, *Phase Separation and Microstructure in Superconducting FeSe1-xTex Materials*, IEEE Trans. Appl. Supercond., vol. 28, no. 4, pp. 1–5, Jun. 2018, doi: 10.1109/TASC.2018.2791547.

[194] Y. Sun, S. Pyon, and T. Tamegai, *Effect of S doping on the critical current density and vortex dynamics in FeSe single crystal*, Phys. C Supercond. Its Appl., vol. 530, pp. 55–57, Nov. 2016, doi: 10.1016/j.physc.2016.05.023.

[195] M. Abdel-Hafiez *et al.*, *Superconducting properties of sulfur-doped iron selenide*, Phys. Rev. B, vol. 91, no. 16, p. 165109, Apr. 2015, doi: 10.1103/PhysRevB.91.165109.

[196] A. Koblischka-Veneva *et al.*, *Comparison of Temperature and Field Dependencies of the Critical Current Densities of Bulk YBCO,* MgB_2*, and Iron-Based Superconductors*, IEEE Trans. Appl. Supercond., vol. 29, no. 5, pp. 1–5, Aug. 2019, doi: 10.1109/TASC.2019.2900932.

[197] X. Ding *et al.*, *Influence of microstructure on superconductivity in KxFe2–ySe2 and evidence for a new parent phase K2Fe7Se8*, Nat. Commun., vol. 4, no. 1, p. 1897, Oct. 2013, doi: 10.1038/ncomms2913.

[198] T. Zhou *et al.*, *Effects of Co and Mn doping in* $K_{0.8}Fe_{2-y}Se_2$ *revisited*, J. Phys. Condens. Matter, vol. 25, no. 27, p. 275701, Jul. 2013, doi: 10.1088/0953-8984/25/27/275701.

[199] K. Sugai, R. Tatsumi, M. Uehara, T. Kuramoto, and Y. Kimishima, *Intrinsic Pinning Property of NaFe2Se2 Superconductor*, Phys. Procedia, vol. 58, pp. 118–121, 2014, doi: 10.1016/j.phpro.2014.09.044.

[200] D. Li *et al.*, *Controllable Phase Transition for Layered β-FeSe Superconductor Synthesized by Solution Chemistry*, Chem. Mater., vol. 29, no. 2, pp. 842–848, Jan. 2017, doi: 10.1021/acs.chemmater.6b04887.

[201] E. S. Reddy and T. Rajasekharan, *Shape Forming Simultaneous with Jc Enhancement in REBa2Cu3O7 Superconductors*, J. Mater. Res., vol. 13, no. 9, pp. 2472–2475, Sep. 1998, doi: 10.1557/JMR.1998.0346.

[202] S. Pavan Kumar Naik, N. Devendra Kumar, P. Missak Swarup Raju, T. Rajasekharan, and V. Seshubai, *Effect of infiltration temperature on the properties of infiltration growth processed YBCO superconductor*, Phys. C Supercond., vol. 487, pp. 72–76, Apr. 2013, doi: 10.1016/j.physc.2013.01.008.

[203] S. Pavan Kumar Naik, M. Muralidhar, M. Jirsa, and M. Murakami, *Growth and physical properties of top-seeded infiltration growth processed large grain (Gd, Dy)BCO bulk superconductors*, J. Appl. Phys., vol. 122, no. 19, p. 193902, Nov. 2017, doi: 10.1063/1.4999164.

[204] L. Vojtkova, P. Diko, D. Volochová, V. Kavečanský, V. Antal, and S. Piovarči, *Top-Seeded Infiltration Growth and Structure of YBCO Bulk Superconductors*, IEEE Trans. Appl. Supercond., vol. 26, no. 3, pp. 1–4, Apr. 2016, doi: 10.1109/TASC.2016.2542275.

[205] E. S. Reddy, M. Herweg, and G. J. Schmitz, *Processing of* Y_2BaCuO_5 *foams*, Supercond. Sci. Technol., vol. 16, no. 5, pp. 608–612, May 2003, doi: 10.1088/0953-2048/16/5/311.

[206] M. Murakami, N. Sakai, T. Higuchi, and S. I. Yoo, *Melt-processed light rare earth element - Ba - Cu - O*, Supercond. Sci. Technol., vol. 9, no. 12, pp. 1015–1032, Dec. 1996, doi: 10.1088/0953-2048/9/12/001.

[207] R. Cloots, T. Koutzarova, J.-P. Mathieu, and M. Ausloos, *From RE-211 to RE-123. How to control the final microstructure of superconducting single-domains*, Supercond. Sci. Technol., vol. 18, no. 3, pp. R9–R23, Dec. 2004, doi: 10.1088/0953-2048/18/3/R01.

[208] M. Tomita and M. Murakami, *High-temperature superconductor bulk magnets that can trap magnetic fields of over 17 tesla at 29 K*, Nature, vol. 421, no. 6922, pp. 517–520, Jan. 2003, doi: 10.1038/nature01350.

[209] E. S. Reddy, M. Herweg, and G. J. Schmitz, *Processing of Y2BaCuO5foams*, Supercond. Sci. Technol., vol. 16, no. 5, pp. 608–612, Mar. 2003, doi: 10.1088/0953-2048/16/5/311.

[210] M. R. Koblischka *et al.*, *Current Flow and Flux Pinning Properties of YBCO Foam Struts*, IEEE Trans. Appl. Supercond., vol. 29, no. 5, pp. 1–5, Aug. 2019, doi: 10.1109/TASC.2019.2894712.

[211] R. Dorget *et al.*, *Design of a 500 kW partially superconducting flux modulation machine for aircraft propulsion*, J. Phys. Conf. Ser., vol. 1975, no. 1, p. 012033, Jul. 2021, doi: 10.1088/1742-6596/1975/1/012033.

[212] J. A. A. J. Perenboom, S. A. J. Wiegers, P. C. M. Christianen, U. Zeitler, and J. C. Maan, *The new installation at the Nijmegen High Field Magnet Laboratory*, Phys. B Condens. Matter, vol. 346–347, pp. 659–662, Apr. 2004, doi: 10.1016/j.physb.2004.01.078.

[213] J. A. A. J. Perenboom, J. C. Maan, S. A. J. Wiegers, and P. H. Frings, *The new Nijmegen installation for DC and pulsed high magnetic fields*, IEEE Trans. Appl. Supercond., vol. 10, no. 1, pp. 1549–1551, Mar. 2000, doi: 10.1109/77.828538.

[214] *Characteristic of the 33 T magnet.* https://www.hfml.ru.nl/luong/cal_cell3.htm (accessed Oct. 03, 2022).

[215] M. R. Koblischka, *Large fishtail effect in DyBa2Cu307_5 single crystals containing columnar defects*, p. 2.

[216] M. Jirsa, M. R. Koblischka, and A. J. J. van Dalen, *Relaxation and scaling of magnetization around the fishtail minimum in single crystal with columnar tracks*, Supercond. Sci. Technol., vol. 10, no. 7, pp. 484–491, Jul. 1997, doi: 10.1088/0953-2048/10/7/004.

[217] G. R. Kumar, M. R. Koblischka, J. C. Martinez, R. Griessen, B. Dam, and J. Rector, *Angular scaling of critical current measurements on laser-ablated YBa2Cu3O7−δ thin films*, Phys. C Supercond., vol. 235–240, pp. 3053–3054, Dec. 1994, doi: 10.1016/0921-4534(94)91053-7.

[218] P. W. Anderson, *Theory of Flux Creep in Hard Superconductors*, Phys. Rev. Lett., vol. 9, no. 7, pp. 309–311, Oct. 1962, doi: 10.1103/PhysRevLett.9.309.

[219] W. Cheng, H. Lin, B. Shen, and H.-H. Wen, *Comparative study of vortex dynamics in CaKFe4As4 and Ba0.6K0.4Fe2As2 single crystals*, Sci. Bull., vol. 64, no. 2, pp. 81–90, Jan. 2019, doi: 10.1016/j.scib.2018.12.024.

[220] Y. Jiao, W. Cheng, Q. Deng, H. Yang, and H.-H. Wen, *Collective vortex pinning and merging of the irreversibility line and second peak effect in optimally doped Ba1−xKxBiO3 single crystals*, Phys. C, p. 7, 2018.

[221] J. Tao, Q. Deng, H. Yang, Z. Wang, X. Zhu, and H.-H. Wen, *Magnetization relaxation, critical current density, and vortex dynamics in a Ba0.66K0.32BiO3+δ single crystal*, Phys. Rev. B, vol. 91, no. 21, p. 214516, juin 2015, doi: 10.1103/PhysRevB.91.214516.

[222] M. D. Ainslie *et al.*, *Numerical modelling of mechanical stresses in bulk superconductor magnets with and without mechanical reinforcement*, Supercond. Sci. Technol., vol. 32, no. 3, p. 034002, Feb. 2019, doi: 10.1088/1361-6668/aaf851.

[223] O. Vakaliuk, F. Werfel, J. Jaroszynski, and B. Halbedel, *Trapped field potential of commercial Y-Ba-Cu-O bulk superconductors designed for applications*, Supercond. Sci. Technol., vol. 33, no. 9, p. 095005, Jul. 2020, doi: 10.1088/1361-6668/ab9fc4.

[224] D. Mendes *et al.*, *Low-cost and high-performance 3D printed YBCO superconductors*, Ceram. Int., vol. 47, no. 1, pp. 381–387, Jan. 2021, doi: 10.1016/j.ceramint.2020.08.143.

[225] X. Wei, R. S. Nagarajan, E. Peng, J. Xue, J. Wang, and J. Ding, *Fabrication of YBa2Cu3O7−x (YBCO) superconductor bulk structures by extrusion freeforming*, Ceram. Int., vol. 42, no. 14, pp. 15836–15842, Nov. 2016, doi: 10.1016/j.ceramint.2016.07.052.

[226] B. Zhang *et al.*, *Efficient Fabrication of Ultralight YBa2Cu3O7−x Superconductors with Programmable Shape and Structure*, Adv. Funct. Mater., vol. 31, no. 22, p. 2100680, 2021, doi: 10.1002/adfm.202100680.

Résumé en Français

I.1. Introduction

I.1.a. Généralités sur les supraconducteurs

Découvert en 1911 par Heike Kamerlingh Onnes en refroidissant du mercure à 4.2 K, la supraconductivité est un état de la matière qui apparait en dessous d'une température dite température critique T_c. Un matériau supraconducteur a la particularité de voir sa résistance électrique chuter à zéro et donc de devenir parfaitement diamagnétique. Néanmoins, sous l'effet d'un champ magnétique externe ou avec le passage d'un courant électrique cet état, dit « état Meissner », disparait et le matériau retourne dans l'état normal dit résistif si c'est un supraconducteur de type I ou entre dans l'état mixte s'il est de type II.

Contrairement à l'état Meissner, l'état mixte permet de transporter une grande quantité de courant et peut résister à de larges champs magnétiques mais il reste tout de même une limite de champ ou de courant à partir desquelles l'échantillon va quitter l'état supraconducteur respectivement appelé champ magnétique critique H_c et densité de courant critique J_c. C'est la mesure de ces 3 grandeurs, T_c, H_c et J_c qui vont permettre de caractériser les propriétés supraconductrices d'un matériau, de les comparer et de pouvoir déterminer leurs potentiels pour des applications technologiques en génie électrique. Un exemple de propriétés supraconductrices est donné avec la Figure 0-1.

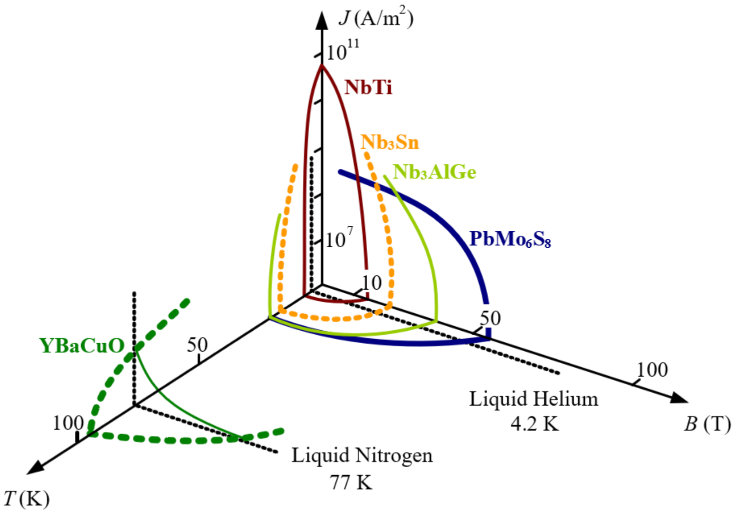

Figure 0-1 : Evolution des propriétés supraconductrices J_c, B_c T_c pour différents matériaux.

Du fait de leurs capacités à supporter de forts champs magnétiques et de larges densités de courants sans échauffement, les matériaux supraconducteurs ont reçu une très forte attention et un très fort développement. Nous pouvons notamment citer les alliages en Niobium-Titane et Niobium-Etain utilisés dans les IRM ou dans les grands instruments pour générer de forts champs (aimants d'accélérateurs ou de TOKAMAK).

En 1986 a été découvert les supraconducteurs à haute température critique (T_c >30 K) avec le LaBaCuO de la famille des cuprates, suivie par d'autres cuprates atteignant une température critique supérieure à la température de l'azote liquide (77 K), ce qui a ouvert de nouvelles applications potentielles. Nous pouvons par exemple citer des applications sur des câbles pour le transport de courant, des limiteurs de courant ou des moteurs électriques. Pour ces applications, les supraconducteurs sont généralement sous la forme de fils, câble ou ruban mais une autre forme peut aussi être utilisée : le supraconducteur massif.

I.1.b. Supraconducteurs massifs

Un massif est un bloc mono ou polycristallin d'un matériau, ici supraconducteur, sous la forme d'un bloc ou d'une pastille de taille ou de configuration parfois très différentes comme on peut le voir sur la Figure 0-2 ou plusieurs supraconducteurs massifs de divers matériaux sont présentés.

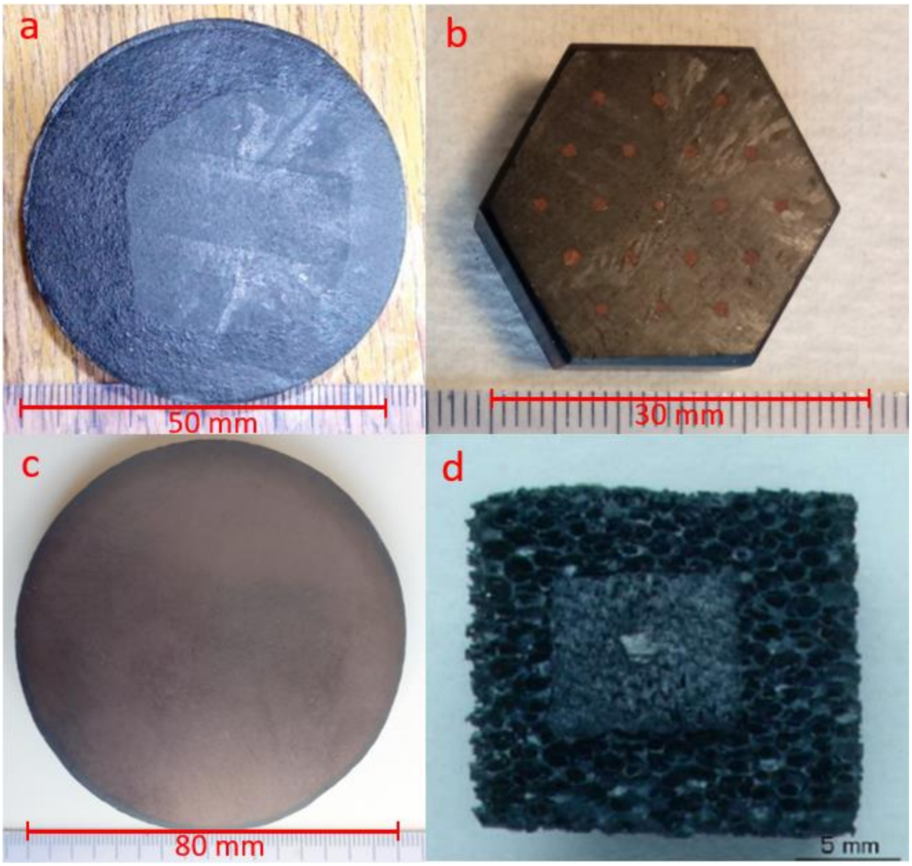

Figure 0-2 : Photos de massifs supraconducteurs avec des designs et des matériaux divers : (a) un massif monocristallin commercial de 50 mm de diamètre en GdBaCuO, (b) autre massif monocristallin commercial en GdBaCuO usiné en forme d'hexagone, (c) massif polycristallin en MgB_2 *de 80 mm de diamètre synthétisé par J. Noudem et enfin (d) une mousse supraconductrice en YBaCuO.*

Ce type de matériau est principalement utilisé comme aimant permanent de par sa capacité à conserver un courant induit après un processus d'aimantation. Mais il peut également être utilisé comme écran magnétique, pour de la lévitation magnétique ou pour le transport de courant. Les blocs supraconducteurs ont l'avantage d'être simple et peu coûteux à produire car ils ne nécessitent que peu de moyens de productions.

I.1.c. Objectifs de la thèse

C’est sur les massifs supraconducteurs, que cette thèse va se concentrer avec pour objectif d’en synthétiser, de déterminer leurs propriétés cristallographiques ou supraconductrices afin d’optimiser leurs performances et de déterminer les méthodes de synthèses et les matériaux les plus compétitifs pour une utilisation dans des applications en génie électrique. Ce manuscrit donne un aperçu du travail réalisé au cours du doctorat et se divise en 3 parties comme suit :

- Une première partie présentant les propriétés cristallographiques et supraconductrices caractéristiques des massifs supraconducteurs et les méthodes de mesures associées à chaque propriété.
- La deuxième partie présentant les résultats de la synthèse et de la caractérisation de Fer-Sélénium supraconducteur polycristallin que j’ai eu l’occasion de faire. Ceci permettra d’apporter des éléments sur le potentiel de ce matériau vis-à-vis d’applications et par rapport à d’autre matériaux plus développés.
- Enfin la troisième partie va présenter les résultats de la caractérisation de massifs supraconducteurs en YBaCuO, préparés par infiltration growth. Pour les comparer, j’ai eu l’occasion d’utiliser un aimant à fort champ et de mesures de forces par cantilever. Ces résultats seront comparés aux performances des massifs YBaCuO synthétisé par Melt Growth pour en déterminer sa maturité et sa compétitivité.

I.2. Caractérisation de supraconducteurs massifs

I.2.a. Analyse de l’aspect, de la structure et des phases dans un supraconducteur massif

Pour analyser la surface d’un supraconducteur massif, la présence de fissures ou de trous, mais également de zones d’amalgame d’impuretés ou de dopants à des échelles microscopiques, j’utilise un microscope optique. Cela permet d’avoir facilement et rapidement des informations sur des échelles supérieures au micromètre (Figure 0-3.a).

Pour de plus faible dimension, l’utilisation d’un microscope à balayage électronique est nécessaire. Ce gain de précision permet d’avoir des informations sur la taille des grains d’un polycristal (typiquement de l’ordre du micromètre), la densité du matériau et de la qualité de la liaison entre les grains. Par une détection des électrons secondaires émis par le matériau lui-même (Electron Back Scatter Diffraction), la détermination du type d’atomes et de leurs répartitions sur la surface étudiée est possible. Avec ceci je peux alors connaitre les phases cristallographiques, ainsi que leurs répartitions et leurs orientations sur la surface étudiée (Figure 0-3.b-d).

Enfin, pour avoir une idée plus globale des phases cristallographiques présentent dans un massif/échantillons, j’ai utilisé la technique de diffraction de rayon-x consistante à mesurer la diffraction d’un rayon X causé par mes échantillons réduits à l’état de poudre ou par leur surface plane. Ainsi je connais la quantité de chaque phase par rapport aux autres, mais j’identifie également la présence d’impuretés ou de phases secondaires non-désirées (Figure 0-3.c).

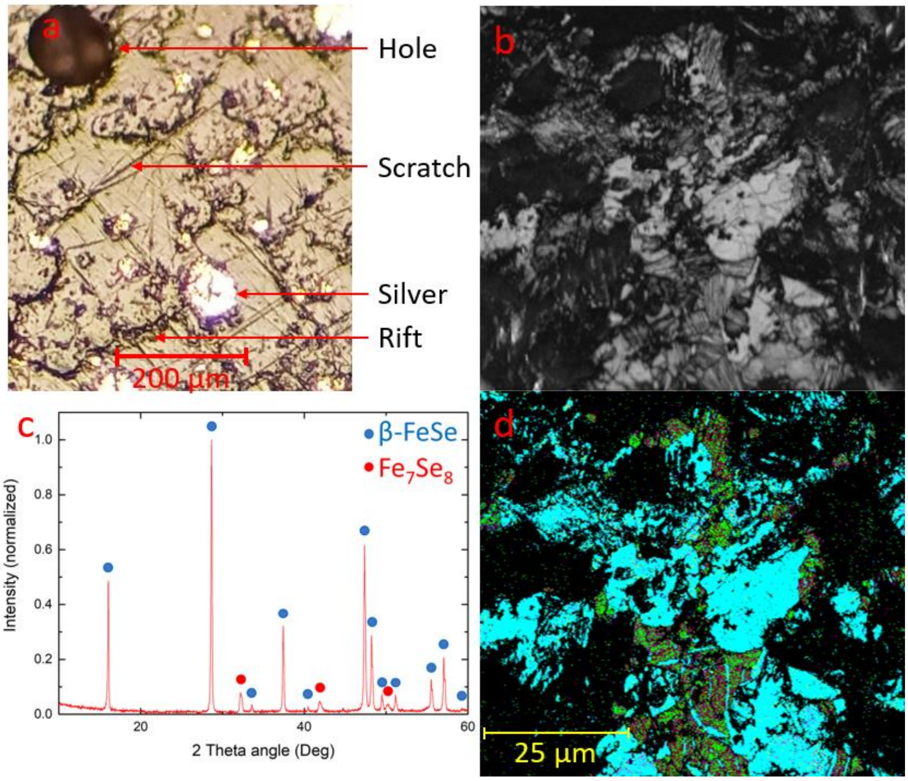

Figure 0-3 : (a) photo de la surface d'un GdBaCuO commercial dopé à l'argent prise à l'aide d'un microscope optique. (b) photo prise par un microscope à balayage électronique d'un massif polycristallin en Fer-Sélénium. (c) Graphique de diffraction de rayon-X d'un massif en Fer-Sélénium, la phase β-FeSe est supraconductrice, la phase Fe_7Se_8 est ferrimagnétique. (d) même photo que (b) mais avec une analyse EBSD donnant la répartition des phases cristallographiques, le bleu (●), le violet (●) et le vert (●) sont respectivement les phases β-FeSe, Fe_7Se_8 et α-Fe.

I.2.b. Mesure des propriétés supraconductrices d'un supraconducteur massif

Les propriétés supraconductrices d'un massif peuvent être séparées en deux catégories : les propriétés physiques locales mesurées sur un petit échantillon et les propriétés globales mesurables sur l'ensemble du massif.

Parmi les propriétés supraconductrices physiques que j'ai mesurées, nous pouvons citer :

- Le moment magnétique m et l'aimantation M.
- Les propriétés critiques ; T_c, H_c, J_c
- Le champ magnétique d'irréversibilité H_{irr}, atteint lorsque $J_c \leq 100$ A.cm^{-2}
- La force de piégeage calculée à partir de J_c : $F_p = J_c \times H$

Ces propriétés peuvent être déterminées à l'aide d'un système MPMS (Magnetic Property Measurement System) qui va mesurer le moment magnétique d'échantillons de petite taille (environ 2 mm de longueur, 1 mm de largeur et 0.3 millimètre d'épaisseur) en appliquant un champ magnétique unidirectionnel tout en contrôlant très précisément la température de l'échantillons de 2 à 300 K. Un exemple de résultat pouvant être obtenu avec ce type de système est présenter Figure 0-4. Ensuite, en utilisant l'épaisseur de la courbe du cycle d'hystérésis mesurée et à l'aide de la formule de Chen, la densité de courant critique et donc les autres propriétés physiques comme la densité de courant critique, le champ d'irréversibilité ou la force de piégeage peuvent être calculés :

$$J_c(H) = \frac{\Delta M(H)}{a\left(1-\frac{a}{3b}\right)}$$

Avec J_c la densité de courant critique, ΔM l'épaisseur de la courbe d'hystérésis et a, b respectivement la largeur et la longueur de l'échantillon.

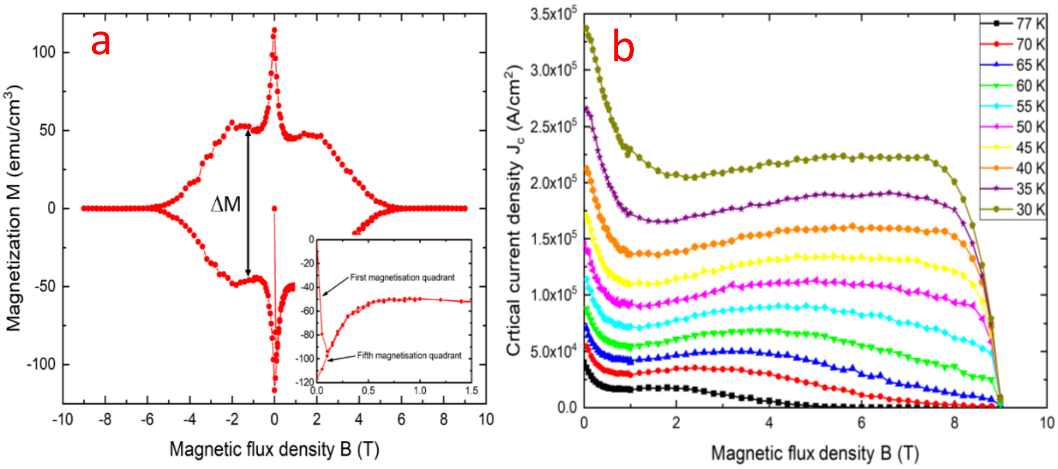

Figure 0-4 : (a) courbe de magnétisation d'un massif supraconducteur GdBaCuO à 77 K calculée à partir du moment magnétique mesuré à l'aide d'un système MPMS. En utilisant l'épaisseur de la courbe d'hystérésis, ΔM, et la formule de Chen, nous pouvons calculer la densité de courant critique J_c présentée en (b) pour différentes valeurs de températures.

Les propriétés globales avec lesquelles j'ai eu l'occasion de travailler sont :

- Le champ magnétique piégé B_T et sa topologie à la surface d'un massif (Figure 0-5.b) induit par un champ magnétique variant lentement (aimant permanant, électroaimant) ou par un champ pulsé (bobine)
- La force de lévitation F_L ou de répulsion émise par un massif supraconducteurs lorsqu'un gradient de champ magnétique lui est appliqué.

Ces propriétés sont mesurées sur le massif en entier et nécessitent donc des équipements expérimentaux adaptés aux dimensions. La plupart du temps ses propriétés sont mesurées à la température de l'azote liquide (77 K) pour des raisons de simplicité, des moyens plus complexes peuvent néanmoins être mis en place pour descendre à de plus basses températures.

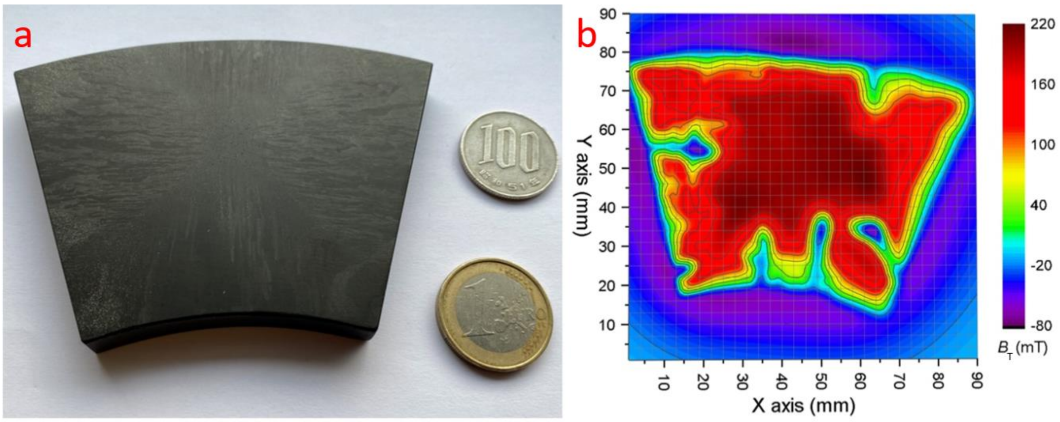

Figure 0-5 : (a) massif monocristallin en GdBaCuO usiné en forme de segment d'anneau pour des applications de moteurs électriques. (b) la topologie d'un champ magnétique piégé du même bulk après application d'un champ extérieur de 0.3 T.

I.3. Supraconducteur polycristallin en Fer-Sélénium

Dans le but de développer des supraconducteurs massifs adaptés à des applications en génie électriques, J'ai eu l'occasion de synthétiser des massifs polycristallins en Fer-Sélénium (FeSe) et d'étudier/optimiser leurs propriétés magnétiques.
En effet, le FeSe polycristallin peut être fabriqué via des méthodes de synthèses rapides (synthèse au four) voir très rapides (synthèse par frittage flash) tout en garantissant de bonnes propriétés mécaniques et supraconductrices.

I.3.a. Synthèse au four

Pour la méthode de synthèse au four j'ai mélangé en proportion stœchiométrique les poudres de Fer et de Sélénium puis le mélange est placé dans une feuille de tantale elle-même placé dans un tube de quartz scellé pour éviter toutes contaminations à l'oxygène pendant la synthèse. Tout ce processus est fait dans une boite à gant avec une atmosphère inerte (Argon). Enfin le tube est placé dans le four, la température de synthèse est appliquée pour faire réagir les deux poudres puis la température de recuit pour générer la phase cristallographique désirée, ici la phase supraconductrice β-FeSe et pour limiter la présence de phases secondaires ferrimagnétique (Fe_7Se_8) ou ferromagnétique (α-Fe).
Le meilleur résultat est présenté ci-dessous, Figure 0-6.a, avec la mesure du moment magnétique normalisé d'un échantillon de FeSe. On peut y voir la présence d'un moment supraconducteur mélangé à un moment ferrimagnétique. Ce résultat est confirmé par une mesure des phrases cristallographiques par diffraction à rayons X, Figure 0-6.b, où l'on peut identifier des pics de diffractions caractéristiques de la phase supraconductrice β-FeSe et de la phase ferrimagnétique Fe_7Se_8.

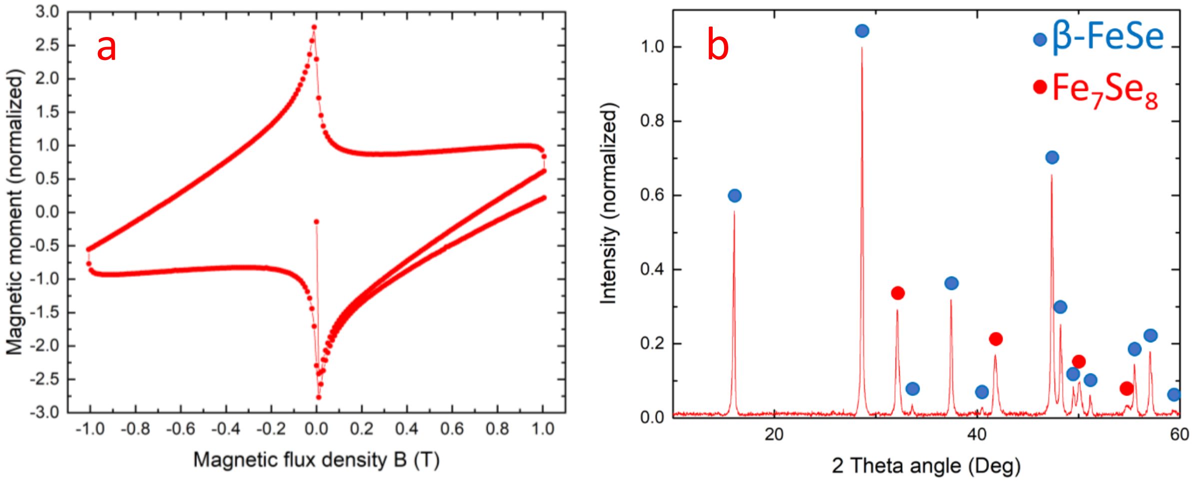

Figure 0-6 : (a) Mesure du moment magnétique normalisé sur les valeurs à B = 1 et -1 T d'un échantillon de FeSe préparé par synthèse four. (b) graphique de diffraction des rayon X du même échantillon permettant d'identifier les phases en présence, le bleu (●) et le rouge (●) sont respectivement les phases β-FeSe et Fe_7Se_8.

I.3.b. Synthèse par frittage flash

Les poudres, également mélangées en proportion stœchiométrique dans une boite à gant, sont placés dans un moule en carbone lui-même placé entre deux amenés de courant dans une chambre à vide. La synthèse par frittage flash consiste à appliquer un courant à travers les poudres à réagir de manière à les chauffer par effet Joule de façon très homogène et très rapide tout en appliquant une pression verticale pour garantir un échantillon très denseIl existe deux techniques de synthèses : la synthèse in-situ consistant à faire la synthèse et le recuit par frittage flash ou la synthèse ex-situ consistant à faire la synthèse avant le frittage flash (via une synthèse au four dans mon cas).

La synthèse in-situ s'est avérée compliquée de par la liquéfaction et donc la fuite de Sélénium pendant le processus et de bons résultats n'ont pu être obtenus.

La synthèse ex-situ a, quant à elle, permit de fabriquer des échantillons supraconducteurs moins performants que ceux obtenue avec une synthèse four (Figure 0-7) car possédant un moment magnétique typique d'un matériau ferrimagnétique et non supraconducteur.

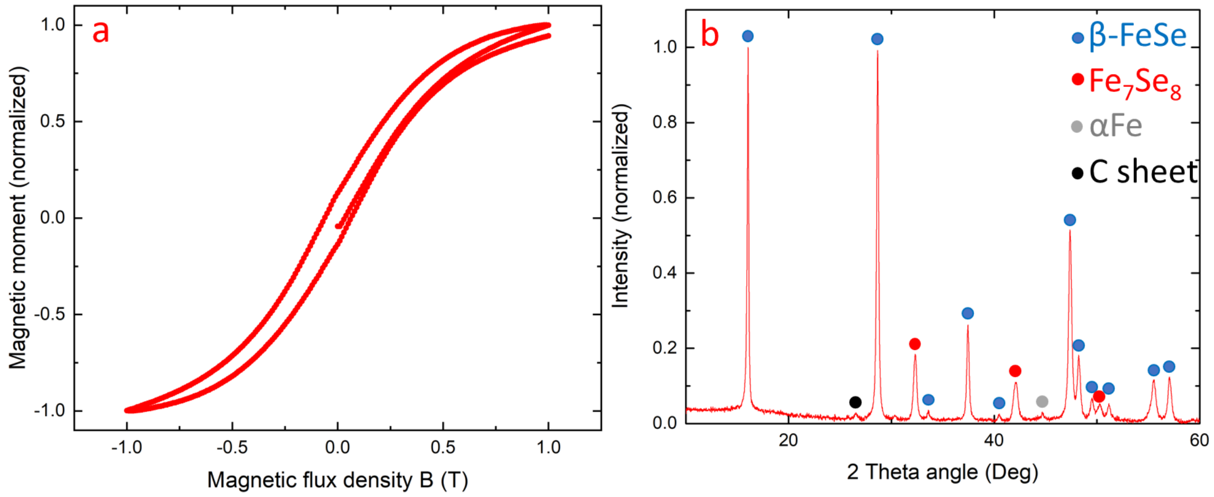

Figure 0-7 : (a) Mesure du moment magnétique normalisé sur les valeurs à B = 1 et -1 T d'un échantillon de FeSe préparé par frittage flash. (b) graphique de diffraction des rayon X du même échantillon permettant d'identifier les phases en présence, le bleu (●), *le rouge* (●), le gris *(●) et le noir (●) sont respectivement les phases β-FeSe, Fe_7Se_8, α-Fe et des restes de carbone du moule.*

I.3.c. Etude complémentaire sur les massifs en Fer-Sélénium

Malgré le grand nombre d'échantillons que j'ai synthétisé, je n'ai pas pu préparer un FeSe avec uniquement la phase supraconductrice, car les phases ferri/ferromagnétiques ont toujours été présentes. Avec ceci, j'ai remarqué une forte dégradation des performances supraconductrices après seulement quelques mois au profit d'une augmentation du moment magnétique ferri/ferromagnétique. Ces observations ont pu être reliées à un phénomène de dégradation de la phase β-FeSe qui se transforme en Fe_7Se_8 et en α-Fe.

Enfin la supraconductivité de la phase β-FeSe de stœchiométrie 1:1 n'apparait qu'avec une légère déficience en Sélénium. Ainsi, lors d'une synthèse avec une stœchiométrie Fe_1Se_1 (1 atome de Fer pour 1 atome de Sélénium) nous observons l'apparition d'une phase trop riche en Sélénium (Fe_7Se_8) et donc un moment magnétique supraconducteur et ferrimagnétique ce qui signifie une phase β-FeSe déficiente en Sélénium. Mais si la synthèse a eu lieu avec une déficience en Sélénium dans la stœchiométrie comme $Fe_1Se_{0.975}$, nous obtenons une phase β-FeSe non déficient en Sélénium et une phase secondaire α-Fe, ce qui se traduit par un moment uniquement ferromagnétique.

Ces éléments m'ont permis de conclure que dans l'état actuel des connaissances, un massif supraconducteur en FeSe polycristallin ne semble pas pouvoir être synthétisé sans phases secondaires ferri/ferromagnétique et ne permet donc pas d'avoir des propriétés suffisantes pour être compétitif avec d'autres matériaux fabriqués avec les mêmes méthodes de synthèses tel que les massifs en MgB_2.

I.4. Caractérisation d'YBaCuO massifs fabriqués par Infiltration Growth

I.4.a. YBaCUO massifs synthétisés par Infiltration Growth

Les massifs supraconducteurs en YBaCuO démontrent des propriétés exceptionnelles quand ils sont synthétisés sous la forme de monocristaux de grande tailles (plusieurs centimètres de diamètre) à l'aide de la méthode dite de Melt Growth (MG). Cette méthode consiste à faire réagir les poudres de précurseurs mélangés ($Y_2Ba_1Cu_1O_5$ et $Ba_3Cu_5O_8$) jusqu'à faire grossir un monocristal.

Ainsi nous pouvons atteindre un excellent courant critique même en présence de fort champ magnétique permettant de piéger des champs magnétiques de 16 T à 40 K.

Néanmoins, cette méthode de synthèse ne permet de fabriquer que des monocristaux denses avec peu de possibilités d'adaptation aux applications en génie électrique.

La méthode de synthèse par Infiltration Growth (IG) permet de synthétiser des monocristaux via l'infiltration du précurseur $Ba_3Cu_5O_8$, liquéfié à haute température, à travers l'autre poudre précurseurs $Y_2Ba_1Cu_1O_5$. L'avantage de cette méthode est d'avoir une plus grande souplesse sur la forme de l'échantillons et sur sa densité en travaillant sur la forme donnée au précurseurs $Y_2Ba_1Cu_1O_5$ jusqu'à, par exemple, pouvoir en faire une mousse (Figure 0-2.d).

Dans cette optique un collègue, Dr. S. Pavan Kumar Naik de l'AIST de Tsukuba, a fabriqué des massifs IG-YBaCuO à l'aide de poudre précurseurs sur lesquelles un traitement aux ultrasons a été appliqué pour réduire la taille des grains et donc optimiser les performances du supraconducteur. Il a donc réalisé deux échantillons, l'un synthétisé avec des poudres ayant reçu 45 min de traitement par ultrason, l'échantillon S-45, et l'autre avec des poudres ayant reçu 60 minutes de traitement par ultrason, l'échantillon S-60. Ce sont ces échantillons que j'ai caractérisé à l'aide d'un aimant à forts champs.

I.4.b. Caractérisation des propriétés supraconductrices sous haut champ magnétique

Pour caractériser les échantillons S-45 et S-60 j'ai pu avoir accès à un aimant « haut champ » mis à disposition par le HFML basé à Nimègue aux Pays Bas. Cet aimant résistif de 20 MW permet de générer jusqu'à 33 T dans un diamètre de 32 mm. Pour mesurer les propriétés magnétiques dans un si petit diamètre j'ai utilisé la méthode de mesure de la force magnétique par cantilever. Elle consiste à mesurer la variation de la capacité C entre une languette de cuivre flexible, le cantilever, où est fixé l'un des échantillons et une plaque fixe juste en dessous. Comme on peut le voir sur la Figure 0-8, la force de Lorentz entre le courant supraconducteur de l'échantillon et le champ extérieur va pousser l'échantillons à s'éloigner du centre du champ de l'aimant lorsqu'il est placé juste au-dessus du dit-centre. Tordant ainsi le cantilever et donc faisant varier la capacité entre celui-ci et la plaque fixe.

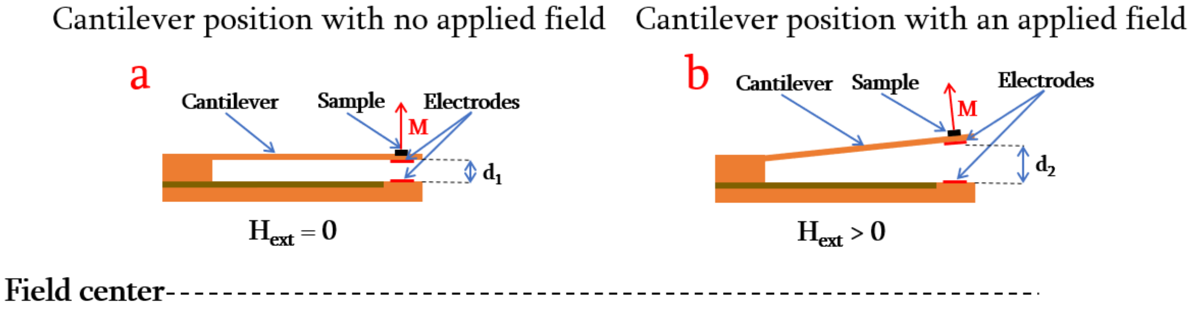

Figure 0-8 : Schéma du cantilever utilisé pour une mesure de force magnétique. En l'absence de champ magnétique, le cantilever est au repos car aucune force n'agit sur l'échantillons (a). Avec l'application d'un champ extérieur, l'échantillon supraconducteur va s'éloigner du centre du champ, tordre le cantilever et donc faire varier la capacité entre les deux plaques.

Avec cette méthode nous pouvons ainsi déterminer la valeur du courant critique circulant dans l'échantillons pour différentes températures et différents champs magnétiques appliqués via la formule suivante :

$$J_c = K\frac{d_1|\Delta C|}{C_2 B_r ABC}$$

Avec J_c la densité de courant critique, k le coefficient d'élasticité linéaire, d_1 la distance d'origine entre les plaques du condensateur, ΔC la variation de la capacité entre les deux plaques, C_2 la valeur de la capacité sous champ, B_r le champ magnétique radial et ABC les respectives longueur, largeur et épaisseur de l'échantillon.

Ne connaissant pas la valeur du coefficient d'élasticité du cantilever, le courant critique n'a pu être calculé qu'en valeur arbitraire. Pour extraire la bonne valeur du courant critique, j'ai utilisé des mesures faites par MPMS jusqu'à 7 T pour remettre à l'échelle les mesures hauts champs, c'est ce qui est présenté avec la Figure 0-9.

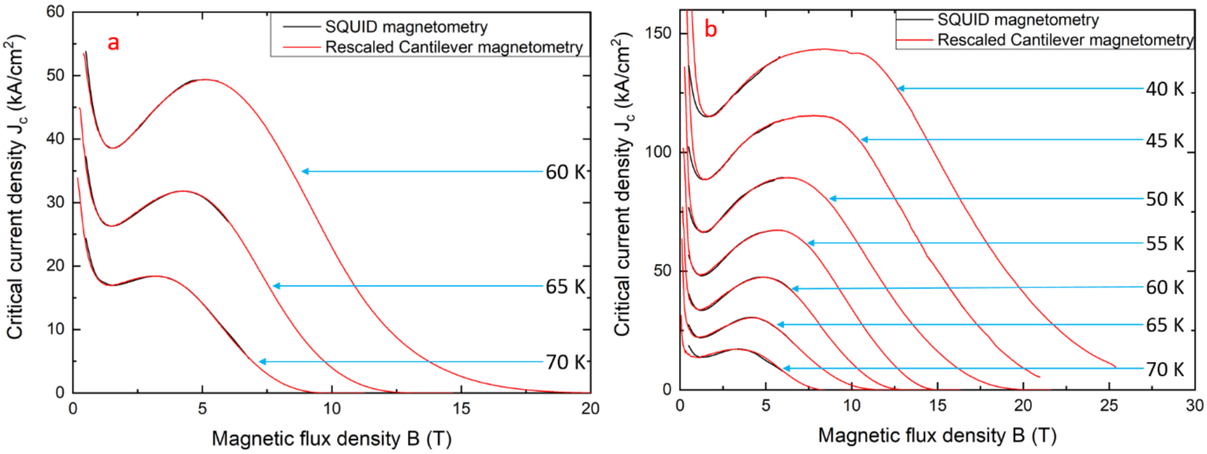

Figure 0-9 : Mesure de la densité de courant critique sous fort champ après remise à l'échelle grâce à des mesures via un système MPMS pour les échantillons S-45 (a) et S-60 (b).

A l'aide des résultats obtenus, j'ai pu simuler et calculer la valeur théorique du champ magnétique piégé à 40 K pour deux massifs de 3 cm de diamètre superposés. Il en résulte un

champ piégé de 18 T ce qui est comparables avec les mesures réalisées sur des massifs fabriqués par méthode melt growth.
Ce résultat tend à montrer que les YBaCuO synthétisés par infiltration growth offre des performances compétitives avec ceux générés par melt growth, encourageant ainsi le développement de cette méthode, parfois plus adaptée à certaines utilisations.

I.5. Conclusion générale

Les résultats obtenus durant cette thèse de doctorat ont permis d'apporter plusieurs conclusions sur les points étudiés :
De par les approximations utilisées pour le calcul des propriétés supraconductrices via le modèle de Bean, il est essentiel de bien choisir et définir les dimensions utilisées, ici $2\times1\times0.3$ mm^3, de définir un protocole et une méthode de calcul appliqués pour chaque échantillon à caractériser afin de les comparer efficacement.

Les méthodes de synthèses utilisées pour fabriquer des échantillons en Fer-Sélénium polycristallins et supraconducteurs ont mis en évidence des difficultés à obtenir de bonnes propriétés supraconductrices pour la phase β-FeSe sans phases secondaires ferro/ferrimagnétiques. Ainsi j'ai pu obtenir une phase supraconductrice fortement majoritaire mais un moment supraconducteur relativement faible
De plus, j'ai observé une forte dégradation des propriétés magnétiques due à la présence d'une transformation de la phase supraconductrice en phase ferro/ferrimagnétique dans mes échantillons. Il semble donc que d'autres méthodes de synthèses sont à privilégier pour la fabrication de supraconducteurs massifs en fer-Sélénium.

Dans une troisième partie, j'ai pu déterminer la densité de courant critique d'échantillons d'IG-YBaCuO en fonction de champ magnétiques extérieurs allant jusqu'à 33 T. Ceci a été possible grâce à une méthode de remise à l'échelle des mesures à haut champ à l'aide de mesures en utilisant un MPMS. Les résultats ont pu mettre en évidence la compétitivité des YBaCuO massifs préparés par infiltration growth avec un pré-traitement aux ultrasons par rapport aux massifs YBaCuO préparés par melt growth. De plus, j'ai pu également montrer l'utilité de la caractérisation de supraconducteurs par mesure de force magnétique avec un cantilever placé dans un aimant à haut champ.

Enfin cette thèse m'a permis de travailler sur des matériaux supraconducteurs de différentes maturités technologiques afin de déterminer les potentiels matériaux qui pourront être utilisés pour des applications en génie électrique. Une part importante de mon travail a donc été de combiner les besoins pour les applications en génie électrique des supraconducteurs avec les possibilités de développement en physique et chimie des matériaux.